

**Tandem mass spectrometry studies of β -D-N-glycopyranosides
derivatives and the wheat straw lignin**

by

Md. Sadiqur Rahman, M.Sc

A thesis submitted to the

School of Graduate Studies

in partial fulfillment of the requirements for the degree of

Master of Science in Chemistry

Faculty of Science

Memorial University of Newfoundland

May, 2014

St. John's

NEWFOUNDLAND

Abstract

Mass spectrometry is the tool of choice for the analysis of complex biomolecules and therefore it has been used for identification and characterization of different biological molecules such as oligosaccharides and glycoconjugates. In this thesis the first aim of this study was to use three different techniques to analyze the synthetic biological bivalent *N*-glycosides. The gas phase fragmentation of this series of synthetic bivalent *N*-glycosides (***I-6***) have been studied by electrospray ionization (ESI), matrix assisted laser desorption ionization (MALDI) mass spectrometry and quadrupole ion-trap mass spectrometry, in conjunction with using different “in-time” and “in-space” tandem mass spectrometers.

In the second aim of this study, MALDI-TOF/TOF-MS and MALDI-TOF/TOF-MS/MS analyses were used which have proven to be a powerful analytical tool capable for ionizing both small and large lignin oligomers. The MALDI mass spectra of the CIMV (CIMV is a world first for the manufacture of whitened paper pulp, sulfur free linear lignin and xylose syrup from annual fiber crops and hardwood).-extracted wheat straw lignin were recorded in the positive ion mode with a high-resolution MALDI-TOF/TOF-MS/MS. The positive ion mode MALDI-MS indicated the exact presence of a multitude of oligomers, from which 30 specific oligomeric ions were identified. The structural characterization of this novel series of 30 specific related oligomers was achieved by calculating the exact molecular masses measured by high-resolution MALDI-TOF-MS. High-energy collision-induced dissociation tandem mass spectrometric analyses MALDI-CID-TOF/TOF-MS/MS provided unique dissociation

patterns of the complete series of novel precursor ions. These MS/MS analyses provided diagnostic product ions, which enabled us to determination of the exact molecular structures and arrangement of the selected 30 different related ionic species.

AKNOWLEDGEMENT

I would like to express my sincere gratitude to my supervisor Dr. Joseph Banoub, Adjunct Professor of Chemistry at Memorial University and Head, Special Projects at the Science Branch of the Department of Fisheries and Oceans, for accepting me into his lab since 2010, for his valuable advice, supervision and his great interest into my research work. I would also like to thank Professors Paris Georghiou and Travis Fridgen for their valuable advice and for their time to be in my supervisory committee. My sincere thanks go to Professor Peter Pickup for his support and help that he provided to me during my study period in the Memorial University.

I would like to thank the Department of Fisheries and Oceans (DFO), St. John's for providing the resources that enabled me to perform my research works.

TABLE OF CONTENTS

ABSTRACT.....	ii
ACKNOWLEDGEMENT.....	iv
LISTS OF FIGURE.....	xiii
LISTS OF SCHEMES.....	xxi
LISTS OF TABLES.....	xxvii
LISTS OF ABBREVIATIONS.....	xxx
CHAPTER 1: INTRODUCTION.....	1
1.1. Glycoconjugates.....	1
1.2. Lectins.....	4
1.3. Divalent glycosides.....	6
1.4. Antigen (Ligand)-antibody interaction.....	6
1.5. Lignin in vascular plants (e.g. Straw lignin).....	8
1.6. Mass spectrometry.....	14
1.6.1. Principles.....	14
1.7. Ionization techniques.....	16
1.7.1. Hard or direct ionization techniques.....	16
1.7.2. Soft ionization techniques.....	18
1.7.2.1. MALDI.....	19
1.7.2.1.1. Principles of MALDI.....	19
1.7.2.2. Electrospray ionization (ESI).....	21
1.7.2.2.1. Principal of the electrospray sources.....	22

1.8. Mass analysers.....	24
1.8.1. The Quadrupole mass filter.....	25
1.8.2. Time-of-flight (TOF) mass analyser.....	28
1.8.2.1. Delayed pulsed extraction.....	30
1.8.2.2. Reflectron.....	31
1.8.3. Quadrupole ion trap.....	32
1.8.4. Ion cyclotron resonance and fourier transform mass spectrometry.....	33
1.9. Tandem mass spectrometry.....	35
1.9.1. High-energy collision dissociation (keV).....	38
1.9.2. Low-energy collision dissociation (Between 1 and 100 eV).....	38
1.10. CID-MS/MS induced dissociation MS/MS analysis using a hybride quadrupole orthogonal time of flight mass spectrometry (QqTOF).....	39
1.11. CID-MS/MS induced dissociation MS/MS analysis using a high energy MALDI	
CHAPTER 2: MATERIALS and METHODS.....	40
2.1. Synthetic bivalent β -D- <i>N</i> -glycosides.....	42
2.1.1. The origin and structure of novel synthetic bivalent β -D- <i>N</i> -glycosides.....	42
2.2. Isotopic Labelling: hydrogen deuterium exchange of the novel synthetic bivalent β - D- <i>N</i> -glycosides.....	43
2.3. Gas-phase fragmentation of glycoconjugates during the mass spectrometry.....	43

2.4.	ESI-QqTOF-MS of the novel synthetic bivalent β -D- <i>N</i> -glycosides.....	44
2.5.	Quadrupole ion traps mass spectrometry (QIT-MS) of the novel bivalent β -D- <i>N</i> -glycosides.....	46
2.6.	MALDI -TOF/TOF-CID-MS/MS of the novel synthetic bivalent β -D- <i>N</i> -glycosides.....	47
2.7.	Wheat straw lignin.....	48
2.7.1.	MALDI-TOF/TOF-MS of straw lignin extracted from CIMV process.....	49
<p>CHAPTER 3: GAS-PHASE FRAGMENTATION STUDY OF NOVEL SYNTHETIC BIVALENT β-D-<i>N</i>-GLYCOSIDES BY ESI-MS AND LOW-ENERGY COLLISION TANDEM MASS SPECTROMETRY (CID-MS/MS) USING AN ESI-QqTOF-HYBRID MS/MS INSTRUMENT (TANDEM IN SPACE).....</p>		
3.1.	Introduction.....	50
3.2.	ESI-QqTOF-MS analysis of the novel synthetic bivalent β -D- <i>N</i> -glycosides (1-6)..	51
3.3.	CID-MS/MS analysis of synthetic bivalent β -D- <i>N</i> -glycosides (1-6).....	52
3.3.1.	Low energy CID-MS/MS of the protonated precursor ion $[M+H]^+$ at m/z 388.1513 selected from the methoxynaphthalene substituted triazole β -D- <i>N</i> -galactopyranosides derivatives (1).....	53
3.3.2.	Low energy CID-MS/MS of the protonated precursor ion $[M+H]^+$ at m/z 438.1754 selected from the ethyltriazole β -D- <i>N</i> -lactopyranosides derivative (2).....	56
3.3.3.	Low energy CID-MS/MS of the protonated precursor ion $[M+H]^+$ at m/z 466.2011 selected from the butyltriazole β -D- <i>N</i> -lactopyranosides derivatives (3).....	59

3.3.4. Low energy CID-MS/MS of the protonated precursor ion $[M+H]^+$ at m/z 500.1900 selected from the anisoletriazole β -D- <i>N</i> -lactopyranosides derivatives (4)....	62
3.1.5. Low energy CID-MS/MS of the precursor ion $[M+H]^+$ at m/z 530.2012 selected from the dimethoxybenzenetriazole β -D- <i>N</i> -lactopyranosides derivatives (5).....	66
3.3.6. Low energy CID-MS/MS of the precursor ion $[M+H]^+$ at m/z 550.2009 selected from the methoxynaphthalene-triazole β -D- <i>N</i> -lactopyranosides derivatives (6).....	70
3.4. Conclusion.....	74
CHAPTER 4: GAS-PHASE FRAGMENTATION OF NOVEL SYNTHETIC BIVALENT <i>N</i> -GLYCOSIDES USING MALDI-MS IN CONJUNCTION WITH HIGH ENERGY COLLISION MASS SPECTROMETRY (MALDI-TOF/TOF-CID-MS/MS).....	76
4.1. Introduction.....	76
4.2. MALDI-TOF/TOF-MS analysis of the novel synthetic bivalent β -D- <i>N</i> -glycosides (1-6).....	77
4.3. MALDI-TOF/TOF-CID-MS/MS analysis of synthetic bivalent β -D- <i>N</i> -glycosides (1-6).....	78
4.3.1. High energy MALDI-TOF/TOF-CID-MS/MS of the sodiated precursor ion $[M+Na]^+$ at m/z 410.1210 selected from the methoxynaphthalene-substituted triazole β -D- <i>N</i> -galactopyranosides derivatives (1).....	79

4.3.2. High energy MALDI-TOF/TOF-CID-MS/MS of the sodiated precursor ion [M+Na] ⁺ at <i>m/z</i> 460.1533 selected from the ethyltriazole β -D- <i>N</i> -lactopyranosides derivative (2).....	83
4.3.3. High energy MALDI-TOF/TOF-CID-MS/MS of the sodiated precursor ion [M+Na] ⁺ at <i>m/z</i> 488.1750 selected from the butyltriazole β -D- <i>N</i> -lactopyranosides derivatives (3).....	88
4.3.4. High energy MALDI-TOF/TOF-CID-MS/MS of the sodiated precursor ion [M+Na] ⁺ at <i>m/z</i> 522.1580 extracted from the anisoletriazole β -D- <i>N</i> -lactopyranosides derivatives (4).....	92
4.3.5. High energy MALDI- TOF/TOF- CID-MS/MS of the sodiated precursor ion [M+Na] ⁺ at <i>m/z</i> 552.1720 extracted from the dimethoxybenzenetriazole β -D- <i>N</i> -lactopyranosides derivatives (5).....	98
4.3.6. High energy MALDI-TOF/TOF-CID-MS/MS of the sodiated precursor ion [M+Na] ⁺ at <i>m/z</i> 572.1750 selected from the methoxynaphthalene-triazole β -D- <i>N</i> -lactopyranosides derivatives (6).....	102
4.4. Conclusion.....	107
CHAPTER 5: GAS PHASE FRAGMENTATION STUDY OF NOVEL SYNTHETIC BIVALENT <i>N</i> -GLYCOSIDES BY THE QUADRUPOLE ION-TRAP EXTERNAL ESI SOURCES.....	110
5.1. Introduction.....	110
5.2. ESI-QIT-MS analysis of the novel synthetic bivalent <i>N</i> -glycosides (1-6).....	111

5.3. QIT-CID-MS/MS analysis of synthetic bivalent β -D- <i>N</i> -glycosides (1-6).....	112
5.3.1. Low energy ESI-QIT-CID-MS/MS of the protonated $[M+H]^+$ precursor ion at m/z 388.1160 selected from the methoxynaphthalene-substituted triazole β -D- <i>N</i> -galactopyranosides derivatives (1).....	113
5.3.2. Low energy ESI-QIT-CID-MS/MS of the sodiated precursor $[M+Na]^+$ at m/z 410.0934 selected from the methoxynaphthalene-substituted triazole β -D- <i>N</i> -galactopyranosides derivatives (1).....	115
5.3.3. Low energy ESI-QIT-CID-MS/MS of the protonated precursor ion $[M+H]^+$ at m/z 438.1528 selected from the ethyltriazole β -D- <i>N</i> -lactopyranosides derivative (2).....	117
5.3.4. Low energy ESI-QIT-CID-MS/MS of the sodiated precursor $[M+Na]^+$ at m/z 460.1248 selected from the ethyltriazole β -D- <i>N</i> -lactopyranosides derivative (2).....	119
5.3.5. Low energy ESI-QIT-CID-MS/MS of the protonated $[M+H]^+$ precursor ion at m/z 466.1814 selected from the butyltriazole β -D- <i>N</i> -lactopyranosides derivatives (3).....	122
5.3.6. Low energy ESI-QIT-CID-MS/MS of the sodiated precursor $[M+Na]^+$ at m/z 488.1896 selected from the butyltriazole β -D- <i>N</i> -lactopyranosides derivatives (3).....	125
5.3.7. Low energy ESI-QIT-CID-MS/MS of the protonated $[M+H]^+$ precursor ion at m/z 500.1234 selected from the anisoletriazole β -D- <i>N</i> -lactopyranosides derivatives (4).....	128
5.3.8. Low energy ESI-QIT-CID-MS/MS of the sodiated precursor $[M+Na]^+$ at m/z 522.0916 selected from the anisoletriazole β -D- <i>N</i> -lactopyranosides derivatives (4).....	131
5.3.9. Low energy ESI-QIT-CID-MS/MS of the protonated $[M+H]^+$ precursor ion at m/z 530.1297 selected from the dimethoxybenzenetriazole β -D- <i>N</i> -lactopyranosides derivatives (5).....	134

5.3.10. Low energy CID-MS/MS of the sodiated precursor $[M+Na]^+$ at m/z 552.0996 selected from the dimethoxybenzenetriazole β -D- <i>N</i> -lactopyranosides derivatives (5)...	136
5.3.11. Low energy ESI-QIT-CID-MS/MS of the protonated $[M+H]^+$ precursor ion at m/z 550.1177 selected from the methoxynaphthalene-triazole β -D- <i>N</i> -lactopyranosides derivatives (6).....	140
5.3.12. Low energy ESI-QIT-CID-MS/MS of the sodiated precursor $[M+Na]^+$ at m/z 572.1292 selected from the methoxynaphthalene-triazole β -D- <i>N</i> -lactopyranosides derivatives (6).....	142
5.4. Conclusion.....	144

CHAPTER 6: STRUCTUTAL ELUCIDATION OF CIMV WHEAT LIGNIN USING MALDI-TOF/TOF-MS AND HIGH-ENERGY CID-MS/MS ANALYSIS.....	148
6.1. Introduction.....	148
6.2. Isolation of Lignin.....	149
6.3. Characterization of the structure of lignin by degradation methods.....	150
6.4. Pyrolysis-gas chromatography- mass spectrometry (Py-GC-MS).....	150
6.5. Mass Spectrometric analyses of lignin with different ionization sources.....	151
6.6 Atmospheric pressure photoionization mass spectrometry and low-energy CID-MS/MS of CIMV lignin measured with a QqTOF-MS/MS instrument.....	153
6.7. MALDI-TOF/TOF-MS analysis of the Straw lignin.....	154
6.9. High energy MALDI-CID-TOF/TOF-MS/MS have been used to ascertain the molecular structure of these ions.....	160

6.9.1. High energy MALDI-TOF/TOF-CID-MS/MS of the protonated [M+H] ⁺ [4-hydroxy-(7→4')-coniferyl ether (8→5')-(3'methoxybenzene)] ion (1) at <i>m/z</i> 331.1173.....	160
6.9.2. High energy MALDI-TOF/TOF-CID-MS/MS of the precursor [4-hydroxyl-3-methoxy-(7→4')-coniferyl ether (8→5')-(1'methylelene 3'methoxybenzene)] ion [M] ⁺ or phenylcoumaran derivatives ion (2) at <i>m/z</i> 341.1011.....	165
6.9.3. High energy MALDI-TOF/TOF-CID-MS/MS of the precursor phenylcoumaran derivatives ion [M] ⁺ (3) at <i>m/z</i> 369.1310.....	168
6.9.4. High energy MALDI-TOF/TOF-CID-MS/MS of the protonated precursor phenylcoumaran derivatives ion [M+H] ⁺ (4) at <i>m/z</i> 403.1349.....	172
6.9.5. High energy MALDI-TOF/TOF-CID-MS/MS of the protonated [M+H] ⁺ trimeric phenylcoumaran precursor ion (5) at <i>m/z</i> 523.1926.....	176
6.9.6. High energy MALDI-TOF/TOF-CID-MS/MS of the protonated [M+H] ⁺ trimer phenylcoumaran derivatives precursor ion (6) at <i>m/z</i> 539.1888.....	180
6.9.7. High energy MALDI-TOF/TOF-CID-MS/MS of the protonated [M+H] ⁺ tetrameric phenylcoumaran precursor derivative ion (7) at <i>m/z</i> 655.2411.....	184
6.9.8. High energy MALDI-TOF/TOF-CID-MS/MS of the protonated [M+H] ⁺ tetrameric phenylcoumaran derivative (8) at <i>m/z</i> 671.2019.....	188
6.9.9. High energy MALDI-TOF/TOF-CID-MS/MS of the radical precursor ion [M] ^{•+} at <i>m/z</i> 491.1672.....	191
6.6. Conclusion.....	197
GENERAL CONCLUSION.....	198
REFERENCES.....	200

LIST OF FIGURES

Figure 1.1: Schematic representations of the physical forces that stabilize a lectin-carbohydrate complex.....	5
Figure 1.2: Schematic representations of possible covalent cross-links between polysaccharides and lignin in walls.....	11
Figure 1.3: Schematic representations of a lignin carbohydrate complex in wheat straw.....	12
Figure 1.4: Phenylpropanoid monomeric lignin precursors.....	12
Figure 1.5: Engymatic dehydrogradation of coniferyl alcohol.....	13
Figure 1.6: Common phenyl propane linkages in lignin.....	13
Figure 1.7: General schematic representation of a mass spectrometer.....	15
Figure 1.8: Schematic representations of principles of MALDI.....	21
Figure 1.9: Schematic representations of atmospheric MALDI Sources.....	21
Figure 1.10: Schematic representations of Electrospray sources.....	23
Figure 1.11: Schematic representations of the production of charged droplets during the ESI ionization process.....	24
Figure 1.12: Schemetric representation of a quadrupole mass spectrometer.....	26
Figure 1.13: Mathieu stability diagram in two dimentions (x and y).....	27
Figure 1.14: Schematic representations of principle of an LTOF instrument turned to analyze positive ions produced by MALDI.....	29

Figure 1.15: Schematic representations of description of a continuous extraction mode and a delayed pulsed extraction mode in a linear time-of-flight mass analyser.....	31
Figure 1.16: Schematic representations of quadrupole ion-trap.....	33
Figure 1.17: Schematic representations of an ion cyclotron resonance instrument.....	34
Figure 1.18: Schematic representations of tandem mass spectrometry in space and in time.....	35
Figure 1.19: Mathieu stability diagram (left) and trajectory of a trapped ion (right).....	37
Figure 2.1: Structure of synthetic bivalent β -D- <i>N</i> -glycosides.....	42
Figure 2.2: Possible fragmentation pathways during CID-MS/MS of a glycoconjugate...	44
Figure 2.3: Schematic representation of the CIMV process biorefinery.....	49
Figure 3.1(a): ESI-QqTOF-MS (+) of the methoxynaphthalene substituted triazole β -D- <i>N</i> -galactopyranosides (1).....	54
Figure 3.1(b): Low energy CID-MS/MS of the selected protonated precursor ion $[M+H]^+$ at m/z 388.1513 extracted from the methoxynaphthalene-substituted triazole β -D- <i>N</i> -galactopyranosides (1).....	54
Figure 3.2(a): ESI-QqTOF-MS(+) of the ethyltriazole β -D- <i>N</i> -lactopyranosides derivative (2).....	57
Figure 3.2(b): Low energy CID-MS/MS of the selected protonated precursor ion $[M+H]^+$ at m/z 438.1754 extracted from ethyltriazole β -D- <i>N</i> -lactopyranosides derivative (2)....	57
Figure 3.3(a): ESI-QqTOF-MS (+) of the butyltriazole β -D- <i>N</i> -lactopyranosides derivative (3).....	60

Figure 3.3(b): Low energy CID-MS/MS of the selected protonated precursor ion $[M+H]^+$ at m/z 466.2011 extracted from butyltriazole β -D- <i>N</i> -lactopyranosides derivatives (3)....	60
Figure 3.4(a): ESI-QqTOF-MS (+) of the anisoletriazole β -D- <i>N</i> -lactopyranosides derivatives (4).....	64
Figure 3.4(b): Low energy CID- MS/MS of the selected protonated precursor ion $[M+H]^+$ at m/z 500.1900 extracted from the anisoletriazole β -D- <i>N</i> -lactopyranosides derivatives (4).....	64
Figure 3.5(a): ESI-QqTOF-MS(+) of the dimethoxybenzenetriazole- β -D- <i>N</i> -lactopyranosides derivatives (5).....	68
Figure 3.5(b): Low energy CID-MS/MS of the selected protonated precursor ion $[M+H]^+$ at m/z 530.2012 extracted from the dimethoxybenzenetriazole β -D- <i>N</i> -lactopyranosides derivatives (5).....	68
Figure 3.6(a): ESI-QqTOF-MS(+) of the methoxynaphthalene-triazole β -D- <i>N</i> -lactopyranosides derivatives (6).....	72
Figure 3.6(b): Low energy CID-MS/MS of the selected protonated precursor ion $[M+H]^+$ at m/z 550.2009 extracted from methoxynaphthalene-triazole β -D- <i>N</i> -lactopyranosides derivatives (6).....	72
Figure 4.1(a): MALDI-TOF/TOF-MS (+) profile of the methoxynaphthalene-substituted triazole β -D- <i>N</i> -galactopyranosides derivatives (1).....	80
Figure 4.1(b): MALDI-TOF/TOF high energy CID-MS/MS of the precursor ion $[M+Na]^+$ at m/z 410.1210 selected from the methoxynaphthalene-substituted triazole β -D- <i>N</i> -galactopyranosides derivatives (1).....	81

Figure 4.2(a): MALDI-TOF/TOF-MS (+) profile of the ethyltriazole β -D- <i>N</i> -lactopyranosides derivative (2).....	85
Figure 4.2(b): High energy MALDI-CID-MS/MS of the selected sodiated precursor ion $[M+Na]^+$ at m/z 460.1533 extracted from the ethyltriazole β -D- <i>N</i> -lactopyranosides derivative (2).....	85
Figure 4.3(a): MALDI-TOF/TOF-MS (+) profile of the butyltriazole β -D- <i>N</i> -lactopyranosides derivatives (3).....	90
Figure 4.3 (b): High energy MALDI-CID-MS/MS of the selected sodiated precursor ion $[M+Na]^+$ at m/z 488.1750 extracted from the butyltriazole β -D- <i>N</i> -lactopyranosides derivatives (3).....	90
Figure 4.4 (a): MALDI-TOF/TOF-MS (+) profile of the anisoletriazole β -D- <i>N</i> -lactopyranosides derivatives (4).....	94
Figure 4.4 (b): High energy MALDI-CID-MS/MS of the selected sodiated precursor ion $[M+Na]^+$ at m/z 522.1580 extracted from the anisoletriazole β -D- <i>N</i> -lactopyranosides derivatives (4).....	94
Figure 4.5(a): MALDI-TOF/TOF-MS (+) profile of the dimethoxybenzenetriazole β -D- <i>N</i> -lactopyranosides derivatives (5).....	99
Figure 4.5 (b): MALDI-TOF/TOF high energy CID-MS/MS of the precursor ion $[M+Na]^+$ at m/z 552.1720 selected from the dimethoxybenzenetriazole β -D- <i>N</i> -lactopyranosides derivatives (5).....	99
Figure 4.6(a): MALDI-TOF/TOF-MS (+) profile of the methoxynaphthalene-triazole β -D- <i>N</i> -lactopyranosides derivatives (6).....	104

Figure 4.6(b): MALDI-TOF/TOF high energy CID-MS/MS of the precursor ion $[M+Na]^+$ at m/z 572.1750 selected from the methoxynaphthalene-triazole β -D- <i>N</i> -lactopyranosides derivatives (6).....	104
Figure 5.1(a): ESI-QIT-MS (+) of the methoxynaphthalene-substituted triazole β -D- <i>N</i> -galactopyranosides derivatives (1).....	113
Figure 5.1(b): ESI-QIT-CID-MS/MS of the selected protonated precursor ion $[M+H]^+$ at m/z 388.1160 extracted from the methoxynaphthalene-substituted triazole β -D- <i>N</i> -galactopyranosides derivatives (1).....	114
Figure 5.1(c): ESI-QIT-CID-MS/MS of the selected sodiated precursor $[M+Na]^+$ ion at m/z 410.0934 extracted the methoxynaphthalene-substituted triazole β -D- <i>N</i> -galactopyranosides derivatives (1).....	116
Figure 5.3(a): ESI-QIT-MS(+) of the ethyltriazole β -D- <i>N</i> -lactopyranosides derivative (2).....	118
Figure 5.3(b): ESI-QIT-CID-MS/MS of the selected protonated precursor ion $[M+H]^+$ at m/z 438.1528 extracted from the ethyltriazole β -D- <i>N</i> -lactopyranosides derivative (2)	118
Figure 5.3(c): ESI-QIT-CID-MS/MS of the selected sodiated precursor ion $[M+Na]^+$ at m/z 460.1248 extracted from the ethyltriazole β -D- <i>N</i> -lactopyranosides derivative (2)	121
Figure 5.5(a): ESI-QIT-MS (+) of the butyltriazole β -D- <i>N</i> -lactopyranosides derivatives (3).....	124
Figure 5.5(b): ESI-QIT-CID-MS/MS of the selected protonated precursor ion $[M+H]^+$ at m/z 466.1814 extracted from the butyltriazole β -D- <i>N</i> -lactopyranosides derivatives (3)	

.....	124
Figure 5.5(c): ESI-QIT-CID-MS/MS of the selected sodiated precursor ion $[M+Na]^+$ ion at m/z 488.1896 extracted from the butyltriazole β -D- <i>N</i> -lactopyranosides derivatives (3)	127
.....	127
Figure 5.7 (a): ESI-QIT-MS (+) of the anisoletriazole β -D- <i>N</i> -lactopyranosides derivatives (4).....	129
Figure 5.7(b): ESI-QIT-CID-MS/MS of the selected protonated precursor ion $[M+H]^+$ at m/z 500.1234 extracted from the anisoletriazole β -D- <i>N</i> -lactopyranosides derivatives (4).....	130
Figure 5.7(c): ESI-QIT-CID-MS/MS of the selected sodiated precursor ion $[M+Na]^+$ ion at m/z 522.0916 extracted from the anisoletriazole β -D- <i>N</i> -lactopyranosides derivatives (4).....	132
Figure 5.9(a): ESI-QIT-MS(+) of the dimethoxybenzenetriazole β -D- <i>N</i> -lactopyranosides derivatives (5).....	135
Figure 5.9(b): ESI-QIT-CID-MS/MS of the selected protonated precursor ion $[M+H]^+$ at m/z 530.1297 extracted from the dimethoxybenzenetriazole β -D- <i>N</i> -lactopyranosides derivatives (5).....	135
Figure 5.9(c): CID-QIT-MS/MS of the selected sodiated precursor ion $[M+Na]^+$ ion at m/z 552.0996 extracted from the dimethoxybenzenetriazole β -D- <i>N</i> -lactopyranosides derivatives (5).....	138
Figure 5.11(a): ESI-QIT-MS (+) of the methoxynaphthalene-triazole β -D- <i>N</i> -lactopyranosides derivatives (6).....	141

Figure 5.11(b): CID-QIT-MS/MS of the selected protonated precursor ion $[M+H]^+$ at m/z 550.1177 extracted from the methoxynaphthalene-triazole β -D- <i>N</i> -lactopyranosides derivatives (6).....	141
Figure 5.11(c): ESI-QIT-CID-MS/MS of the selected sodiated precursor ion $[M+Na]^+$ ion at m/z 572.1292 extracted from the methoxynaphthalene-triazole β -D- <i>N</i> -lactopyranosides derivatives (6).....	143
Figure 6.4 (a): Characteristic ions obtained from the MALDI-TOF/TOF-MS analysis of the wheat straw lignin recorded in the positive ion mode scanning m/z 300–400.....	156
Figure 6.4(b): Characteristic ions obtained from the MALDI-TOF/TOF-MS analysis of the wheat straw lignin recorded in the positive ion mode scanning m/z 400–500.....	157
Figure 6.4(c): Characteristic ions obtained from the MALDI-TOF/TOF-MS analysis of the wheat straw lignin recorded in the positive ion mode scanning m/z 500 – 600.....	157
Figure 6.4(d): Characteristic ions obtained from the MALDI-TOF/TOF-MS analysis of the wheat straw lignin recorded in the positive ion mode scanning m/z 600–700.....	158
Figure 6.5 (c): Tentative structures of the nine different ions isolated obtained from the wheat straw lignin, recorded by positive mode by MALDI-TOF/TOF-MS.....	159
Figure 6.9.1: High Energy MALDI-TOF/TOF-CID-MS/MS of the selected protonated $[M+H]^+$ phenylcoumaran derivatives precursor ion (1) at m/z 331.1173.....	162
Figure 6.9.2: High energy MALDI-TOF/TOF-CID-MS/MS of the selected precursor ion $[M]^+$ phenylcoumaran derivatives ion (2) at m/z 341.1011.....	166
Figure 6.9.3: High energy MALDI-CID-MS/MS of the selected precursor ion $[M]^+$ phenylcoumaran derivatives ion (3) at m/z 369.1310.....	170

Figure 6.9.4: High energy MALDI-CID-MS/MS of the selected protonated precursor ion $[M+H]^+$ phenylcoumaran derivatives ion (4) at m/z 403.1349.....	174
Figure 6.9.5: High energy MALDI-TOF/TOF-CID-MS/MS of the selected protonated precursor ion $[M+H]^+$ phenylcoumaran derivatives ion (5) at m/z 523.1926.....	178
Figure 6.9.6: High energy MALDI-TOF/TOF-CID-MS/MS of the selected protonated $[M+H]^+$ precursor ion phenylcoumaran derivatives ion (6) at m/z 539.1888.....	182
Figure 6.9.7: High energy MALDI-CID-MS/MS of the selected protonated $[M+H]^+$ phenylcoumaran derivatives precursor ion (7) at m/z 655.2411.....	186
Figure 6.9.8: High energy MALDI-TOF/TOF-CID-MS/MS of the selected protonated $[M+H]^+$ ion (8) at m/z 671.2019.....	190
Figure 6.9.9: High energy MALDI-CID-MS/MS of the selected radical precursor ion $[M]^{\bullet+}$ (9) at m/z 491.1672.....	194

LIST OF SCHEMES

Scheme 3.1: The tentative proposed fragmentation routes obtained during the ESI-CID-MS/MS of the protonated molecule $[M+H]^+$ at m/z 388.1513 extracted from the methoxynaphthalene substituted triazole β -D- <i>N</i> -galactopyranosides (1).....	55
Scheme 3.2: The tentative proposed fragmentation routes obtained during the ESI-CID-MS/MS of the protonated molecule $[M+H]^+$ at m/z 438.1754 extracted from the ethyltriazole β -D- <i>N</i> -lactopyranosides derivative (2).....	58
Scheme 3.3: The tentative proposed fragmentation routes obtained during the ESI-CID-MS/MS of the protonated molecule $[M+H]^+$ at m/z 466.2011 extracted from butyltriazole β -D- <i>N</i> -lactopyranosides derivative (3).....	61
Scheme 3.4: The tentative proposed fragmentation routes obtained during the ESI-CID-MS/MS of the protonated molecule $[M+H]^+$ at m/z 500.1900 extracted from the anisoletriazole β -D- <i>N</i> -lactopyranosides derivatives (4).....	65
Scheme 3.5: The tentative proposed fragmentation routes obtained during the ESI-CID-MS/MS of the protonated molecule $[M+H]^+$ at m/z 530.2012 extracted from the dimethoxybenzenetriazole- β -D- <i>N</i> -lactopyranosides derivatives (5).....	69
Scheme 3.6: The tentative proposed fragmentation routes obtained during the ESI-CID-MS/MS of the protonated molecule $[M+H]^+$ at m/z 550.2009 extracted from methoxynaphthalene-triazole β -D- <i>N</i> -lactopyranosides derivatives (6).....	73
Scheme 4.1: The tentative proposed fragmentation routes obtained during MALDI-TOF/TOF high energy CID-MS/MS of the sodiated precursor ion $[M+Na]^+$ at m/z 410.1210 selected from methoxynaphthalene-substituted triazole β -D- <i>N</i> -galactopyranosides derivatives (1).....	82

Scheme 4.2: (a) The tentative proposed fragmentation routes obtained during MALDI-TOF/TOF high energy CID-MS/MS of the sodiated precursor ion $[M+Na]^+$ at m/z 460.1533 selected from the ethyltriazole β -D- <i>N</i> -lactopyranosides derivative (2).....	86
Scheme 4.2: (b) The tentative proposed fragmentation routes obtained during MALDI-TOF/TOF high energy CID-MS/MS of the sodiated precursor ion $[M+Na]^+$ at m/z 460.1533 selected from the ethyltriazole β -D- <i>N</i> -lactopyranosides derivative (2).....	87
Scheme 4.3: The tentative proposed fragmentation routes obtained during MALDI-TOF/TOF high energy CID-MS/MS of the sodiated precursor ion $[M+Na]^+$ at m/z 488.1750 extracted from the butyltriazole β -D- <i>N</i> -lactopyranosides derivatives (3).....	91
Scheme 4.4(a): The tentative proposed fragmentation routes obtained during MALDI -TOF/TOF high energy CID-MS/MS of the sodiated precursor ion $[M+Na]^+$ at m/z 522.1580 selected from anisoletriazole β -D- <i>N</i> -lactopyranosides derivatives (4).....	95
Scheme 4.4(b): The tentative proposed fragmentation routes obtained during MALDI-TOF/TOF high energy CID-MS/MS of the sodiated precursor ion $[M+Na]^+$ at m/z 522.1580 selected from anisoletriazole β -D- <i>N</i> -lactopyranosides derivatives (4).....	96
Scheme 4.5: (a) The tentative proposed fragmentation routes obtained during MALDI-TOF/TOF high energy CID-MS/MS of the sodiated precursor ion $[M+Na]^+$ at m/z 552.1720 selected from dimethoxybenzenetriazole β -D- <i>N</i> -lactopyranosides derivatives (5).....	100
Scheme 4.5(b): The tentative proposed fragmentation routes obtained during MALDI-TOF/TOF high energy CID-MS/MS of the sodiated precursor ion $[M+Na]^+$ at m/z 552.1720 selected from dimethoxybenzenetriazole β -D- <i>N</i> -lactopyranosides derivatives (5).....	101

Scheme 4.6(a): The tentative proposed fragmentation routes obtained during MALDI-TOF/TOF high energy CID-MS/MS of the sodiated precursor ion $[M+Na]^+$ at m/z 572.1750 selected from the methoxynaphthalene-triazole β -D- <i>N</i> -lactopyranosides derivatives (6).....	105
Scheme 4.6(b): The tentative proposed fragmentation routes obtained during MALDI-TOF/TOF high energy CID-MS/MS of the sodiated precursor ion $[M+Na]^+$ at m/z 572.1750 selected from the methoxynaphthalene-triazole β -D- <i>N</i> -lactopyranosides derivatives (6).....	106
Scheme 5.1(a): The tentative proposed fragmentation routes obtained during the low energy ESI-QIT-CID-MS/MS of the protonated molecules $[M+H]^+$ at m/z 388.1160 extracted from methoxynaphthalene-substituted triazole β -D- <i>N</i> -galactopyranosides derivatives (1).....	114
Scheme 5.1(b): The tentative proposed fragmentation routes obtained during the low energy ESI-QIT-CID-MS/MS of the sodiated molecule $[M+Na]^+$ at m/z 410.0934 extracted from the methoxynaphthalene-substituted triazole β -D- <i>N</i> -galactopyranosides derivatives (1).....	116
Scheme 5.2(a): The tentative proposed fragmentation routes obtained during the low energy ESI-QIT-CID-MS/MS of the protonated molecular ion $[M+H]^+$ at m/z 438.1528 extracted from the ethyltriazole β -D- <i>N</i> -lactopyranosides derivative (2).....	119
Scheme 5.2(b): The tentative proposed fragmentation routes obtained during the low energy ESI-CID-MS/MS of the sodiated molecular ion $[M+Na]^+$ at m/z 460.1248 extracted from the ethyltriazole β -D- <i>N</i> -lactopyranosides derivative (2).....	122

Scheme 5.3(a): The tentative proposed fragmentation routes obtained during the low energy ESI-QIT-CID-MS/MS of the protonated molecular ion $[M+H]^+$ at m/z 466.1814 extracted from the butyltriazole β -D- <i>N</i> -lactopyranosides derivatives (3).....	125
Scheme 5.3(b): The tentative proposed fragmentation routes obtained during the low energy ESI-QIT-CID-MS/MS of the sodiated molecular ion $[M+Na]^+$ at m/z 488.1896 extracted from the butyltriazole β -D- <i>N</i> -lactopyranosides derivatives (3).....	128
Scheme 5.4(a): The tentative proposed fragmentation routes obtained during the low energy ESI-QIT-CID-MS/MS of the protonated molecular ion $[M+H]^+$ at m/z 500.1234 extracted from the anisoletriazole β -D- <i>N</i> -lactopyranosides derivatives (4).....	130
Scheme 5.4(b): The tentative proposed fragmentation routes obtained during the low energy ESI-QIT-CID-MS/MS of the sodiated molecular ion $[M+Na]^+$ at m/z 522.0916 extracted from the anisoletriazole β -D- <i>N</i> -lactopyranosides derivatives (4).....	133
Scheme 5.5(a): The tentatively proposed fragmentation routes obtained during the low energy ESI-QIT-CID-MS/MS of the protonated molecular ion $[M+H]^+$ at m/z 530.1297 extracted from the dimethoxybenzenetriazole β -D- <i>N</i> -lactopyranosides derivatives (5).....	136
Scheme 5.5(b): The tentative proposed fragmentation routes obtained during the low energy ESI-QIT-CID-MS/MS of the sodiated molecular ion $[M+Na]^+$ at m/z 552.0996 extracted from the dimethoxybenzenetriazole β -D- <i>N</i> -lactopyranosides derivatives (5).....	139
Scheme 5.6 (a): The tentative proposed fragmentation routes obtained during the low energy ESI-CID-QIT-MS/MS of the protonated molecule $[M+H]^+$ at m/z 550.1177	

extracted from the methoxynaphthalene-triazole β -D- <i>N</i> -lactopyranosides derivatives (6).....	142
Scheme 5.6 (b): The tentatively proposed fragmentation routes obtained during the low energy ESI-QIT-CID-MS/MS of the sodiated molecule $[M+Na]^+$ at m/z 572.1292 extracted from the methoxynaphthalene-triazole β -D- <i>N</i> -lactopyranosides derivatives (6).....	144
Scheme 6.1: The tentatively proposed fragmentation routes obtained during MALDI- TOF/TOF high energy CID-MS/MS of the protonated $[M+H]^+$ phenylcoumaran derivatives precursor ion (1) at m/z 331.1173.....	163
Scheme 6.2: The tentatively proposed fragmentation routes obtained during MALDI- TOF/TOF high energy CID-MS/MS of the molecular ion $[M]^+$ phenylcoumaran derivatives ion (2) at m/z 341.1011.....	167
Scheme 6.3: The tentatively proposed fragmentation routes obtained during MALDI- TOF/TOF high energy CID-MS/MS of the protonated ion $[M]^+$ phenylcoumaran derivatives ion (3) at m/z 369.1310.....	171
Scheme 6.4: The tentatively proposed fragmentation routes obtained during MALDI- TOF/TOF high energy CID-MS/MS of the protonated ion $[M+H]^+$ phenylcoumaran derivatives ion (4) at m/z 403.1349.....	175
Scheme 6.5: The tentatively proposed fragmentation routes obtained during MALDI- TOF/TOF high energy CID-MS/MS of the protonated phenylcoumaran derivatives ion (5) $[M+H]^+$ at m/z 523.1926.....	179

Scheme 6.6: The tentative proposed fragmentation routes obtained during MALDI-TOF/TOF high energy CID-MS/MS of the protonated ion $[M+H]^+$ phenylcoumaran derivatives ion (6) at m/z 539.1888.....	183
Scheme 6.7: The tentative proposed fragmentation routes obtained during MALDI-TOF/TOF high energy CID-MS/MS of the protonated ion $[M+H]^+$ (7) at m/z 655.2411.....	187
Scheme 6.8: The tentative proposed fragmentation routes obtained during MALDI-TOF/TOF high energy CID-MS/MS of the protonated ion $[M+H]^+$ (8) at m/z 671.2019.....	191
Scheme 6.9: The tentative proposed fragmentation routes obtained during MALDI-TOF/TOF high energy CID-MS/MS of the $[M]^+$ (9) at m/z 491.1652.....	195

LISTS OF TABLES

Table 1.A: Classification of antibodies.....	7
Table 1.B: Classification of antigens.....	7
Table 1.C: Linkage found in soft wood.....	10
Table 1.D: Types of analysers used in mass spectrometry.....	25
Table 3.A: Characteristic product ions observed in the low energy ESI-CID-MS/MS of the protonated methoxynaphthalene substituted triazole β -D- <i>N</i> -galactopyranosides (1) precursor ion $[M+H]^+$ at m/z 388.1513.....	55
Table 3.B: Characteristic product ions observed in the low energy ESI-CID-MS/MS of the protonated ethyltriazole β -D- <i>N</i> -lactopyranosides derivative (2) precursor ion $[M+H]^+$ at m/z 438.1754.....	58
Table 3.C: Characteristic products ions observed in the low energy ESI-CID-MS/MS of the protonated the butyltriazole β -D- <i>N</i> -lactopyranosides derivatives (3) precursor ion $[M+H]^+$ at m/z 466.2011.....	62
Table 3.D: Characteristic product ions observed in the low energy ESI-CID-MS/MS of the protonated the anisoletriazole β -D- <i>N</i> -lactopyranosides derivative (4) precursor ion $[M+H]^+$ at m/z 500.1900.....	66
Table 3.E: Characteristic product ions observed in the low energy ESI-CID-MS/MS of the dimethoxybenzenetriazole β -D- <i>N</i> -lactopyranosides derivatives (5) precursor ion $[M+H]^+$ at m/z 530.2012.....	70
Table 3.F: Characteristic product ions observed in the low energy ESI-CID-MS/MS of the protonated the methoxynaphthalene-triazole β -D- <i>N</i> -lactopyranosides derivatives (6) precursor ion $[M+H]^+$ at m/z 550.2009.....	74

Table 4.A: Characteristic product ions observed in the MALDI-TOF/TOF high energy CID-MS/MS of the sodiated the methoxynaphthalene-substituted triazole β -D- <i>N</i> -galactopyranosides derivatives (1) precursor ion $[M+Na]^+$ at m/z 410.1210.....	83
Table 4.B: Characteristic product ions observed in the MALDI-TOF/TOF high energy CID-MS/MS of the sodiated ethyltriazole β -D- <i>N</i> -lactopyranosides derivative (2) molecule precursor ion $[M+Na]^+$ at m/z 460.1533.....	88
Table 4.C: Characteristic product ions observed in the MALDI-TOF/TOF high energy CID-MS/MS of the sodiated butyltriazole β -D- <i>N</i> -lactopyranosides derivatives (3) precursor ion precursor ion $[M+Na]^+$ at m/z 488.1750.....	92
Table 4.D: Characteristic product ions observed in the MALDI-TOF/TOF high energy CID-MS/MS of the sodiated the anisoletriazole β -D- <i>N</i> -lactopyranosides derivatives (4) precursor ion $[M+Na]^+$ at m/z 522.1580.....	97
Table 4.E: Characteristic product ions observed in the MALDI-TOF/TOF high energy CID-MS/MS of the sodtated the dimethoxybenzenetriazole β -D- <i>N</i> -lactopyranosides derivatives (5) precursor ion $[M+Na]^+$ at m/z 552.1720.....	102
Table 4.F: Characteristic product ions observed in the MALDI-TOF/TOF high energy CID-MS/MS of the sodiated methoxynaphthalene-substituted triazole β -D- <i>N</i> -lactopyranosides derivatives (6) precursor ion $[M+Na]^+$ at m/z 572.1750.....	107
Table 6: Characteristic ions obtained from the MALDI-TOF/TOF-MS analysis of the wheat straw lignin.....	155
Table 6.A: Characteristic product ions observed in the high energy MALDI-TOF/TOF- CID-MS/MS of the protonated $[M+H]^+$ phenylcoumaran derivatives precursor ion (1) at m/z 331.1173.....	164

Table 6.B: Characteristic product ions observed in the high energy MALDI-TOF/TOF-CID-MS/MS of the molecular ion $[M]^{\cdot+}$ phenylcoumaran derivatives ion (2) at m/z 341.1011.....	168
Table 6.C: Characteristic product ions observed in the high energy MALDI-TOF/TOF-CID-MS/MS of the precursor phenylcoumaran derivatives ion $[M]^{\cdot+}$ (3) at m/z 369.1310.....	172
Table 6.D: Characteristic product ions observed in the high energy MALDI-TOF/TOF-CID-MS/MS of the protonated ion $[M+H]^+$ phenylcoumaran derivatives ion (4) at m/z 403.1234.....	176
Table 6.E: Characteristic product ions observed in the high energy MALDI-TOF/TOF-CID-MS/MS of the selected protonated precursor ion $[M+H]^+$ (5) at m/z 523.1926....	180
Table 6.F: Characteristic product ions observed in the high energy MALDI-TOF/TOF-CID-MS/MS of the selected protonated $[M+H]^+$ precursor ion phenylcoumaran derivatives ion (6) at m/z 539.1888.....	184
Table 6.G: Characteristic product ions observed in the high energy MALDI-TOF/TOF-CID-MS/MS of the protonated $[M+H]^+$ ion (7) at m/z 655.2411.....	188
Table 6.H: Characteristic product ions observed in the high energy MALDI-TOF/TOF-CID-MS/MS of the protonated $[M+H]^+$ precursor ion (8) at m/z 671.2019.....	192
Table 6.I: Characteristic product ions observed in the high energy MALDI-TOF/TOF-CID-MS/MS of the precursor ion $[M]^{\cdot+}$ (9) at m/z 491.1652.....	196

LIST OF ABBREVIATION

AP: Atmospheric Pressure

BeqQ-MS: A hybrid mass spectrometer of BEQQ geometry (B, magnetic sector; E, electric sector; Q, quadrupole mass filter)

CI: Chemical Ionisation

CID: Collision Induced Dissociation

CIMV: CIMV is a world first for the manufacture of whitened paper pulp, sulfur free linear lignin and xylose syrup from annual fiber crops and hardwood

Da : Dalton

DIOS: Desorption/ Ionization on Silicon

DMSO: dimethyl sulfoxide

DNA: Deoxyribonucleic acid

DP: Declustering Potential

DC: Current Potential

EI: Electron Impact

ESI: Electrospray Ionization

FAB: Fast Atom Bombardment

FP: Focusing Potential

FT-ICR: Fourier Transform Ion Cyclotron Resonance

GC-MS: Gas Chromatography Mass Spectrometry

G: Coniferyl alcohol

H/D : Hydrogen / Deuterium

H: *p*-hydroxycinnamyl alcohol

LC-MS: Liquid Chromatography-Mass Spectrometry

LSIMS: Liquid Secondary Ion Mass Spectrometry

LIAD-MS: Laser-Induced Acoustic Desorption Mass Spectrometry

MS/MS: Tandem Mass Spectrometry

m/z: mass to charge ratio

MALDI: Matrix Assisted Laser Desorption Ionization

RF: Radiofrequency

S: Sinalbin alcohol

TOF: Time of Flight

Qq-TOF: Quadrupole Orthogonal Time of Flight

QIT: Quadrupole Ion Trap

Qhq: Quadrupole Hexapole Quadrupole

PA-IL and PA-III: The cytotoxic lectins are regulated via quorum sensing.

RpoS : The production of virulence factors and stationary-phase genes sigma factor.

CHAPTER 1: INTRODUCTION

1.1. Glycoconjugates

Glycans, are expressed on all mammalian cell surfaces and are responsible for triggering the initial contacts between microorganisms and circulating proteins.^{[1],[2]} Consequently, glycoconjugates are also responsible for the modulation of protein functions; they represent an important class of signalling triggers between extra- and intracellular events,^{[1],[2]} in addition to being responsible for bacterial/viral infections.^{[3]–[5]}

Glycoconjugates constitute the initial points of contact for the attachment and tissue colonization of several pathogens expressing carbohydrate-binding proteins. Although carbohydrate–protein interactions mediate ubiquitous physiological and pathophysiological processes, they are generally characterized by fragile association (milli to micromolar) with limited specificity and selectivity on a per-saccharide basis.^[6] ^[7] Nature usually compensates for this situation by exposing several copies of the same carbohydrate ligands on the extracellular domains of the cells.

More specifically, bacterial adhesion processes are commonly achieved through carbohydrate-binding lectins expressed on or shed from bacterial surfaces that can also be involved in host-tissue colonization and biofilm formation. In spite of the weaknesses of these key binding interactions in terms of avidity and selectivity on a per-saccharide basis, these attractive forces are dramatically and naturally reinforced by the presence of multiple copies of both the ligands and the receptor interactions.

Consequently, these interactions are transformed into potent attractive forces, dramatically and naturally reinforced when multiple ligand copies are presented to

similarly clustered receptors. This phenomenon, resulting from a synergistic and cooperative effect, is known as the glycocluster or dendritic effect.^[8] In its prevalent version, it is usually thought that this effect starts off from the enhanced affinity of a given multivalent glycoside toward a CRD (carbohydrate recognition domain) by fully occupying one active site at a time. Therefore the stabilization of the complex by macroscopic cross-linking effects with the multivalent protein receptors which are freely circulating in biological fluids is now an accepted phenomenon.

In addition, multivalency can induce particular clustering organization on the cell surface, which notably provides a strategy for controlling signal transduction pathways.^[9] Moreover; multivalency is regularly used in protein engineering to improve the affinity and specificity of biomolecular interactions.

Since a thorough understanding of biochemical pathways is hampered by the natural complexity of carbohydrates, chemical or chemo-enzymatic synthesis of multivalent carbohydrate ligands is likely to remain the method of choice for obtaining tailored architectures.^[10] Besides useful but polydisperse multivalent glycomimetics, new synthetic families of well-defined and monodisperse synthetic macromolecules have emerged, including glycoclusters and hyperbranched glycodendrimers.^[11]

Hence, multivalent presentation of an optimized monovalent glycomimetic, a so-called “lead”, and validation thereof using a wide range of biological, biophysical, and classical QSTAR techniques (The Applied Biosystems QSTAR XL quadrupole time-of-flight mass spectrometer is equipped with electrospray (ESI), nanospray, atmospheric pressure chemical ionization (APCI) and orthogonal MALDI ion sources.), can afford

artificial glycoforms,^[12] and these have played crucial roles in our understanding of multivalent carbohydrate–protein interactions.

The following is a quick explanation on how bacterial infections are initiated in human biological systems. For example, *Pseudomonas aeruginosa*, which is an opportunistic pathogen responsible for numerous nosocomial infections (A nosocomial, or hospital-acquired, infection is a new infection that develops in a patient during hospitalization. It is usually defined as an infection that is identified at least forty-eight to seventy-two hours following admission, so infections incubating, but not clinically apparent, at admission are excluded) in immuno-compromised or cystic fibrosis (CF) patients, employs specific carbohydrate–protein interactions for its infection strategy. These Gram-negative bacterium can be found in various environments, and causes a wide range of diseases. Accordingly, these bacteria initiate lung colonization of patients with chronic lung diseases as well as those under mechanical ventilation, and are often fatal to CF patients.^[13] In fact, CF patients show modifications in their respiratory and salivary mucins characterized by a higher percentage of heavily glycosylated ligands, which constitute active binding sites for the bacterium. For this reason, the different carbohydrate-binding proteins of this pathogen (pilin, flagellin, and non-pili lectins) constitute valuable therapeutic targets.

P. aeruginosa expresses several such carbohydrate-binding proteins, including two intracellular and outer membrane lectins, PA-IL and PA-IIL (also referred to as Lec A and Lec B), which show specificity for D-galactose and L-fucose, respectively. These two lectins are produced in high levels in association with the secondary cytotoxic virulence factors under quorum sensing control and RpoS,^{[14]–[16]} and therefore constitute

potentially interesting targets for the prevention of bacterial colonization and biofilm formation.^[17]

It is interesting to note that the activity of the galactophilic PA-I lectin/adhesin (PA-IL) is dependent upon the presence of Ca^{2+} cations.^[18] This soluble lectin is a virulence factor that has been recognized to induce toxicity for respiratory epithelial cells in primary culture,^[19] a high rate of mortality in a mouse model of gut-derived sepsis when associated with other toxins such as exotoxin A and elastase,^[20] and destruction of the alveolar–capillary barrier in mice.^[21] PA-IL is composed of 121 amino acids (51 kDa) associated as homotetramers.^[22] PA-IL displays medium-range affinity for D-galactose, with an association constant determined by an equilibrium dialysis study.^[23]

Accordingly, biological applications of synthetic poly-glycosylated derivatives, extend from the specific screening and targeting of lectins toward anti-infective strategies to their use in photodynamic therapy (Photodynamic therapy syndicates a drug (called a photosensitizer or photosensitizing agent) with a specific form of light to kill cancer cells.) or as vaccines, adjuvants, immunotherapy, and antiangiogenic agents.^[3]

1.2. Lectins

Lectins are universal carbohydrate-binding proteins of non-immune origin. This evolutionarily-conserved group comprises multi-subunits formed of multivalent protein responsible for the diverse biological function such as cell adhesion, cell recruitment, intercellular trafficking and immune recognition.^{[3], [24]-[26]}

The carbohydrate-binding location of lectins are generally thin structures on the surface of the protein that do not undergo tangible structural change upon ligand binding.^{[24], [27]} A single stage binding between monosaccharide or oligosaccharide and

lectin is defined as a monovalent binding. Nonetheless, monovalent carbohydrate-protein binding generally involves a very weak binding and weak binding constants. Solvent recognition of the hydrates surface of the lectin and the carbohydrates as well as the conformation changes of carbohydrates contributes greatly to the stabilization of the complex as explained in Figure 1.1

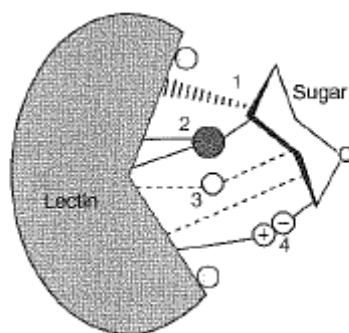


Figure 1.1: Schematic representations of the physical forces that stabilize a lectin-carbohydrate complex. These forces include (1) hydrophobic interactions; (2) Ca^{2+} coordination, direct and (3) water molecules- mediated hydrogen bonding; and (4) ionic interaction (in limited instances). Reorganisation of water molecules at the binding site of the lectin also contributes to binding. From T. K. Dam and C. F. Brewer. *Fundamental of lectin-carbohydrate interactions*. Elsevier. **2007**, pp 397. Reproduced with permission.

Usually, the multivalent interactions between carbohydrate and protein are involved to strengthen the binding and enhance the multivalent binding in the biosystem. In addition, the strength of binding and its specificity, enhance the multivalent interactions. Multivalent glycoassemblies of various kinds were designed to interfere effectively with and control multivalent carbohydrate-protein interactions.

In this contribution, the principal chemical architectures which have been introduced so far are briefly surveyed followed by a number of interesting and recent examples of biological applications. As part of our ongoing research program aimed at the understanding of initial steps involved in infectious phenomena via saccharide-lectin

recognition processes, the structural mass identification and biological evaluation of multivalent glycomimetic inhibitors are needed.^{[3]-[5]} Hence, the straightforward preparation of a new family of multivalent glycosylated architectures built around a more rigid hexaphenyl-benzene scaffold was proposed by Professor Rene Roy's group in the Department of Chemistry, University of Quebec, Montreal. This multivalent glycosylated architectures will help pursuing our systematic investigations regarding the roles played by the subtle but critical modulations of structural parameters responsible for high avidity, with specific and tailored presentation of peripheral recognition moieties.^[3]

1.3. Divalent glycosides

Multivalent ligand-lectin interactions usually occur with divalent glycosides. Indeed, it is important to determine the biological properties of bivalent ligands in order to understand how a given lectin can interact with the clusters and dendrimetric glycosyls of higher valency ligands.^{[28]-[33]}

1.4. Antigen (Ligand)-antibody interaction

An antigen is a specific molecule present on the cell surfaces of a pathogen, or a foreign molecular organism, which triggers antibody generation, or provokes a specific immune system. Antigens are usually present on macromolecules which can possess either one or more antigenic determinants. They are also called immunogens. Different kinds of antigen are summarized in Table 1.B.

The antibodies produced to a specific antigen are immunoglobins (protein molecules) containing one or more binding sides named paratope which are specific to this antigen. Five types of immunoglobins are listed in Table 1.A

Table 1.A: Classification of antibodies

Class	Additional Info	Functional Description
<i>IgG</i>	IgG1-IgG4	Predominant antibody found in blood and lymph. Predominant antibody involved in material immunity (The introduction of material into a person in order to provoke immunity to a disease. “Inoculate” is often used to refer to the historical practice of variolation). ^[34]
<i>IgA</i>	IgA1 (serum), IgA2 (secretory)	Predominant antibody found in saliva, tears, sweat, milk, intestinal secretions, and colostrum. ^[35]
<i>IgM</i>	Macroglobulin	First antibody type produced during a clonal response. Bound to lymphocytes and in serum. ^[36]
<i>IgD</i>	Surface bound	Bound to the surface of lymphocytes, very low concentrations in serum. ^[34]
<i>IgE</i>	Parasite Protection	Has a role in the protection from parasites. Low levels in serum. ^[34]

Table 1.B: Classification of antigens.^[34]

Class	Origin	Examples	
		Example type	Specific example
Natural	Plants, Bacteria, Animals	Particulate	Blood cell, Bacteria, Virus
		Soluble	Toxins, toxoids, proteins, carbohydrates, glycoproteins. Lipoproteins
Artificial	Chemically modified natural antigens	Iodinated proteins, protein-hapten conjugates	
Synthetic	Chemically synthesized molecules	Polypeptides, polyaminoacids, multichain aminoacid copolymers	

1.5. Lignin in vascular plants (e.g. Straw lignin)

The plant cell wall (CW) of all vascular plants and woods are composed of cellulose, hemicelluloses and lignins. Year after year, these plant constituents are reformed in large quantity by means of solar energy which means that a trophic structure used to describe the flow of mass and energy in the ecosystem. The original sources of all energy of an ecosystem is the solar energy into plant constituent and they provide mechanical strength, maintain cell shape, control cell expansion, regulate transport, provide protection, function in signalling processes, and finally store food reserves.^[37] The relevance of CW structure to biological sciences has driven many investigators to itemize, quantify, and structurally analyze components of CW structure which is composed of primary and secondary CW parts. Both cellular plant parts CW are composed of cellulose microfibrils (9-25%) and an interpenetrating matrix of hemicelluloses (25-50%), pectins (10-35%) and proteins (10%).^[38] Cellulose forms the framework of the CW while hemicelluloses cross-link non-cellulosic and cellulosic polymers.^{[39], [40]} Pectins provide cross-links and structural support to the CW, whereas proteins can function either structurally or enzymatically. Cellulose is composed of approximately 8×10^3 D-glucopyranose residues linked by β -D-(1 \rightarrow 4)-glycosidic bonds.^[41]

Hydrogen bonds hold about 40 of these glycan chains together to form a cellulose microfibril. The cellulose microfibril arrangements in the primary wall are random. Cellulose microfibrils are linked to hemicellulosic polysaccharides composed of xylans, mannans, galactans, or combinations thereof, which are attached to the cellulose fibers by H-bonding and through covalent linkages. Additionally, cross-linkages are formed by α -

D-(1→4)-linked-polygalacturonan (pectin) and the glycoprotein extension which is rich in hydroxyproline; these cross-linkages assist support and extension of the CW.^{[40],[42]-[44]} It is well accepted that the chemical structures of the various lignin biomolecules depend on the botanical origin and chemical compositing of the vegetable fibres.^[45] Proteins other than extensions are found in the CW and these include enzymes such as the cellulose synthases, hydrolases and oxidases.^[46] These enzymes are needed during the secondary growth process. They are especially important for the formation and thickening of the secondary CW and for the lignifications process, respectively. Thus, during cell growth, reorganization, *de novo* synthesis and insertion of new CW polymers, lead to formation of the secondary CW.^[47] It is at this stage that the inclusion of lignin into CW wall occurs and contributes to the strengthening of the CW matrix. In general, secondary walls are derived from primary walls by thickening and inclusion of lignin into the CW matrix. Secondary plant CWs contain hemicelluloses (10-40%) and are embedded in lignin (25%). Historically, this type of arrangement has been compared to steel rods embedded in concrete to form prestressed concrete.^[47] Cellulose and hemicelluloses appear to be more structurally-organized in the secondary CW than in the primary CW.

The diverse and complex nature of lignin monomers and hemicellulosic moieties in lignohemicellulosic bonds make stereotypic conceptualizations of secondary wall structures for all plants extremely difficult.

Phenolic moieties are present in plant CW. They can be classified generally into two main classes. The major class, known as lignin, is formed from oxidative cross-linking of phenolic alcohols. The second class is comprised of relatively simple phenolic

esters which are attached to wall polysaccharides, and which can be used for producing covalent cross-links through peroxidative and related activity.^[48]

A monolignol free radical which is describe in the Fig.1.5 can then undergo radical coupling reactions, producing different dimers, called dilignols. The percent abundance of this and other linkages found in softwood lignin has been determined and is shown in Table 1.C ^{[49],[50],[51]}

Table 1.C: Linkage found in soft wood

Linkage Type	Dimer Structure	Percent of Total Linkages (%)
β -O-4	Phenylpropane β - aryl ether	45-50
5-5	Biphenyl and Dibenzodioxocin	18-25
β -5		9-12
β -1	1,2-Diaryl propane	7-10
α -O-4	Phenylpropane α -aryl ether	6-8
4-O-5	Diaryl ether	4-8
β - β	β - β -linked structures	3

Lignin does not exist in the plant tissue as an independent polymer but it is bonded with other polymers, celluloses and hemicelluloses forming a complex through covalent bonds. Covalent Cross-Links in the Cell Wall is summarized in Figure 1.2

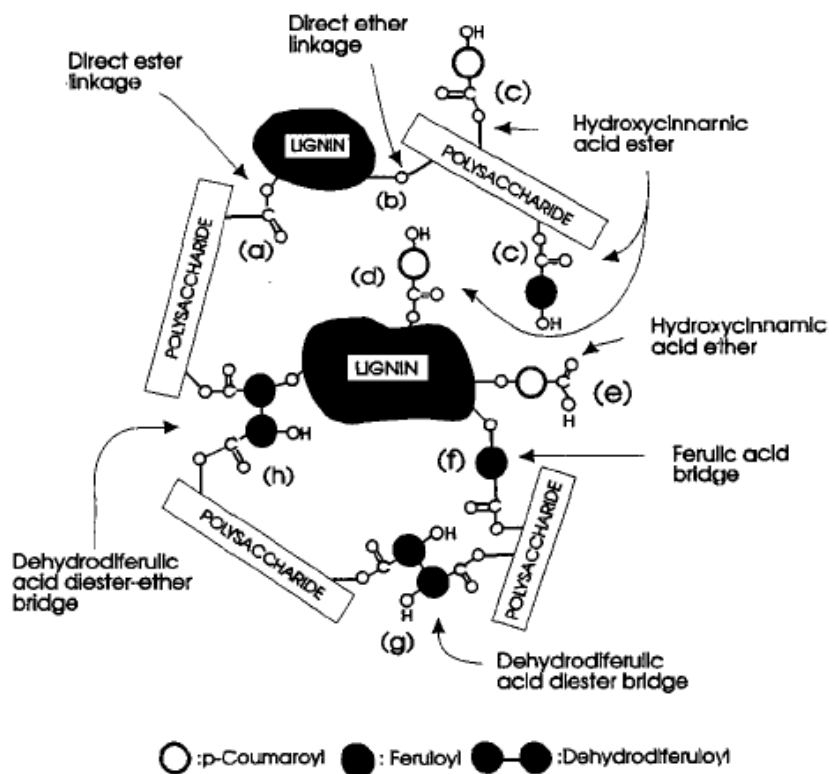


Figure 1.2: Schematic representations of possible covalent cross-links between polysaccharides and lignin in walls. From Kenji Iiyama, Thi Bach-Tuyet Lam, and Bruce A. Stone. Covalent Cross-Links in the Cell Wall. *Plant Physiol.* **1994**, *104*, 315-320. Reprinted, with permission.

Lignin is always associated with carbohydrates especially with hemicellulose having covalent bonds at two sites, namely the α -carbon and C-4 in the benzene ring and this association is called lignin carbohydrates complex formation.^[52] A lignin-carbohydrate complex is shown in Figure 1.3

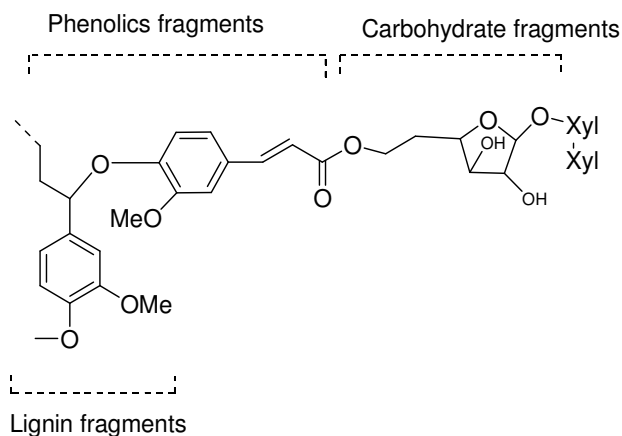


Figure 1.3: Schematic representations of a lignin carbohydrate complex in wheat straw. From R. Sun, J. M. Lawther, W. B. Banks. A tentative chemical structure of wheat straw lignin. *Ind. Crops Prod.* **1997**, 6, 1–8. Reprinted, with permission

Numerous studies with radioactive carbon confirms^[53] that there are three cinnamyl alcohols namely (1) *p*-hydroxycinnamyl alcohol, (2) coniferyl alcohol, and (3) sinapyl alcohol shown in Figure 1.4

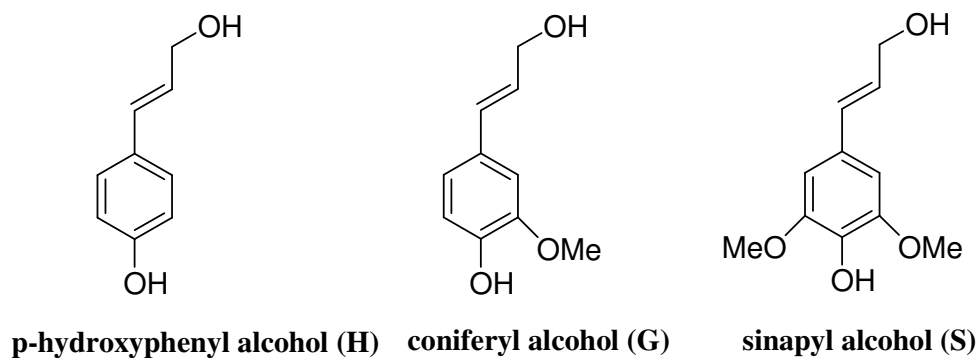


Figure 1.4: Phenylpropanoid monomeric lignin precursors. From S. Reale, A. D. Tullio, N. Spredi, and F. D. Angelis. Mass spectrometry in the biosynthetic and structural investigation of lignin. *Mass Spectrometry Reviews by Wiley Periodicals, Inc.*, **2004**, 23, 87–126. Reproduced, with permission.

In the presence of laccase, coniferyl alcohol undergoes dehydrogenation by losing its phenolic hydrogen to form a phenoxy radical stabilized by resonance shown in Figure 1.5

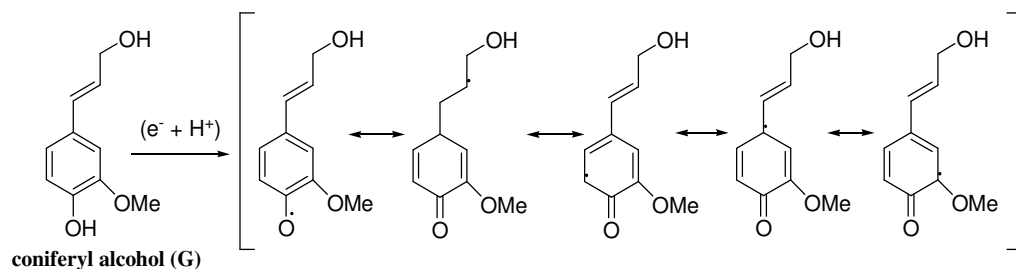


Figure 1.5: Engymatic dehydrogradation of coniferyl alcohol. From S. Reale, A. D. Tullio, N. Spreti, and F. D. Angelis. *Mass Spectrometry in the biosynthetic and structural investigation of lignin. Mass Spectrometry Reviews by Wiley Periodicals, Inc.*, **2004**, 23, 87– 126. Reproduced, with permission.

During the lignification process, these monolignols produce a complex three-dimensional amorphous lignin polymer via β -O-4, β -O-4, β -5, β -1, 5-5, 4-O-5 and β - β linkages^[52] which lacks the regular and ordered repeating units found in other polymers are described in Figure 1.6

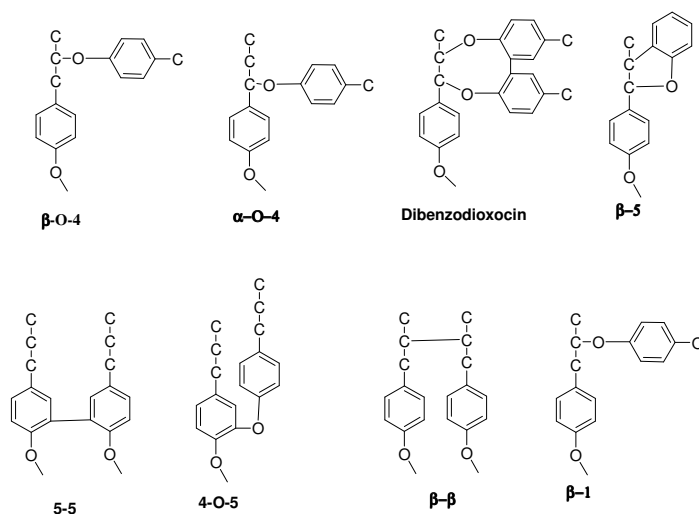


Figure 1.6: Common phenyl propane linkages in lignin. From Anvar U. Buranov, G. Mazza. *Lignin in straw of herbaceous crops. Industrial crops and products.* **2008**, 28, 237–259. Reproduced, with permission.

In the present thesis we will present the structural elucidation of wheat straw lignin extracted by the CIMV ^[54] procedure.

1.6. Mass spectrometry

Mass spectrometry is a technique used to determine the masses of molecules. A electrical charge is placed on the molecule and resulting molecular or fragments ions are separated by their mass-to-charge ratios (m/z). There are numerous types of mass spectrometers, varying in the types of ionization source and mass analyser configuration. The following sections summarize the key techniques of mass spectrometry used in the context of this thesis.

Mass spectrometry (MS) has become a powerful analytical tool for both quantitative and qualitative applications. In 1980's the development of soft ionization such as electrospray ionization (ESI) and matrix-assisted laser desorption ionization (MALDI) has allowed the conversion of biomolecules into gas-phase ions. These techniques possess a vital place in analytical chemistry due to their sensitivities, their tiny sample consumptions and their relative rapid time for analysis.

1.6.1. Principles

Generally, a mass spectrometer is composed of three main parts: the ionization sources, the analyser and the detector are described in Figure 1.7.

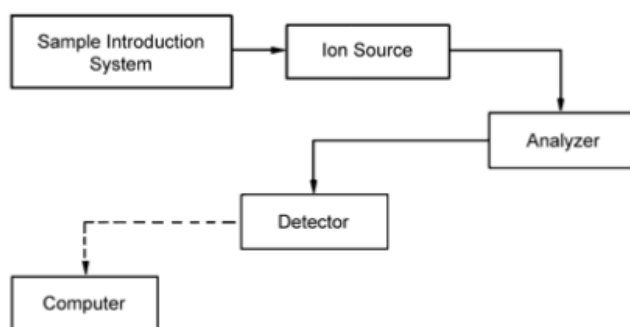


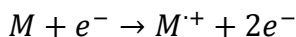
Figure 1.7: General schematic representation of a mass spectrometer.

In the mass spectrometer, the sample is first ionised in what is known as the ion source. In the source, which is normally heated, the volatilization of the molecules occurs and these will undergo ionization under a reduced vacuum atmosphere (10^{-5} Pa). In the ion source, the molecular ions M^{+} , and the fragment ions are also formed. The gaseous ions are then accelerated into a mass analyser. In the mass analyser the molecular ion and the fragment ions, are separated according to their mass-to-charge (m/z) ratio. Ultimately the detector collects the ions and their intensities are further quantified and amplified. Except for the sample introduction and the data part of the acquisition, all of these process are conducted in a low pressure 10^{-5} - 10^{-8} torr vacuum in order to decrease collisions between ions and neutral molecules. After the detector, a computer system processes the data and generates the mass spectrum, which specifies the difference of ion current observed according to the mass-to-charge ratio (m/z). The proper choice of ionization sources and analyser type will depend on the nature of the analytes (polarity variance) and on the information type desired (sensitivity, resolution, and mass range)

1.7. Ionization techniques

1.7.1. Hard or direct ionization techniques

Regardless of the method by which the sample is loaded into mass spectrometer (GC and/or direct injection), the ion source area is the only place where the charged species are normally created. These then pass to the gate of other compartments of the instrument, namely, the analyser and then the detector. Electron ionization (EI) and chemical-ionization (CI) are both traditional techniques using energetic electron beams during the ionization. Compared to EI, the CI process uses less energy. Chemical ionization has some advantages since it can produce spectra with less fragmentation than EI-MS, so it is easier to identify fragmentation processes. Both the electron- impact and the chemical-ionization techniques operate at high vacuum, while the sample is already in the gas phase. In EI, a tungsten filament produces a beam of electrons. A mixture of compounds to be analysed is initially injected into the GC where the mixture is vaporized in a heated chamber. The gas mixture travels through a GC column, where the compounds become separated as they interact with the column. The chromatogram on the right shows peaks which result from this separation. Those separated compounds then immediately enter the mass spectrometer. These electrons are accelerated and collide with the gaseous phase analyte injected into the sources and produce positively charged radical cations.

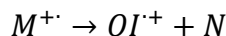


The resulting molecular ion normally undergoes fragmentations due to the hard nature of the EI process. Because it is a radical cation with an odd number of electrons, it can

fragment to give either a radical or an ion with an even number of electrons, or a molecule and a new radical cation. Both of the ways of ionization is shown below:



Even ion Radical

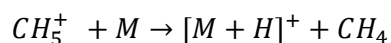
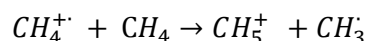
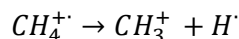
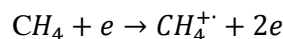


Odd ion Molecule

In proton transfer CI, that are other types like electron transfer , the electron beam ionises some reagent gas, which in its turn ionises the analytes by either providing, or abstracting, protons.

Chemical Ionization (CI) is a soft ionization technique that produces ions with not extensive but little excess energy. Consequently, less fragmentation is observed in the mass spectrum. Since this increases the abundance of the molecular ion, the technique is complimentary to 70 eV EI. CI is often used to confirm the molecular mass of unknown samples. In CI the source is enclosed in a small cell with openings for the electron beam, the reagent gas and the sample. The reagent gas in the CI source is ionised with an electron beam to produce a cloud of ions. When analyte molecules (M) are introduced to a source region with this cloud of ions, the reagent gas ions provide a proton to the analyte molecule and produce $[M+H]^+$ ions. The most common reagent gases are methane, isobutane and ammonia. Methane is a very powerful as a proton donor. Fragmentation is minimized in CI by dropping the amount of excess energy produced by

the reaction. If methane is introduced into the ion volume through the tube, the primary reaction with the electrons will be a classical EI reaction:



Both electron impact and chemical ionization are suitable for volatile and thermally stable organic compounds.^[55]

1.7.2. Soft ionization techniques

The development of soft ionization techniques such as electrospray (ESI) and matrix assisted laser desorption ionization (MALDI), have been instrumental for the structure elucidation of biomolecules (proteomics, genomics and glycomics). The contribution of MALDI and ESI to the different fields of analysis specially in biological molecules have resulted in the award of the Nobel Prize in Chemistry (2002) to John Fenn for developing ESI and Koichi Tanaka for developing MALDI.^{[56], [57]}

Thus, these soft ionization methods, like ESI and MALDI, guide from protonated molecular ions such as $[M+H]^+$, which can be used for molecular mass determination. These methods give minimal internal energy to the analyte and henceforth prevent its fragmentation. There are different soft ionizations techniques such as fast atom

bombardment (FAB),^{[58],[59]} liquid secondary mass spectrometry (LSIMS),^[60] matrix assisted laser desorption ionization (MALDI),^{[61],[62]} and electrospray ionization (ESI).^[63]

1.7.2.1. MALDI

MALDI was introduced by M. Karas, D. Bachmann and F. Hillenkamp^{[64]-[66]} in 1985. Since then it has become a powerful widespread sources for the production of intact gas-phase ions from a broad range of large, non-volatile and thermally-unstable compound. The representations of atmospheric MALDI Sources is illustrated in Figure 1.9. The uses of a suitable MALDI matrix for both desorption and ionization is very important for the accomplishment of this ionization method. This method build on the easy sample preparation and has a large tolerance for the contamination by salts, buffers, detergents and.^{[67], [68]} This method is very good for producing molar mass information from polar and high molecular mass biochemicals such olegonucleotides, carbohydrates, protein^[69] glycoconjugates,^[69] and lipids.^[70] In addition, MALDI is well- suited for the direct analysis of biomolecules in tissues. MALDI has also been used for the structural characterisation of vitellogenin protein a fish biomarker.^{[72],[73]} In addition, numerous investigations have also involved conventional MALDI instruments combined with thin-layer chromatography and MALDI mass spectrometry and the detection of affinity of purified crosslinked peptides by MALDI-TOF-MS combined with chemical cross-linking of protein.^{[73], [74]}

1.7.2.1.1. Principles of MALDI

The matrix and sample mixture are placed on a plate and, after evaporation of the solvent, the matrix will co-crystallize simultaneously with the analyte. The proper choice

of matrix is very important. Sometimes, it depends on various trials to get the proper matrix for the analytes. Usually 2,5-dihydroxybenzoic acid (DHB)^[75], sinapinic acid (SA) and α -cyano-4-hydroxycinnamic acid (CHCA) are the most commonly used matrix material for the analysis of proteins and peptides.^{[76],[77]} Matching of matrix with analyte is very important for optimizing the quality of results. The matrix molecules must have a strong absorption at the laser wavelength. The most commonly used laser type is the nitrogen laser (337nm). The solvent used depends on the solubility of the samples and matrix.

The precise mechanism of the MALDI process is not properly understood.^{[78],[79]} The irradiation by the laser heats the crystals by excitation of the matrix molecule. This produces a great amount of energy in the condensed phase. This fast heating causes localized sublimation of the matrix crystals, ablation of a portion of the crystal surface and spreading out of the matrix into the gas phase, with intact analyte in the expanding matrix plume.^[80] is shown in Figure 1.8. As this improvement has expanded the possibilities and applications of MALDI sources^{[81],[82]} such as Desorption ionization on silicon mass spectrometry DIOS^[83] which does not need a matrix, and SELDI^[84] (surface enhanced desorption ionization) in which the surface is modified with chemical functionality.

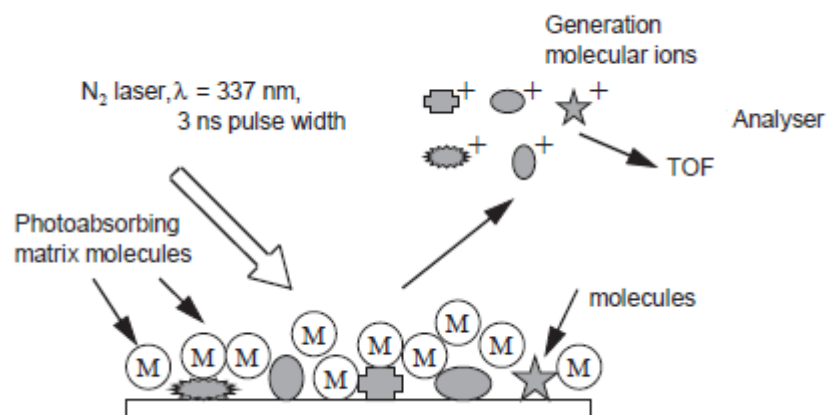


Figure 1.8: Schematic representations of principles of MALDI. From Hans J. Griessera,b, Peter Kingshottb,c, Sally L. McArthurb,d, Keith M. McLeanb, Gary R. Kinsele, Richard B. Timmonse Surface-MALDI mass spectrometry in biomaterialsresearch. *Biomaterials*. **2004**, 25, 4861– 4875. Reproduced with permission

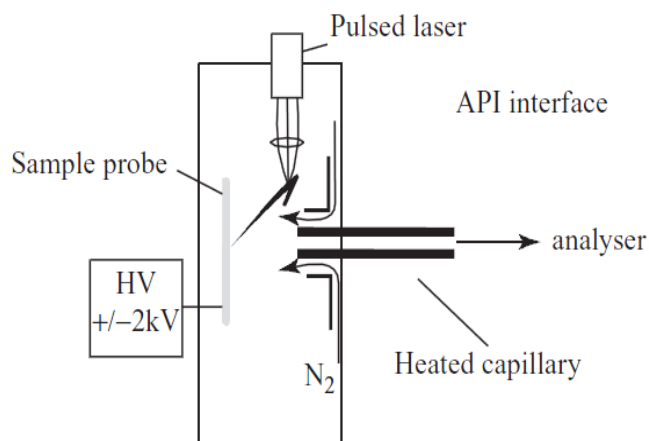


Figure 1.9: Schematic representations of atmospheric MALDI Sources. From E. D. Hoffmann, V. Stroobant. Principles and application mass spectrometry. Third edition. *John wily and sons. Ltd*. **2007**, pp 40. Reproduced, with permission

1.7.2.2. Electrospray ionization (ESI)

In 1980's concept of electrospray ionization achievement, abbreviated (ESI) was attributed to Fenn et al.^[56] who showed that multiply-charged ions could be produced from proteins. Initially, ESI was considered to be an ionization source dedicated to

protein analysis. After that, its popularity was extended not only to other polymers and complex biopolymers, but also to the analysis of small polar molecules. ESI allows for very high sensitivity to be reached, and it is very easy to couple to high-performance liquid chromatography HPLC,^[85] μ HPLC or capillary electrophoresis.^[86] The ESI principle and its complex biological applications have been widely reviewed.^{[87], [88]} One of the most important differences between MALDI and ESI is that although the sample is introduced to the ion source at atmospheric pressure, ESI uses a solvated sample that is infused into the instrument. However in the case of MALDI the introduction is in the solid state and under vacuum. When interfaced with LC, it is possible to efficiently utilize ESI for quantitative measurements.

1.7.2.2.1. Principal of the electrospray sources

In ESI-MS, the sample should be soluble preferably in a polar solvent, which can be infused into the ionization source via a thin needle, under atmospheric pressure is described in Figure 1.10. Before the sample goes to the mass analyser, the solvent is removed from the analyte. ESI is done by applying a strong electric field, under atmospheric pressure, to the liquid passing through a capillary tube (1–10 μLmin^{-1}).^[89]^[93] The electric potential difference applied between the capillary tube is 3–6 kV and the counter-electrode, separated by 0.3–2 cm, can produce electric fields of the order of 10^6Vm^{-1} .^[94] This results in the formation of highly-charged droplets, also called nebulisation. These droplets are then driven electrically and are evaporated by a warm neutral gas (usually nitrogen). In this situation the droplets break down and the size of the droplet continuously is being reduced.

As the droplet moves, solvent evaporates very fast from the droplet surface and the droplet gets smaller and smaller is summarized in Figure 1.11. The electrical charge density on the surface of the droplet increases and finally repulsive forces (Coulombic forces) exceed the surface tension of the solvent which results in breakdown of the droplets (Rayleigh limits) and the ions desorb into the gas phase. For this reason, the theory of ESI ion formation is also called ion evaporation method.^{[95], [96]} HPLC is highly efficient for separating complex mixture and a robust technique for identification of single substance.

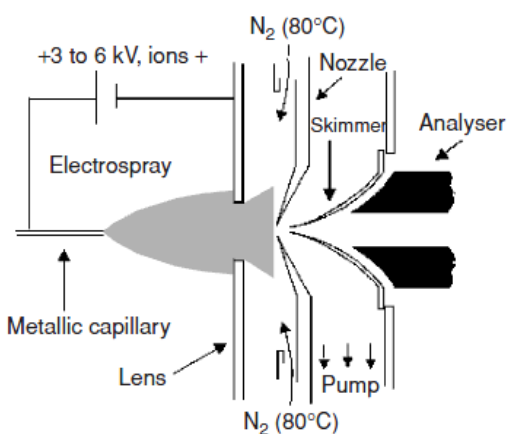


Figure 1.10: Schematic representations of Electrospray sources. From E. D. Hoffmann, V. Stroobant. Principles and application mass spectrometry. Third edition. John wily and sons. Ltd. 2007, pp 44. Reproduced, with permission.

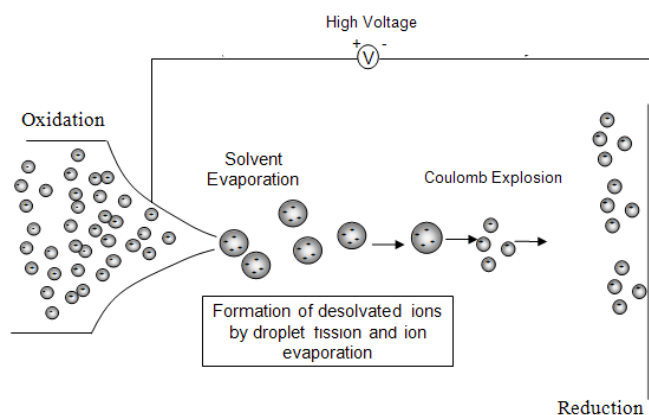


Figure 1.11: Schematic representations of the production of charged droplets during the ESI ionization process. From E. D. Hoffmann, V. Stroobant. Principles and application mass spectrometry. Third edition. *John wily and sons. Ltd.* **2007**, pp 52. Reproduced, with permission

1.8. Mass analysers

When the analytes are ionised into the gas-phase ions, they are analyzed separated according to their masses. The major role of a mass analyser is to separate different species (molecules, cluster or atoms) in their ionised form according to their mass-to-charge ratio (m/z).

Indeed, the separation of ions according to their mass-to-charge ratio can be based on different principles are described in Table 1.D. Hybrid mass spectrometer were also developed which consist of the combination of different kinds of mass analysers. For example, the quadrupole time-of-flight (Q-TOF) mass spectrometer is widely used in proteomics. Another type of mass analyser was developed the quadrupole ion-trap (QIT). In these mass trapping analysers, select a fragment in the trap, and let it fragment further. This step can be repeated to provide MS^n spectra. The most used ion-trap mass analyzers are the quadrupole ion trap, the orbitrap and the Fourier Transform Ion Cyclotron Resonance (FTICR).

Table1.D: Types of analysers used in mass spectrometry.

Type of analyser	Symbol	Principle of separation
Electric sector	E or ESA	Kinetic energy
Magnetic sector	B	Momentum
Quadrupole	Q	m/z (trajectory stability)
Ion trap	IT	m/z (trajectory stability)
Time-of-flight	TOF	Velocity (flight time)
Fourier transform ion cyclotron resonance	FTICR	m/z (resonance frequency)
Fourier transform orbitrap	FT-OT	m/z (resonance frequency)

1.8.1. The Quadrupole mass filter

The principle of operation of the quadrupole mass analyser is based upon the trajectory of the ion inside the quadrupole chamber. Quadrupole analysers ^{[97], [98]} are made up of four parallel metal rods of circular or hyperbolic geometry as shown in Figure 1.12. The simultaneous application of a direct potential (DC) and a radiofrequency potential (RF) causes the ion oscillate between the cylinders.

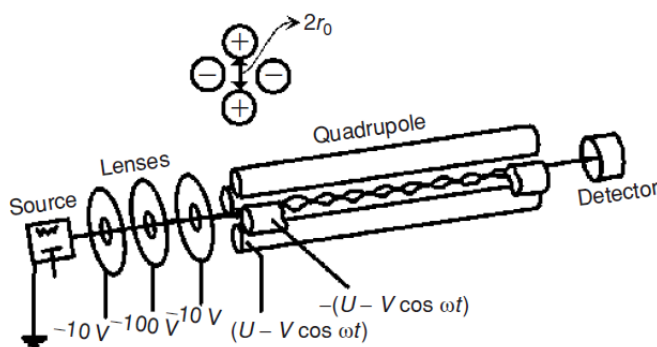


Figure 1.12: Schematic representation of a quadrupole mass spectrometer. From E. D. Hoffmann, V. Stroobant. Principles and application mass spectrometry. Third edition. John wily and sons. Ltd. 2007, pp 90. Reproduced, with permission.

Two opposite rods have an applied potential of $[U + V \cos(\omega t)]$ and the other two rods have a potential of $-[U + V \cos(\omega t)]$, where U is a DC voltage and $V \cos(\omega t)$ is the RF voltage amplitude. The applied voltages affect the trajectory of ions traveling down the flight path centered between the four rods. For given DC and RF voltages, only ions of a certain mass-to-charge ratio pass through the quadrupole filter and all other ions are thrown out of their original path. A mass spectrum is obtained by monitoring the ions passing through the quadrupole filter as the voltages on the rods are varied. There are two methods: varying ω and holding U and V constant, or varying U and V with (U/V) fixed for a constant angular frequency, ω . By a suitable choice of RF/DC ratio, the two directions together give a mass filter which is capable of resolving individual atomic masses. The quadrupole mass analyser presents several advantages: excellent transmission efficiency, suitability for GC, LC and CE, low cost, robustness, easy to use. However, the mass range of the quadrupole (less than 4000 Da), its low resolution and the need to couple more than two quadrupoles to achieve tandem mass spectrometry analysis are the major limitations of this analyser.

The motion of ions in a quadrupole field can be described mathematically by the solutions to the second-order linear differential equation described originally by Mathieu. The following equation was established in 1866 in order to describe the propagation of waves in membranes:

$$\frac{d^2u}{d\xi^2} + (a_u - 2q_u \cos 2\xi)u = 0$$

Considering the equations

$$a_u = \frac{8zeU}{m\omega^2 r_0^2}$$

$$q_u = \frac{4zeV}{m\omega^2 r_0^2}$$

where u represents the coordinate axes x , y and z . ξ is a dimensionless parameter equal to $\omega t/2$ such that ω must be a frequency as t is time, and a_u and q_u are additional dimensionless parameters known as trapping or stability parameters.

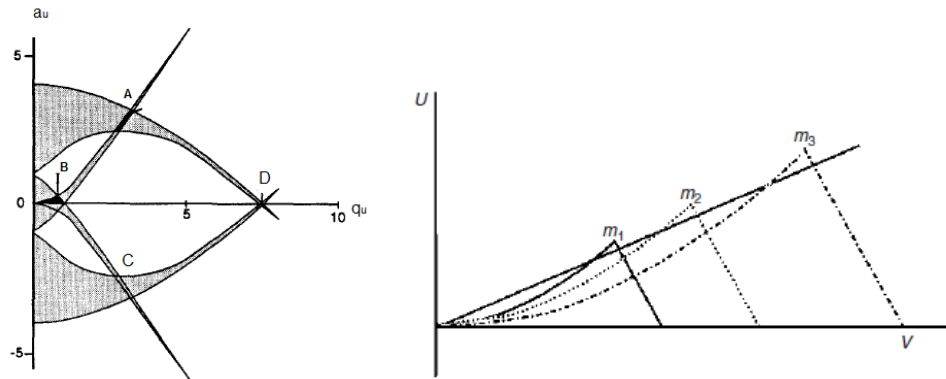


Figure 1.13: Mathieu stability diagram in two dimensions (x and y). Region of simultaneous overlap are labeled A, B, C and. Superimposed stability diagrams in U , V space for ions in order of increasing m/z ratio. From Z. Du, T. N. Olney, and D. J. Douglas. Inductively coupled plasma mass spectrometry with a quadrupole mass filter operated in the third stability region. *J. Am. Soc. Mass Spectrom.* **1997**, 8, 1230-1236. Reproduced (modified) with permission.

The four stability areas are labelled A to D and the area B is commonly used in mass spectrometers. The direct potential part is shown for positive U or negative U . Thus we shall consider only the positive area and all of the ions that have a stable trajectory so, V is within the limits of their stability area. By ramping the DC and RF potentials, only the peak of each individual stability diagram will be intersected.

1.8.2. Time-of-flight (TOF) mass analyser

The main idea of time-of-flight (TOF) analysers was first described by Stephens in 1946 and there has been a continuous interest in these instruments since the end of the 1980s. Due to the progress in electronics and the handling of high data flow, the TOF analyser has become well compatible with pulsed nature of the laser desorption ionization.

TOF mass spectrometry follows the principle that when ions are accelerated with the same potential from a fixed point and at a fixed initial time, and then allowed to drift, the ions are separated according to their mass to charge (m/z) ratio as explained in Figure 1.13. Their initial acceleration by an electric field, the ion drifts according to their velocities in a free-field region that is called a flight tube.

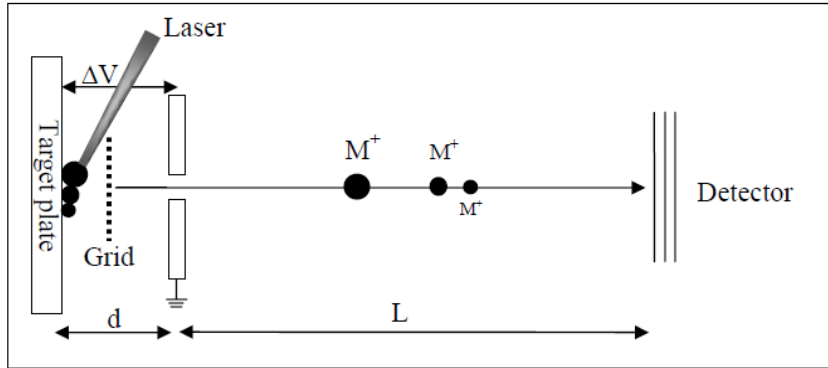


Figure 1.14: Schematic representations of principle of an LTOF instrument turned to analyze positive ions produced by MALDI.

Mass-to-charge ratios are determined by measuring the time it takes for ions take to move through a field-free region between the source and the detector. The mass of an ion m and total charge $q=ze$ is accelerated in the sources by a potential V_s . Its electric potential energy E_p is converted into kinetic energy E_k :

$$E_k = \frac{1}{2} mv^2 = qV_s = zeV_s = E_p$$

So, the velocity

$$v = (2zeV_s/m)^{1/2}$$

After initial acceleration, the ion travels in a straight line at constant velocity to the detector. The time t needed to travel the distance L before reaching the detector is given by

$$t = \frac{L}{v}$$

The equation becomes

$$t^2 = \frac{m}{L^2} \frac{1}{z \frac{2eV_s}{m}}$$

It is quite applicable for the soft ionization method because the higher mass of the TOF has no limits. For example, samples with masses above 300 kDa have been observed by MALDI-TOF.^{[99], [100]} The developments of matrix-assisted laser desorption ionization TOF has opened the way for new applications not only for biomolecules but also for synthetic polymers and polymer / biomolecule conjugates. This situation is substantially improved with the development of two techniques: delayed pulsed extraction and the uses of reflectron.

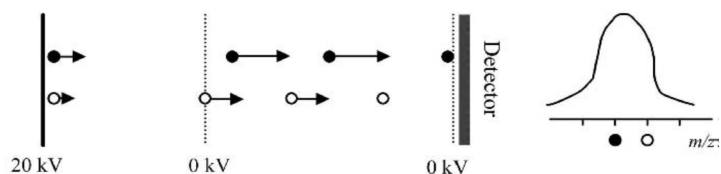
1.8.2.1. Delayed pulsed extraction

When the ions in the source are formed, ions with same m/z may have different velocities. This causes a great problem in the resolution. So ions having same the m/z but different kinetic energies travel to the detector at different time is summarized in Figure 1.15. The different kinetic energy of the same m/z , the more kinetic energy of same mass travel to the detector faster than the ions of lower kinetic energy and this results in the broadening of the peak, which results in the decrease resolution [Figure 1.15].

To solve this problem, a pulse voltage is applied outside of the source. The process is called pulse ion extraction. In the delayed pulse extraction mode, ions are allowed to separate according to the kinetic energy in the drift tube.

Continuous extraction

Sources flight Tube



Delayed pulse extraction

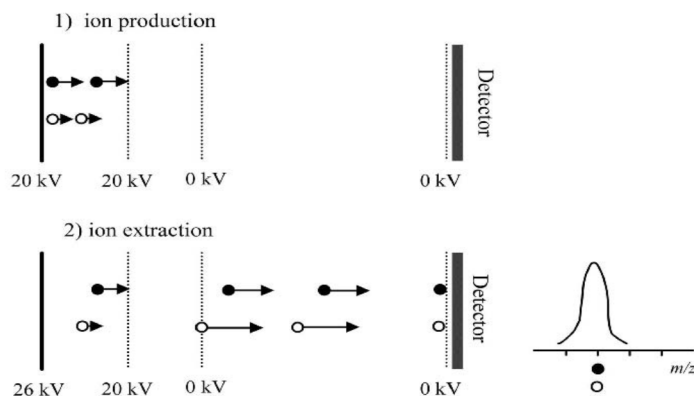


Figure 1.15: Schematic representations of description of a continuous extraction mode and a delayed pulsed extraction mode in a linear time-of-flight mass analyser. From E. D. Hoffmann, V. Stroobant. Principles and application mass spectrometry. Third edition. John wily and sons. Ltd. **2007**, pp 130. Reproduced with permission.

1.8.2.2. Reflectron

Another way to improve the mass resolution of ions having same m/z but different kinetic energies is done by using an electrostatic reflector called a reflectron. The simplest types of reflector consist of equally spaced series of grid electrode connected through a resistive network of the same resistive value network. The first resistive ring has the lowest potential and whereas the last ring has the highest potential to produce an

electrostatic field. The reflectron solves the kinetic energy dispersion of the ions leaving the ion source with the same m/z ratio. The faster ions spend more time in the reflectron than the lower kinetic energy ions the reflectron increases the flight path without increasing the dimensions of the mass spectrometer. However, although the reflectron increases the mass resolution, it also introduces a mass range limitation.

1.8.3. Quadrupole ion trap

The first mass spectrometer (MS) was invented 100 years by A. J. Dempster, F. W. Aston. This MS used the principle of electric and magnetic fields to accelerate ions and established the trajectories of ions according to their mass-to-charge ratio. In the 1950s W. Paul showed that the magnetic field could be eliminated, by a clever design, which used an alternating quadrupolar electric field rather than having a magnetic field. This new invented mass spectrometer was called a Quadrupole Ion-Trap mass spectrometer.

The QIT analyser is a device which uses the stability of the trajectories of ions in oscillating electric fields, which can separate the ions according to their m/z ratios. This analyser is frequently coupled with an on-line separation technique, such as liquid chromatography (LC), gas chromatography (GC) and capillary electrophoresis (CE).^{[101]-[103]}

The quadrupole ion-trap QIT exists in two different forms: a 3-D and 2-D. The 3-D configuration is summarized in Figure 1.15. The 3-D configuration ion trap is called Pauls ion trap. The Paul's ion-trap is made of two endcaps on the top and bottom and one hyperbolic electrode.^{[104], [105]} A direct current and radio frequency current is applied

between the electrodes and the ions are trapped in between the hyperbolic electrodes. In the quadrupole ion trap, the voltages are adjusted, so that the selected ion is trapped, and all other ions are expelled from the ion-trap.

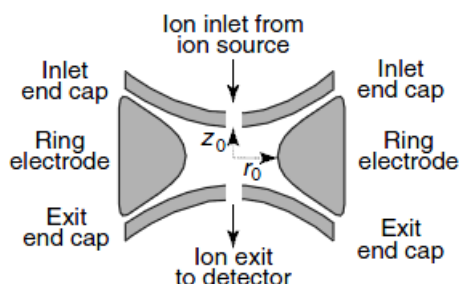


Figure 1.16: Schematic representations of quadrupole ion-trap. From E. D. Hoffmann, V. Stroobant. Principles and application mass spectrometry. Third edition. *John wily and sons*. Ltd. **2007**, pp 130. Reproduced, with permission

1.8.4. Ion cyclotron resonance and fourier transform mass spectrometry

Fourier transform mass spectrometry (FTMS) was first introduced by Comisarow and Marshall in 1974^{[106], [107]} and was reviewed by Amster^[108] in 1996 and by Marshall *et al.*^[109] in 1998 is shown in Figure 1.16 . In this technique, the cell is positioned inside a spatially uniform superconducting high magnetic field surrounded. When the gas phase ions are produced, they enter to the cell in a bent circular motion perpendicular to the field.

The rotation frequency of the ions depend on their m/z ratio. In the beginning when the radius of the motion is very small no signal is observed. With a swept RF pulse across the excitation plates of the cell, excitation of each individual m/z is attained. In this process each individual excitation frequency will combine with the ions natural motion

and consequently excite them to a higher orbit where they induce an alternating current between the detector plates. The frequency of this obtained current is identical to the cyclotron frequency of the ions and the strength is proportional to the number of ions present in the system. The ions drop back down to their natural orbit (relax) when the RF goes off resonance for a particular m/z value and then the next m/z packet starts to excite. The RF sweep can be made up of a series of frequencies or all frequencies can be considered simultaneously. The simultaneous frequency method measures all the ions at a time and produces a complex frequency vs. time spectrum containing all the available signals.

Fourier Transform methods deconvolute the obtained signal and results in the deconvoluted frequency vs. intensity spectrum and subsequently converted to the mass vs. intensity spectrum (the mass spectrum).

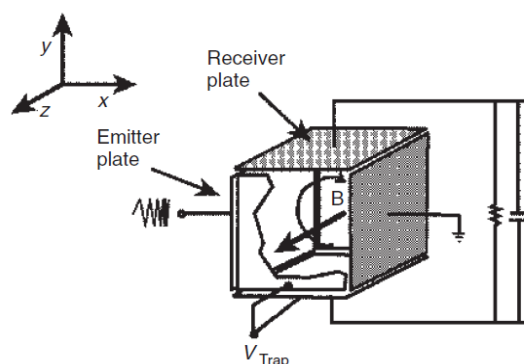


Figure 1.17: Schematic representations of an ion cyclotron resonance instrument. From E. D. Hoffmann, V. Stroobant. Principles and application mass spectrometry. Third edition. *John wily and sons*. Ltd. **2007**, pp 158. Reproduced, with permission

1.9. Tandem mass spectrometry

Tandem mass spectrometry using a triple quadrupole instrument involves at least two steps of mass analysis. These involve selection of a precursor ion followed by the collision induced dissociation in the collision chamber which causes the formation of the product ions. In general a first analyser is utilized in tandem mass spectrometry experiment to isolate a precursor ion to produce product ions and neutral fragments. The product ions formed are analysed by the second analyser (Tandem in space). The principle is illustrated in Figure 1.17. Generally if the selected precursor m/z contains only one isotope for each atomic species then the product ions spectrum will not show isotope peaks.

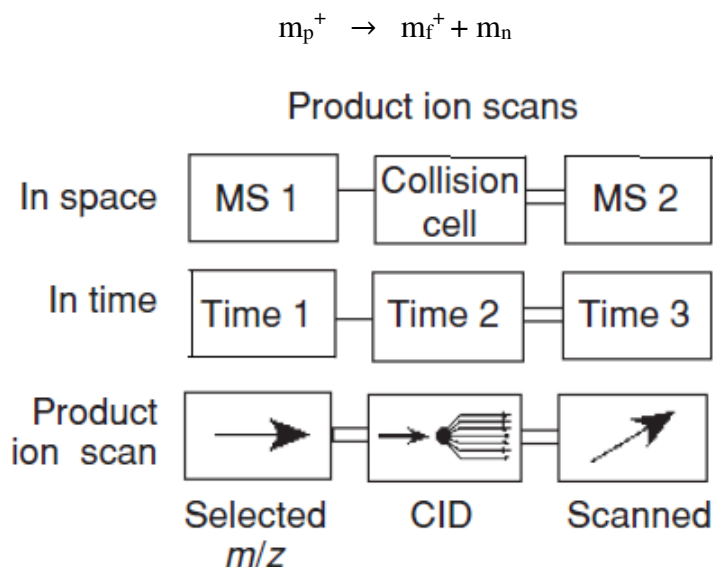


Figure 1.18: Schematic representations of tandem mass spectrometry in space and in time. From E. D. Hoffmann, V. Stroobant. Principles and application mass spectrometry. Third edition. *John wily and sons. Ltd.* **2007**, pp 191. Reproduced, with permission

In the MS/MS analysis using a quadrupole ion-trap the fragmentation of the isolated precursor ion can then induced by CID experiments. The isolation and fragmentation

steps can be repeated a number of times and is only limited by the trapping efficiency of the instrument. This is defined as an MS/MS/MS or MS^3 experiment. The number of steps can be increased to produce MS^n experiments where n refers to the number of generations of ions being analysed. (Tandem in time)

Mass spectra are produced by a ion-trap through scanning the content by linear increase of the RF voltage that utilizes a supplemental resonance ejection voltage applied to all sectors of the trap. Above action chronologically move ions from within the stability plane to a location where they become unstable in the X-direction and leave the trapping field to be detected.

The coordinates of the stability area are the Mathieu parameters a_z and q_z . Here, we plot a_z versus q_z . Stability diagram in (a_z, q_z) space for the area of simultaneous stability in both the r - and z -directions near the origin for the three-dimensional quadrupole ion trap [Figure 1.16] ; the $iso-\beta_r$ and $iso-\beta_z$ lines are shown in the diagram. This stability region is displayed again in Figure 1.19 where $iso-\beta$ curves are drawn for intermediate values between 0 and 1. The q_z -axis intersect the $\beta_z=1$ boundary at $q_z = 0.908$ which corresponds to q_{max} the mass-selective instability mode

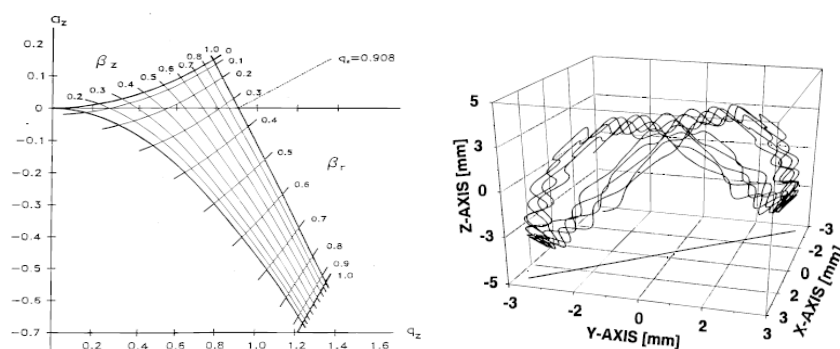


Figure 1.19: Mathieu stability diagram (left) and trajectory of a trapped ion (right). From Raymond E. March. From *An Introduction to quadrupole ion trap mass spectrometry*. *Journal of mass spectrometry*. **1997**. 32, 351-369. Reproduced, with permission.

To obtain the desired parent ion in preparation for subsequent fragmentation and mass analysis, the RF voltage is tuned and multi frequency resonance ejection waveforms are applied to the trap. The above process rejects all unnecessary ions.

A supplemental resonance excitation voltage is applied to all segments of two rods located on the X-axis to increase the energy of the selected ion. This escalated energy causes dissociation of the selected ions when collide with the damping gas. The produced ions are retained retained in the trapping field.

MS/MS spectra are produced by a ion-trap through scanning the product ion by linear increase of the RF voltage that utilizes a supplemental resonance ejection voltage applied to all sectors of the trap. Above action chronologically move ions from within the stability zone to a location where they become unstable in the X-direction and leave the trapping field to be detected.

In this thesis different “in space” and “in time” tandem mass spectrometer instruments, namely, the hybrid instrument of ESI-QqTOF-MS, MALDI-TOF/TOF-MS, and QIT-MS are used for the determinations described in this thesis.

1.9.1. High-energy collision dissociation (keV)

Sector analyzers such as electromagnetic and electric field's instruments or a combination of these two in a tandem mass spectrometer produce very high translational high energy to fragment the precursor ions. This means that the collision energy inside the collision cell is nearly one kilovolt or higher. The high energy CID is very reproducible.

1.9.2. Low-energy collision dissociation (Between 1 and 100 eV)

The triple quadrupole, QqTOF, QIT and FT-ICR tandem mass spectrometers afford MS/MS analyses produced by low-energy collision. At low energy, the ion's excitation energy is mostly of a vibrational nature.^[110] This means that the collision energy of the precursor ions have a kinetic energies in the range of a few eV to a few hundred eV. The low energy usually excites the vibrational state and produces small internal energy distributions. The MS/MS instruments can be divided into two classes:

1. Tandem in space (ESI-QqTOF-MS and MALDI-QqTOF-MS), these instruments are called tandem in space because the analysis is performed by different mass analyser in different space.

2. Tandem in time (QIT and FT-ICR-MS), these instruments are called tandem in time.

These are trapping instruments, because all the ions are ejected except the selected mass-

to-ratio (m/z). This selected m/z is fragmented in the same space. The ion trap device can perform multiple fragmentations (MS^n) in the same space, which is a powerful tool for structural studies. The ion intensity is the only limitation to the extent of an MS^n analysis in a QIT mass spectrometer.

1.10. CID-MS/MS induced dissociation MS/MS analysis using a hybride quadrupole orthogonal time of flight mass spectrometry (QqTOF).

The hybrid quadrupole orthogonal time-of-flight mass spectrometer was first described by Morris and his co-workers in 1996. This type of instrument is composed of three quadrupole analyzers MS0, MS1 and MS2, and one reflectron time-of-flight (TOF) analyzer which are connected in series. The function of the first quadrupole MS0 is an RF focusing quadrupole only, while the second quadrupole MS1 acts as a selector of the precursor ions, the third quadrupole (MS2) plays the role of the collision cell, and the TOF analyzer separates the ions according-to-their m/z ratios. The advantage of using this hybrid instrument is shown by the extreme ease of switching the ion source from ESI to MALDI, the possibility of operating in a moderate resolution mode, and the ability to measure high mass ranges with high accuracy.

In the MS/MS experiments the selected precursor ions fragmentation are primarily induced in the collision cell of the tandem mass spectrometer by collisions with neutral gas molecules using either low energy (QIT and QQQ) or high energy (MALDI-TOF/TOF instrument).^{[111]-[117]}

The term orthogonal QqTOF is a type of hybrid mass spectrometer in which quadrupole analyser (Q) is coupled to the time-of-flight analyser. The TOF analyser can

be beneficial as the second stage of the instrument is capable to transmit simultaneously every ion which, leads to a useful increase of sensitivity and resolution. The mass analyser is connected to the TOF analysers and acceleration of ions in the TOF analyser take place perpendicular to the first trajectory of the ion. These couplings give a good sensitivity advantages to analyse a broad range of masses.

The (CID) collision induced fragmentation MS/MS study (CID-MS/MS) is equivalent to the fragmentation of a selected ion which occurs in space within a mass analyser. In mass spectrometry, the MS/MS analysis the selected precursor ion within the collision cell undergoes collision with a stream of inert gas (e, g here nitrogen is used). The fragmentation of the precursor ion is the results of the increase of internal energy of the precursor ion followed by the breakdown of the ion by forming a product ion. The collision induced dissociation (CID) which was first described by Jennings in 1968 and was confirmed by McLafferty and his co-workers in 1973.^{[118], [119]} MS/MS analysis using QSTAR QqTOF-MS/MS hybrid instrument is a good example of low-energy CID analysis.

1.11. CID-MS/MS induced dissociation MS/MS analysis using a high energy MALDI

The 4800 MALDI-TOF/TOF analyzer takes advantage of: (1) Time-of-flight ion detection; (2) Time-of-flight/time-of-flight ion detection and; (3) Time-delay ion extraction followed by CID and mass analysis using the TOF analysre. When the laser pulses, the matrix transfers the protons to the analytes. The laser operates at 355 nm to ionize samples. The isolation of the precursor ion of interest (MS/MS mode) is done by

means of a timed ion selector (TIS), which allows only ions of a specific mass to pass through to the collision cell. A field-free region that provides collision-induced dissociation (CID) to fragment the precursor ions in MS/MS mode. Accordingly, the precursor ions will collide with the gas that is introduced into the cell, causing some of them to fragment into product ions.

CHAPTER 2: MATERIALS and METHODS

2.1. Synthetic bivalent β -D-*N*-glycosides

2.1.1. The origin and structure of novel synthetic bivalent β -D-*N*-glycosides

The six synthetic bivalent β -D-*N*-glycosides are presented in Figure 2.1 and were synthesized by Professor Rene Roy's group in the Department of Chemistry, University of Quebec, Montreal.

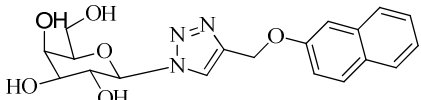
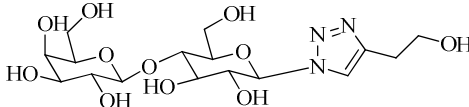
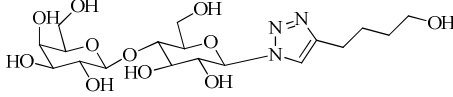
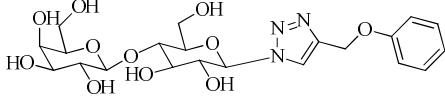
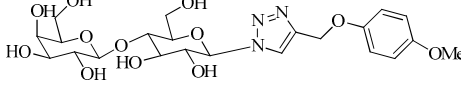
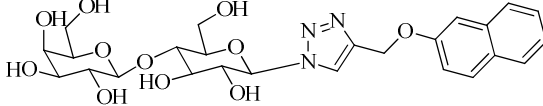
1	 <p>Chemical Formula: C₁₉H₂₁N₃O₆ Molecular Weight: 387.39</p>	Methoxynaphthalene-substituted triazole- β -D- <i>N</i> -galactopyranosides derivative (1)
2	 <p>Chemical Formula: C₁₆H₂₇N₃O₁₁ Molecular Weight: 437.40</p>	Ethyltriazole β -D- <i>N</i> -lactopyranosides derivative (2)
3	 <p>Chemical Formula: C₁₈H₃₁N₃O₁₁ Molecular Weight: 465.45</p>	Butyltriazole β -D- <i>N</i> -lactopyranosides derivatives (3)
4	 <p>Chemical Formula: C₂₁H₂₉N₃O₁₁ Molecular Weight: 499.47</p>	Anisoletriazole β -D- <i>N</i> -lactopyranosides derivative (4)
5	 <p>Chemical Formula: C₂₂H₃₁N₃O₁₂ Molecular Weight: 529.49</p>	Dimethoxybenzenetriazole- β -D- <i>N</i> -lactopyranosides derivative (5)
6	 <p>Chemical Formula: C₂₅H₃₁N₃O₁₁ Molecular Weight: 549.53</p>	Methoxynaphthalene-triazole β -D- <i>N</i> -lactopyranosides derivative (6)

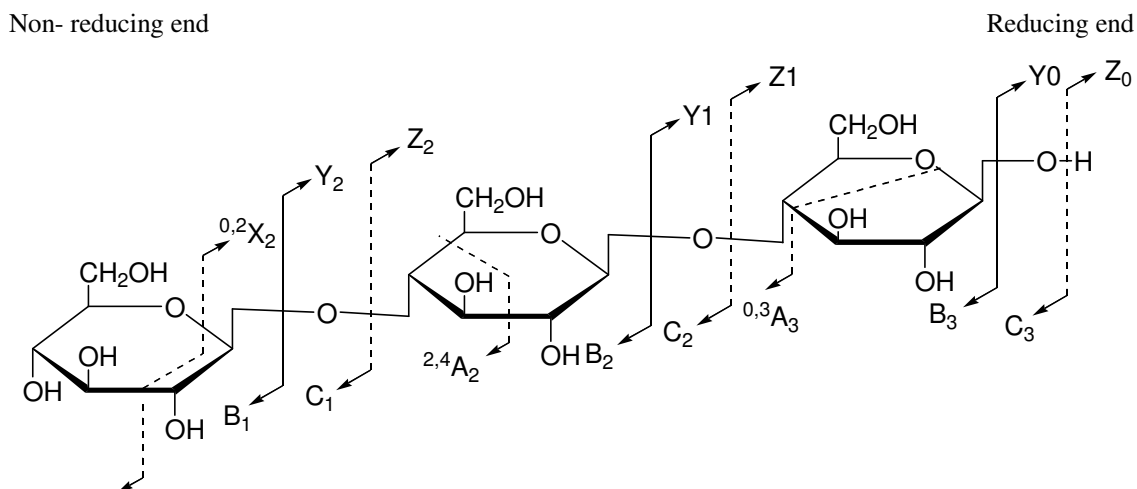
Figure 2.1: Structure of synthetic bivalent β -D-*N*-glycosides

2.2. Isotopic Labelling: hydrogen deuterium exchange of the novel synthetic bivalent β -D-*N*-glycosides

In order to confirm the fragment ions obtained by ESI-CID-MS/MS analysis of each bivalent β -D-*N*-glycosides (**I-6**), they each first were dissolved in 99.9% deuterium oxide- (D_2O) with a concentrations of $0.25 \mu\text{g}.\mu\text{L}^{-1}$ to form the solutions. Then, the six novel synthetic bivalent-glycosides were directly infused into the tandem mass spectrometer (ESI-QqTOF).

2.3. Gas-phase fragmentation of glycoconjugates during the mass spectrometry

The nomenclature of ions observed in mass spectrometry and collision induced dissociation CID-MS/MS of glycoconjugates has been explained by Domon and Costello.^{[120a], [120b]} The glycoconjugates are formed by a covalent linkage between the glycosyl chains (oligosaccharide and polysaccharide) and the protein, peptide and lipid aglycone. Mass spectrometry was shown to be an excellent means for the structural elucidation and characterisation of glycoconjugates.^{[120a], [120b], [121a], [121b]} Domon and Costello proposed the universal mechanism of fragmentation routes during FAB-MS/MS analysis of complex glycoproteins. This universal mechanism of fragmentation routes can be applied to other technique like ESI-MS, MALDI-MS and ion-trap-MS in both in positive and negative ion modes.



Types of carbohydrate fragmentation of cellobiose

Figure 2.2: Possible fragmentation pathways during CID-MS/MS of a glycoconjugate.

The fragment ions that contain a non-reducing terminus are labelled with uppercase letters A, B, C where ions that contain the reducing end of the oligosaccharide are labelled with letters X, Y, Z. The subscripts indicate the sugar residue numbered from the nonreducing end. B ions are oxonium ions. Y ions are protonated species that include an H-transfer. C as protonated molecular ions and Z ions result from cleavage of glycosidic (O-C bond), Z fragments are rarely observed in MALDI mass spectrometry.

2.4. ESI-QqTOF-MS of the novel synthetic bivalent β -D-N-glycosides

Electrospray ionization-mass spectra of all the biological bivalent β -D-N glycosides were acquired in the positive ion mode using an Applied Biosystems API-QSTAR XL quadrupole orthogonal time-of-flight (QqTOF)-MS/MS hybrid tandem mass spectrometer (Applied Biosystems International-MDS Sciex, Foster City, California, USA). This instrument is capable of analyzing a mass range of m/z 5 to 40 000, with a

resolution of 10,000 in the positive ion mode. ESI was performed with the Turbo Ionspray source operated at 5.5 kV. The ESI-MS were recorded with a cone voltage setting (Declustering Potential 1) varying from 60 to 120 volts. All other instrument parameters were kept constant for the ESI-MS analysis (N₂; Curtain Gas = 20 psi; ion source gas 1 = 20 psi; Air, ion source gas 2 = 0 psi; Declustering potential DP1= 50-120 V; Declustering Potential 2 = 250 V, Focusing potential = 10V and temperature = ambient). The bivalent β -D-*N*-glycosides were dissolved in 1:1 acetonitrile / water (1 mg ml⁻¹). The Sample solution was then infused directly, with an integrated Harvard syringe pump (Harvard Apparatus, Hollister, MA) at a rate of 5 μ L min⁻¹.

The TOF analyzer was calibrated for high masses using a Pep-Tyf peptide which was dissolved in a 1:1 mixture of acetonitrile (ACN or CH₃CN): water (H₂O) and checking for the exact masses of the [M+H]⁺ at m/z 1638.8485 and [M+2H]²⁺ at m/z 819.9279. For low masses, the TOF analyzer was calibrated using penta-*O*-acetyl- β -D-galactopyranose and checking for the exact masses of the [M+H-AcOH]⁺ ion [C₁₄H₁₉O₉]⁺ at m/z 331.1024 and octa-*O*-acetyl- β -D-lactopyranose and checking for the [M+H-AcOH]⁺ ion [C₂₆H₃₃O₁₇]⁺ at m/z 617.1712. The [M+H-AcOH]⁺ ion [C₂₆H₃₃O₁₇] at m/z 617.1712.

2.5. Quadrupole ion traps mass spectrometry (QIT-MS) of the novel bivalent β -D-*N*-glycosides

The mass spectra of the novel bivalent β -D-*N*-glycosides were acquired in the positive ion mode in the mass range 100 to 600 m/z using the orthogonal-spray ion source Agilent 1100 Series LC/MSD Trap SL spectrometer. For the positive ion mode analysis, samples (1mg/ml) were dissolved in acetonitrile: water (1:1). This instrument is capable of analyzing a mass range of m/z 50-2200 mass range, with a resolution of 10,000 in the positive ion mode. A high performance liquid chromatography (HPLC) system is the most common form of sample delivery for the ion-trap. A small syringe pump also is included with the ion trap system to introduce samples directly to either the electrospray (ESI) or APCI ion sources. When used with the electrospray (ESI) interface, two modes of operation are available to inject the sample in solution directly to the nebulizer under low-flow conditions (5 μ L/min.), or the sample in solution can be injected into the HPLC main flow system through a T-connector.

Samples (1 mg.ml⁻¹) were directly infused into the QIT-MS under low flow condition; this combined operation is particularly convenient for the optimization of instrument parameters and the development of MS/MS methods.

Dry gas 8.00 l/min trap drive 51.5 volt, octapole amplitude RF 177.2 Volt, skimmer 40.0 volt, Oct 1 DC 12 volt, Oct DC 1.70 volt , scan begins at m/z 100 and end at m/z 600, max accusation time 200000 μ s. For low masses the quadrupole ion trap analyzer was calibrated using penta-*O*-acetyl- β -D-galactopyranose and checking for the

exact masses of the $[M+H-AcOH]^+$ ion $[C_{14}H_{19}O_9]^+$ at m/z 331.1024 and octa-*O*-acetyl- β -D-lactopyranose and checking for the $[M+H-AcOH]^+$ ion $[C_{26}H_{33}O_{17}]^+$ at m/z 617.1712.

2.6. MALDI -TOF/TOF-CID-MS/MS of the novel synthetic bivalent β -D-*N*-glycosides

The solvent used was J. T Baker (Phillipsburg, NJ, USA) reagent grade. The matrix used dihydroxy benzoic acid (DHB) was purchased from the Aldrich Chemical. Co. (Milwaukee, WI, USA). There are various kinds of sample-matrix preparations, which have been described in different kind of literature.^{[122], [123]} In this work, the dried droplet method was used. This consists of mixing some saturated matrix solution (5-10 μ l) with a smaller volume of analyte solution. Then the mixture is spotted on the MALDI plate and was allowed to dry on the plate. The solvent used in this experiment acetonitrile: water (80:20).

Mass spectra of the novel bivalent β -D-*N*-glycosides active were acquired in the positive reflectron ion mode. The MALDI-TOF/TOF-MS (MALDI 4800, Applied Bioscience) was used in this experiment for the analysis of these the novel bivalent β -D-*N*-glycosides active. The MALDI-TOF/TOF-MS data was acquired in the mass range 200 to 600 m/z in the positive ion using the reflectron mode. The laser used was a Nd:YAG 200-Hz laser. All the spectra were accumulated using 400 individual laser shoots. The accelerating potential was 29KV. The focusing guide wire was held at a potential 0.17%. The MALDI-TOF/TOF-MS possessed a high mass accuracy (5ppm) and resolution of

15000-25000 (FWHM). High energy CID-MS/MS spectra were generated by 1 kV collisions with ambient air and accumulation of maximally 1000 laser shots.

For the low masses, the TOF analyzer was calibrated using penta-*O*-acetyl- β -D-galactopyranose and checking for the exact masses of the $[M+Na-AcOH]^+$ ion $[C_{14}H_{19}O_9Na]^+$ at m/z 354.0927 and octa-*O*-acetyl- β -D-lactopyranose and checking for the $[M+Na-AcOH]^+$ ion $[C_{26}H_{33}O_{17}Na]^+$ at m/z 640.1615.

2.7. Wheat straw lignin

There are different kinds of methods used to isolate the lignin. These methods involve the chemical, mechanical and enzymatic methods developed to isolate lignin from woods. These extraction method can change the native structure of lignin and give the modified lignin.^{[124], [125]} Lignan are the natural dimers of monolignols and are widely distributed in plants.^[52]

The technical wheat straw lignin used in this work was extracted by the novel CIMV^{[54],[126]} procedure which selectively separates the cellulose, hemicelluloses and lignin is described in Figure 2.3. Wheat straw grass measuring 53 cm length pieces of (30 g) were impregnated using mixture of formic acid, acetic acid, and water (30:50:20 v/v/v, 300 mL) at 60 °C for 1 h, and the resulting mixture was heated at 107 °C for 3 h. Pulp filtration, pressing, and repeated washing steps with 0.5 N aqueous acetic acid and water afforded pulp (49%) and lignin liquor. After concentration of the liquor, lignin was precipitated by addition of water to the residue, filtered, thoroughly washed with water, and dried at 40 °C. Crude lignin was obtained in 17% yield with respect to starting wheat

straw grass. Thus the CIMV method affords a technical lignin which has not been modified further upon release from the vascular plants.

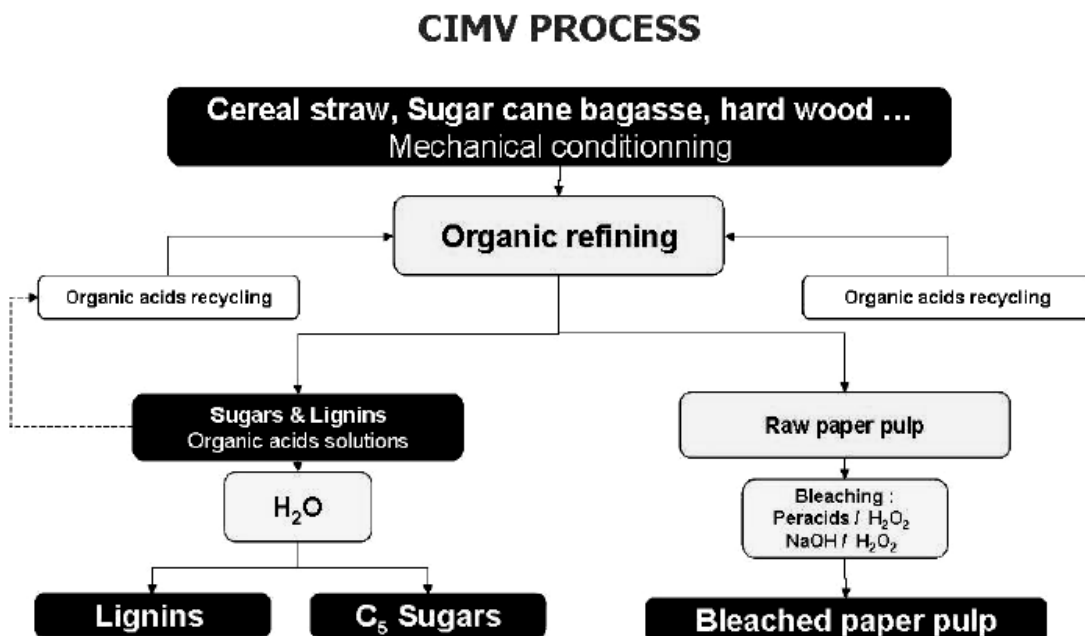


Figure 2.3: Schematic representation of the CIMV process biorefinery. From M. Delmas. Vegetal refining and agrochemistry. *Chem. Eng. Technol.* **2008**, 31(5), 792. Reproduced, with permission.

2.7.1. MALDI-TOF/TOF-MS of straw lignin extracted from CIMV process

Mass spectra of The CIMV lignin were acquired in the positive reflectron ion mode. The MALDI time-of-flight TOF/TOF mass spectrometer (MALDI 4800, Applied Bioscience) was used in this experiment for the analysis of straw lignin. The MS data was acquired in the mass range 300 to 800 m/z in the positive ion reflectron mode. The mass spectra instrument was equipped with Nd:YAG 200-Hz laser. The accelerating potential was 25KV.

CHAPTER 3:
GAS-PHASE FRAGMENTATION STUDY OF NOVEL SYNTHETIC
BIVALENT β -D-N-GLYCOSIDES BY ESI-MS AND LOW-ENERGY
COLLISION TANDEM MASS SPECTROMETRY (CID-MS/MS) USING
AN ESI-QqTOF-HYBRID MS/MS INSTRUMENT (TANDEM IN SPACE)

3.1. Introduction

The aim of this study was to establish the structural characterization and the fragmentation routes of six synthesized biological bivalent active *N*-glycosides by electrospray ionization mass spectrometry with an ESI-QqTOF-MS/MS hybrid instrument operating in the positive ion mode. In addition, low-energy collision-induced dissociation (CID) tandem mass spectrometry (MS/MS) analyses of the various precursor $[M+H]^+$ molecular ions confirmed the characteristic fingerprint pattern obtained in the conventional ESI-MS.

The development of ESI-QqTOF-MS instruments has substantially increased the sensitivity and resolution at which carbohydrate tandem mass spectra can be obtained.^{[127],[128]} Most observed fragment ions corresponded to glycosidic bond cleavage rather than cross-ring cleavage.

Low-energy collision CID-MS/MS is a valuable method for generating structural information. In this latter process, a portion of the kinetic energy of the ion is converted into internal energy by collision with a neutral gas-phase species, usually in the pressurized collision cell of the tandem mass spectrometer, and the ions that have undergone collision excitation may subsequently fragment into product ions.^[129]

Rationalization of the CID-fragmentation routes was made by obtaining the product-ion spectra (daughter scan) and precursor-ion spectra (parent scan) of the various intermediate ions.

3.2. ESI-QqTOF-MS analysis of the novel synthetic bivalent β -D-*N*-glycosides (**1-6**)

The ESI-QqTOF-MS analyses of this series were all recorded in the positive ion mode, (DP1 = 60-120 volt) and afforded in all cases the expected $[M+H]^+$ protonated molecules, $[M+Na]^+$ sodiated molecules and the $[2M+H]^+$ ions. The ESI-MS of methoxynaphthalene-substituted triazole β -D-*N*-galactopyranosides derivative (**1**) produced the $[M+H]^+$ protonated molecule at m/z 388.1513, the $[M+Na]^+$ sodiated adduct at m/z 410.4152 and $[2M+H]^+$ at m/z 775.2809 [Figure 3.1(a)]. The ESI-MS of ethyltriazole β -D-*N*-lactopyranosides derivative (**2**) formed the $[M+H]^+$ at m/z 438.1754, $[M+Na]^+$ at m/z 460.1265 and $[2M+H]^+$ at m/z 875.3097 [Figure 3.2(a)]. The ESI-MS of the butyltriazole β -D-*N*-lactopyranosides derivatives (**3**) afforded the $[M+H]^+$ at m/z 466.2011, the $[M+Na]^+$ sodiated adduct at m/z 488.1966 and the $[2M+H]^+$ at m/z 931.424 [Figure 3.3(a)]. The ESI-MS of anisoletriazole β -D-*N*-lactopyranosides derivatives (**4**) afforded the $[M+H]^+$ at m/z 500.1900, the $[M+Na]^+$ sodiated adduct at m/z 552.1871 and $[2M+H]^+$ at m/z 999.385 [Figure 3.4(a)]. The ESI-MS of the dimethoxybenzenetriazole- β -D-*N*-lactopyranosides derivatives (**5**) afforded the $[M+H]^+$ at m/z 530.2012, the $[M+Na]^+$ sodiated adduct at m/z 552.1993 and the $[2M+H]^+$ at m/z 1059.4009 [Figure (3.5a)]. Finally the ESI-QqTOF-MS of the methoxynaphthalene-triazole β -D-*N*-

lactopyranosides derivatives (**6**) afforded the $[M+H]^+$ at m/z 550.2009, the $[M+Na]^+$ sodiated adduct at m/z 572.2006 and the $[2M+H]^+$ at m/z 1099.4427 [Figure 3.6(a)].

In order to confirm the gas-phase fragmentation study of the novel synthetic bivalent *N*-glycosides, the ESI-QqTOF-MS of deuterated the novel synthetic bivalent *N*-glycosides was also carried out. The H/D exchange for each individual bivalent β -D-*N*-glycosides was shown to be total (100%). For example, during the ESI-QqTOF-MS analysis of the methoxynaphthalene substituted triazole β -D-*N*-galactopyranosides derivatives (**1**), we observed that all 4 exchangeable H atoms are replaced by D atoms. Moreover, the additional H^+ charge is also replaced by D^+ .

3.3. CID-MS/MS analysis of synthetic bivalent β -D-*N*-glycosides (**1-6**)

Low-energy collision induced dissociation CID-MS/MS analyses of the different precursor protonated species $[M+H]^+$ were analyzed with different collision energies. Tables 3.A-3.F, summarize the formation of the various diagnostic product ions observed in the CID-MS/MS analyses of the precursor protonated molecules $[M+H]^+$ selected from the various synthetic bivalent β -D-*N*-glycosides (**1-6**). The various coding used for the product ion tagging was based on the nature of the bivalent β -D-*N*-glycosides. The product ion scans of the precursor protonated molecules selected from the six bivalent β -D-*N*-glycosides (**1-6**) are shown in Figures 3.1(b)-3.6(b) and in Schemes 3.1-3.6. In addition, the CID-MS/MS analyses of the different deuterated precursor species in Tables 3.A-3.F were also formed to confirm the formation of the major product ions.

3.3.1. Low energy CID-MS/MS of the protonated precursor ion $[M+H]^+$ at m/z 388.1513 selected from the methoxynaphthalene substituted triazole β -D-*N*-galactopyranosides derivatives (*I*)

The product ion scan of the selected protonated molecular ion $[M+H]^+$ at m/z 388.1513 extracted from methoxynaphthalene-substituted triazole β -D-*N*-galactopyranosides (*I*) was recorded with a collision energy (32eV) and a declustering potential (DP1) of 72 V. The major product ions formed were observed at m/z 226.0991 and 163.0629 tentatively shown in Scheme 3.1 and their structural identities are indicated in Table 3.A.

The precursor ion $[M+H]^+$ at m/z 388.1548 eliminates the neutral galactosyl moiety $[(C_6H_{10}O_5), (162.0528 \text{ Da})]$ to afford the aglycone product ion at m/z 226.0991 which was assigned as $[Y_0]^+$. This latter product ion can also be assigned as $[BH_2]^+$ by using the conventional nucleoside nomenclature.^[130] Conversely, the precursor ion at m/z 388.1548 can also eliminate the neutral aglycone moiety $[(C_{13}H_{11}N_3O), (225.0902 \text{ Da})]$ to give the galactosyl oxonium ion $[B_2]^+$ at m/z 163.0629.

All the exact mass assignments of the product ions were verified by conducting separate CID-MS/MS analysis of the deuterated methoxynaphthalene substituted triazole- β -D-*N*-galactopyranosides derivatives (*I*) at m/z 393.1845 (Table 3.A). The proposed CID-MS/MS fragmentation routes of the protonated precursor ion $[M+H]^+$ are tentatively shown in Scheme 3.1

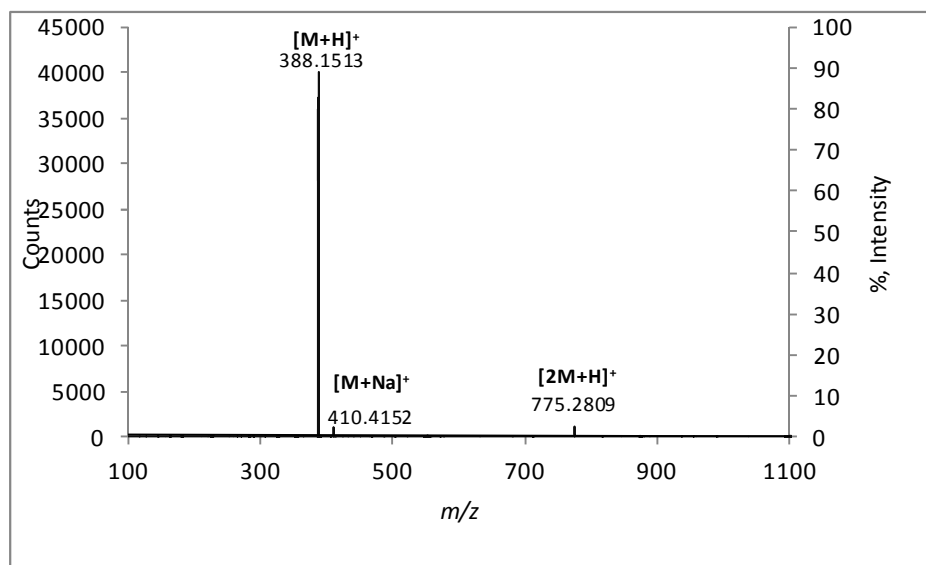


Figure 3.1(a): ESI-QqTOF-MS (+) of the methoxynaphthalene substituted triazole β -D-*N*-galactopyranosides (*I*)

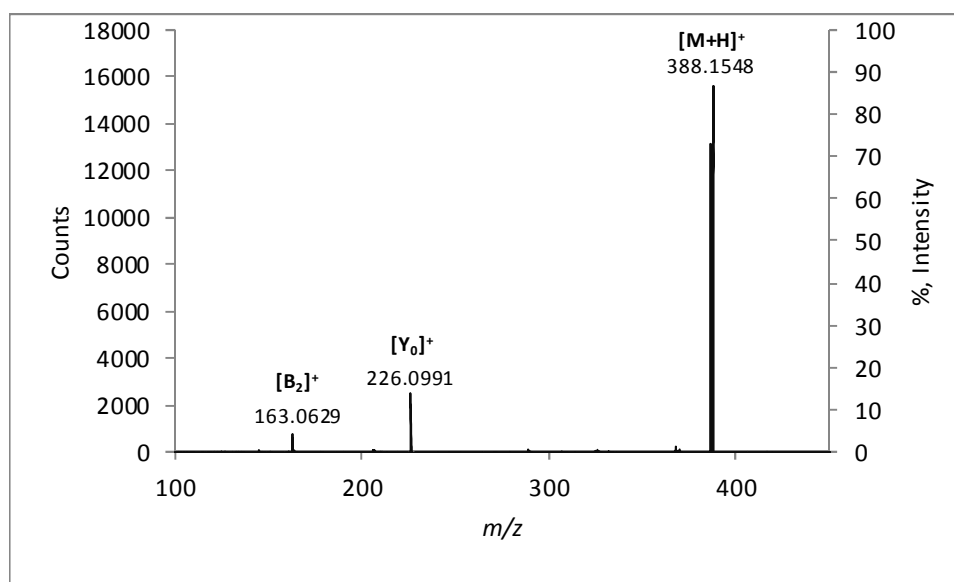
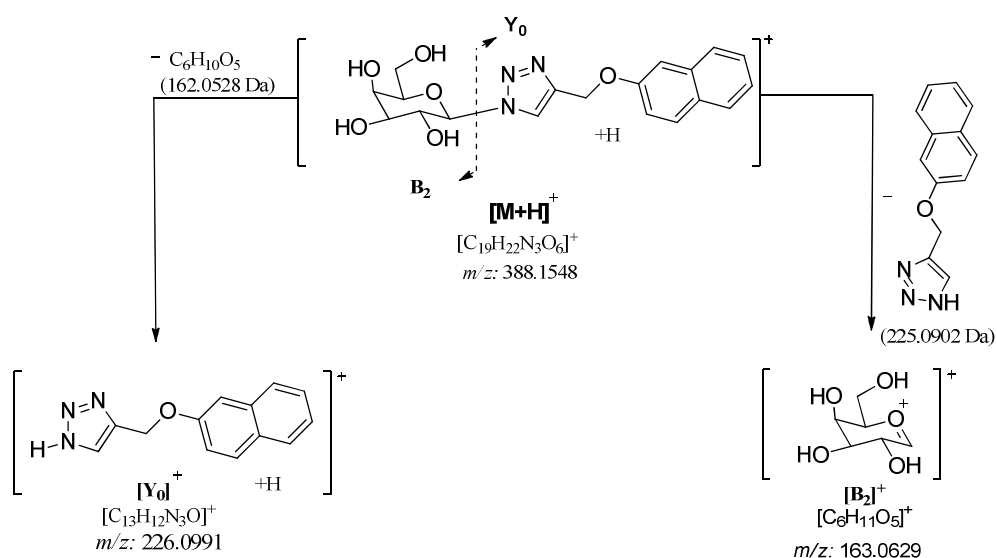


Figure 3.1(b): Low energy CID-MS/MS of the selected protonated precursor ion [M+H]⁺ at m/z 388.1513 extracted from the methoxynaphthalene-substituted triazole β -D-*N*-galactopyranosides (*I*)



Scheme 3.1: The tentative proposed fragmentation routes obtained during the ESI-CID-MS/MS of the protonated molecule $[M+H]^+$ at m/z 388.1513 extracted from the methoxynaphthalene substituted triazole β -D-*N*-galactopyranosides (**1**).

Table 3.A: Characteristic product ions observed in the low energy ESI-CID-MS/MS of the protonated methoxynaphthalene substituted triazole β -D-*N*-galactopyranosides (**1**) precursor ion $[M+H]^+$ at m/z 388.1513.

Characteristic ions	Calculated mass (m/z)	Observed mass (m/z)	Difference (in ppm)
$[\text{C}_{19}\text{H}_{22}\text{N}_3\text{O}_6]^+$	388.1509	388.1548	10
$[\text{C}_{19}\text{H}_{17}\text{D}_5\text{N}_3\text{O}_6]^+$	393.1817	393.1845	7
$[\text{C}_{13}\text{H}_{12}\text{N}_3\text{O}]^+$	226.0980	226.0991	5
$[\text{C}_{13}\text{H}_{10}\text{D}_2\text{N}_3\text{O}]^+$	228.1106	228.1127	12
$[\text{C}_6\text{H}_{11}\text{O}_5]^+$	163.0606	163.0629	14
$[\text{C}_6\text{H}_7\text{D}_4\text{O}_5]^+$	167.0858	167.087	11

3.3.2. Low energy CID-MS/MS of the protonated precursor ion $[M+H]^+$ at m/z 438.1754 selected from the ethyltriazole β -D-*N*-lactopyranosides derivative (2)

The product ion scan of the selected protonated molecular ion $[M+H]^+$ at m/z 438.2854 extracted from the ethyltriazole β -D-*N*-lactopyranosides derivative (2) was recorded with a collision energy (40eV) and a declustering potential (DP1) of 80 V. The major product ions formed were observed at m/z 276.1213 and 114.0673 shown in Figure 3.3 (b) and their structural identities were tentatively assigned in Table 3.B.

Thus, the precursor ion at m/z 438.1768 eliminates the neutral lactosyl disaccharide moiety $[(C_{12}H_{20}O_{10}), (324.1056 \text{ Da})]$ to produces the aglycone product ion at m/z 114.0673 which is assigned as $[Y_0]^+$. The precursor ion $[M+H]^+$ can also eliminate the neutral galactosyl moiety $[(C_6H_{10}O_5), (162.0528 \text{ Da})]$ to form the ethyltriazole β -D-*N*-glucopyranoside product ion at m/z 276.1213 assigned as $[Y_1]^+$ [glucose-($C_4H_7N_3O$)] $^+$.

All the exact mass assignment of the product ions were verified by conducting separate CID-MS/MS analysis of the deuterated ethyltriazole β -D-*N*-lactopyranosides derivative (2) at m/z 447.2332 (Table 3.B).

The proposed low energy CID-MS/MS fragmentation routes of the protonated precursor ion $[M+H]^+$ are tentatively shown in Scheme 3.2

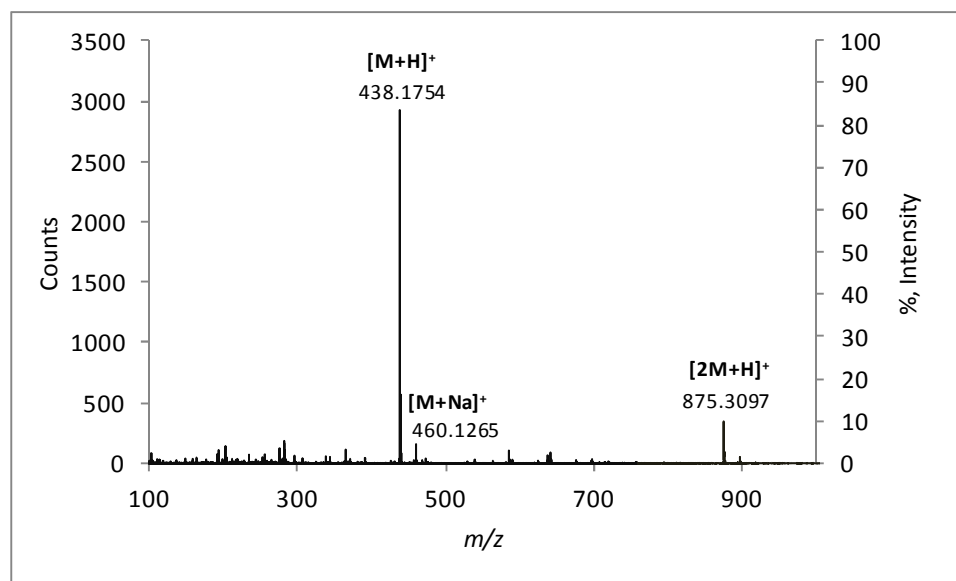


Figure 3.2(a): ESI-QqTOF-MS(+) of the ethyltriazole β -D-*N*-lactopyranosides derivative (**2**)

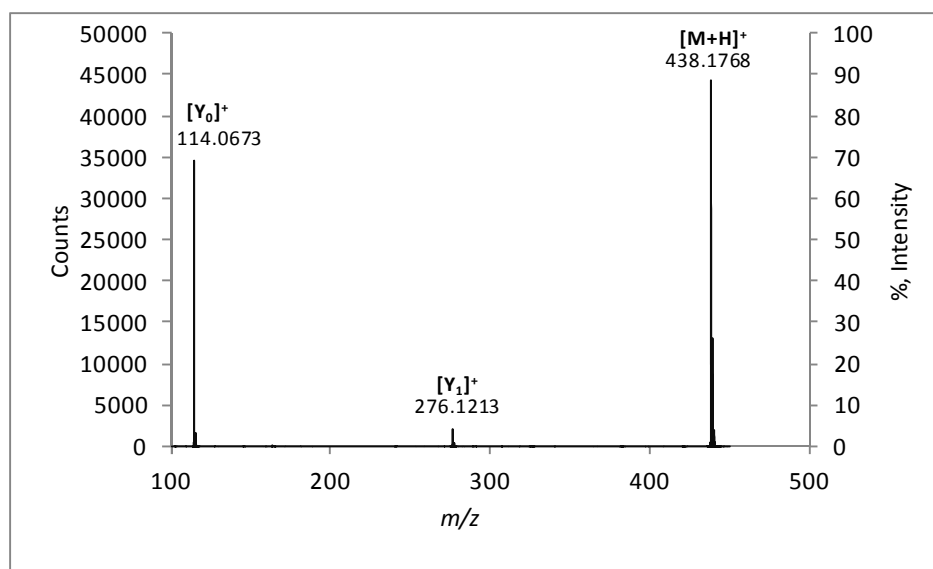
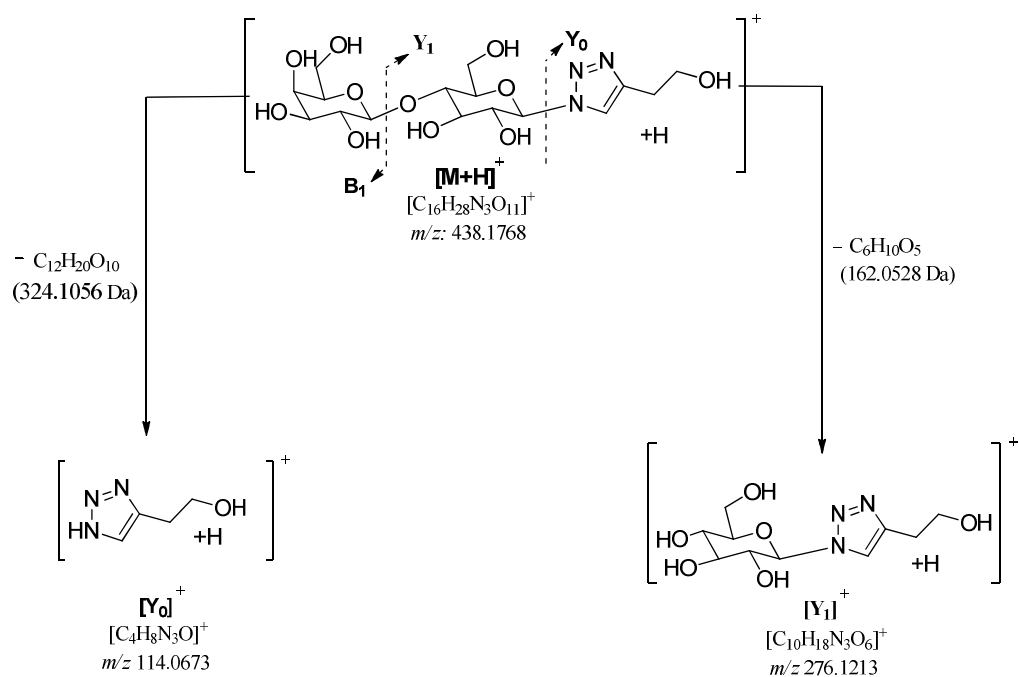


Figure 3.2(b): Low energy CID-MS/MS of the selected protonated precursor ion $[M+H]^+$ at m/z 438.1754 extracted from ethyltriazole β -D-*N*-lactopyranosides derivative (**2**)



Scheme 3.2: The tentative proposed fragmentation routes obtained during the ESI-CID-MS/MS of the protonated molecule $[M+H]^+$ at m/z 438.1754 extracted from the ethyltriazole β -D-*N*-lactopyranosides derivative (**2**)

Table 3.B: Characteristic product ions observed in the low energy ESI-CID-MS/MS of the protonated ethyltriazole β -D-*N*-lactopyranosides derivative (**2**) precursor ion $[M+H]^+$ at m/z 438.1754.

Characteristic ions	Calculated mass (m/z)	Observed mass (m/z)	Difference (in ppm)
$[C_{16}H_{28}N_3O_{11}]^+$	438.1724	438.1768	10
$[C_{16}H_{20}D_9N_3O_{11}]^+$	447.2283	447.2332	11
$[C_{10}H_{18}N_3O_6]^+$	276.1196	276.1213	6
$[C_{10}H_{12}D_6N_3O_6]^+$	282.1567	282.1592	9
$[C_4H_8N_3O]^+$	114.0667	114.0673	5
$[C_4H_5D_3N_3O]^+$	117.0850	117.0865	13

3.3.3. Low energy CID-MS/MS of the protonated precursor ion $[M+H]^+$ at m/z 466.2011 selected from the butyltriazole β -D-*N*-lactopyranosides derivatives (**3**)

The CID-MS/MS analysis of selected protonated molecules $[M+H]^+$ at m/z 466.2011 extracted from the butyltriazole β -D-*N*-lactopyranosides derivatives (**3**) shown in Figure 3.3(b), was recorded with collision energy CE of 30 eV and declustering potential DP1 of 50 V. This product ion scan afforded the same series of product ion obtained from compounds 1 and 2. The afforded product ions at m/z 304.1545, 142.0977 and 124.0887 and their assigned structural identities of the major product ion are indicated in Table 3.C and their geneses are tentatively shown in Scheme 3.3.

In the CID-fragmentation, the protonated precursor ion $[M+H]^+$ at m/z 466.2088 eliminate the galactosyl moiety $[(C_6H_{10}O_5), (162.0528 \text{ Da})]$ to form the aglycone product ion at m/z 304.1545 assigned as $[Y_1]^+$. This latter eliminates the glucosyl moiety $[(C_6H_{10}O_5), (162.0528 \text{ Da})]$ to afford the thiazole ion [4(1H-1, 2, 3-triazole-4-yl) butan-1-ol] $^+$ at m/z 142.0977 which is assigned as either $[Y_0]^+$ and /or $[BH_2]^+$. Similarly, this product ion $[Y_0]^+$ can also be created from the precursor ion $[M+H]^+$ at m/z 466.2088 by elimination of lactosyl disaccharide moiety $[(C_{12}H_{20}O_{10}), (324.1056 \text{ Da})]$ as shown in Scheme 3.3. In addition, the product ion $[Y_0]^+$ can also eliminates water to form the 4-(but-3-en-1-yl)-1H-1,2,3-triazole ion assigned as $[Y_0-H_2O]^+$ at m/z 124.0887.

All the exact mass assignment of the product ions were verified by conducting separate CID-MS/MS analysis of the deuterated butyltriazole β -D-*N*-lactopyranosides derivatives (**3**) at m/z 475.2648 (Table 3.C).

The proposed low energy CID-MS/MS of protonated precursor ion $[M+H]^+$ fragmentation routes are tentatively shown in Scheme 3.3

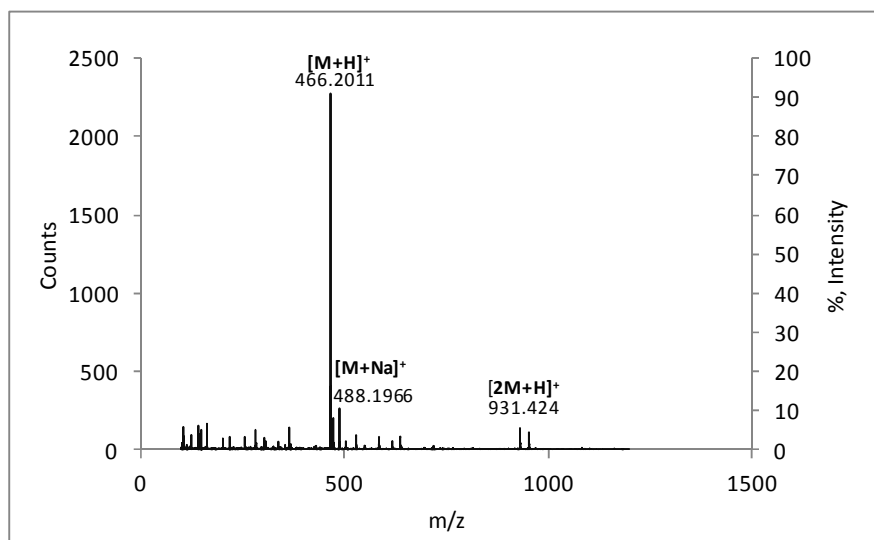


Figure 3.3(a): ESI-QqTOF-MS (+) of the butyltriazole β -D-*N*-lactopyranosides derivative (**3**)

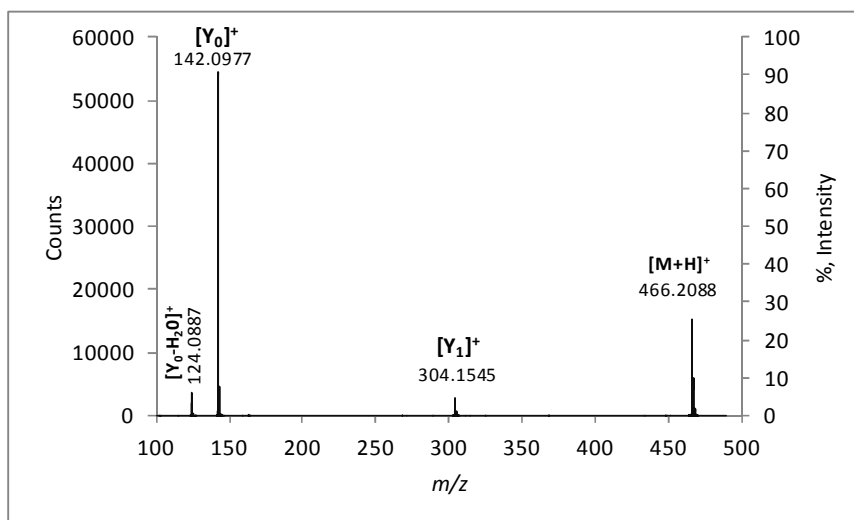
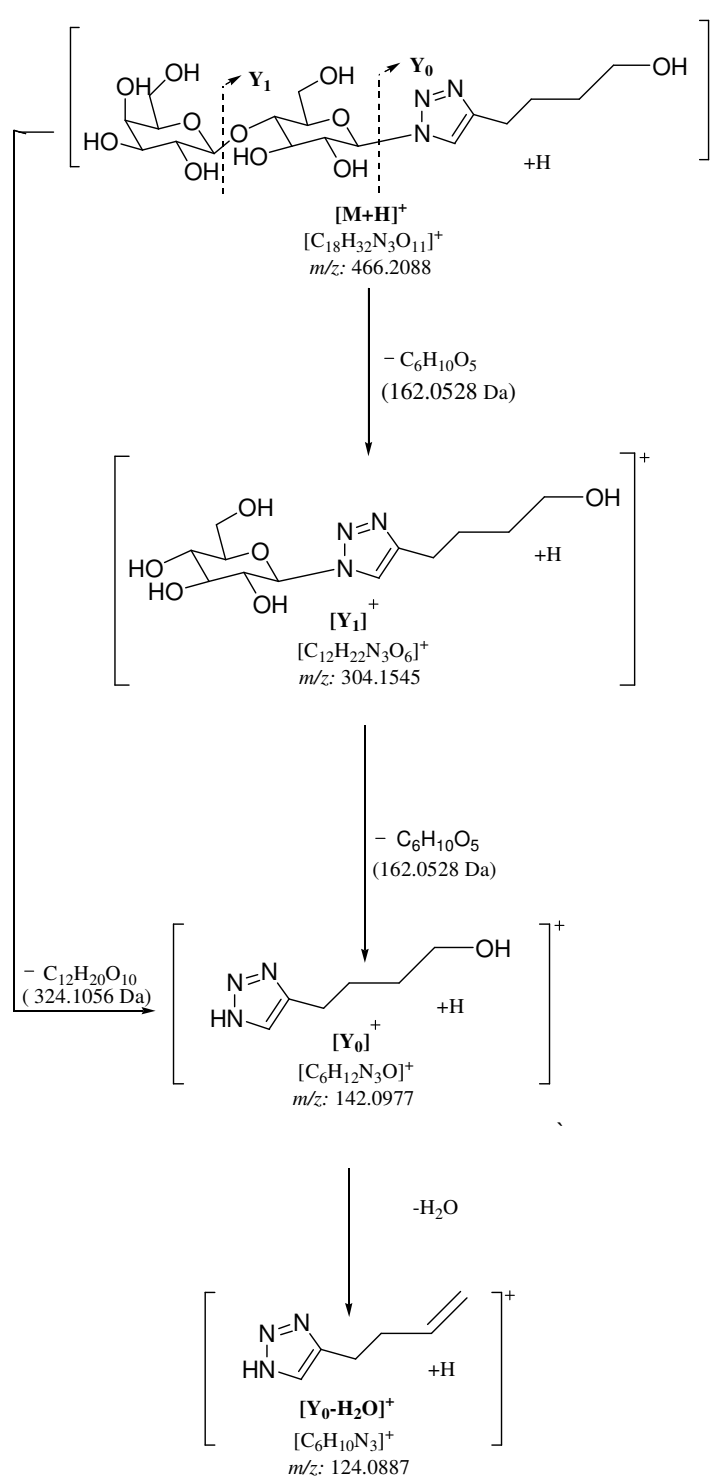


Figure 3.3(b): Low energy CID-MS/MS of the selected protonated precursor ion $[M+H]^+$ at m/z 466.2011 extracted from butyltriazole β -D-*N*-lactopyranosides derivatives (**3**)



Scheme 3.3: The tentative proposed fragmentation routes obtained during the ESI-CID-MS/MS of the protonated molecule $[M+H]^+$ at m/z 466.2011 extracted from butyltriazole β -D-*N*-lactopyranosides derivative (**3**).

Table 3.C: Characteristic products ions observed in the low energy ESI-CID-MS/MS of the protonated the butyltriazole β -D-*N*-lactopyranosides derivatives (**3**) precursor ion $[M+H]^+$ at m/z 466.2011

Characteristic ions	Calculated mass (m/z)	Observed mass (m/z)	Difference (in ppm)
$[C_{18}H_{32}N_3O_{11}]^+$	466.2037	466.2088	11
$[C_{18}H_{23}D_9N_3O_{11}]^+$	475.2596	475.2648	11
$[C_{12}H_{22}N_3O_6]^+$	304.1509	304.1545	12
$[C_{12}H_{16}D_6N_3O_6]^+$	310.1880	310.1923	14
$[C_6H_{12}N_3O]^+$	142.0980	142.0977	2
$[C_6H_9D_3N_3O]^+$	145.1163	145.1183	13
$[C_6H_{10}N_3]^+$	124.0875	124.0887	10
$[C_6H_8D_2N_3]^+$	126.0995	126.101	12

3.3.4. Low energy CID-MS/MS of the protonated precursor ion $[M+H]^+$ at m/z 500.1900 selected from the anisoletriazole β -D-*N*-lactopyranosides derivatives (**4**).

The CID-MS/MS analysis of the selected protonated molecular ion $[M+H]^+$ at m/z 500.1900 extracted from the anisoletriazole β -D-*N*-lactopyranosides derivatives (**4**) was recorded with a CE of 35eV and a DP 1 of 90 V at the. It produced a series of major product ions observed at m/z 338.1315, 325.1174, 176.0838, and 163.063 shown in Figure 3.4 (b). The structural identities of the major product ion are indicated in Table 3.D and their formation geneses are tentatively shown in Scheme 3.4.

The observed product ion at m/z 338.1315 assigned as $[Y_1]^+$, was formed by elimination of galactosyl moiety $[(C_6H_{10}O_5), (162.0528 \text{ Da})]$ from the precursor ion $[M+H]^+$ at m/z 500.1930. In addition, this product ion $[Y_1]^+$ loses the aglycone triazole

derivative [(4-(phenoxymethyl)-1H-1,2,3-triazole),(175.0746 Da)] to form the glucosyl-oxonium ion at m/z 163.063 which is assigned as $[B_1]^+$. This latter product ion at m/z $[B_1]^+$ can also be formed by direct cleavage from the precursor ion $[M+H]^+$ by the elimination of neutral molecule $[(C_{15}H_{19}N_3O_6), (337.1274 \text{ Da})]$. The lactosyl disaccharide-oxonium ion at m/z 325.1174 was formed from the precursor ion $[M+H]^+$ by the elimination of neutral aglycone moiety [4-(phenoxymethyl)-1H-1,2,3-triazole, (175.0746) Da] which is assigned as $[B_2]^+$. The precursor ion $[M+H]^+$ can also eliminate the disaccharide moiety $[(C_{12}H_{20}O_{10}), (324.1056 \text{ Da})]$ to form the aglycone product ion at m/z 176.0838 which is assigned as $[Y_0]^+$.

All the exact mass assignment of the product ions were verified by conducting separate CID-MS/MS analysis of the deuterated anisoletriazole β -D-*N*-lactopyranosides derivatives (**4**) at m/z 508.2411 (Table 3.A).

The proposed low energy CID-MS/MS of protonated precursor ion $[M+H]^+$ fragmentation routes are tentatively shown in Scheme 3.4

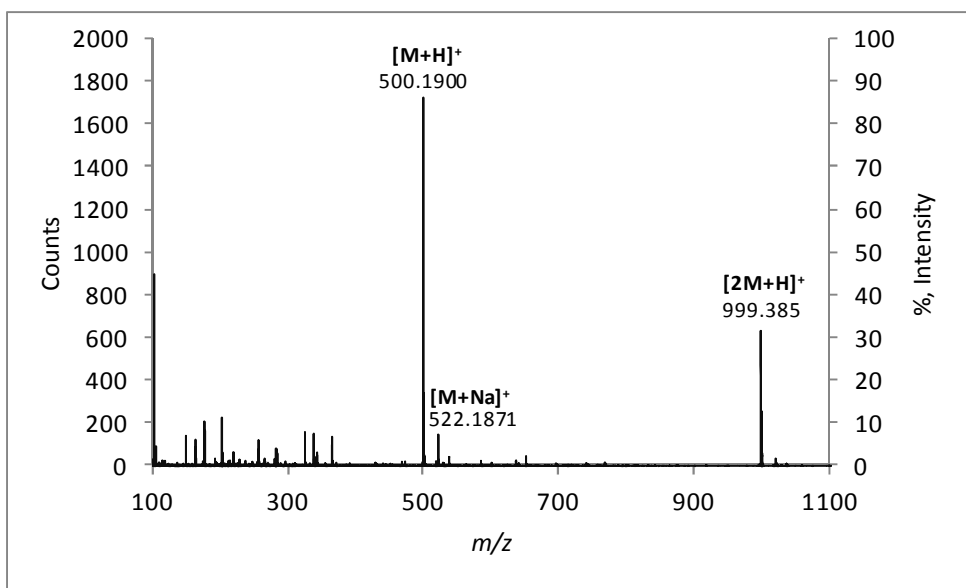


Figure 3.4(a): ESI-QqTOF-MS(+) of the anisoletriazole β -D-*N*-lactopyranosides derivatives (**4**).

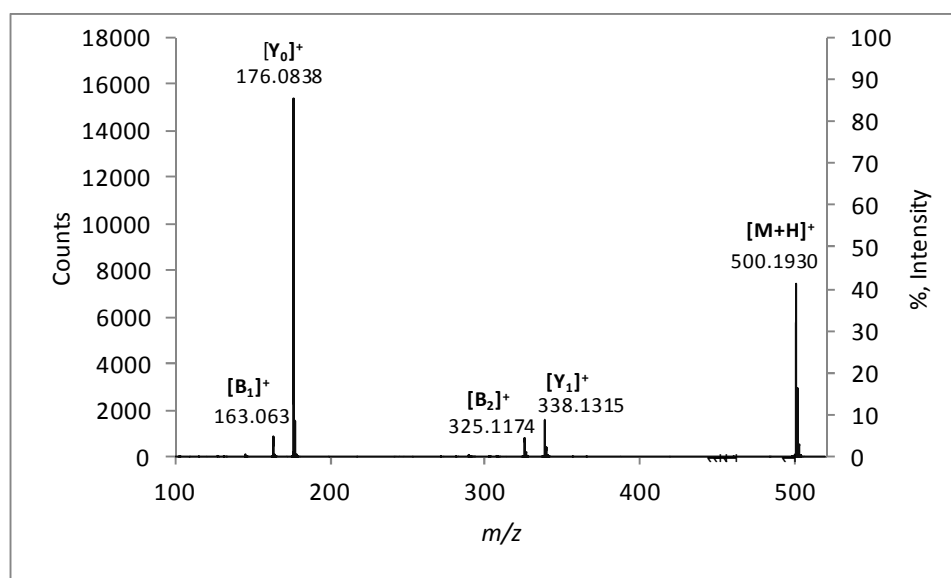
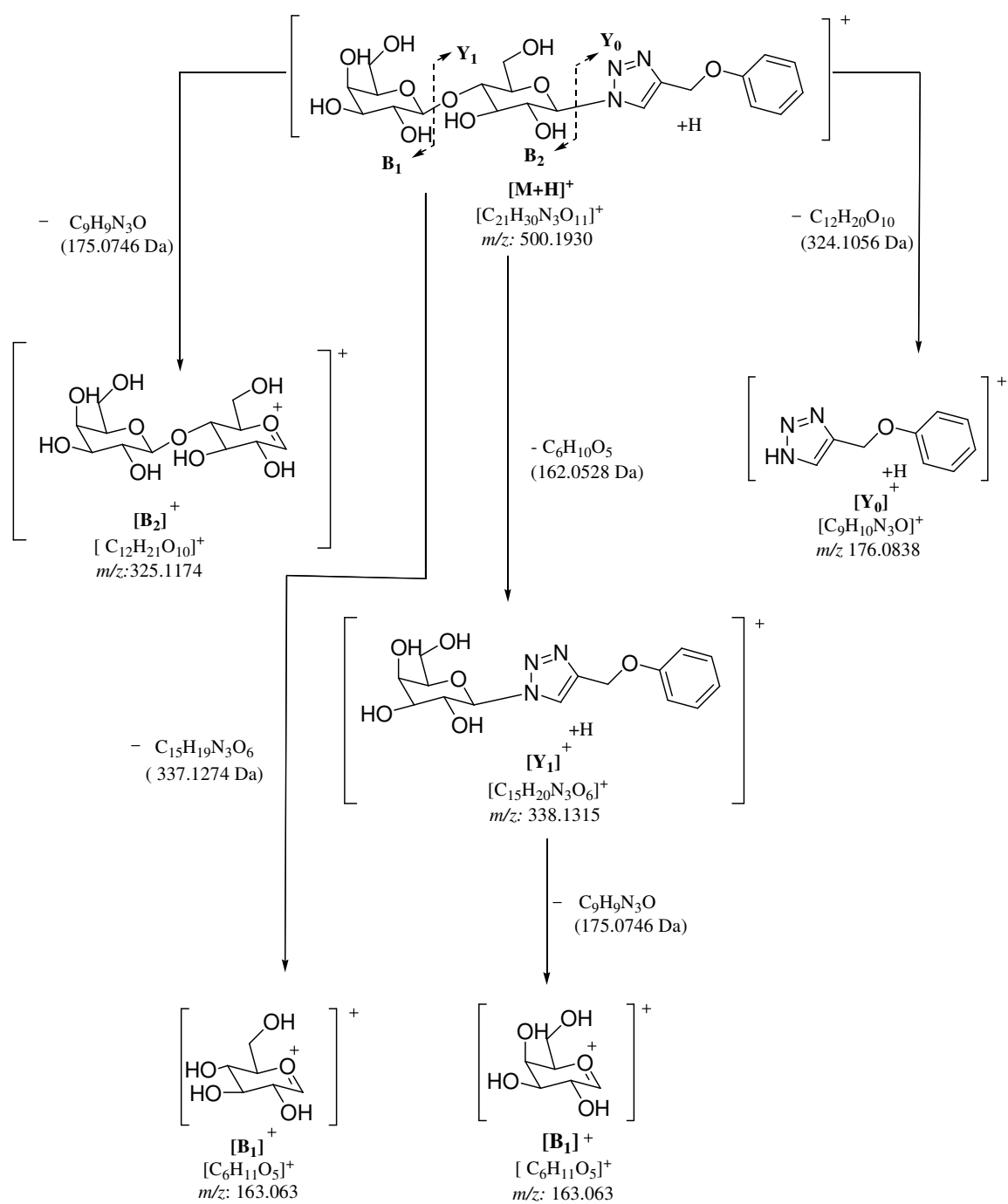


Figure 3.4(b): Low energy CID-MS/MS of the selected protonated precursor ion [M+H]⁺ at m/z 500.1900 extracted from the anisoletriazole β -D-*N*-lactopyranosides derivatives (**4**).



Scheme 3.4: The tentative proposed fragmentation routes obtained during the ESI-CID-MS/MS of the protonated molecule $[M+H]^+$ at m/z 500.1900 extracted from the anisoletriazole β -D-*N*-lactopyranosides derivatives (**4**).

Table 3.D: Characteristic product ions observed in the low energy ESI-CID-MS/MS of the protonated the anisoletriazole β -D-*N*-lactopyranosides derivative (**4**) precursor ion $[M+H]^+$ at m/z 500.1900.

Characteristic ions	Calculated mass (m/z)	Observed mass (m/z)	Difference (in ppm)
$[C_{21}H_{30}N_3O_{11}]^+$	500.1880	500.1930	10
$[C_{21}H_{22}D_8N_3O_{11}]^+$	508.2377	508.2411	11
$[C_{15}H_{20}N_3O_6]^+$	338.1352	338.1315	11
$[C_{15}H_{15}D_5N_3O_6]^+$	343.1660	343.1694	10
$[C_{12}H_{21}O_{10}]^+$	325.1135	325.1174	12
$[C_{12}H_{14}D_7O_{10}]^+$	332.1569	332.1596	8
$[C_9H_{10}N_3O]^+$	176.0824	176.0838	8
$[C_9H_8D_2N_3O]^+$	178.0944	178.0958	8
$[C_6H_{11}O_5]^+$	163.0606	163.063	15
$[C_6H_7D_4O_5]^+$	167.0852	167.0877	15

3.1.5. Low energy CID-MS/MS of the precursor ion $[M+H]^+$ at m/z 530.2012 selected from the dimethoxybenzenetriazole β -D-*N*-lactopyranosides derivatives (**5**)

The CID-MS/MS analysis of the selected protonated precursor ion $[M+H]^+$ at m/z 530.2012 extracted from the dimethoxybenzenetriazole β -D-*N*-lactopyranosides derivatives (**5**) was recorded with a collision energy of 36eV and a DP1 of 76 V and produced the product ion at m/z 368.1491, 325.1174, 206.0946, and 163.0586 shown in Figure 3.5 (b). The structural identities of the major product ion are indicated in Table 3.E and their genesis of formation is tentatively shown in Scheme 3.5.

Thus, the precursor ion $[M+H]^+$ at m/z 530.2044 fragments to afford the product ion at m/z 368.1491 formed by elimination of galactosyl moiety $[(C_6H_{10}O_5), (162.0528 \text{ Da})]$ assigned as $[Y_1]^+$. This latter product ion $[Y_1]^+$ fragments by elimination of the neutral aglycone moiety $[(C_{10}H_{11}N_3O_2), (205.0851 \text{ Da})]$ to form the product ion at m/z 163.0586 ion assigned as the $[B_1]^+$ galactosyl oxonium ion. The product ion $[B_1]^+$ can also be formed from the direct cleavage of the precursor ion $[M+H]^+$ at m/z 530.2044 as shown in Scheme 3.5. The protonated precursor ion $[M+H]^+$ can also eliminate the lactosyl disaccharide moiety $[(C_{12}H_{20}O_{10}), (324.1056 \text{ Da})]$ to form the triazole derivative product ion $[Y_0]^+$. In addition, the precursor ion $[M+H]^+$ also eliminates the triazole moiety $[(C_{10}H_{11}N_3O_2), (205.0851 \text{ Da})]$ to form the disaccharide lactosyl oxonium ion at m/z 325.1174 assigned as $[B_2]^+$.

All the exact mass assignment of the product ions were verified by conducting separate CID-MS/MS analysis of the deuterated dimethoxybenzenetriazole β -D-N-lactopyranosides derivatives (**5**) at m/z 538.2558 (Table 3.E).

The proposed low energy CID-MS/MS of protonated precursor ion $[M+H]^+$ fragmentation routes are tentatively shown in Scheme 3.5

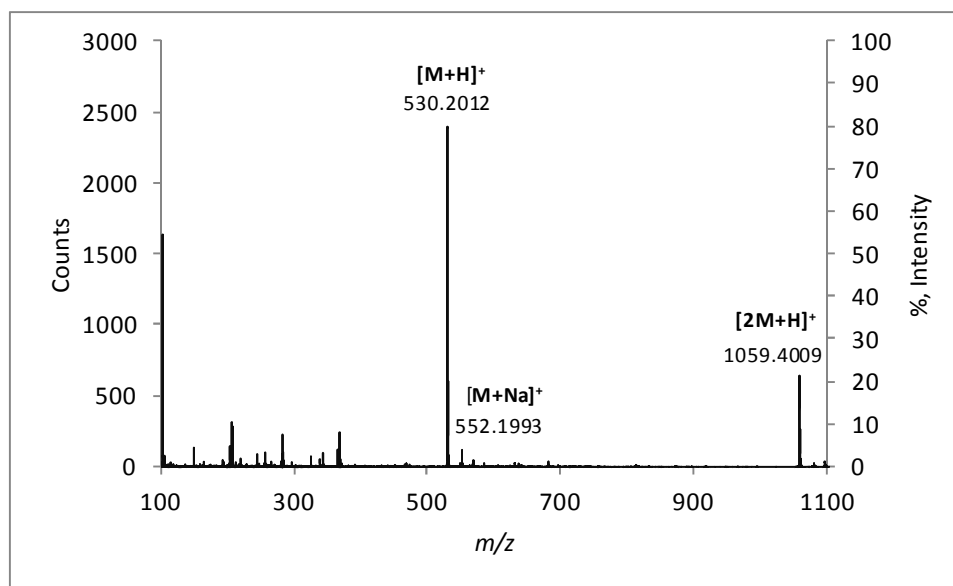


Figure 3.5(a): ESI-QqTOF-MS(+) of the dimethoxybenzenetriazole- β -D-*N*-lactopyranosides derivatives (**5**)

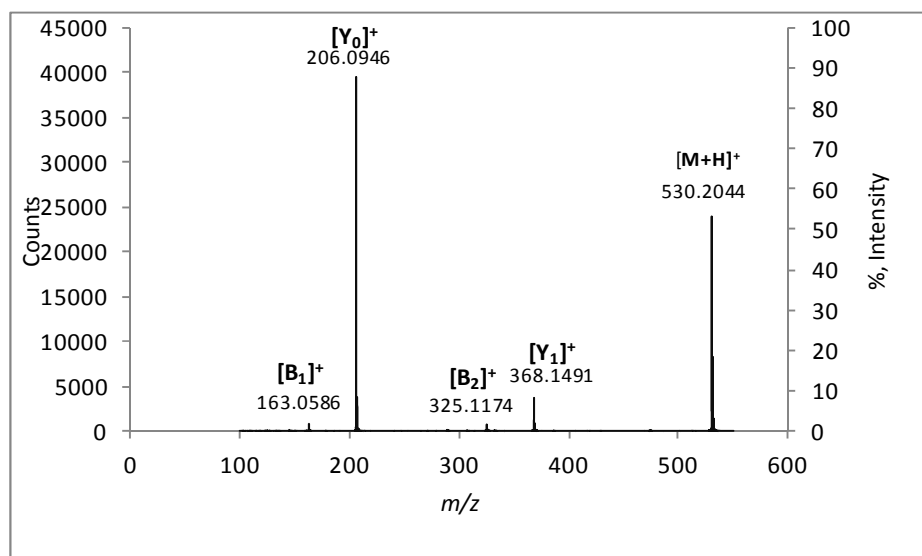
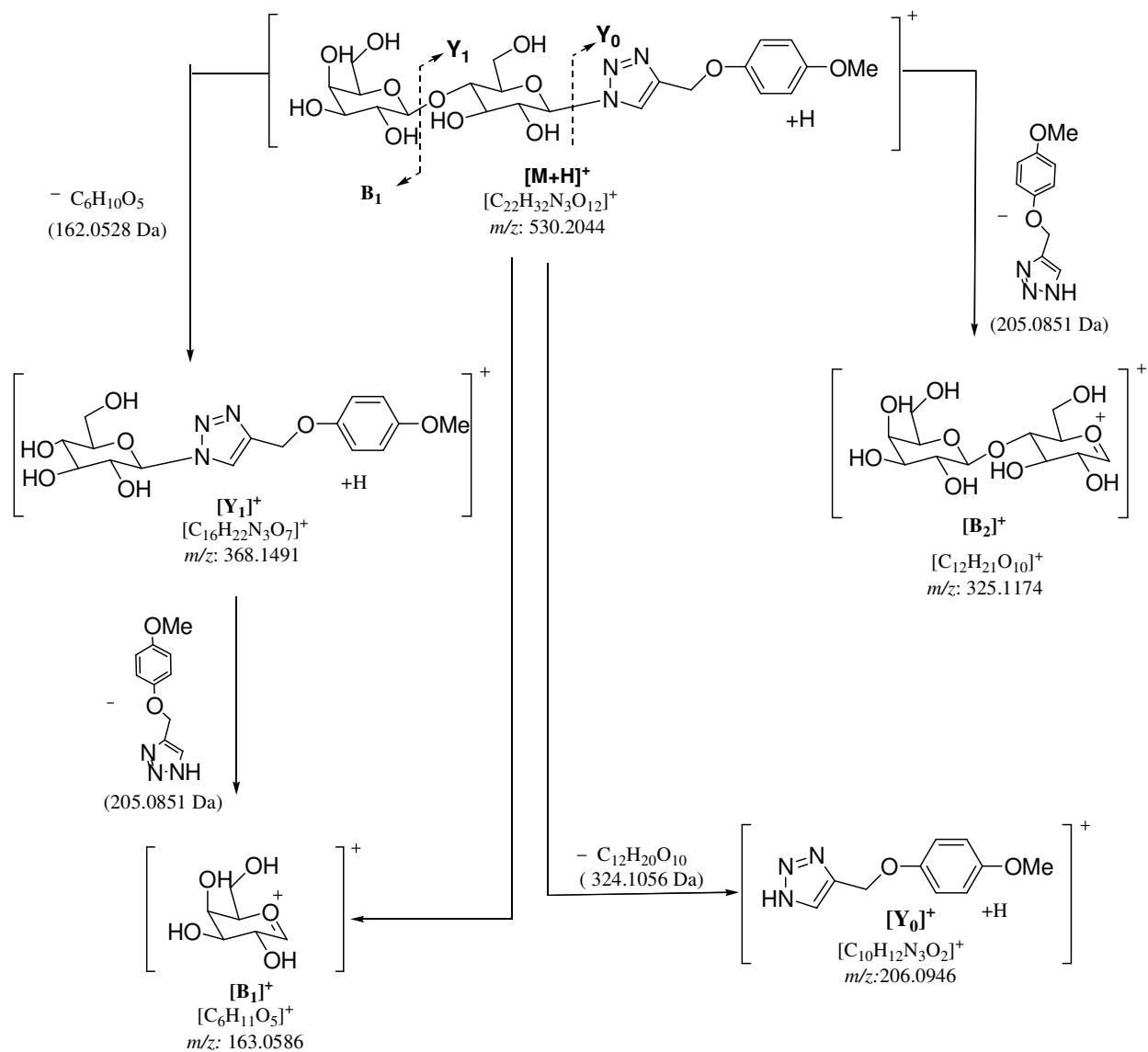


Figure 3.5(b): Low energy CID-MS/MS of the selected protonated precursor ion [M+H]⁺ at m/z 530.2012 extracted from the dimethoxybenzenetriazole β -D-*N*-lactopyranosides derivatives (**5**)



Scheme 3.5: The tentative proposed fragmentation routes obtained during the ESI-CID-MS/MS of the protonated molecule $[M+H]^+$ at m/z 530.2012 extracted from the dimethoxybenzenetriazole- β -D-*N*-lactopyranosides derivatives (**5**)

Table 3.E: Characteristic product ions observed in the low energy ESI-CID-MS/MS of the dimethoxybenzenetriazole β -D-*N*-lactopyranosides derivatives (**5**) precursor ion $[M+H]^+$ at m/z 530.2012

Characteristics ions	Calculated mass (m/z)	Observed mass (m/z)	Difference (in ppm)
$[C_{22}H_{32}N_3O_{12}]^+$	530.1986	530.2044	11
$[C_{22}H_{24}D_8N_3O_{12}]^+$	538.2483	538.2558	14
$[C_{16}H_{22}N_3O_7]^+$	368.1458	368.1491	9
$[C_{16}H_{17}D_5N_3O_7]^+$	373.1766	373.1800	9
$[C_{12}H_{21}O_{10}]^+$	325.1135	325.1174	12
$[C_{12}H_{14}D_7O_{10}]^+$	332.1569	332.1592	7
$[C_{10}H_{12}N_3O_2]^+$	206.0930	206.0946	8
$[C_{10}H_{10}D_2N_3O_2]^+$	208.1050	208.1062	6
$[C_6H_{11}O_5]^+$	163.0606	163.0586	12
$[C_6H_7D_4O_5]^+$	167.0852	167.0870	11

3.3.6. Low energy CID-MS/MS of the precursor ion $[M+H]^+$ at m/z 550.2009 selected from the methoxynaphthalene-triazole β -D-*N*-lactopyranosides derivatives (**6**)

The CID-MS/MS of precursor ion $[M+H]^+$ at m/z 550.2009 extracted from the methoxynaphthalene-triazole β -D-*N*-lactopyranosides derivatives (**6**) was recorded with collision energy of 45 eV and a DPI of 62 V. The major product ions formed were observed at m/z 388.1530, 325.1145, 226.1007 and 163.0630 shown in Figure 3.6(b). The structural identities of the major product ion are indicated in Table 3.F and their genesis of formation is tentatively indicated in Scheme 3.6.

Thus, the protonated precursor ion $[M+H]^+$ at m/z 550.2020 eliminates the galactosyl moiety $[(C_6H_{11}O_5), (162.0528 \text{ Da})]$ to form the methoxynaphthalene-triazole β -D-*N*-glucopyranoside derivatives product ion at m/z 388.1530, assigned as $[Y_1]^+$. In addition, the precursor ion $[M+H]^+$ fragments by elimination of $[(C_{13}H_{11}N_3O), (225.0902 \text{ Da})]$ to form the disaccharide oxonium ion at m/z 325.1145, assigned as $[B_2]^+$. The product ion $[B_1]^+$ at m/z 163.0630 can be formed by elimination of aglycone $[(C_{13}H_{11}N_3O), (225.0902 \text{ Da})]$. This product ion $[B_1]^+$ can also originate by direct cleavage of precursor ion as shown in Scheme 3.6. Finally, the product ion $[Y_0]^+$ at m/z 226.1007 was obtained from the precursor ion $[M+H]^+$ by elimination the lactosyl moiety $[(C_{12}H_{22}O_{10}), (326.1056 \text{ Da})]$.

All the exact mass assignment of the product ions was verified by conducting separate CID-MS/MS analysis of the deuterated methoxynaphthalene-triazole β -D-*N*-lactopyranosides derivatives (**6**) at m/z 558.2594 (Table 3.F).

The proposed low energy CID-MS/MS fragmentation routes of the protonated precursor ion are tentatively shown in Scheme 3.6.

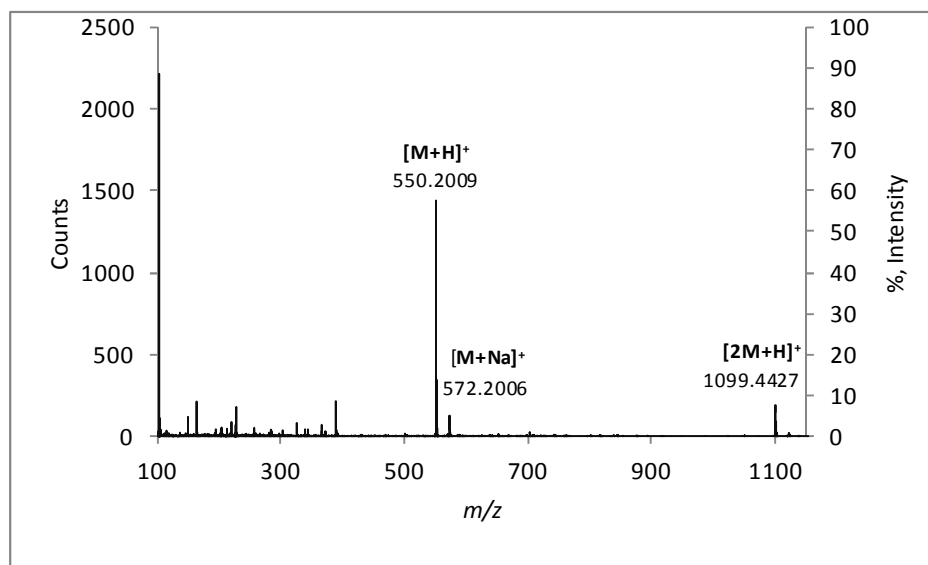


Figure 3.6(a): ESI-QqTOF-MS(+) of the methoxynaphthalene-triazole β -D-*N*-lactopyranosides derivatives (**6**)

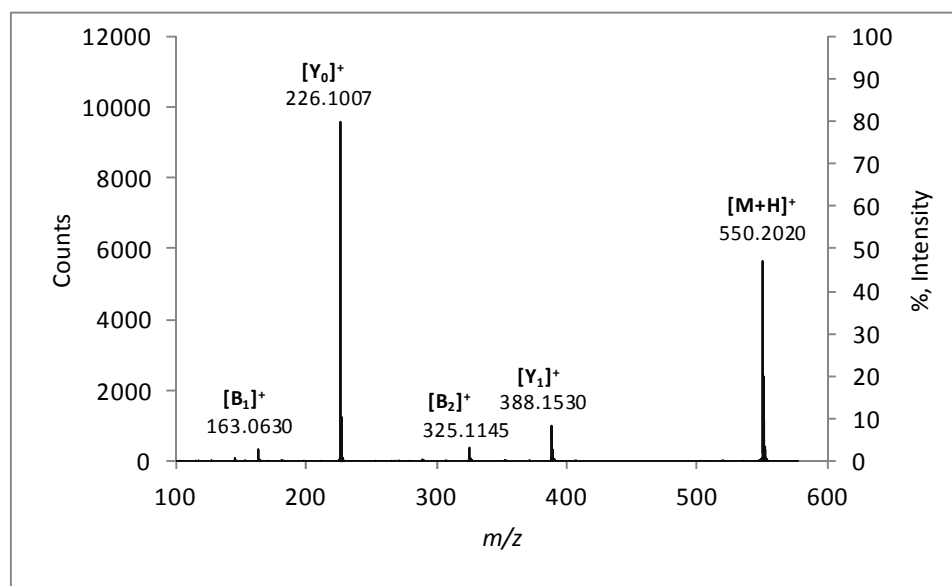
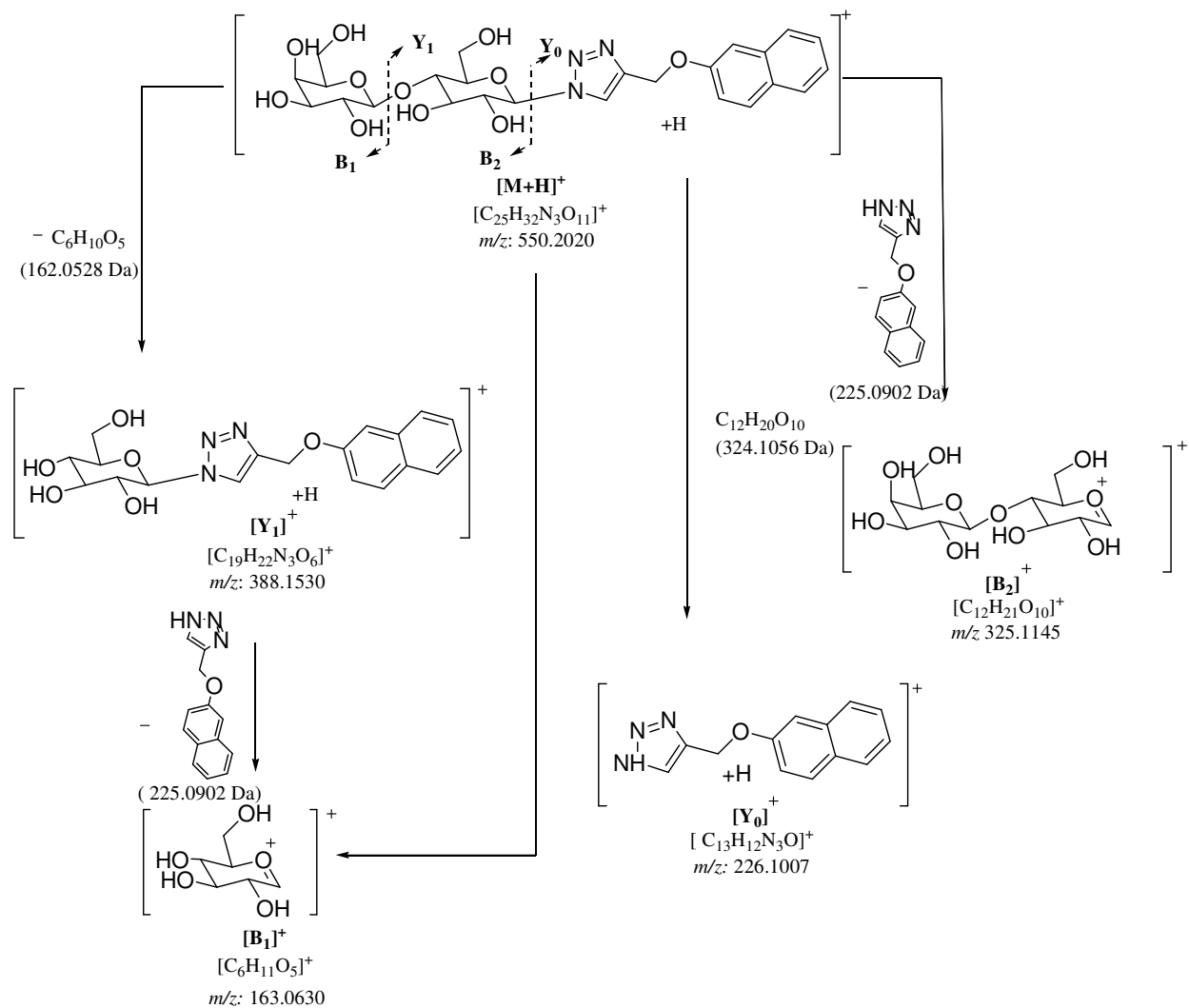


Figure 3.6(b): Low energy CID-MS/MS of the selected protonated precursor ion [M+H]⁺ at m/z 550.2009 extracted from methoxynaphthalene-triazole β -D-*N*-lactopyranosides derivatives (**6**)



Scheme 3.6: The tentative proposed fragmentation routes obtained during the ESI-CID-MS/MS of the protonated molecule $[M+H]^+$ at m/z 550.2009 extracted from methoxynaphthalene-triazole β -D-N-lactopyranosides derivatives (**6**).

Table 3.F: Characteristic product ions observed in the low energy ESI-CID-MS/MS of the protonated the methoxynaphthalene-triazole β -D-*N*-lactopyranosides derivatives (**6**) precursor ion $[M+H]^+$ at m/z 550.2009

Characteristic ions	Calculated mass (m/z)	Observed mass (m/z)	Difference (in ppm)
$[C_{22}H_{32}N_3O_{12}]^+$	550.2037	550.2020	3
$[C_{25}H_{24}D_8N_3O_{11}]^+$	558.2533	558.2594	11
$[C_{16}H_{22}N_3O_7]^+$	388.1509	388.1530	5
$[C_{19}H_{17}D_5N_3O_6]^+$	393.1817	393.1837	5
$[C_{12}H_{21}O_{10}]^+$	325.1135	325.1145	3
$[C_{12}H_{14}D_7O_{10}]^+$	332.1569	332.1609	12
$[C_{10}H_{12}N_3O_2]^+$	226.0980	226.1007	11
$[C_{13}H_{10}D_2N_3O]^+$	228.1100	228.1123	10
$[C_6H_{11}O_5]^+$	163.0606	163.0630	15
$[C_6H_7D_4O_5]^+$	167.0852	167.0862	7

3.4. Conclusion

In this study, the gas-phase fragmentations of the novel synthetic bivalent *N*-glycosides (**1-6**) using ESI-MS and CID-MS/MS analyses with a QqTOF-MS/MS hybrid instrument were evaluated. The results presented demonstrated that during ESI-MS and CID-MS/MS analyses, the bivalent *N*-glycosides follow a universal fragmentation

pattern. In general it was observed that the CID-MS/MS fragmentation routes of the six precursor protonated molecules obtained from the bivalent *N*-glycosides (**1-6**) afforded similar series of product ions formed essentially by the same gas-phase mechanisms.

As expected, it was noticed that as the collision energy of the CID-MS/MS analyses was increased, an enhancement in the gas-phase fragmentation was produced. A quick scrutiny of Tables (3A-F) will indicate the presence of some common product ions.

The genesis of the MS/MS fragmentations and the structural identities of the product ions are shown in Figures 3.1(b)-3.6(b) and Schemes 3.1-3.6. The CID-MS/MS analyses of the different deuterated precursor species Tables 3.A-3.F were also created to verify the formation of the major product ions. This fragmentation pattern can be used to easily predict the fragmentation patterns of new compounds with the same general backbone structure. Accordingly, this series of precursor ions afforded upon CID-MS/MS analyses gave the diagnostic product ion $[B_1]^+$, $[B_2]^+$, $[Y_1]^+$ and $[Y_0]^+$

CHAPTER 4: GAS-PHASE FRAGMENTATION OF NOVEL SYNTHETIC BIVALENT *N*-GLYCOSIDES USING MALDI-MS IN CONJUNCTION WITH HIGH ENERGY COLLISION MASS SPECTROMETRY (MALDI-TOF/TOF-CID-MS/MS).

4.1. Introduction

Matrix assisted laser desorption/ionization mass spectrometry (MALDI-TOF/TOF-MS) is an extremely dominant technique for the analysis of biomolecules. Indeed the analysis of carbohydrates is of high importance in modern biochemistry. It has been shown that during the structural determination of unknown carbohydrates, it is essential to elucidate the exact sugar sequences, the assignment of the reducing end, the linkage type between the monosaccharides and the anomeric configuration.

MALDI-TOF/TOF-MS is a soft desorption ionization method, which possesses large mass range and high sensitivity; MALDI-TOF/TOF-MS is nowadays broadly used for the molecular weight determination of underivatized small and large carbohydrates.^{[131],[132]} Indeed different types of MALDI-TOF/TOF-MS instruments, allowed the recording of fragment ion spectra of sodiated ions from neutral carbohydrates.

It has been shown that a large amount information could be obtained by MALDI-PSD-TOF experiments. Moreover, PSD (metastable decay) spectra of sodiated ions from neutral carbohydrates are subjugated by glycosidic and internal cleavages, providing information related to sequence and branching of the carbohydrate molecules.^{[133], [134]}

On the other hand, a lack of abundant cross-ring cleavages obtained by MALDI-PSD-TOF limited the linkage information that could have been deduced from such

experiments. Recently, it was shown that cross-ring fragmentation provided information on glycosidic linkages. This information is usually obtained upon high energy collision-induced dissociation (CID) on MALDI-TOF/TOF instruments.^{[135], [136]} In contrast to other desorption techniques infrared laser desorption mass spectrometry of carbohydrates produces a unique fragmentation pattern that can be described as two-bond ring cleavages within the cyclic sugar units.^{[137], [138]}

4.2. MALDI-TOF/TOF-MS analysis of the novel synthetic bivalent β -D-*N*-glycosides (*1-6*)

The MALDI-TOF/TOF-MS analyses of this series were all recorded in the positive ion mode and the afforded only the sodiated molecular ion at $[M+Na]^+$ and the potassium adduct $[M+K]^+$. There was also absence of protonated molecules.^{[139], [140]} Accordingly, the MALDI-TOF/TOF-MS of the methoxynaphthalene-substituted triazole β -D-*N*-galactopyranosides derivative (**1**) produced the $[M+Na]^+$ sodiated molecular ion at m/z 410.1210 and the $[M+K]^+$ potassium adduct at m/z 425.9593 [Figure 4.1(a)]; The MALDI-TOF/TOF-MS of ethyltriazole β -D-*N*-lactopyranosides derivative (**2**) formed the $[M+Na]^+$ at m/z 460.1533 and $[M+K]^+$ potassium adduct at m/z 475.9542 [Figure 4.2(a)]; The MALDI-TOF/TOF-MS of the butyltriazole β -D-*N*-lactopyranosides derivatives (**3**) afforded the $[M+Na]^+$ sodiated molecular ion at m/z 488.1750 and the $[M+K]^+$ potassium adduct at m/z 503.9928 [Figure 4.3(a)]; MALDI-TOF/TOF-MS of anisoletriazole β -D-*N*-lactopyranosides derivatives (**4**) afforded the $[M+Na]^+$ sodiated molecular ion at m/z 522.1580 and $[M+K]^+$ potassium adduct at m/z 537.9698 [Figure 4.4(a)]; MALDI-TOF/TOF-MS of the dimethoxybenzenetriazole β -D-*N*-lactopyranosides derivatives (**5**)

afforded the $[M+Na]^+$ sodiated molecular ion at m/z 552.1720 and $[M+K]^+$ potassium adduct at m/z 567.9633 [Figure 4.5(a)] and finally MALDI-TOF/TOF-MS of the methoxynaphthalene-triazole β -D-*N*-lactopyranosides derivatives (**6**) afforded the only $[M+Na]^+$ sodiated adduct at m/z 572.1750 [Figure 4.6a].

In order to study the detailed gas- fragmentation of this series of sodiated molecular ions, these were subjected to high-energy collision induced dissociation (CID) using the TOF/TOF-MS/MS.

4.3. MALDI-TOF/TOF-CID-MS/MS analysis of synthetic bivalent β -D-*N*-glycosides (1-6**)**

High-energy collision induced dissociation CID-MS/MS analyses of the different precursor sodiated species $[M+Na]^+$ were found. Tables 4.A-3.F, summarize the formation of the various diagnostic product ions observed in the CID-MS/MS analyses of the precursor sodiated molecules $[M+Na]^+$ selected from the various synthetic bivalent β -D-*N*-glycosides (**1-6**). The various coding used for the product ion tagging was based on the nature of the bivalent β -D-*N*-glycosides. The product ion scans of the precursor sodiated molecules selected from the six bivalent β -D-*N*-glycosides (**1-6**) are shown in Figures 4.1(b)-4.6(b) and in Schemes 4.1-4.6.

4.3.1. High energy MALDI-TOF/TOF-CID-MS/MS of the sodiated precursor ion $[M+Na]^+$ at m/z 410.1210 selected from the methoxynaphthalene-substituted triazole β -D-*N*-galactopyranosides derivatives (*I*)

The product ion scan of selected sodiated molecular ion $[M+Na]^+$ at m/z 410.1210 extracted from the methoxynaphthalene-substituted triazole β -D-*N*-galactopyranosides derivatives (*I*) was recorded. The main high-energy CID-fragmentation pathway observed in this spectrum corresponds to the glycosidic cleavage (B types) associated with ring cleavage and elimination of the aglycone moiety.

Thus, CID-MS/MS of the $[M+Na]^+$ ion at m/z 410.1210 afforded the series of product ions at m/z 382.1210, 329.1012, 267.0812, 238.0677, and 185.0417 shown in Figure 4.1 (b). The structural identities of the major product ion are indicated in Table 4.A and their genesis is shown in Scheme 4.1. The precursor ion $[M+Na]^+$ at m/z 410.1279 loses a nitrogen molecule N_2 to form product ion at m/z 382.1210, which is assigned as $[M+Na-N_2]^+$. This latter product ion at m/z 382.1210 loses two water molecules and a hydroxyl radical to form the radical cation product ion at m/z 329.1012. The precursor ion $[M+Na]^+$ can also consecutively lose the neutral [naphthalen-2-ol, (144.0575 Da)] and a nitrogen molecule from the triazole ring cleavage to form the product ion at m/z 238.0677. The precursor ion $[M+Na]^+$ again loses naphthalene-2-ol radical [$(C_{10}H_7O^\bullet)$, (143.0497 Da)] to form the radical cation product ion at m/z 267.0812. The product radical cation at m/z 267.0812 can also lose the triazole radical [$(C_3H_4N_3^\bullet)$, (82.0405 Da)] to form the product ion at m/z 185.0417 which is assigned as

$[B_2]^+$. This product ion at $[B_2]^+$ can also be formed from the direct cleavage from the sodiated precursor ion $[M+Na]^+$ by elimination of $[(C_{13}H_{11}N_3O), (225.0908 \text{ Da})]$ as shown in Scheme 4.1.

The proposed high energy MALDI-CID-MS/MS of sodiated precursor ion $[M+Na]^+$ fragmentation routes are tentatively shown in Scheme 4.1

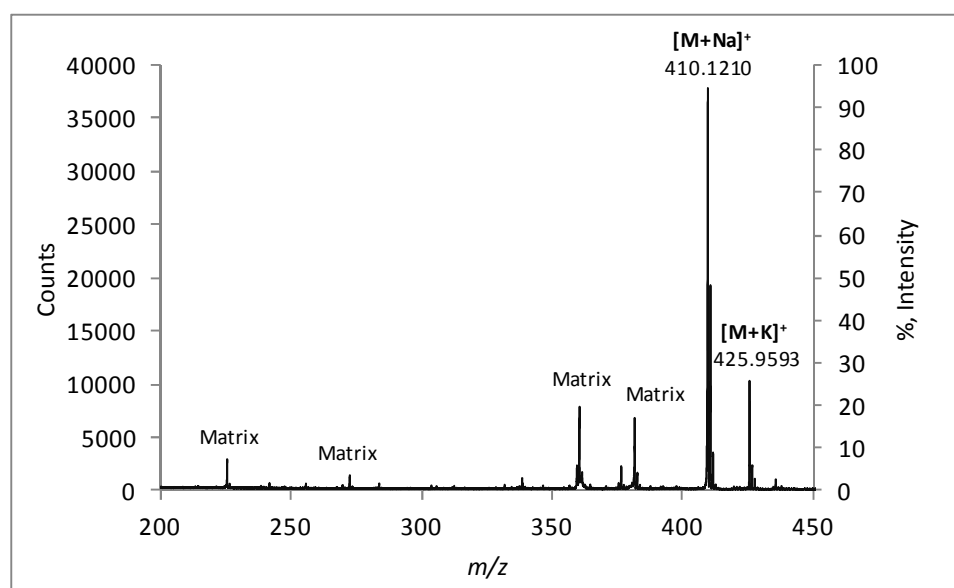


Figure 4.1(a): MALDI-TOF/TOF-MS (+) profile of the methoxynaphthalene-substituted triazole β -D-*N*-galactopyranosides derivatives (**1**)

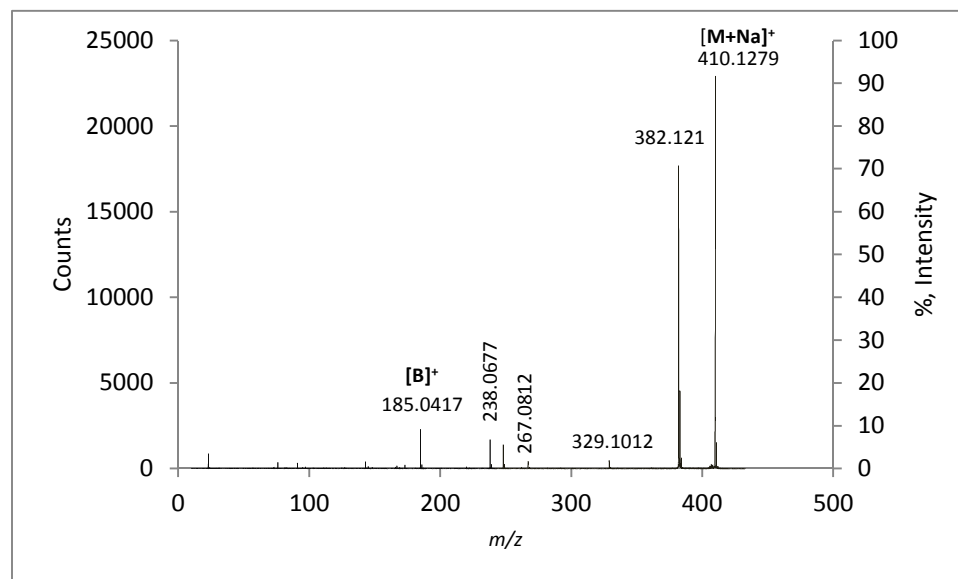
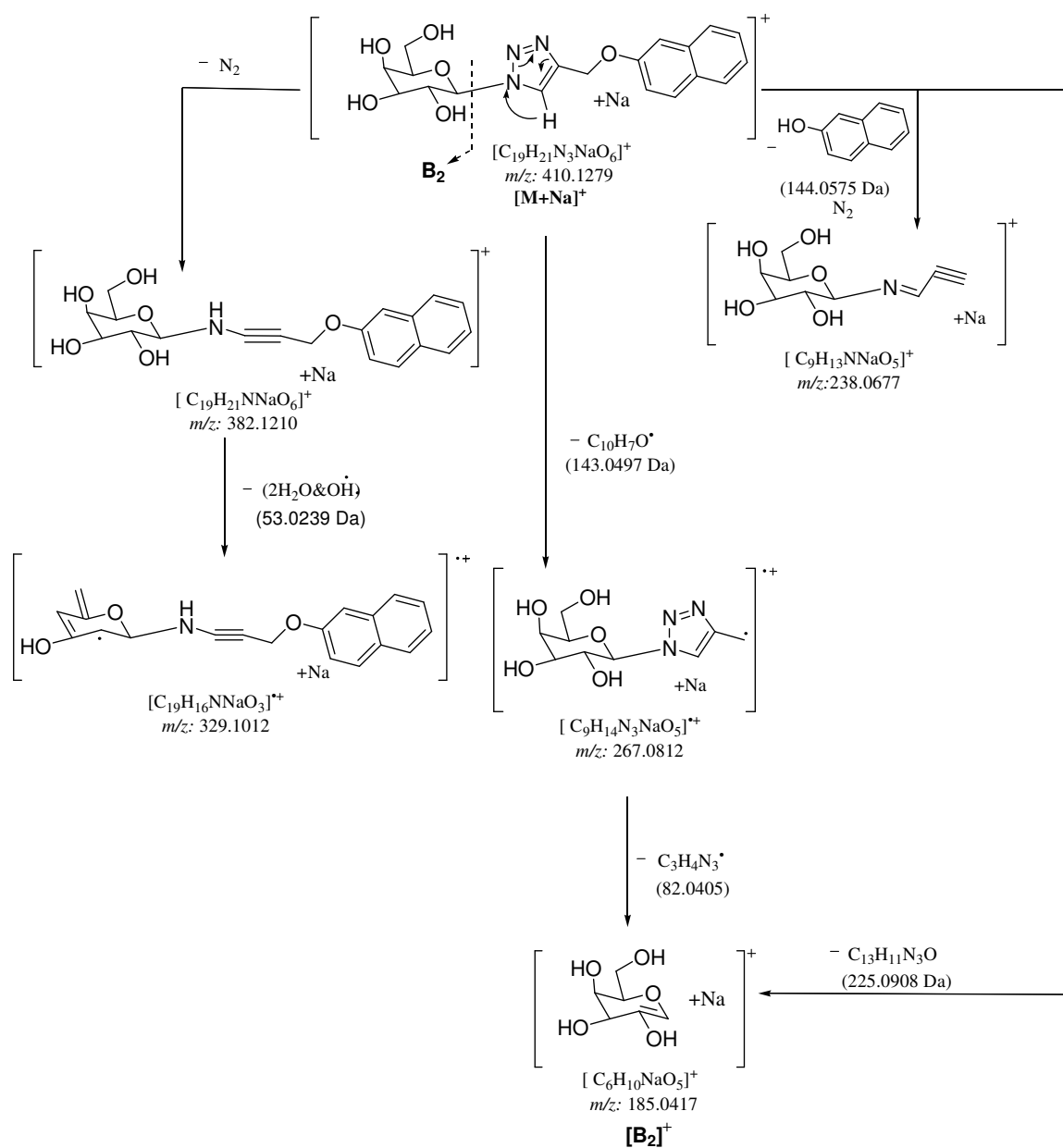


Figure 4.1(b): MALDI-TOF/TOF high energy CID-MS/MS of the precursor ion $[M+Na]^+$ at m/z 410.1210 selected from the methoxynaphthalene-substituted triazole β -D-*N*-galactopyranosides derivatives (**I**)



Scheme 4.1: The tentative proposed fragmentation routes obtained during MALDI-TOF/TOF high energy CID-MS/MS of the sodiated precursor ion [M+Na]^+ at m/z 410.1210 selected from methoxynaphthalene-substituted triazole β -D-*N*-galactopyranosides derivatives (**1**)

Table 4.A: Characteristic product ions observed in the MALDI-TOF/TOF high energy CID-MS/MS of the sodiated the methoxynaphthalene-substituted triazole β -D-*N*-galactopyranosides derivatives (**1**) precursor ion $[M+Na]^+$ at m/z 410.1210

Characteristic ions	Calculated mass (m/z)	Observed mass (m/z)	Difference (in ppm)
$[C_{19}H_{21}N_3NaO_6]^+$	410.1328	410.1279	12
$[C_{19}H_{21}NNaO_6]^+$	382.1267	382.1210	15
$[C_{19}H_{16}NNaO_3]^{++}$	329.1028	329.1012	5
$[C_9H_{14}N_3NaO_5]^{++}$	267.0831	267.0812	7
$[C_9H_{13}NNaO_5]^+$	238.0691	238.0677	6
$[C_6H_{10}NaO_5]^+$	185.0426	185.0417	5

4.3.2. High energy MALDI-TOF/TOF-CID-MS/MS of the sodiated precursor ion $[M+Na]^+$ at m/z 460.1533 selected from the ethyltriazole β -D-*N*-lactopyranosides derivative (**2**)

The product ion scan of the selected sodiated ethyltriazole β -D-*N*-lactopyranosides derivative (**2**) molecular ion $[M+Na]^+$ at m/z 460.1533 afforded main fragmentation pathways corresponding to glycosidic cleavage (B and Y) associated with radical cation product ion; ring cleavage and elimination of the aglycone. The CID-MS/MS of $[M+Na]^+$ at m/z 460.1533 afforded the product ions at m/z 432.1426, 402.1447, 361.1189, 347.0926, 331.0988, 305.0825, 259.0809, 201.0363, 169.0498 and 136.0498; shown in Figure 4.2 (a). The structural identities of the major product ions are tentatively indicated in Table 4.B and their formation genesis are indicated in Scheme 4.2(a) and 4.2(b).

Thus, the precursor ion $[M+Na]^+$ at m/z 460.1583 loses a nitrogen molecule to afford the product ion at m/z 432.1426 [Scheme 4.2(a)] ,which was assigned as $[M+Na-$

$\text{N}_2]^+$ ion. This latter product ion at m/z 432.1426 loses the [(4-(hydroxyamino) but-3-yn-1-
 o molecule, (101.0477 Da)] to form the product ion at m/z 331.0988 [Scheme 4.2(a)]
 assigned as $[\text{M}+\text{Na}-\text{C}_4\text{H}_7\text{NO}_2-\text{N}_2]^+$. This latter product ion can be created by direct
 elimination of $[(\text{C}_4\text{H}_7\text{N}_3\text{O}_2), (129.0538 \text{ Da})]$ from the precursor ion $[\text{M}+\text{Na}]^+$ as shown in
 the [Scheme 4.2(a)]. The product ion at m/z 402.1447 which is assigned as $^{[2,4]}\text{X}_2^+$
 [Scheme 4.2(b)] is formed by elimination of the neutral fragment $[(\text{C}_2\text{H}_2\text{O}_2), (58.0055$
 Da)]. This the precursor ion $[\text{M}+\text{Na}]^+$ [Scheme 4.2(b)], in its turn lose consecutively
 $[(\text{C}_4\text{H}_3\text{NO}), (81.0215 \text{ Da})]$ and water molecule to form product ion at m/z 361.1189. The
 precursor ion $[\text{M}+\text{Na}]^+$ can also lose $[(\text{C}_4\text{H}_7\text{N}_3\text{O}), (113.0589 \text{ Da})]$ to form the product ion
 at m/z 347.0926 [Scheme 4.2(a)] which is assigned as $[\text{B}_2]^+$. The precursor ion $[\text{M}+\text{Na}]^+$
 undergoes ring fragmentation by losing $[(\text{C}_6\text{H}_9\text{N}_3\text{O}_2), (155.0695 \text{ Da})]$ to form the product
 ion at m/z at 305.0825 which is assigned as $^{[0,2]}\text{A}_2^+$. This latter eliminates a neutral
 molecule $[(\text{C}_4\text{H}_8\text{O}_3), (104.0473 \text{ Da})]$ to form product ion at m/z 201.0363 [Scheme
 4.2(b)]. In addition, the product ion at m/z 201.0363 can also eliminate the methanol
 molecule to form the product ion at m/z 169.0498 [Scheme 4.2(b)]. The product ion at m/z
 201.0363 can also be formed from the direct cleavage from the precursor ion $[\text{M}+\text{Na}]^+$ as
 shown in the [Scheme 4.2(b)]. Finally, the precursor ion $[\text{M}+\text{Na}]^+$ may also eliminate the
 disaccharide moiety $[(\text{C}_{12}\text{H}_{20}\text{O}_{10}), (324.1056 \text{ Da})]$ to form the product ion aglycone $[\text{Y}_0]^+$
 at m/z 136.0498. The product ion $^{[0,2]}\text{A}_2^+$ also eliminate water and carbon monoxide to
 form the product ion at m/z 259.0809 [Scheme 4.2(b)].

The proposed high energy MALDI-CID-MS/MS fragmentation routes are tentatively
 shown in Scheme 4.2(a)] and Scheme 4.2(b)

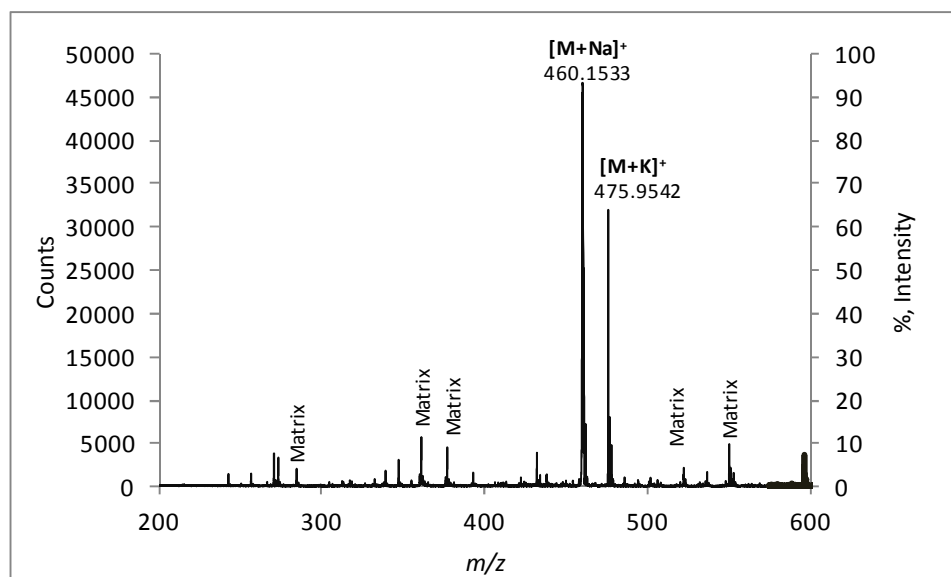


Figure 4.2(a): MALDI-TOF/TOF-MS (+) profile of the ethyltriazole β -D-N-lactopyranosides derivative (2)

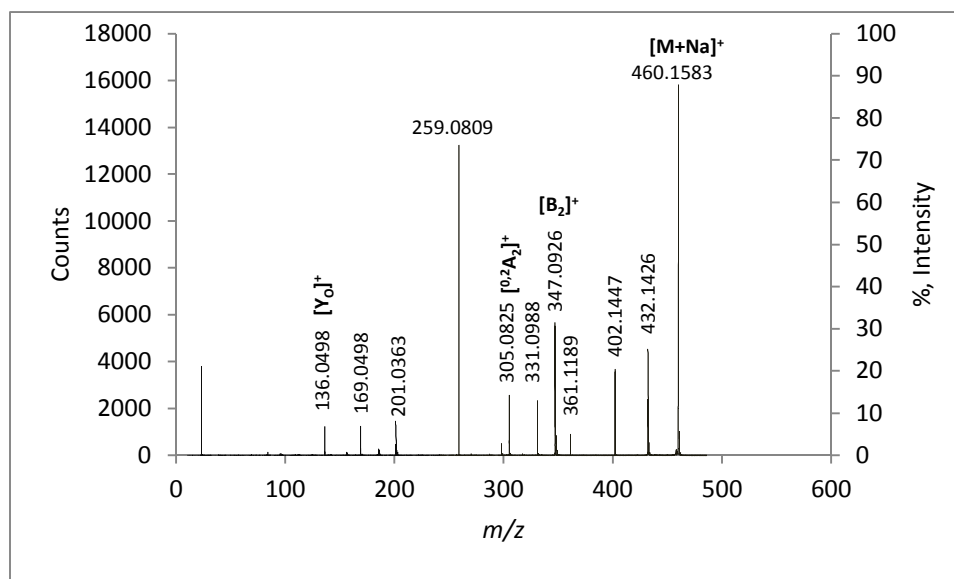
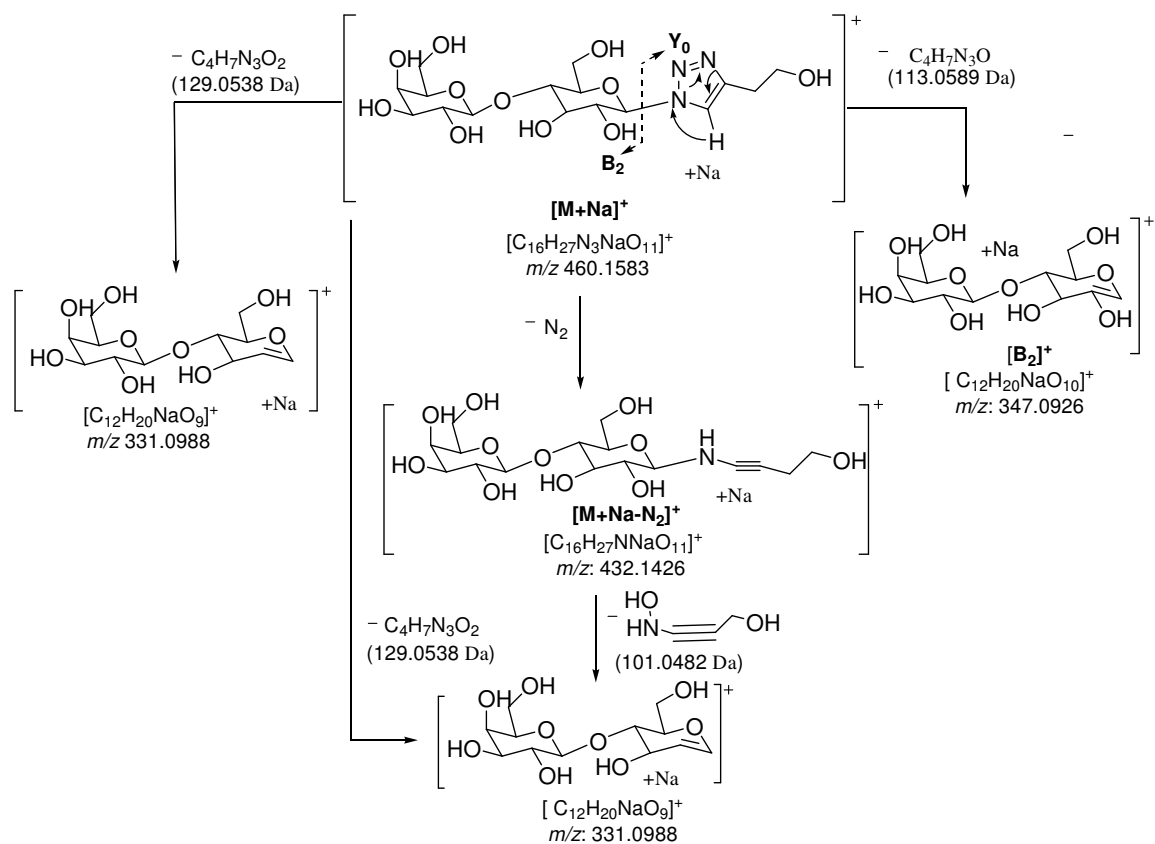
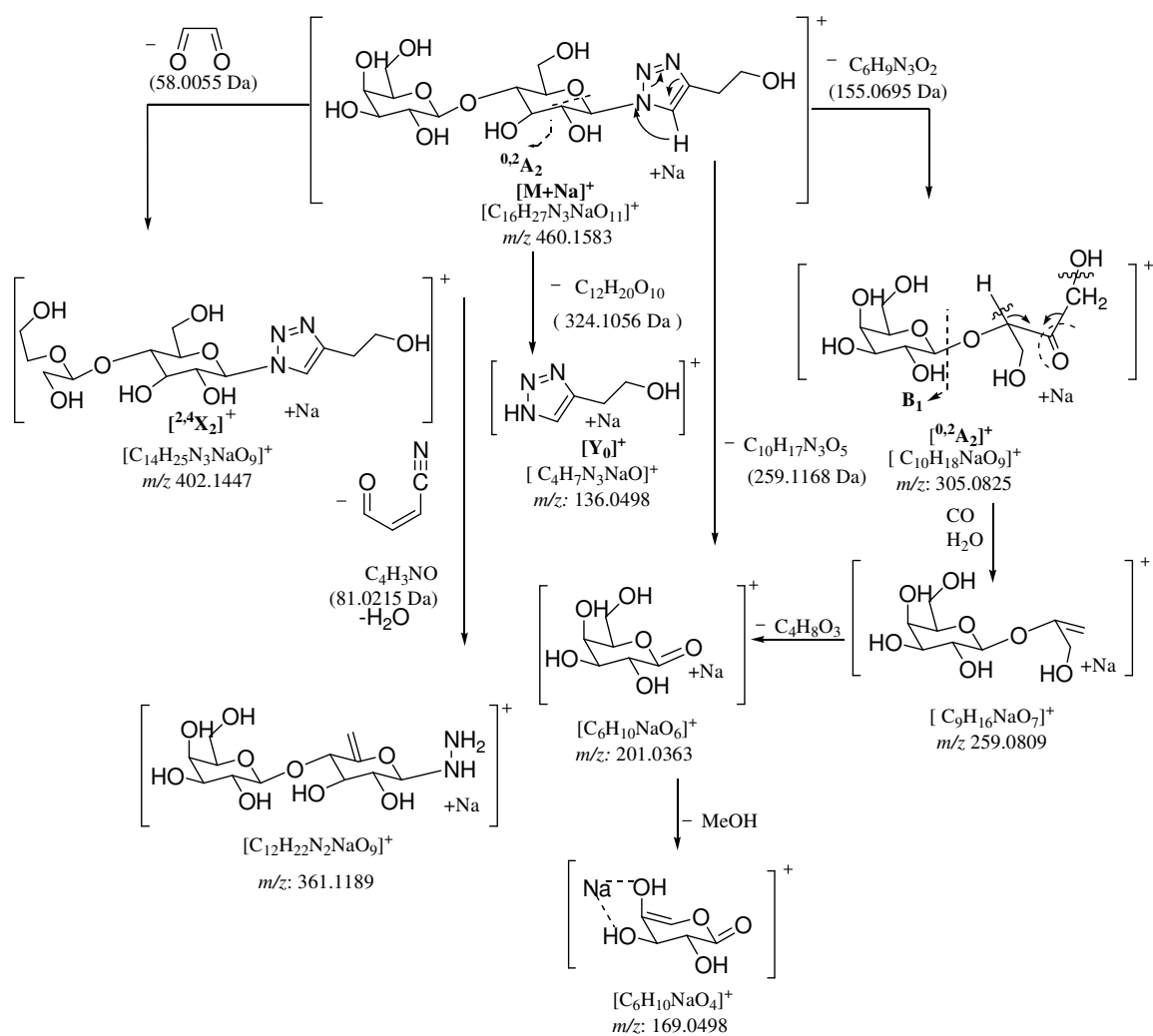


Figure 4.2(b): High energy MALDI-CID-MS/MS of the selected sodiated precursor ion $[M+Na]^+$ at m/z 460.1533 extracted from the ethyltriazole β -D-N-lactopyranosides derivative (2)



Scheme 4.2: (a) The tentative proposed fragmentation routes obtained during MALDI-TOF/TOF high energy CID-MS/MS of the sodiated precursor ion $[M+Na]^+$ at m/z 460.1533 selected from the ethyltriazole β -D-*N*-lactopyranosides derivative (**2**).



Scheme 4.2: (b) The tentative proposed fragmentation routes obtained during MALDI-TOF/TOF high energy CID-MS/MS of the sodiated precursor ion $[M+Na]^+$ at m/z 460.1533 selected from the ethyltriazole β -D-*N*-lactopyranosides derivative (2).

Table 4.B: Characteristic product ions observed in the MALDI-TOF/TOF high energy CID-MS/MS of the sodiated ethyltriazole β -D-*N*-lactopyranosides derivative (**2**) molecule precursor ion $[M+Na]^+$ at m/z 460.1533

Characteristic ions	Calculated mass (m/z)	Observed mass (m/z)	Difference (in ppm)
$[C_{16}H_{27}N_3NaO_{11}]^+$	460.1543	460.1583	9
$[C_{16}H_{27}NNaO_{11}]^+$	432.1482	432.1426	13
$[C_{14}H_{25}N_3NaO_9]^+$	402.1483	402.1447	9
$[C_{12}H_{22}N_2NaO_9]^+$	361.1218	361.1189	10
$[C_{12}H_{20}NaO_{10}]^+$	347.0954	347.0926	8
$[C_{12}H_{20}NaO_9]^+$	331.1005	331.0988	5
$[C_{10}H_{18}NaO_9]^+$	305.0849	305.0825	8
$[C_9H_{16}NaO_7]^+$	259.0794	259.0809	6
$[C_6H_{10}NaO_6]^+$	201.0375	201.0363	6
$[C_6H_{10}NaO_4]^+$	169.0477	169.0498	12
$[C_4H_7N_3NaO]^+$	136.0487	136.0498	8

4.3.3. High energy MALDI-TOF/TOF-CID-MS/MS of the sodiated precursor ion $[M+Na]^+$ at m/z 488.1750 selected from the butyltriazole β -D-*N*-lactopyranosides derivatives (**3**)

The high energy MALDI-CID-MS/MS analysis of the sodiated butyltriazole β -D-*N*-lactopyranosides derivatives (**3**) precursor ion $[M+Na]^+$ at m/z 488.1750 afforded the major product ions observed at m/z 460.1731, 373.0915, 347.0947, 331.0945, 305.0803, 201.0359, and 169.0474 shown in Figure 4.3(b).

The major product ions are tentatively assigned in Table 4.B. Thus, the product ion scan of the sodiated precursor ion $[M+Na]^+$ at m/z 488.1807 by elimination of a nitrogen molecule afforded the product ion at m/z 460.1731, which is assigned as $[M+Na-N_2]^+$. This latter product ion subsequently eliminated a molecule of [(6-(hydroxyamino) hex-5-yn-1-ol, (129.0790 Da)] to form the secondary product ion at m/z 331.0945. The precursor sodiated ion $[M+Na]^+$ can also afford the product ion $[B_2]^+$ at m/z 347.0947, by elimination of the aglycone moiety $[(C_6H_{11}N_3O), (141.0902 \text{ Da})]$. The sodiated precursor ion $[M+Na]^+$ at m/z 488.1807 breaks down by ring fragmentation to afford the ion $[^{0,2}A_2]^+$ at m/z 305.0803 with the elimination of $[(C_8H_{13}N_3O_2), (183.1008 \text{ Da})]$. This latter product ion $[^{0,2}A_2]^+$ at m/z 305.0803 can fragment by elimination of $[(C_4H_8O_3), (104.0473 \text{ Da})]$ to create the product ion at m/z 201.0359 and then the product ion at m/z 201.0359 eliminates of a methanol molecule to give the product ion at m/z 169.0474. In addition, this does not preclude the direct formation of $[C_1]^+$ by direct elimination from the precursor $[M+Na]^+$ ion. In addition, the precursor ion at m/z 488.1807 forms the product ion at m/z 373.0915 by elimination of the [5-aminohept-5-en-1-ol molecule, (115.0997 Da)] from the triazole ring.

The proposed high energy MALDI-CID-MS/MS of sodiated precursor ion $[M+Na]^+$ fragmentation routes are tentatively shown in Scheme 4.3

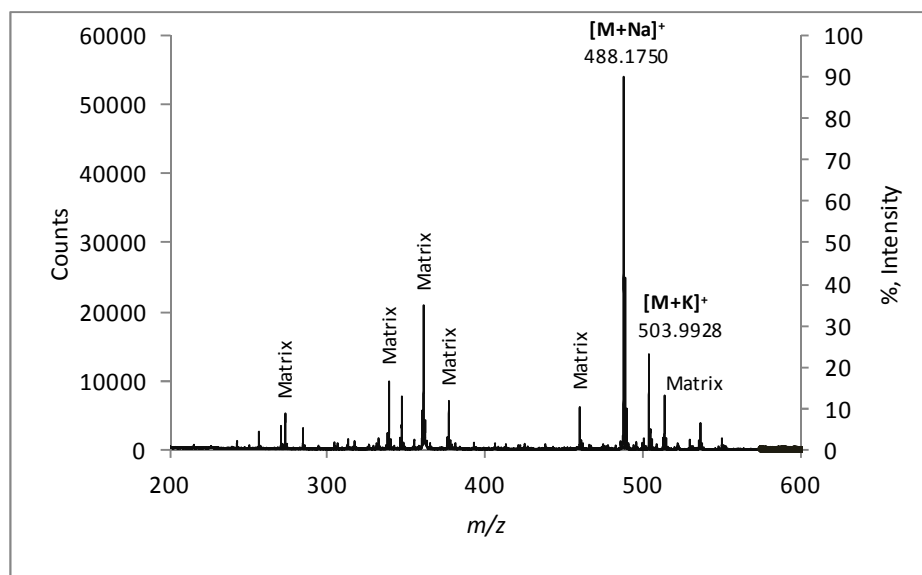


Figure 4.3: (a) MALDI-TOF/TOF-MS (+) profile of the butyltriazole β -D-N-lactopyranosides derivatives (3)

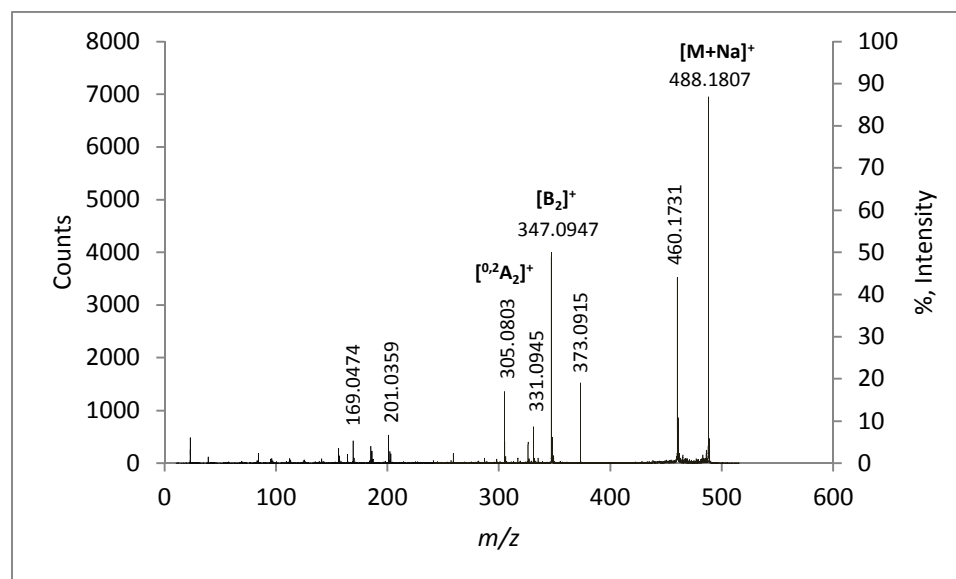
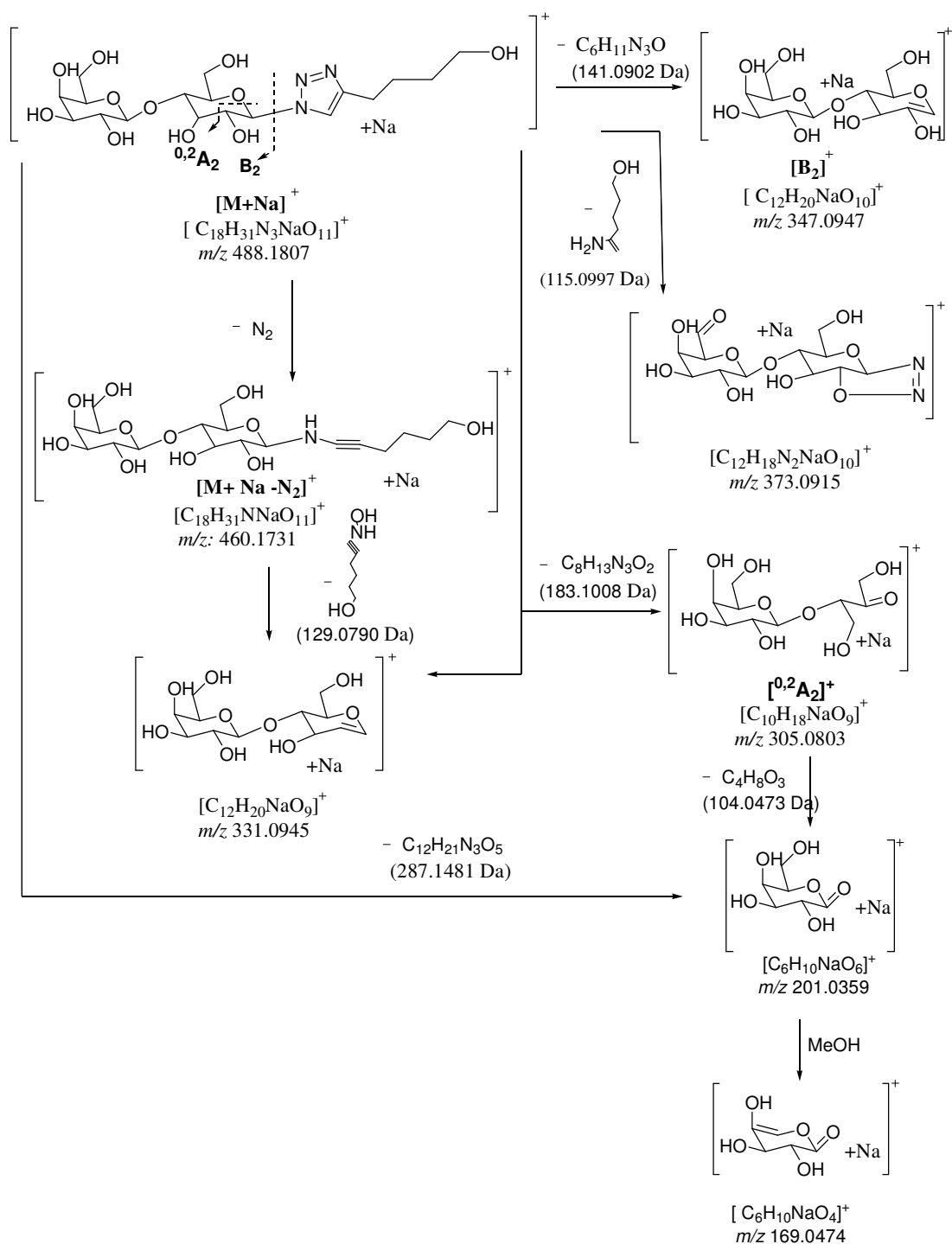


Figure 4.3: (b) High energy MALDI-CID-MS/MS of the selected sodiated precursor ion $[M+Na]^+$ at m/z 488.1750 extracted from the butyltriazole β -D-N-lactopyranosides derivatives (3)



Scheme 4.3: The tentative proposed fragmentation routes obtained during MALDI-TOF/TOF high energy CID-MS/MS of the sodiated precursor ion $[M+Na]^+$ at m/z 488.1750 extracted from the butyltriazole β -D-*N*-lactopyranosides derivatives (**3**)

Table 4.C: Characteristic product ions observed in the MALDI-TOF/TOF high energy CID-MS/MS of the sodiated butyltriazole β -D-*N*-lactopyranosides derivatives (**3**) precursor ion precursor ion $[M+Na]^+$ at m/z 488.1750

Characteristic ions	Calculated mass (m/z)	Observed mass (m/z)	Difference (in ppm)
$[C_{18}H_{31}N_3NaO_{11}]^+$	488.1856	488.1807	10
$[C_{18}H_{31}NNaO_{11}]^+$	460.1795	460.1731	13
$[C_{12}H_{18}N_2NaO_{10}]^+$	373.0859	373.0915	15
$[C_{12}H_{20}NaO_{10}]^+$	347.0954	347.0947	2
$[C_{12}H_{20}NaO_9]^+$	331.1005	331.0945	18
$[C_{10}H_{18}NaO_9]^+$	305.0849	305.0803	7
$[C_6H_{10}NaO_6]^+$	201.0375	201.0359	8
$[C_6H_{10}NaO_6]^+$	169.0477	169.0474	2

4.3.4. High energy MALDI-TOF/TOF-CID-MS/MS of the sodiated precursor ion $[M+Na]^+$ at m/z 522.1580 extracted from the anisoletriazole β -D-*N*-lactopyranosides derivatives (4**).**

The product ion scan of the selected sodiated molecular ion $[M+Na]^+$ at m/z 522.1580 extracted from the anisole-substituted triazole β -D-*N*-lactopyranosides derivatives (**4**) gave the major product ions observed tentatively at m/z 494.1618, 441.1347, 400.1040, 360.1118, 347.0898, 305.0865, 259.0768, 203.0514, and 185.0442 [Figure 4.4 (b)] . The structural identities of this series of major product ions are tentatively assigned in Table 4.D

Thus, the selected precursor ion $[M+Na]^+$ at m/z 522.1643 eliminates a nitrogen molecule to form the product ion at m/z 494.1618 [Scheme 4.4(a)], assigned as $[M+Na-$

$\text{N}_2]^+$. The precursor ion $[\text{M}+\text{Na}]^+$ can also eliminate the aglycone moiety $[(\text{C}_9\text{H}_9\text{N}_3\text{O}), (175.0746 \text{ Da})]$ to form the product ion at m/z 347.0898 [Scheme 4.4 (a)], assigned as $[\text{B}_2]^+$. The precursor ion also eliminates a molecule of galactosyl moiety to get the product ion at m/z 360.1118 which is assigned as $[\text{Y}_1]^+$. The precursor ion $[\text{M}+\text{Na}]^+$ loses a molecule of $[(\text{C}_{11}\text{H}_{11}\text{N}_3\text{O}), (217.0851 \text{ Da})]$ to give the product ion at m/z 305.0865 [Scheme 4.4 (b)], assigned as $^{[0,2]}\text{A}_2^+$. The product ion $^{[0,2]}\text{A}_2^+$ later on fragmented to give product ion at m/z 259.0768 [Scheme 4.4 (b)] with the elimination of water and carbon monoxide. In addition, the same product can also eliminate $[(\text{C}_4\text{H}_6\text{O}_3), (102.0317 \text{ Da})]$ to afford the product ion at m/z 203.0514 [Scheme 4.4 (b)], assigned as $[\text{C}_1]^+$. This product ion $[\text{C}_1]^+$ eliminates water to form the product ion $[\text{B}_1]^+$ at m/z 185.0442, assigned as $[\text{C}_1-\text{H}_2\text{O}]^+$. Needless to say, that these pairs of product ions $[\text{C}_1]^+$ and $[\text{B}_1]^+$ can also be created by direct cleavage from the precursor ion at m/z 522.1643. The product ion at m/z 494.1618 also consecutively eliminates by ring cleavage and loss of the $[(\text{C}_3\text{H}_6\text{O}_5), (90.0317 \text{ Da})]$ and two moles of hydrogen to give the product ion $^{[0,3]}\text{X}_2^+$ at m/z 400.1040 [Scheme 4.4 (a)]. The product ion at m/z 494.1618 [Scheme 4.4 (a)] also eliminate two molecules of water and a hydroxyl radical (53.0239 Da) to form the radical cation product ion at m/z 441.1347 [Scheme 4.4 (a)].

The proposed high energy MALDI-CID-MS/MS of sodiated precursor ion $[\text{M}+\text{Na}]^+$ fragmentation routes are tentatively shown in [Scheme 4.4 (a)] and [Scheme 4.4 (b)]

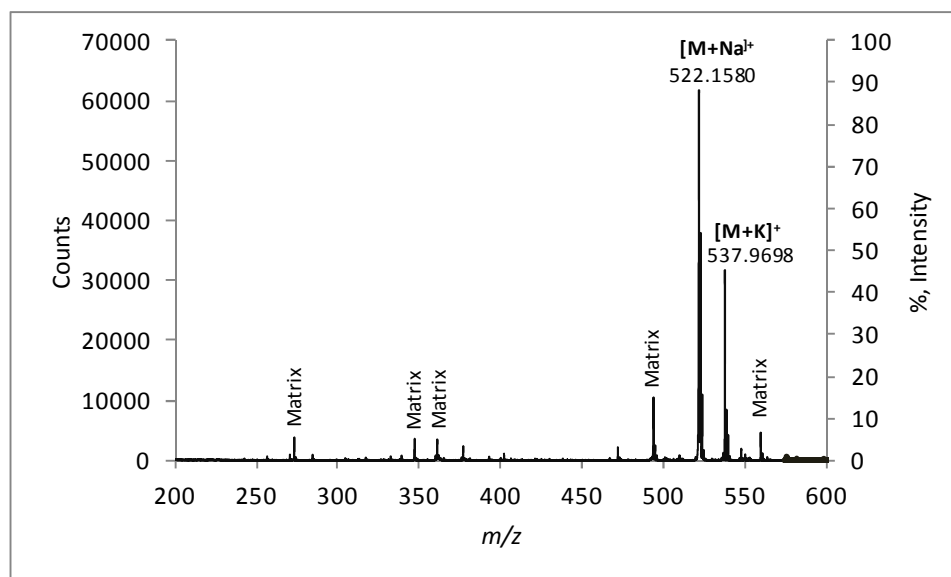


Figure 4.4 (a): MALDI-TOF/TOF-MS (+) profile of the anisoletriazole β -D-*N*-lactopyranosides derivatives (**4**).

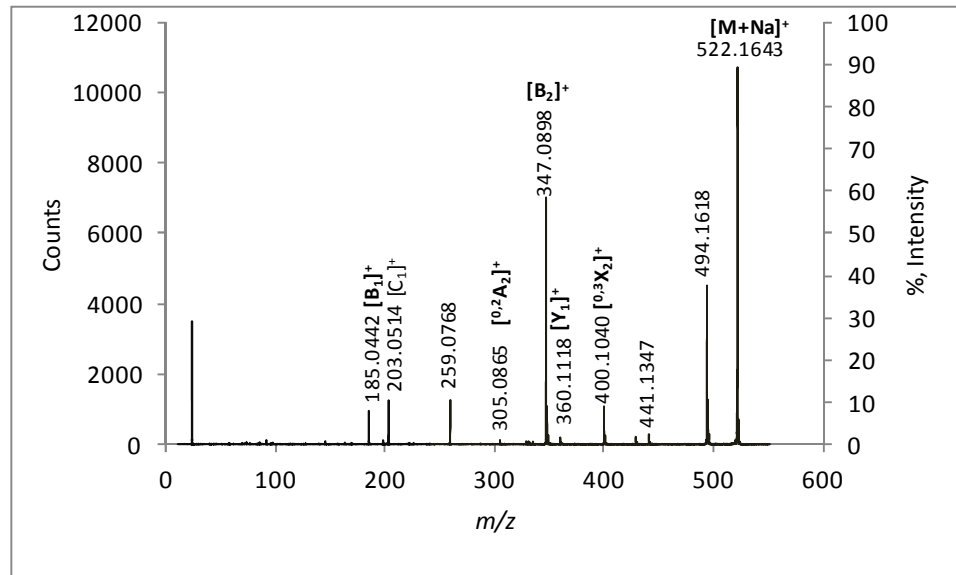
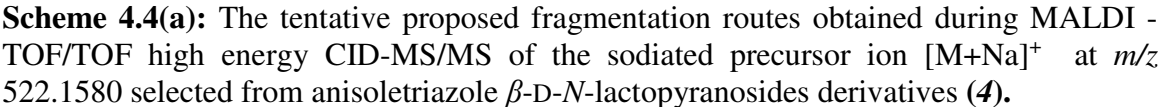
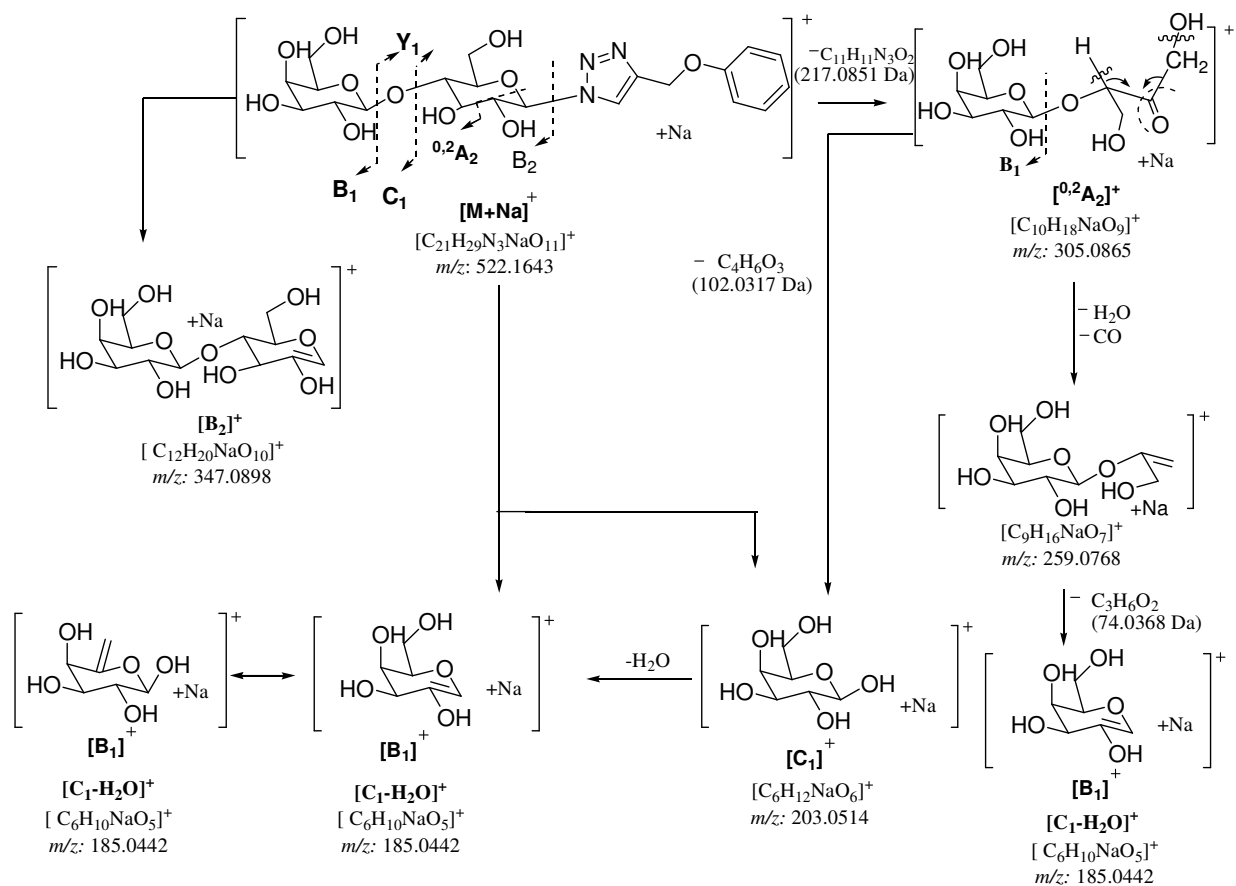


Figure 4.4 (b): High energy MALDI-CID-MS/MS of the selected sodiated precursor ion $[M+Na]^+$ at m/z 522.1580 extracted from the anisoletriazole β -D-*N*-lactopyranosides derivatives (**4**).





Scheme 4.4(b): The tentative proposed fragmentation routes obtained during MALDI-TOF/TOF high energy CID-MS/MS of the sodiated precursor ion $[M+Na]^+$ at m/z 522.1580 selected from anisoletriazole β -D-N-lactopyranosides derivatives (**4**).

Table 4.D: Characteristic product ions observed in the MALDI-TOF/TOF high energy CID-MS/MS of the sodiated the anisoletriazole β -D-*N*-lactopyranosides derivatives (**4**) precursor ion $[M+Na]^+$ at m/z 522.1580

Characteristic ions	Calculated mass (m/z)	Observed mass (m/z)	Difference (in ppm)
$[C_{21}H_{29}N_3NaO_{11}]^+$	522.1700	522.1643	11
$[C_{21}H_{29}NNaO_{11}]^+$	494.1638	494.1618	4
$[C_{21}H_{24}NNaO_8]^{++}$	441.1400	441.1347	12
$[C_{18}H_{19}NNaO_8]^+$	400.1008	400.1040	8
$[C_{15}H_{19}N_3NaO_6]^+$	360.1172	360.1118	15
$[C_{12}H_{20}NaO_{10}]^+$	347.0954	347.0898	16
$[C_{10}H_{18}NaO_9]^+$	305.0849	305.0865	5
$[C_9H_{16}NaO_7]^+$	259.0794	259.0768	10
$[C_6H_{12}NaO_6]^+$	203.0532	203.0514	8
$[C_6H_{10}NaO_5]^+$	185.0426	185.0442	9

4.3.5. High energy MALDI-TOF/TOF-CID-MS/MS of the sodiated precursor ion $[M+Na]^+$ at m/z 552.1720 extracted from the dimethoxybenzenetriazole β -D-N-lactopyranosides derivatives (5)

The product ion scan of selected sodiated molecular ion $[M+Na]^+$ at m/z 552.1794 for the dimethoxybenzenetriazole β -D-N-lactopyranosides derivatives (5) afforded a series of product ions at m/z 524.1718, 471.1496, 429.1342, 400.1192, 347.0923, 305.0825, 259.0766 and 185.0463 shown in Figure 4.5 (b). The structural identities of the major product ion are tentatively assigned in Table 4.E.

Thus, the precursor ion $[M+Na]^+$ at m/z 552.1794 loses a nitrogen molecule to give the product ion at m/z 524.1718, assigned as $[M+Na-N_2]^+$. This latter product ion loses two molecules of water and a hydroxyl radical $[(2H_2O + OH^\bullet), (53.0239 \text{ Da})]$ to form the radical cation product ion at m/z 471.1496. The precursor ion $[M+Na]^+$ at m/z 552.1794 can also lose a neutral radical $[(C_7H_7O_2^\bullet), (123.0446 \text{ Da})]$ to form the product ion at m/z 429.1342 [Scheme 4.5(a)]. This latter product ion at m/z 429.1342 can also lose a nitrogen molecule and a hydrogen radical $[(N_2 + H^\bullet), (29.0145 \text{ Da})]$ to afford the product ion at m/z 400.1192 [Scheme 4.5(a)]. The precursor ion $[M+Na]^+$ may also eliminate a molecule of $[(C_{10}H_{11}N_3O_2), (205.0851 \text{ Da})]$ to form the sodiated disaccharide product ion at m/z 347.0923 [Scheme 4.5(b)], assigned as $[B_2]^+$. This latter precursor ion $[M+Na]^+$ undergoes ring fragmentations by eliminating a molecule of $[(C_{12}H_{13}N_3O_3), (247.0957 \text{ Da})]$ to form the product ion at m/z 305.0825 [Scheme 4.5(a)] assigned as $[^{0,2}A_2]^+$. This latter ion eliminates a molecule of water and carbon monoxide to form product ion at m/z 259.0766 which subsequently loses a molecule of prop-2-ene-1,2-diol

$[(C_3H_6O_2), (74.0368 \text{ Da})]$ to yield the product ion $[B_1]^+$ at m/z 185.0463 by elimination of $[(C_{16}H_{21}N_3O_7), (367.1380 \text{ Da})]$. The product ion $[B_1]^+$ at m/z 185.0463 can be formed from the precursor ion $[M+Na]^+$ as shown in Scheme 4.5 (b)

The proposed high energy MALDI-CID-MS/MS of sodiated precursor ion $[M+Na]^+$ fragmentation routes are tentatively shown in Scheme 4.5(a) and Scheme 4.5(b)

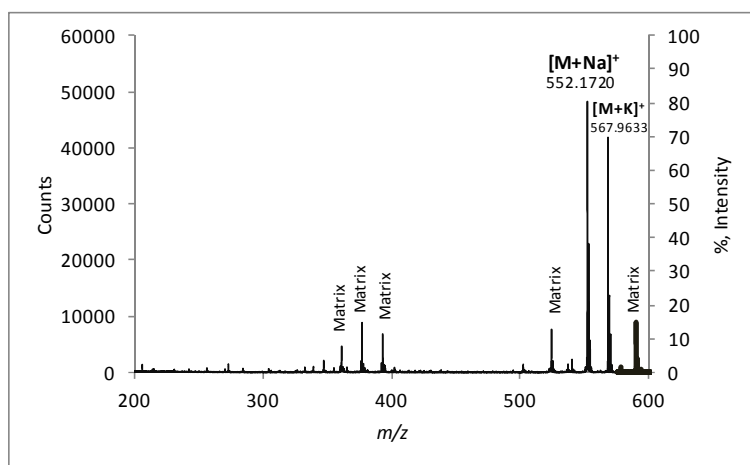


Figure 4.5(a): MALDI-TOF/TOF-MS (+) profile of the dimethoxybenzenetriazole β -D-*N*-lactopyranosides derivatives (**5**)

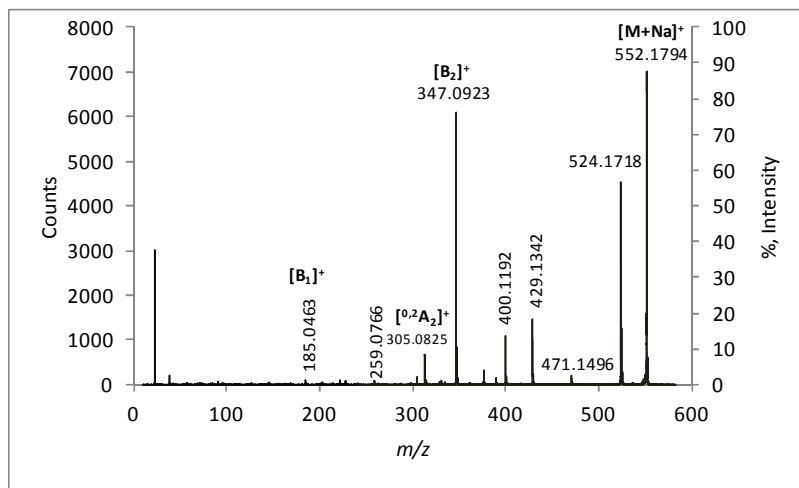
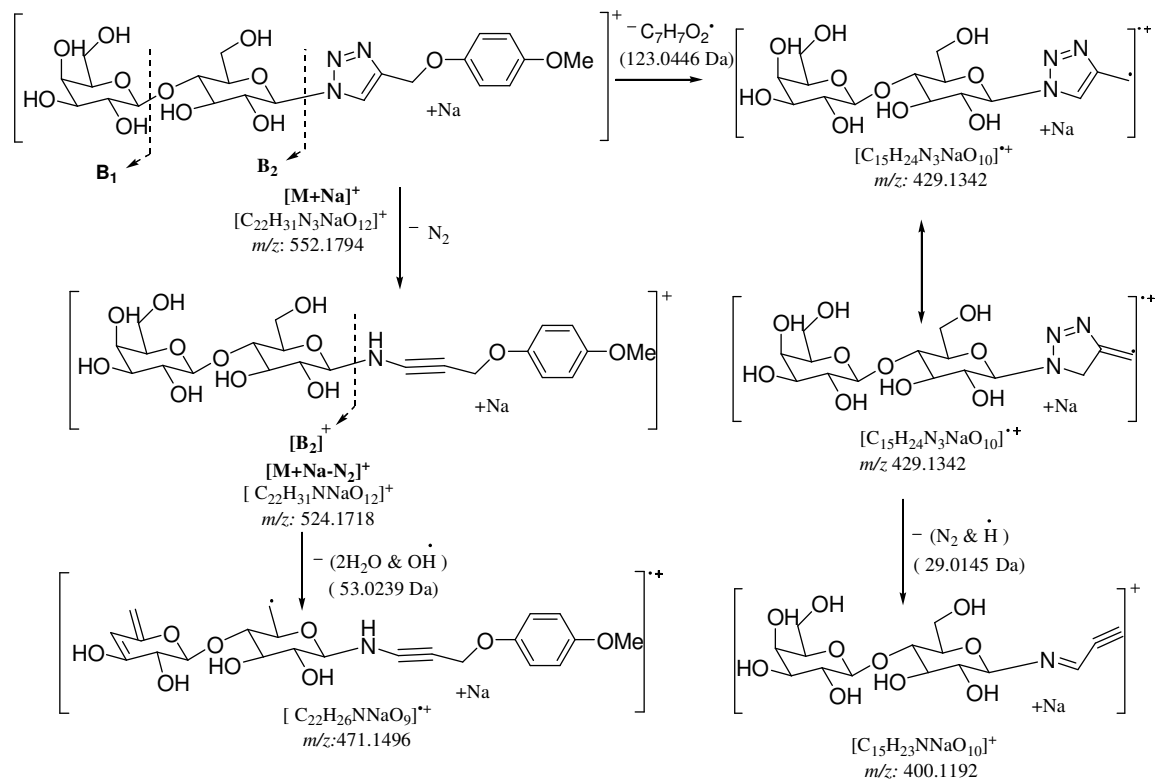
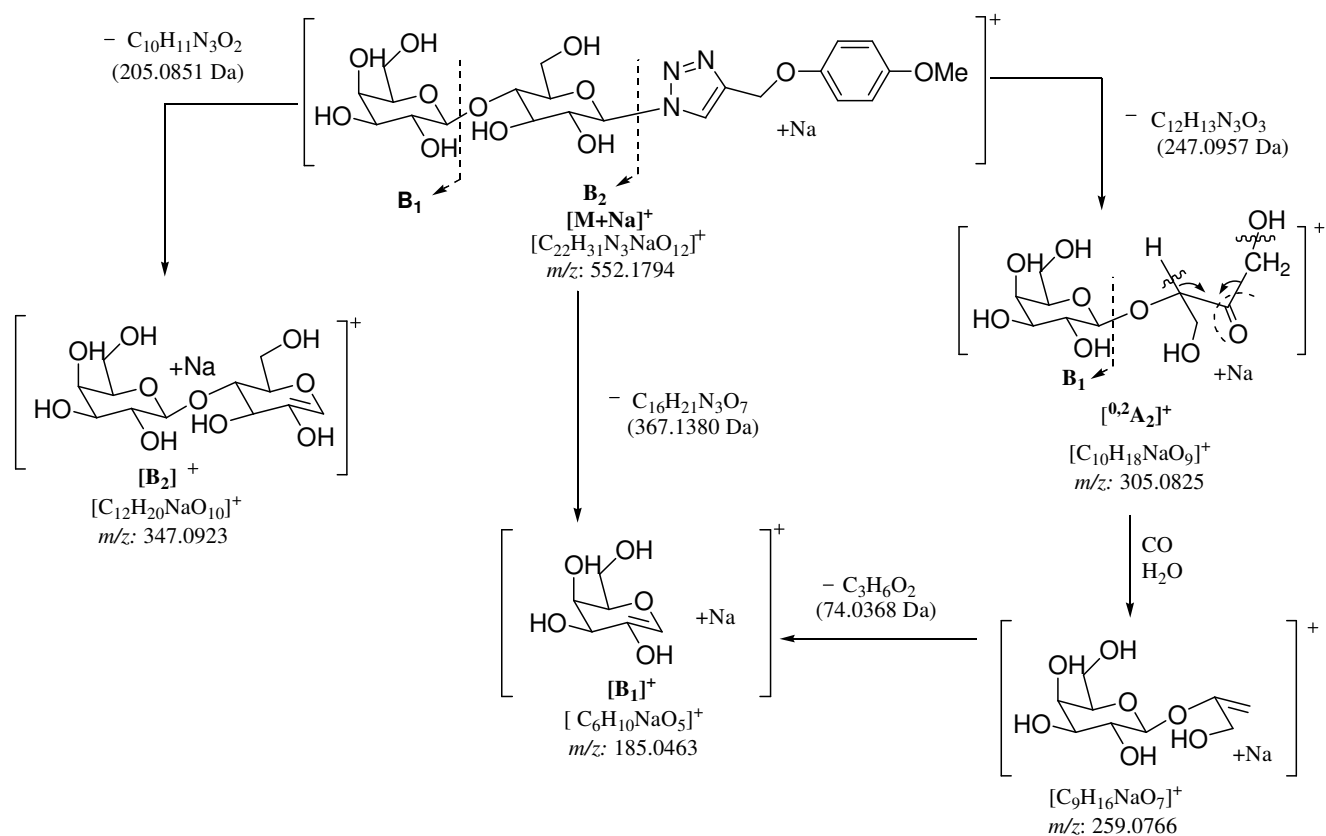


Figure 4.5 (b): MALDI-TOF/TOF high energy CID-MS/MS of the precursor ion $[M+Na]^+$ at m/z 552.1720 selected from the dimethoxybenzenetriazole β -D-*N*-lactopyranosides derivatives (**5**)



Scheme 4.5: (a) The tentative proposed fragmentation routes obtained during MALDI-TOF/TOF high energy CID-MS/MS of the sodiated precursor ion $[\text{M}+\text{Na}]^+$ at m/z 552.1720 selected from dimethoxybenzenetriazole β -D-*N*-lactopyranosides derivatives (5)



Scheme 4.5(b): The tentative proposed fragmentation routes obtained during MALDI-TOF/TOF high energy CID-MS/MS of the sodiated precursor ion $[\text{M}+\text{Na}]^+$ at m/z 552.1720 selected from dimethoxybenzenetriazole β -D-*N*-lactopyranosides derivatives (5)

Table 4.E: Characteristic product ions observed in the MALDI-TOF/TOF high energy CID-MS/MS of the sodiated the dimethoxybenzenetriazole β -D-*N*-lactopyranosides derivatives (**5**) precursor ion $[M+Na]^+$ at m/z 552.1720

Characteristic ions	Calculated mass (m/z)	Observed mass (m/z)	Difference (in ppm)
$[C_{22}H_{31}N_3NaO_{12}]^+$	552.1805	552.1794	2
$[C_{22}H_{31}NNaO_{12}]^+$	524.1744	524.1718	5
$[C_{22}H_{26}NNaO_9]^{++}$	471.1505	471.1496	2
$[C_{15}H_{24}N_3NaO_{10}]^{++}$	429.1359	429.1342	4
$[C_{15}H_{23}NNaO_{10}]^+$	400.1220	400.1192	7
$[C_{12}H_{20}NaO_{10}]^+$	347.0954	347.0923	9
$[C_{10}H_{18}NaO_9]^+$	305.0849	305.0825	8
$[C_9H_{16}NaO_7]^+$	259.0794	259.0766	10
$[C_6H_{10}NaO_5]^+$	185.0426	185.0463	20

4.3.6. High energy MALDI-TOF/TOF-CID-MS/MS of the sodiated precursor ion $[M+Na]^+$ at m/z 572.1750 selected from the methoxynaphthalene-triazole β -D-*N*-lactopyranosides derivatives (**6**)

The product ion scan of selected sodiated molecular ion $[M+Na]^+$ at m/z 572.1750 for the methoxynaphthalene-substituted triazole β -D-*N*-lactopyranosides derivatives (**6**) afforded the product ions at m/z 544.1741, 491.1497, 429.1282, 400.1160, 347.0930, 305.0822, 248.0783, 145.0233 and 91.0150 . The structural identities of this series of major product ions are tentatively assigned in Table 4.F.

Thus, the precursor ion $[M+Na]^+$ at m/z 572.1793 loses a naphthyl radical $[(C_{10}H_7O^\cdot), (143.0497 \text{ Da})]$ to form the radical cation product ion at m/z 429.1282 [Scheme 4.6(a)]. This latter product ion loses a nitrogen and a hydrogen radical $[(N_2\& H^\cdot), (29.0145 \text{ Da})]$ to form the product ion at m/z 400.1160 [Scheme 4.6(a)]. The precursor ion $[M+Na]^+$ can also lose a nitrogen molecule to give the product ion at m/z 544.1741 assigned as $[M+Na-N_2]^+$. This latter product ion $[M+Na-N_2]^+$ can lose two molecules of water and a hydroxyl radical $[(2H_2O\& OH^\cdot), (53.0239 \text{ Da})]$ to form the radical cation product ion at m/z 491.1497 [Scheme 4.6(a)]. The precursor ion $[M+Na]^+$ eliminates the aglycone moiety of $[(C_{13}H_{11}N_3O), (225.0902 \text{ Da})]$ to form the product ion $[B_2]^+$ at m/z 347.0930 [Scheme 4.6(a)]. The precursor ion $[M+Na]^+$ loses a molecule of $[(C_{15}H_{13}N_3O_2), (267.1008 \text{ Da})]$ to form the product ion at m/z 305.0822 [Scheme 4.6(b)], assigned as the $[^{0,2}A_2]^+$. The aglycone product ion at m/z 248.0783 [Scheme 4.6(b)] assigned as the $[Y_0]^+$ can be created by elimination of disaccharide moiety $[(C_{12}H_{20}O_{10}), (324.1056 \text{ Da})]$ from the precursor ion $[M+Na]^+$. Finally, the radical product ion at m/z 91.0150 [Scheme 4.6(b)] was formed by elimination of [2-methoxynaphthalene radical, (157.0653 Da)] from the product ion $[Y_0]^+$. Similarly, the radical cation product ion at m/z 145.0233 is created from the product ion at m/z 429.1282 [Scheme 4.6(a)] by elimination of $[(C_{10}H_{20}O_9), (284.1107 \text{ Da})]$.

The proposed high energy MALDI-CID-MS/MS fragmentation routes of sodiated precursor ion $[M+Na]^+$ at m/z 572.1793 are tentatively shown in Scheme 4.6(a) and Scheme 4.6(b)

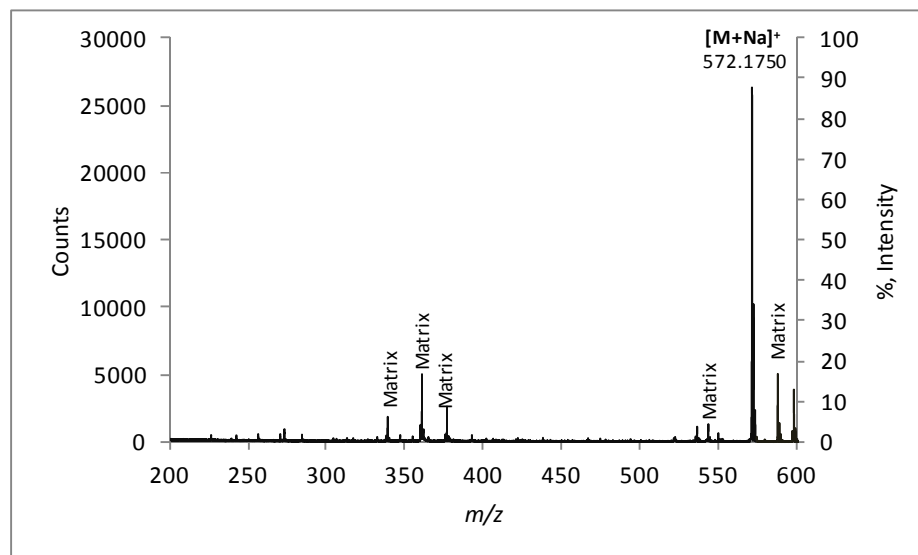


Figure 4.6(a): MALDI-TOF/TOF-MS (+) profile of the methoxynaphthalene-triazole β -D-*N*-lactopyranosides derivatives (**6**)

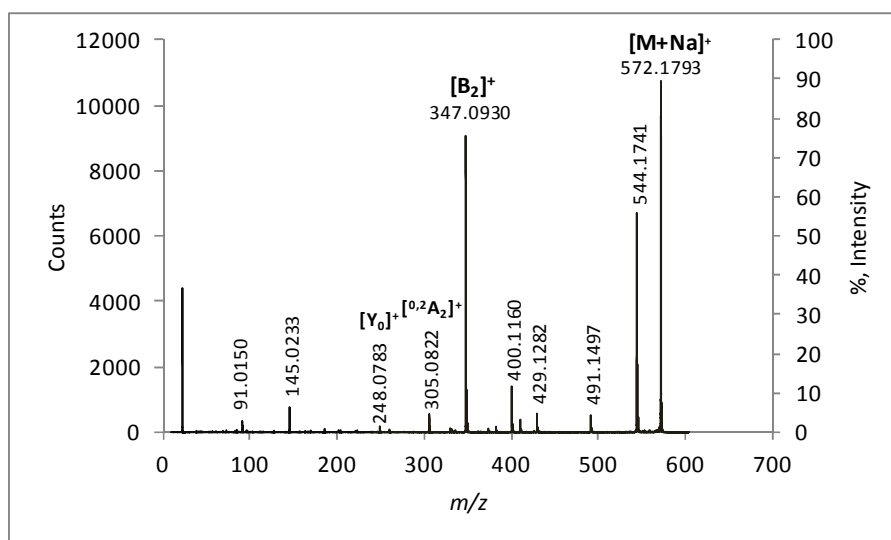
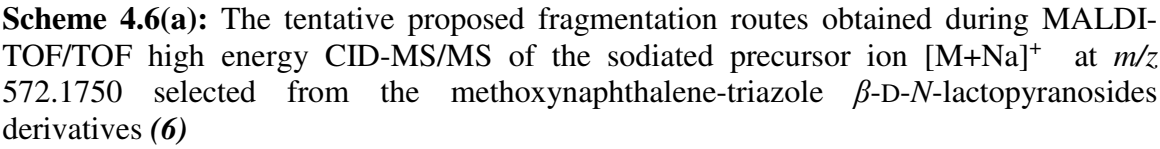
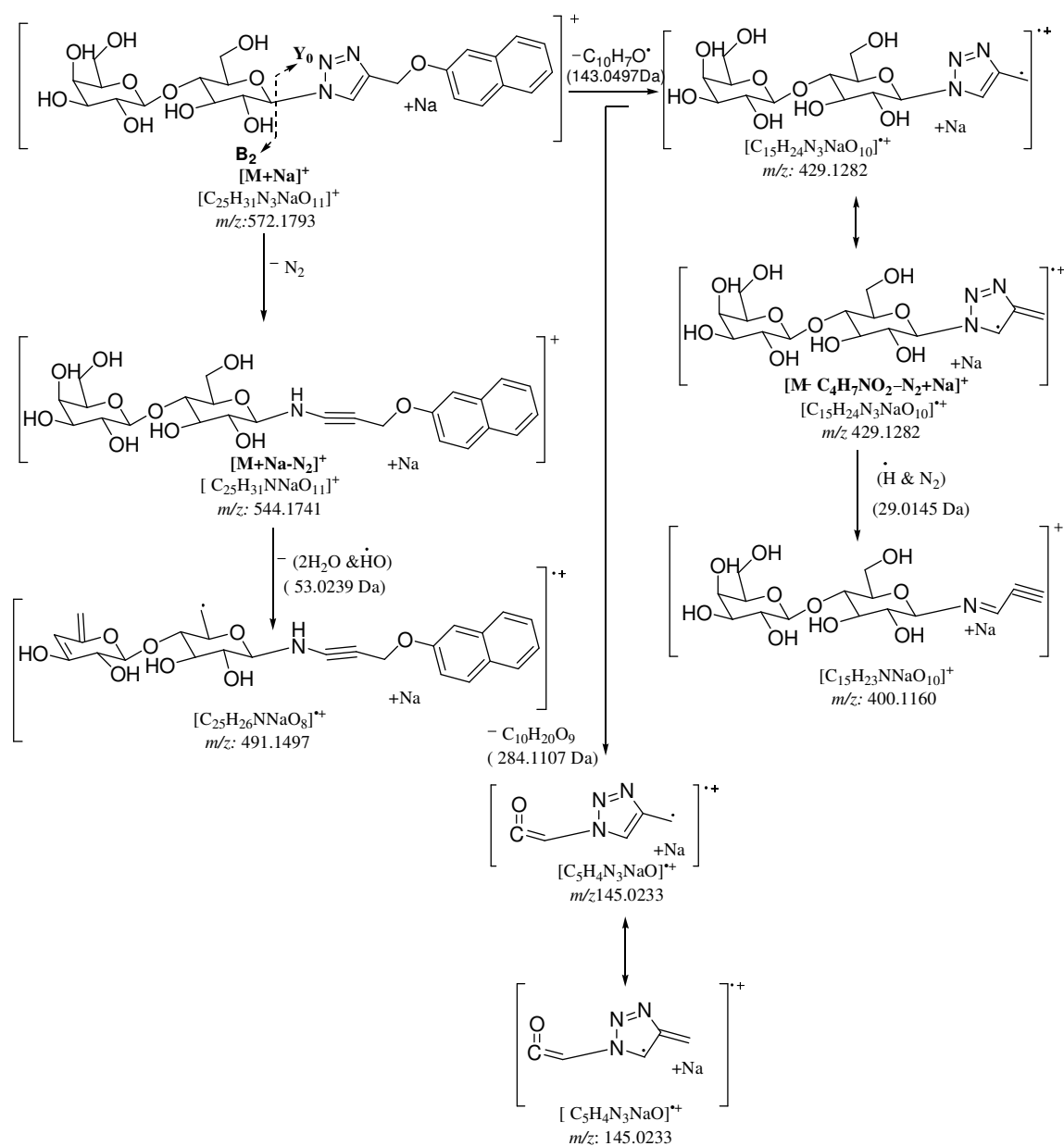


Figure 4.6(b): MALDI-TOF/TOF high energy CID-MS/MS of the precursor ion $[M+Na]^+$ at m/z 572.1750 selected from the methoxynaphthalene-triazole β -D-*N*-lactopyranosides derivatives (**6**)





Scheme 4.6(b): The tentative proposed fragmentation routes obtained during MALDI-TOF/TOF high energy CID-MS/MS of the sodiated precursor ion $[M+\text{Na}]^+$ at m/z 572.1750 selected from the methoxynaphthalene-triazole β -D-*N*-lactopyranosides derivatives (**6**)

Table 4.F: Characteristic product ions observed in the MALDI-TOF/TOF high energy CID-MS/MS of the sodiated methoxynaphthalene-substituted triazole β -D-*N* lactopyranosides derivatives (**6**) precursor ion $[M+Na]^+$ at m/z 572.1750

Characteristic ions	Calculated mass (m/z)	Observed mass (m/z)	Difference (in ppm)
$[C_{25}H_{31}N_3NaO_{11}]^+$	572.1856	572.1793	11
$[C_{25}H_{31}NNaO_{11}]^+$	544.1795	544.1741	10
$[C_{25}H_{26}NNaO_8]^{*+}$	491.1556	491.1497	12.
$[C_{15}H_{24}N_3NaO_{10}]^{*+}$	429.1359	429.1282	18
$[C_{15}H_{23}NNaO_{10}]^+$	400.1220	400.1160	15
$[C_{12}H_{20}NaO_{10}]^+$	347.0954	347.0930	7
$[C_{10}H_{18}NaO_9]^+$	305.0849	305.0822	9
$[C_{13}H_{11}N_3NaO]^+$	248.0800	248.0783	7
$[C_5H_4N_3NaO]^{*+}$	145.0252	145.0233	11
$[C_2H_2N_3Na]^{*+}$	91.0141	91.0150	10

4.4. Conclusion

MALDI-CID-TOF/TOF spectra of *N*-glycosides allowed the differentiation between the isomeric structures, and the determination of the sequence of the oligosaccharides and the linkage positions. In the MALDI-CID-MS/MS spectra, a considerably greater number of fragments are found in comparison to other mass spectrometry fragmentation techniques, and, although this may complicate their interpretation, it permits acquisition of more information on linkage position and points of branching. A macro (Microsoft

excell) can be used to automate the interpretation of the peaks present in MALDI-CID-TOF/TOF spectra.

To summarize it up, the CID-MS/MS analyses showed the following: In the observation nitrogen elimination is very common in every case. The sodiated precursor ion isolated from the methoxynaphthalene-substituted triazole β -D-*N*-galactopyranosides derivatives (**1**) afforded the product ions found $[B_2]^+$ and at m/z 382.1210, and the radical cation product ion at m/z 329.1012 [Elimination of (2H₂O & OH[•])] and 267.0812 (Radical cation). The product ion scan of the sodiated molecular ion extracted from ethyltriazole β -D-*N*-lactopyranosides derivative (**2**) afforded the product ions $[B_2]^+$, $[Y_0]^+$, $[^{0,2}A_2]^+$, $[^{2,4}A_1]^+$ respectively, at m/z 347.0926, 136.0498, 305.0825, 402.1447, and other product ions are formed at m/z 432.1426 (Elimination of nitrogen molecule), 331.0988, 361.1189, 259.0809, 201.0363, 169.0498. The CID-MS/MS of the sodiated molecular ion extracted from the butyltriazole β -D-*N*-lactopyranosides derivative (**3**), afforded the product ions $[B_2]^+$ and $[^{0,2}A_2]^+$ respectively, at m/z 347.0947, 305.0803 and other product ions formed at m/z 460.1713 (Elimination of nitrogen molecule), 373.0915, 331.0945, 201.0359, 169.0474. The product ion scan of the sodiated molecular ion extracted from the anisoletriazole β -D-*N*-lactopyranosides derivative (**4**) afforded the product ions $[B_1]^+$, $[B_2]^+$, $[^{0,2}A_2]^+$, $[C_1]^+$, $[Y_1]^+$, $[^{0,3}X_2]^+$ respectively at m/z 185.0442, 347.0898, 305.0865, 203.0514, 360.1118, 400.1040, and other product ions at m/z 494.1618 (Elimination of nitrogen), 441.1347 (Radical cation) and 259.0768. The product ion scan of the sodiated molecular ion extracted from the dimethoxybenzenetriazole- β -D-*N*-lactopyranosides derivative (**5**) afforded the product ions $[B_1]^+$, $[B_2]^+$, $[^{0,2}A_2]^+$ respectively at m/z 185.0463, 347.0923, 305.0825 and other product ion at m/z 524.1718 (Elimination of

nitrogen), 471.1496 (Radical cation), 429.1342 (Radical cation), 400.1192 (Elimination of N₂ and H⁺). The precursor ion scan of the sodiated molecular ion extracted from the methoxynaphthalene-substituted triazole β -D-*N*-lactopyranosides derivative (**6**) afforded the product ions [B₂]⁺, [^{0,2}A₂]⁺, [Y₀]⁺ respectively at *m/z* 347.0930, 305.0822, 248.0783 and other ion at *m/z* 544.1741 (Elimination of nitrogen molecule), 491.1497, 429.1282, 400.1160, 145.0233 (Radical cation), 91.0150 (Radical cation). It is worth mentioning that in these novel high-energy CID-MS/MS analysis, we have noticed the elimination N₂ and H⁺ from the product ion containing the glycosyl portion attached the aglycone which has lost the aromatic moiety. This loss seems universal for this series of compounds and is the first time that such a loss has been resolved.

CHAPTER 5: GAS PHASE FRAGMENTATION STUDY OF NOVEL SYNTHETIC BIVALENT *N*-GLYCOSIDES BY THE QUADRUPOLE ION-TRAP EXTERNAL ESI SOURCES

5.1. Introduction

Over the last decade, analysis of simple and complex carbohydrates using tandem-in-time instruments such as the QIT-MSⁿ and FT-MSⁿ, in which, the multiple analysis stages of mass spectrometry are performed in the same space, have become more common. These tandem-in-time instruments have inherently greater MS/MS efficiency due to their configuration, as compared to tandem-in-space instruments, which lead to greater sensitivity and selectivity.

Thus, the QIT-MSⁿ instrument has emerged as a remarkably sensitive and selective instrument that is small, low in cost, and capable of efficient MS/MS.^{[141]-[144]} It is a common norm that all commercially-available QIT-MSⁿ instruments are capable to accurately isolate and fragment the selected precursor ion, thus forming the resulting fragment ions. Because of the small time necessary to acquire an MSⁿ mass spectrum, it is possible to couple the QIT-MSⁿ to a high pressure liquid chromatography instrument (HPLC) to gain more specific information about the sample composition. Newer capabilities of commercially-available QIT-MSⁿ instruments include the ability to develop methods for intelligent, data-dependent scanning.

When using the ESI-QIT-MS for the analysis of carbohydrates, it is possible to contain the formation of the non-reducing terminal substituents, which suppresses the cross-ring carbohydrate cleavage in CID-spectra of permethylated complex *N*-linked

oligosaccharides.^{[145]-[146]} The data produced from MS³ and MS⁴ stages allow sequence and linkages information to be revealed.

By using ESI-QIT-MS, it is possible to remove non-reducing terminal substituents that suppress cross-ring and core-carbohydrate cleavage in the tandem mass spectra of permethylated complex *N*-linked oligosaccharides.^[147]

Thus, sequential stages of MSⁿ have been used as virtual degradative steps to reduce the structures of complex sialylated and fucosylated oligosaccharides to subunits, the spectra of which can be matched against known standards.^[148]

In addition, mass spectrometric degradation of oligosaccharides, has been combined with a library of known structures to characterize sub-structural motifs expressed by families of *N*-linked glycoproteins.^[149] It was shown that different glycan structures can contain common sub-structural motifs, that result in common features in tandem mass spectrometric profiles. The tandem mass spectra of known sub-structural motifs constitute a catalogue library, against which the data generated from unknowns can be researched.

5.2. ESI-QIT-MS analysis of the novel synthetic bivalent *N*-glycosides (*1-6*)

The ESI-QIT-MS analyses of this series were all recorded in the positive ion mode, and they afforded in all cases the expected [M+H]⁺ protonated molecular ion (base peak) and sodiated molecular ion [M+Na]⁺. Henceforth, the ESI-QIT-MS of methoxynaphthalene-substituted triazole β -D-*N*-galactopyranosides derivative (**1**) produced the [M+H]⁺ protonated molecular ion at *m/z* 388.1160 and the [M+Na]⁺

sodiated adduct at m/z 410.0934 [Figure 5.1(a)]; The ESI-QIT-MS of ethyltriazole β -D-*N*-lactopyranosides derivative (**2**) formed the $[M+H]^+$ at m/z 438.1528 and $[M+Na]^+$ at m/z 460.1248 [Figure 5.3(a)]; The ESI-QIT-MS of the butyltriazole β -D-*N*-lactopyranosides derivatives (**3**) afforded the $[M+H]^+$ at m/z 466.1814, and the $[M+Na]^+$ sodiated adduct at m/z 488.1896 [Figure 5.5(a)]; The ESI-QIT-MS of anisoletriazole β -D-*N*-lactopyranosides derivatives (**4**) afforded the $[M+H]^+$ at m/z 500.1234 and the $[M+Na]^+$ sodiated adduct at m/z 552.0916 and [Figure 5.7(a)]; The ESI-QIT-MS of the dimethoxybenzenetriazole β -D-*N*-lactopyranosides derivatives (**5**) afforded the $[M+H]^+$ at m/z 530.1297 and the $[M+Na]^+$ sodiated adduct at m/z 552.0996 [Figure 5.9(a)]; and finally ESI-QIT-MS of the methoxynaphthalene-triazole β -D-*N*-lactopyranosides derivatives (**6**) afforded the $[M+H]^+$ at m/z 550.1177 and the $[M+Na]^+$ sodiated adduct at m/z 572.1292 [Figure 5.11(a)].

5.3. QIT-CID-MS/MS analysis of synthetic bivalent β -D-*N*-glycosides (**1-6**)

Low-energy collision induced dissociation CID-MS/MS analyses of the different precursor protonated $[M+H]^+$ and sodiated $[M+Na]^+$ molecular ion were found, the formation of the various diagnostic product ions observed in the CID-MS/MS analyses of the precursor protonated and sodiated molecular ions selected from the various synthetic bivalent β -D-*N* glycosides (**1-6**). The various coding used for the product ion tagging was based on the nature of the bivalent β -D-*N*-glycosides. The product ions scan of the protonated precursor molecular ions selected from the six bivalent β -D-*N*-glycosides (**1-6**) are shown in Figures 5.1(b)-5.6(b) and in Schemes 5.1(a)-5.6(a). The product ions scan of the sodiated precursor molecular ions selected from the six bivalent β -D-*N*-glycosides (**1-6**) are shown in Figures 5.1(c)-5.6(c) and in Schemes 5.1(b)-5.6(b).

5.3.1. Low energy ESI-QIT-CID-MS/MS of the protonated $[M+H]^+$ precursor ion at m/z 388.1160 selected from the methoxynaphthalene-substituted triazole β -D-*N*-galactopyranosides derivatives (*I*)

The CID-MS/MS analysis of selected protonated molecular ion $[M+H]^+$ at m/z 388.1160 extracted from the methoxynaphthalene-substituted triazole β -D-*N*-galactopyranosides derivatives (*I*) was recorded by ESI in the positive ion mode, afforded only one product ion shown ion in Figure 5.1(b). This product ion is tentatively shown in Scheme 5.1 (a).

The protonated precursor ion $[M+H]^+$ loses the neutral glycosyl moiety $[(C_6H_{10}O), (162.0528 \text{ Da})]$ to form the aglycone product ion at m/z 225.9706, assigned as $[Y_0]^+$.

The proposed CID-MS/MS of protonated precursor ion $[M+H]^+$ fragmentation route is tentatively shown in Scheme 5.1. (b)

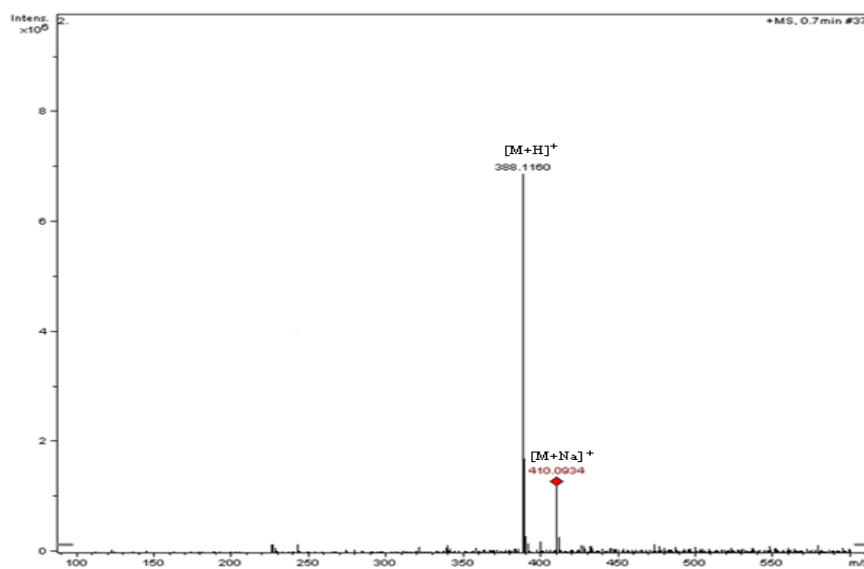


Figure 5.1(a): ESI-QIT-MS (+) of the methoxynaphthalene-substituted triazole β -D-*N*-galactopyranosides derivatives (*I*)

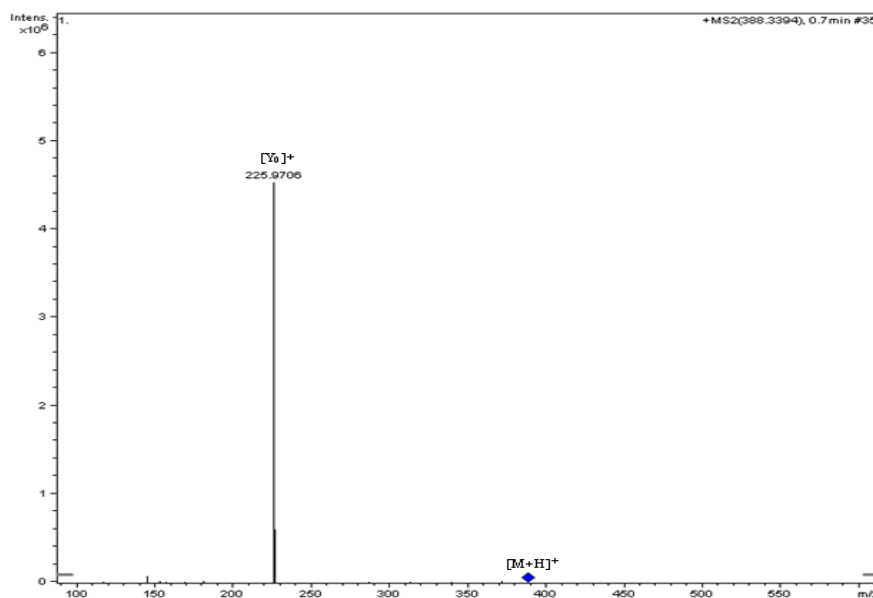
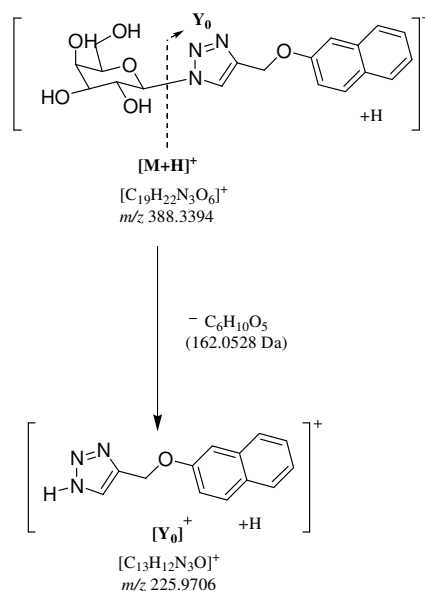


Figure 5.1(b): ESI-QIT-CID-MS/MS of the selected protonated precursor ion $[M+H]^+$ at m/z 388.1160 extracted from the methoxynaphthalene-substituted triazole β -D-*N*-galactopyranosides derivatives (**I**)



Scheme 5.1(a): The tentative proposed fragmentation routes obtained during the low energy ESI-QIT-CID-MS/MS of the protonated molecules $[M+H]^+$ at m/z 388.1160 extracted from methoxynaphthalene-substituted triazole β -D-*N*-galactopyranosides derivatives (**I**)

5.3.2. Low energy ESI-QIT-CID-MS/MS of the sodiated precursor $[M+Na]^+$ at m/z 410.0934 selected from the methoxynaphthalene-substituted triazole β -D-N-galactopyranosides derivatives (*I*)

The CID-MS/MS analysis of selected sodiated precursor ion $[M+Na]^+$ at m/z 410.0934 extracted from methoxynaphthalene-substituted triazole- β -D-N-galactopyranosides derivatives (*I*) was recorded by ESI in the positive ion mode shown in Figure 5.1(c). It produced product ion at m/z 382.0698 and 237.9457. Their genesis of formation of these product ions are tentatively shown in Scheme 5.2(b).

The sodiated precursor ion $[M+Na]^+$ eliminate nitrogen molecule to form the product ion at m/z 382.0698 which is assigned as $[M+Na-N_2]^+$. The precursor ion $[M+Na]^+$ also consecutively eliminate neutral fragment [(naphthalen-2-ol), (144.0575 Da)] and nitrogen molecule to produce product ion at m/z 237.9457.

The proposed CID-MS/MS of sodiated precursor ion $[M+Na]^+$ fragmentation routes are tentatively shown in Scheme 5.1(b)

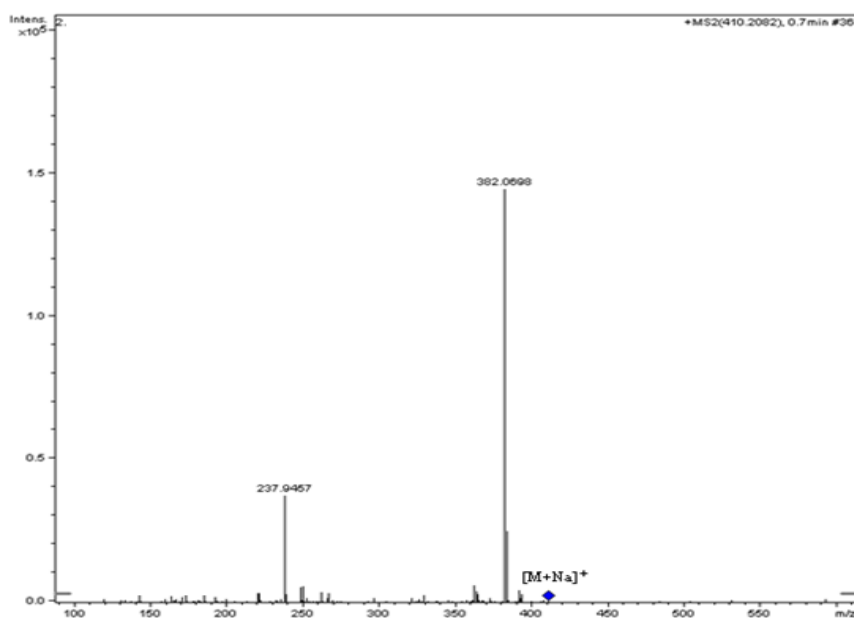
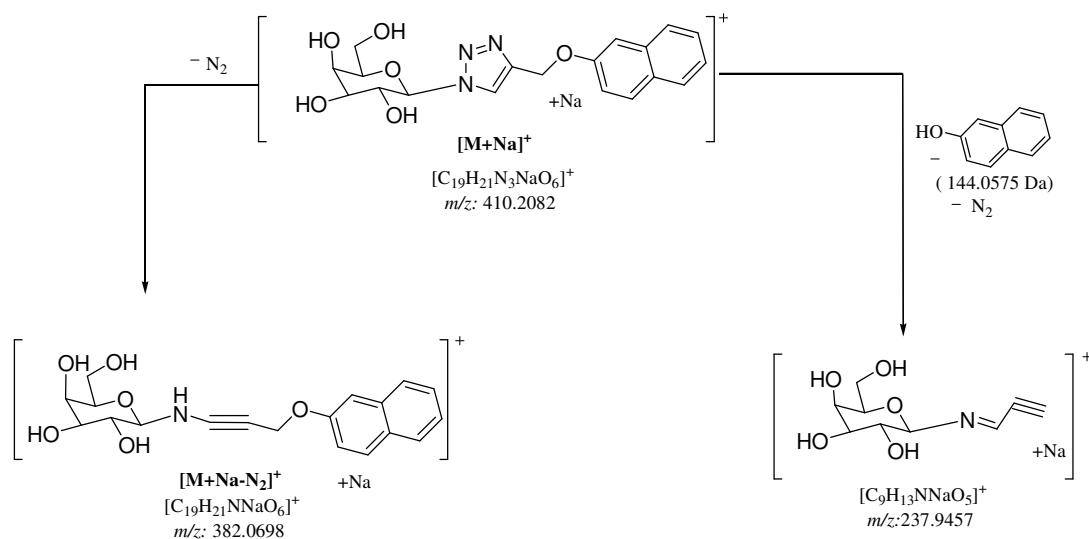


Figure 5.1(c): ESI-QIT-CID-MS/MS of the selected sodiated precursor $[M+Na]^+$ ion at m/z 410.0934 extracted the methoxynaphthalene-substituted triazole β -D-*N*-galactopyranosides derivatives (**I**)



Scheme 5.1(b): The tentative proposed fragmentation routes obtained during the low energy ESI-QIT-CID-MS/MS of the sodiated molecule $[M+Na]^+$ at m/z 410.0934 extracted from the methoxynaphthalene-substituted triazole β -D-*N*-galactopyranosides derivatives (**I**)

5.3.3. Low energy ESI-QIT-CID-MS/MS of the protonated precursor ion $[M+H]^+$ at m/z 438.1528 selected from the ethyltriazole β -D-*N*-lactopyranosides derivative (2)

The CID-MS/MS of the selected protonated molecular ion $[M+H]^+$ at m/z 438.1528 extracted from the ethyltriazole β -D-*N*-lactopyranosides derivative (2) shown in Figure 5.3(b) was recorded in the positive ion mode by ESI. The major product ions observed at m/z , 420.1551, 391.1729, and 276.9904 shown in Scheme 5.3(a)

The precursor ion $[M+H]^+$ at m/z 438.3938 eliminates the neutral galactosyl moiety $[(C_6H_{10}O_5), (162.0528 \text{ Da})]$ to form the product ion at m/z 276.9904 which is assigned as $[Y_1]^+$. The same time the precursor ion $[M+H]^+$ loses water molecule to obtain the product ion at m/z 420.1551 which is assigned as $[M+H-H_2O]^+$. The product ion at m/z 420.1551 loses a molecule of N_2 and proton H^+ to produces radical cation product ion at m/z 391.1729.

The proposed CID-MS/MS of protonated precursor ion $[M+H]^+$ fragmentation routes are tentatively shown in Scheme 5.2(a)

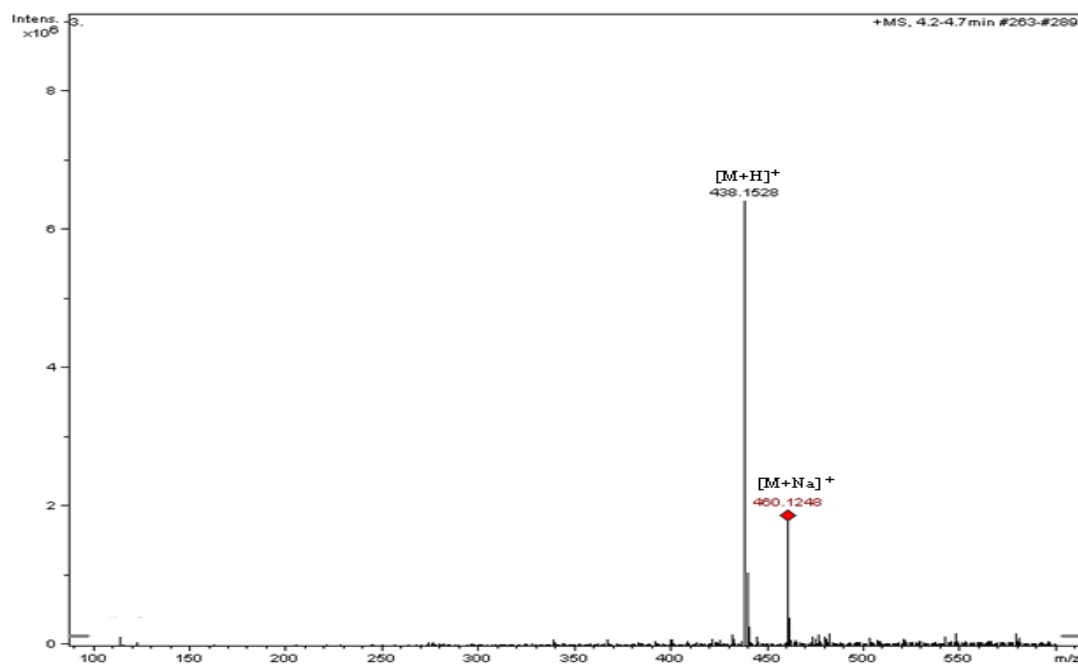


Figure 5.3(a): ESI-QIT-MS(+) of the ethyltriazole β -D-*N*-lactopyranosides derivative (2)

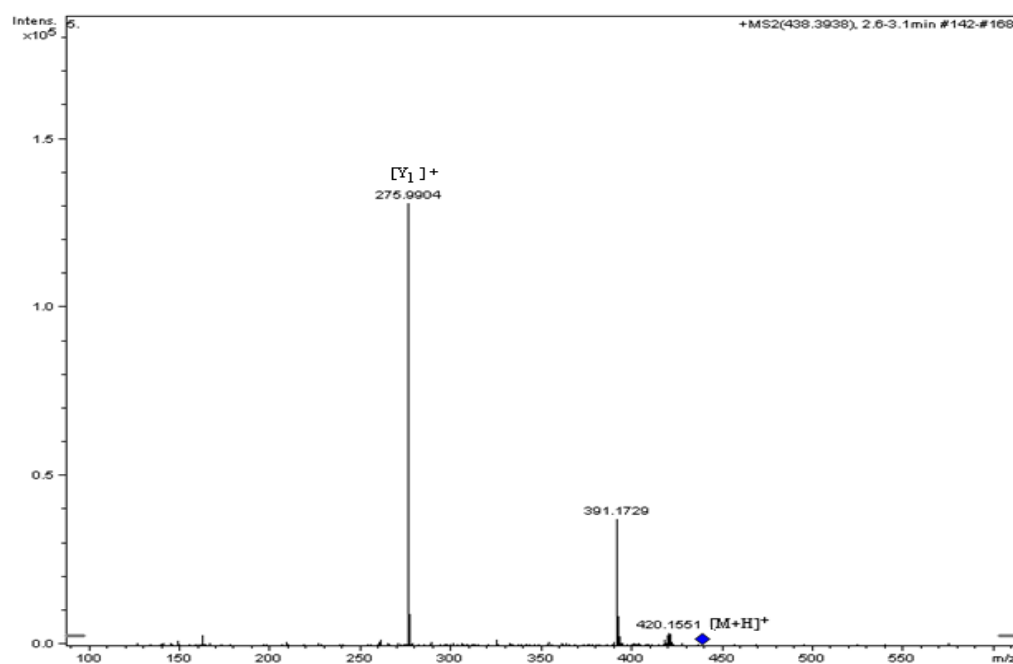
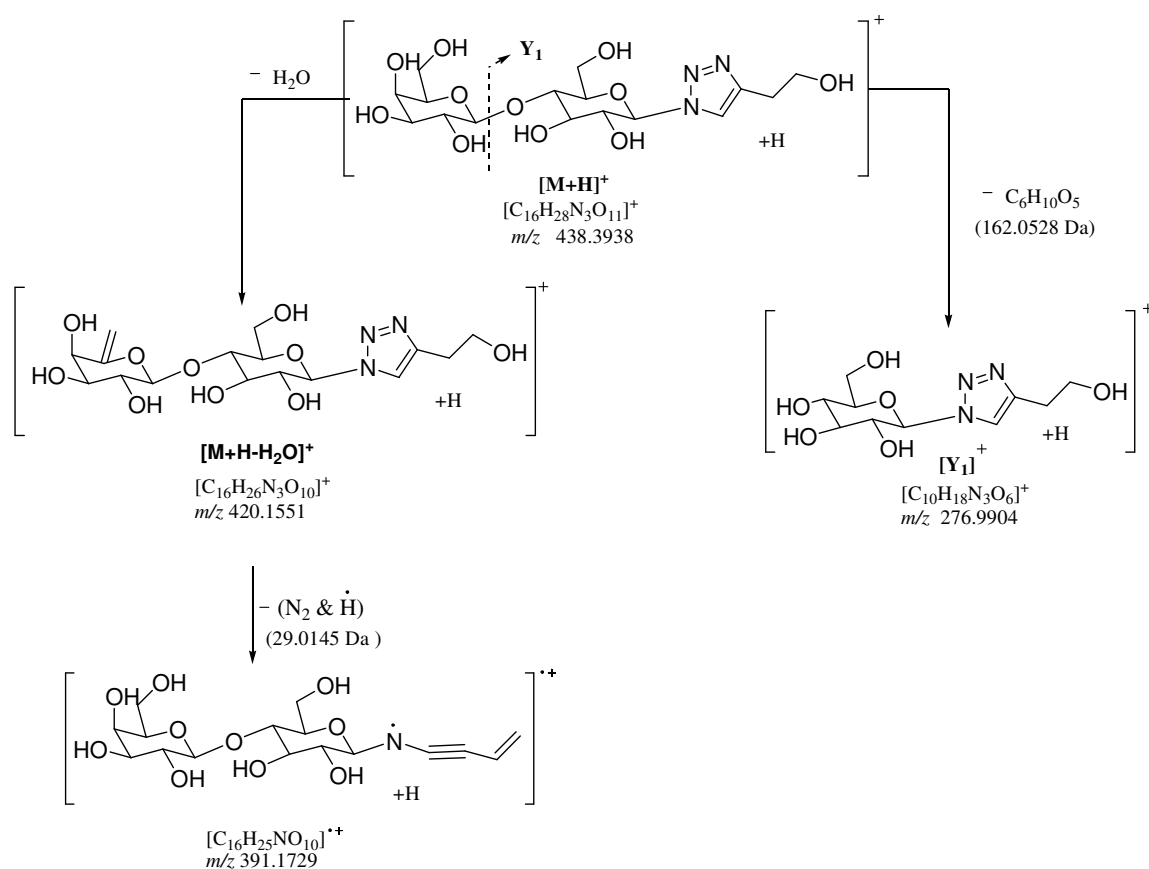


Figure 5.3(b): ESI-QIT-CID-MS/MS of the selected protonated precursor ion $[M+H]^+$ at m/z 438.1528 extracted from the ethyltriazole β -D-*N*-lactopyranosides derivative (2)



Scheme 5.2(a): The tentative proposed fragmentation routes obtained during the low energy ESI-QIT-CID-MS/MS of the protonated molecular ion $[M+H]^+$ at m/z 438.1528 extracted from the ethyltriazole β -D-*N*-lactopyranosides derivative (**2**)

5.3.4. Low energy ESI-QIT-CID-MS/MS of the sodiated precursor $[M+Na]^+$ at m/z 460.1248 selected from the ethyltriazole β -D-*N*-lactopyranosides derivative (**2**)

The CID-MS/MS of the selected sodiated molecular ion $[M+Na]^+$ at m/z 460.1248 extracted from the ethyltriazole β -D-*N*-lactopyranosides derivative (**2**) shown in Figure 5.4(c) was recorded by ESI in the positive ion mode. The major product ions observed at m/z 432.0714, 347.0420, 298.0487, 245.0049 and 184.9448 are tentatively shown in Scheme 5.4(b)

The precursor ion $[M+Na]^+$ at m/z 460.3898 eliminates nitrogen molecule to form the product ion at m/z 432.0714. The precursor ion $[M+Na]^+$ loses neutral galactosyl moiety $[(C_6H_{10}O_5), (162.0528 \text{ Da})]$ to form the product ion at m/z 298.0487 which is assigned as $[Y_1]^+$. The product ion $[Y_1]^+$ at m/z 298.0487 loses the neutral aglycone moiety $[(C_4H_7N_3O), (113.0589 \text{ Da})]$ to form the sodiated sugar product ion at m/z 184.9448 which is assigned as $[B_1]^+$. The product ion $[B_1]^+$ can be found from the direct cleavage from the precursor ion as shown in Scheme 5.4(b). The same time the precursor ion $[M+Na]^+$ loses ethanol substituted the aglycone moiety $[(C_4H_7N_3O), (113.0589 \text{ Da})]$ to obtain the sodiated lactosyl product ion at m/z 347.0420 which is assigned as $[B_2]^+$. The precursor ion $[M+Na]^+$ also undergoes ring fragmentation to form the product ion at m/z 245.0049 with the elimination of neutral $[(C_8H_{13}N_3O_4), (215.0906 \text{ Da})]$ which is assigned as $[^{2,4}A_2]^+$. The product ion $[^{2,4}A_2]^+$ at m/z 245.0049 can be formed by elimination of neutral fragment $[(C_4H_6O_3), (102.0317 \text{ Da})]$ from the product ion at m/z 347.0420 as shown in Scheme 5.4(b).

The proposed CID-MS/MS of sodiated precursor ion $[M+Na]^+$ fragmentation routes are shown in Scheme 5.2(b)

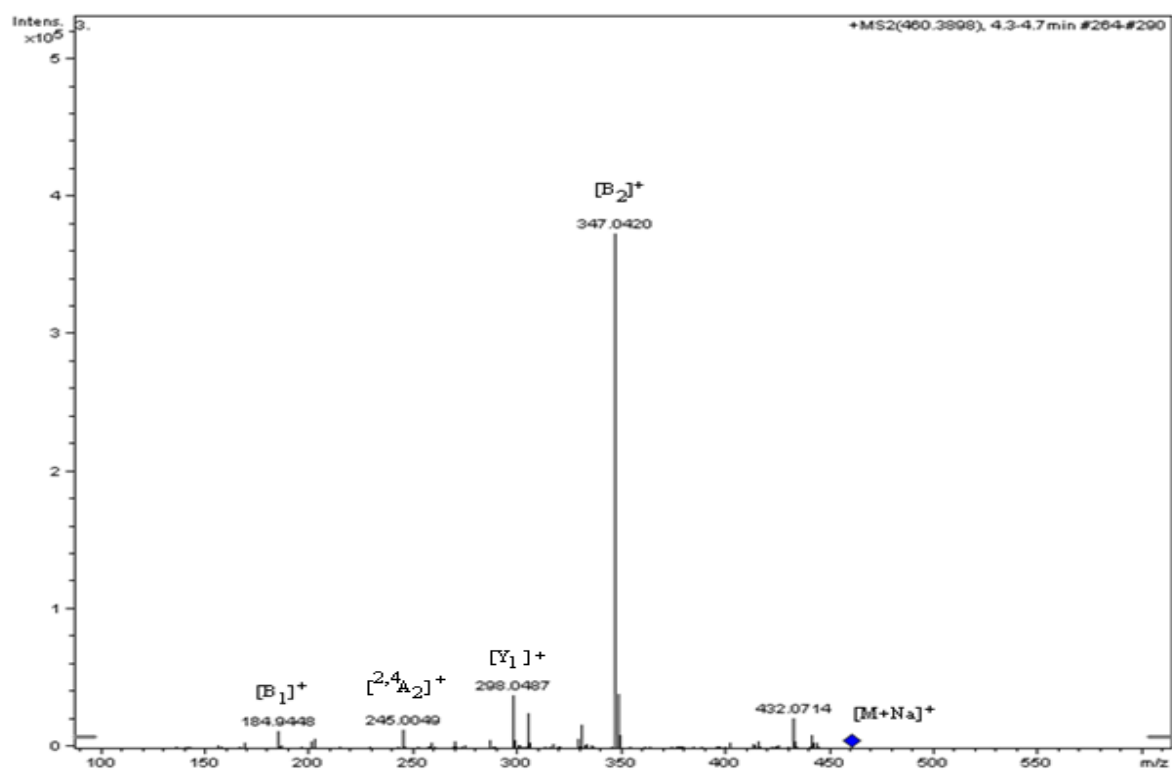
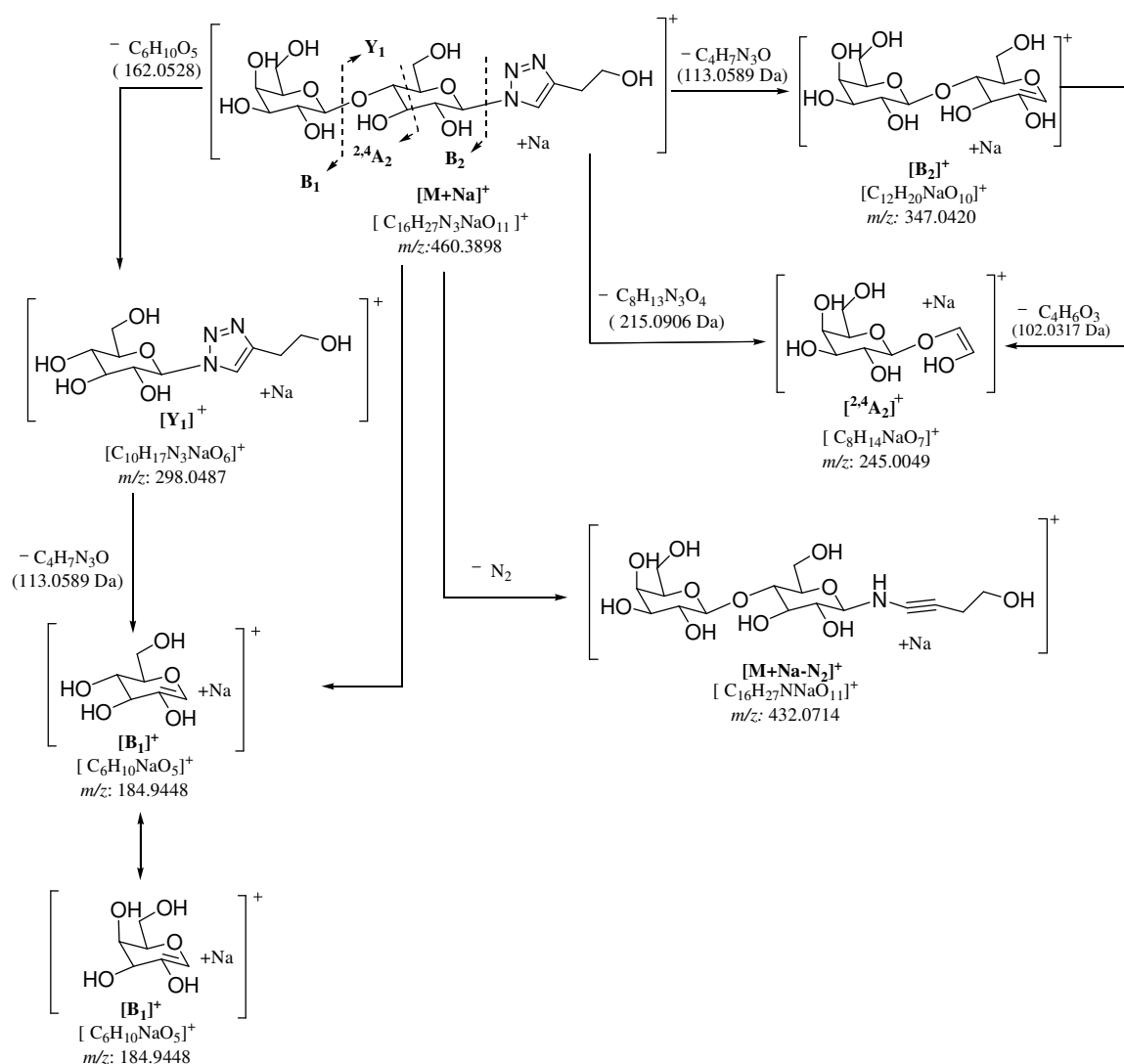


Figure 5.3(c): ESI-QIT-CID-MS/MS of the selected sodiated precursor ion $[M+Na]^+$ at m/z 460.1248 extracted from the ethyltriazole β -D-*N*-lactopyranosides derivative (**2**)



Scheme 5.2(b): The tentative proposed fragmentation routes obtained during the low energy ESI-CID-MS/MS of the sodiated molecular ion $[M+Na]^+$ at m/z 460.1248 extracted from the ethyltriazole β -D-*N*-lactopyranosides derivative (2)

5.3.5. Low energy ESI-QIT-CID-MS/MS of the protonated $[M+H]^+$ precursor ion at m/z 466.1814 selected from the butyltriazole β -D-*N*-lactopyranosides derivatives (3)

The CID-MS/MS analysis of selected protonated molecular ion $[M+H]^+$ at m/z 466.1814 shown in Figure 5.5(b) was recorded by ESI in the positive ion mode. The

afforded product ion at m/z 419.2309, 304.0386 and 142.0236 are tentatively shown in Scheme 5.3(a).

The protonated precursor ion $[M+H]^+$ at m/z 466.3596 eliminates anhydrous neutral galactosyl moiety $[(C_6H_{10}O_5), (162.0528 \text{ Da})]$ to form the product ion at m/z 304.0386 which is assigned as $[Y_1]^+$. The product ion $[Y_1]^+$ eliminates anhydrous neutral glucose moiety $[(C_6H_{10}O_5), (162.0528 \text{ Da})]$ to form triazole derivative product ion $[4(1H-1,2,3-triazole-4-yl)butan-1-ol + H]^+$ at m/z 142.0236 which is assigned as $[Y_0]^+$. The product ion $[Y_0]^+$ is formed from the precursor ion by elimination of lactosyl moiety $[(C_{12}H_{20}O_{10}), (324.1056 \text{ Da})]$ as shown in Scheme 5.3(a). The precursor ion also eliminates the consecutively hydrogen molecule, a nitrogen molecule and hydroxyl radical to form the radical cation product ion at m/z 419.2309.

The proposed CID-MS/MS of protonated precursor ion $[M+H]^+$ fragmentation routes are tentatively shown in Scheme 5.3(a)

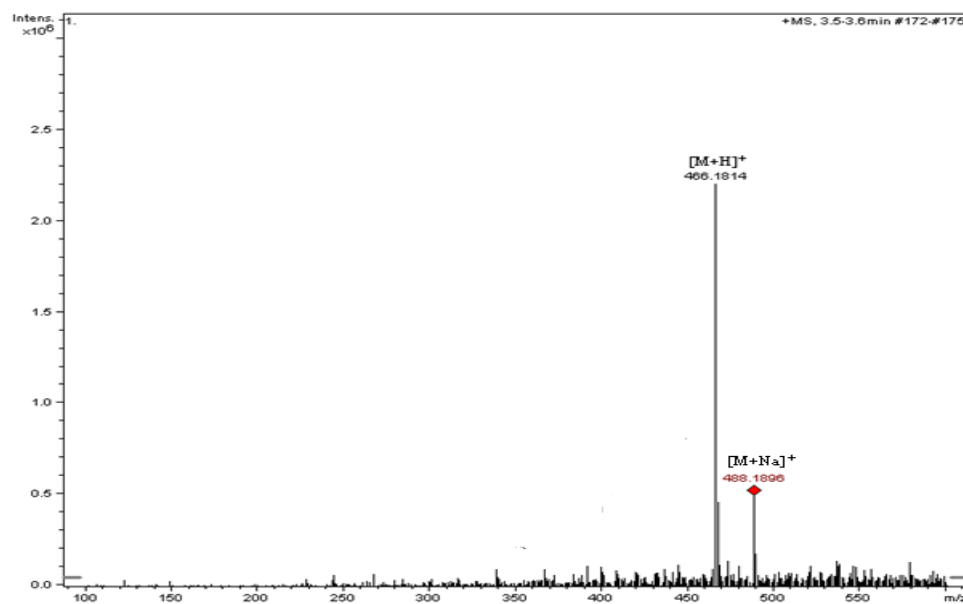


Figure 5.5(a): ESI-QIT-MS (+) of the butyltriazole β -D-*N*-lactopyranosides derivatives

(3)

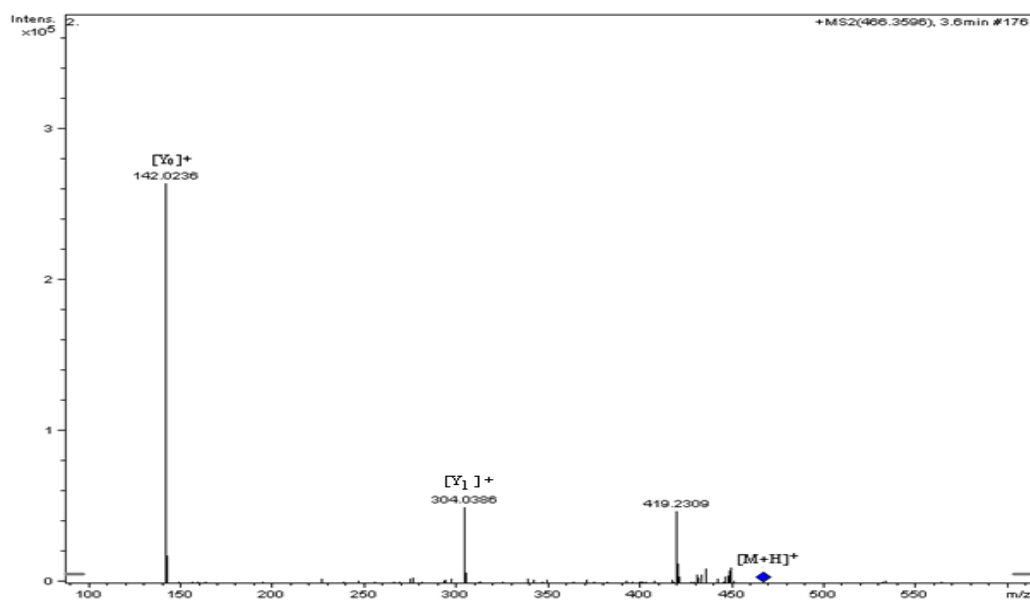
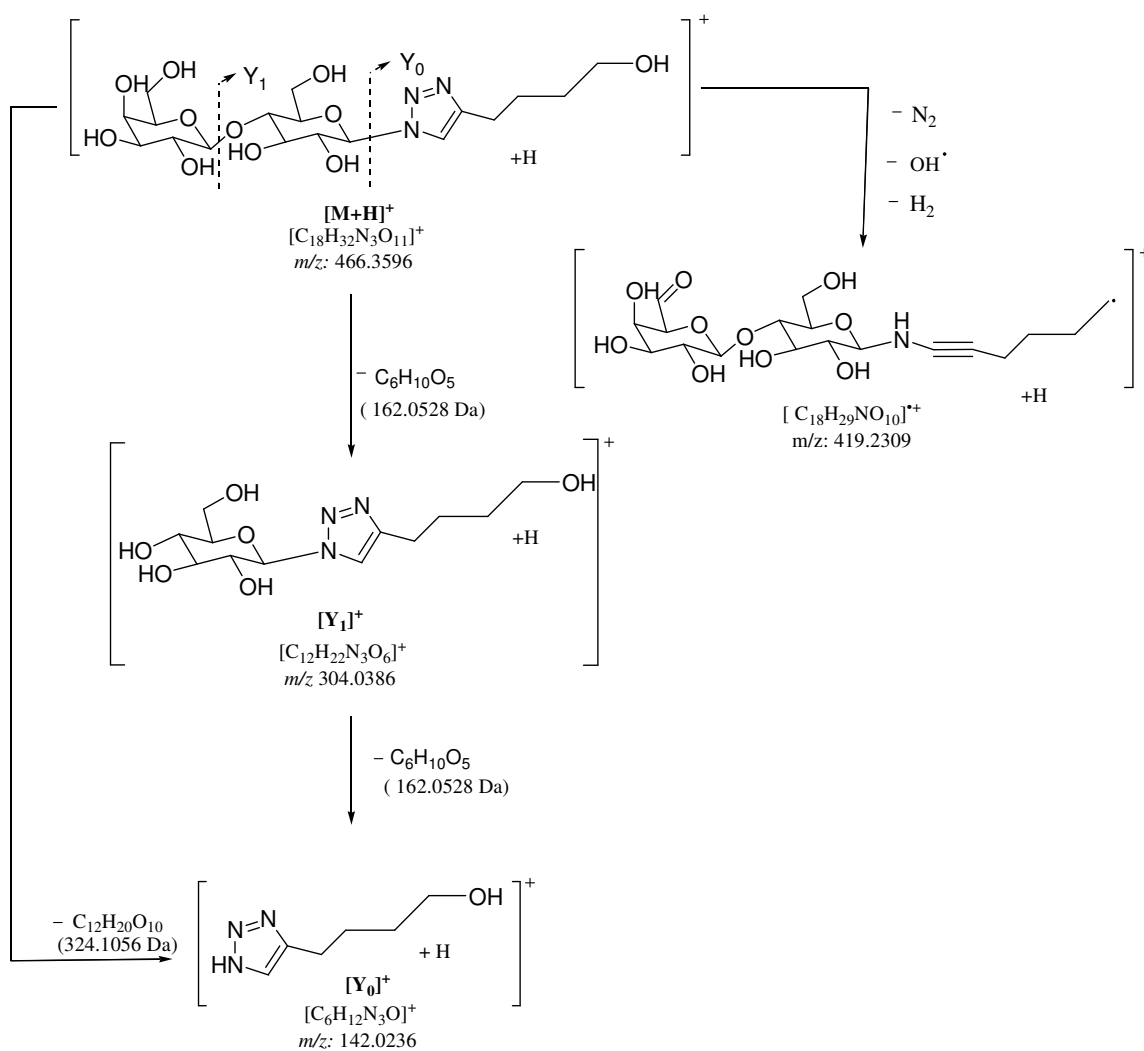


Figure 5.5(b): ESI-QIT-CID-MS/MS of the selected protonated precursor ion [M+H]⁺ at m/z 466.1814 extracted from the butyltriazole β -D-*N*-lactopyranosides derivatives (3)



Scheme 5.3(a): The tentative proposed fragmentation routes obtained during the low energy ESI-QIT-CID-MS/MS of the protonated molecular ion $[M+H]^+$ at m/z 466.1814 extracted from the butyltriazole β -D-*N*-lactopyranosides derivatives (**3**)

5.3.6. Low energy ESI-QIT-CID-MS/MS of the sodiated precursor $[M+Na]^+$ at m/z 488.1896 selected from the butyltriazole β -D-*N*-lactopyranosides derivatives (**3**)

The product ion scan of the selected sodiated molecular ion $[M+Na]^+$ at m/z 488.1896 extracted from the butyltriazole β -D-*N*-lactopyranosides derivatives (**3**) shown in Figure 5.6(c) was recorded by ESI with ion polarity (positive). The major product ions

observed at m/z 460.1280, 347.0654, 305.0571, and 245.0253 are tentatively shown in Scheme 5.3(b)

The precursor ion $[M+Na]^+$ at m/z 488.5867 eliminates nitrogen molecule to form the product ion at m/z 460.1280. The precursor ion $[M+Na]^+$ loses neutral triazole derivative moiety $[(C_6H_{11}N_3O), (141.0902 \text{ Da})]$ to form the product ion at m/z 347.0654 which is assigned as $[B_2]^+$. Then the precursor ion $[M+Na]^+$ undergoes ring fragmentation at m/z 305.0571 which is assigned as $[^{0,2}A_2]^+$ with a elimination of neutral fragment $[(C_8H_{13}N_3O_2), (183.1008 \text{ Da})]$. The precursor ion $[M+Na]^+$ also undergoes ring fragmentation to form the product ion at m/z 245.0253 with the elimination of the neutral fragment $[(C_{10}H_{17}N_3O_4), (243.1219 \text{ Da})]$ which is assigned as $[^{2,4}A_2]^+$. The product ion $[^{2,4}A_2]^+$ also can be formed from the product ion $[B_2]^+$ by elimination of neutral fragment $[(C_4H_6O_3), (102.0317 \text{ Da})]$.

The proposed CID-MS/MS of sodiated precursor ion $[M+Na]^+$ fragmentation routes are tentatively shown in Scheme 5.3(b)

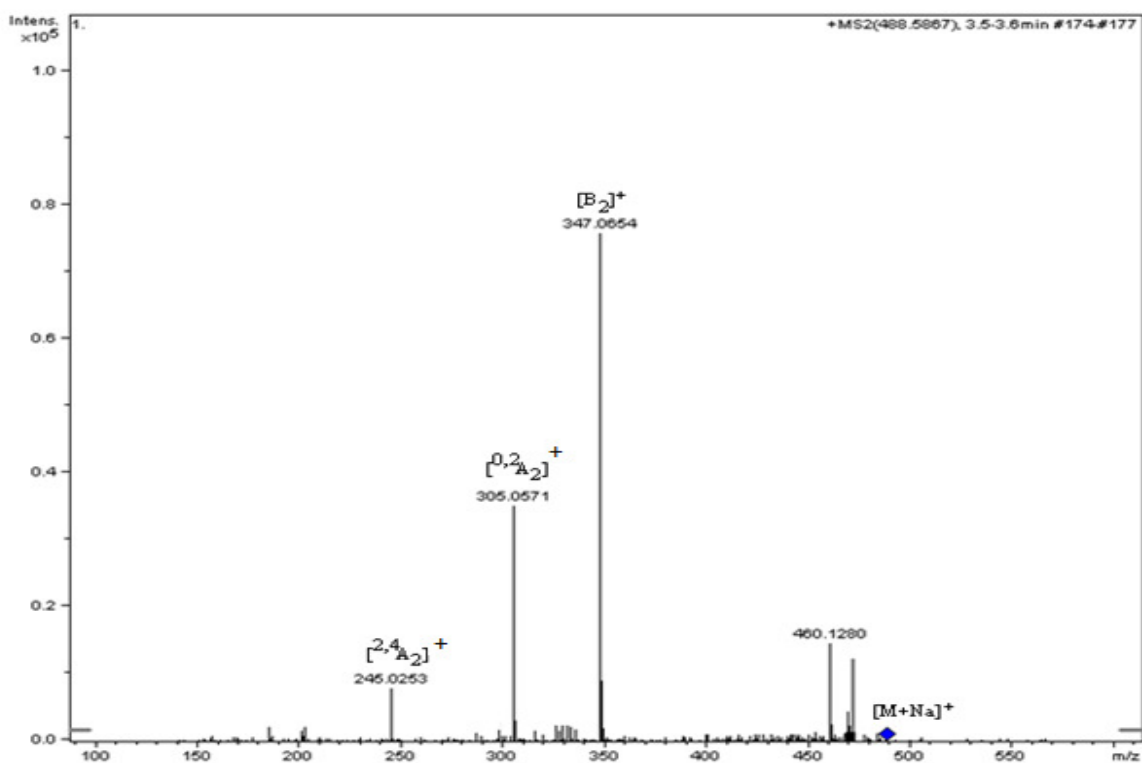
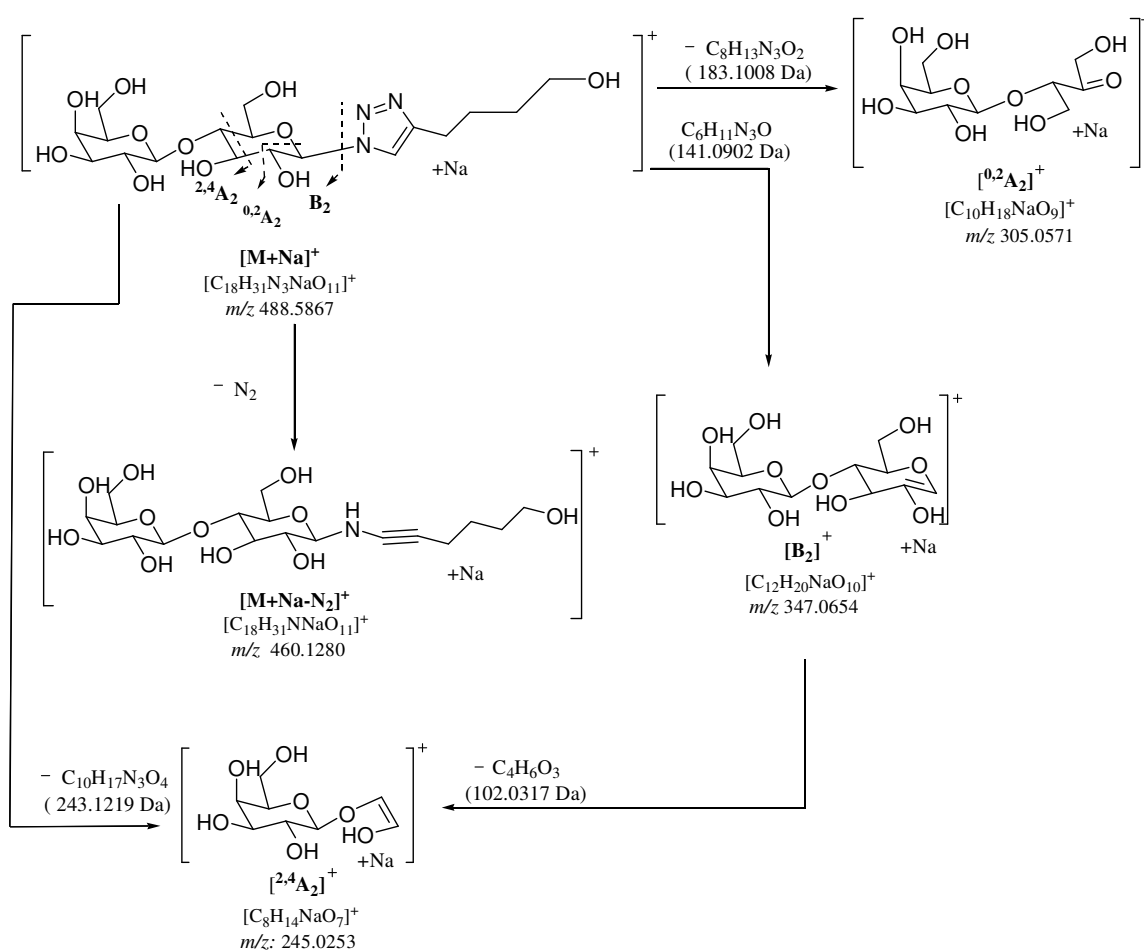


Figure 5.5(c): ESI-QIT-CID-MS/MS of the selected sodiated precursor ion $[M+Na]^+$ ion at m/z 488.1896 extracted from the butyltriazole β -D-*N*-lactopyranosides derivatives (**3**)



Scheme 5.3(b): The tentative proposed fragmentation routes obtained during the low energy ESI-QIT-CID-MS/MS of the sodiated molecular ion $[M+Na]^+$ at m/z 488.1896 extracted from the butyltriazole β -D-*N*-lactopyranosides derivatives (**3**)

5.3.7. Low energy ESI-QIT-CID-MS/MS of the protonated $[M+H]^+$ precursor ion at m/z 500.1234 selected from the anisoletriazole β -D-*N*-lactopyranosides derivatives (**4**).

The CID-MS/MS analysis of selected protonated molecular ion $[M+H]^+$ at m/z 500.1234 extracted from the anisoletriazole β -D-*N*-lactopyranosides derivatives (**4**) shown

in Figure 5.7(b) was recorded by ESI in the positive mode. The afforded product ion at m/z 337.9837 and 175.9751 tentatively shown in Scheme 5.4(a).

The protonated precursor ion $[M+H]^+$ at m/z 500.4 eliminates the neutral galactosyl moiety $[(C_6H_{10}O_5), (162.0528 \text{ Da})]$ to form the product ion at m/z 337.9837 which is assigned as $[Y_1]^+$. The precursor ion $[M+H]^+$ at m/z 500.4 eliminates neutral lactosyl moiety $[(C_{12}H_{20}O_{10}), (324.1056 \text{ Da})]$ to form the aglycone product ion at m/z 175.9751 which is assigned as $[Y_0]^+$.

The proposed CID-MS/MS of protonated precursor ion $[M+H]^+$ fragmentation routes are tentatively shown in Scheme 5.4(a)

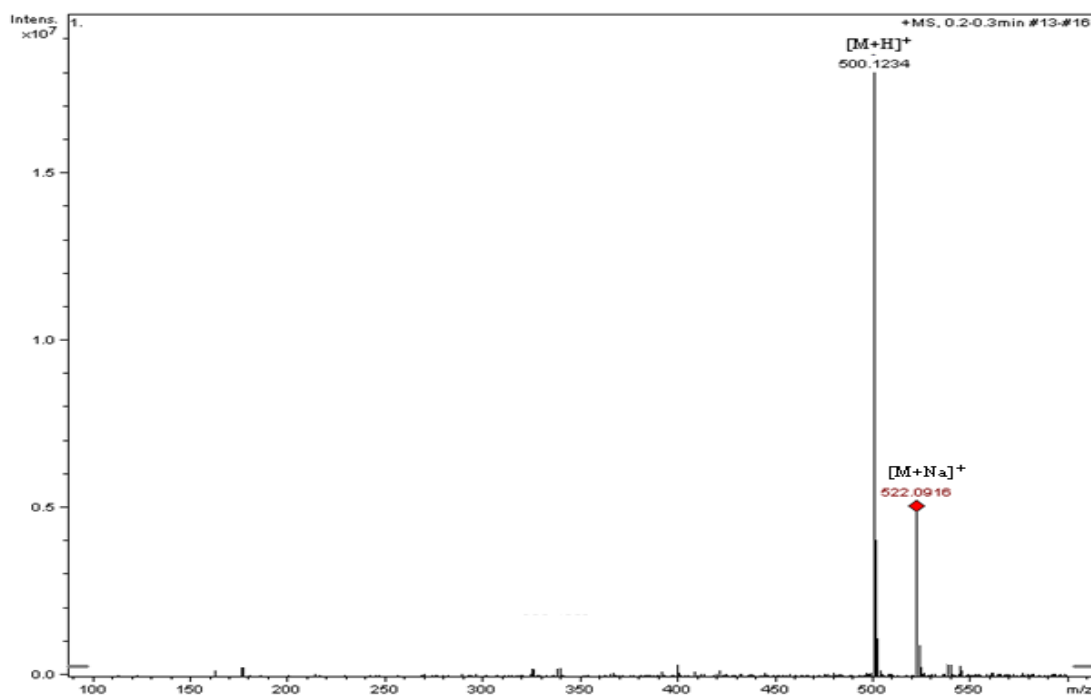


Figure 5.7: (a) ESI-QIT-MS (+) of the anisoletriazole β -D-*N*-lactopyranosides derivatives (4).

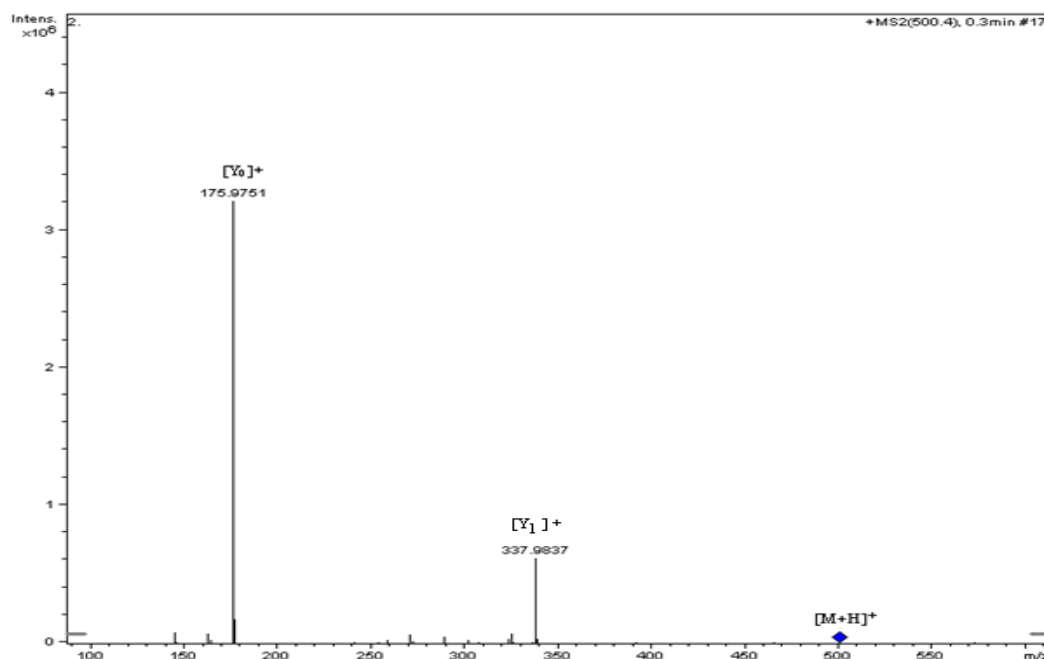
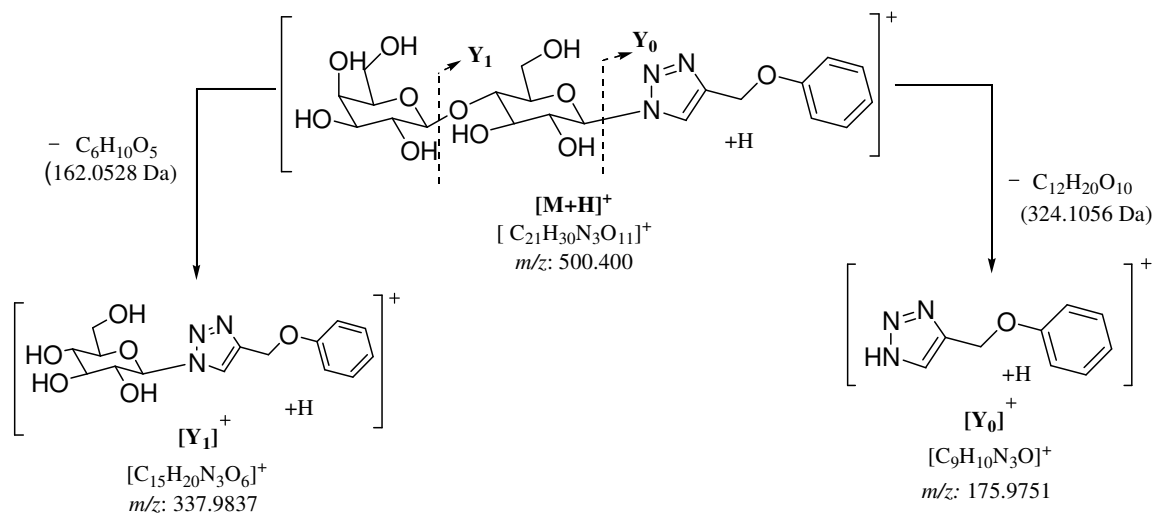


Figure 5.7(b): ESI-QIT-CID-MS/MS of the selected protonated precursor ion $[M+H]^+$ at m/z 500.1234 extracted from the anisoletriazole β -D-*N*-lactopyranosides derivatives (**4**).



Scheme 5.4(a): The tentative proposed fragmentation routes obtained during the low energy ESI-QIT-CID-MS/MS of the protonated molecular ion $[M+H]^+$ at m/z 500.1234 extracted from the anisoletriazole β -D-*N*-lactopyranosides derivatives (**4**).

5.3.8. Low energy ESI-QIT-CID-MS/MS of the sodiated precursor $[M+Na]^+$ at m/z 522.0916 selected from the anisoletriazole β -D-*N*-lactopyranosides derivatives (4).

The CID-MS/MS analysis of selected sodiated molecular ion $[M+Na]^+$ at m/z 522.0916 extracted from the anisoletriazole β -D-*N*-lactopyranosides derivatives (4) shown in Figure 5.7(c) was recorded by ESI in the positive mode. The afforded product ion at m/z 494.0901, 400.0571, 347.0414, 304.9969, 244.9483 and 184.9219 tentatively shown in Scheme 5.4(b).

The sodiated precursor ion $[M+Na]^+$ at m/z 522.3 eliminates nitrogen molecule to produce product ion at m/z 494.0901 which is assigned as $[M+Na-N_2]^+$. The product ion at m/z 494.0901 undergoes ring fragmentation to afford the product ion at m/z 400.0571 with the neutral elimination of $[(C_3H_8O_3), (92.0473 \text{ Da})]$ and hydrogen molecule which is assigned as $[^{0,3}X_2]^+$. The sodiated precursor ion $[M+Na]^+$ at m/z 522.3 then fragmented to form the product ion at m/z 347.0414 with the elimination of neutral triazole derivatives which is assigned as $[B_2]^+$. The sodiated precursor ion $[M+Na]^+$ undergoes ring fragmentation with neutral elimination of $[(C_{11}H_{11}N_3O_2), (217.0851 \text{ Da})]$ to form the product ion at m/z 304.9969 which is assigned as the $[^{0,2}A_2]^+$. The sodiated precursor ion $[M+Na]^+$ also can be gone ring fragmentation at m/z 244.9483 by losing a neutral elimination of $[(C_{13}H_{15}N_3O_4), (277.1063 \text{ Da})]$ which is assigned as $[^{2,4}A_2]^+$. The product ion $[^{2,4}A_2]^+$ can be formed by elimination of neutral fragment $[(C_4H_6O_3), (102.0317 \text{ Da})]$ from the product ion $[B_2]^+$. Then the product ion $[^{2,4}A_2]^+$ loses $[(\text{ethene-1,2-diol}), (60.0211 \text{ Da})]$ to form the product ion at m/z 184.9219 which is assigned as $[B_1]^+$. The $[B_1]^+$ can be found from the direct cleavage of precursor ion $[M+Na]^+$ as shown in Scheme 5.4(b).

The proposed CID-MS/MS of sodiated precursor ion $[M+Na]^+$ fragmentation routes are tentatively shown in Scheme 5.4(b).

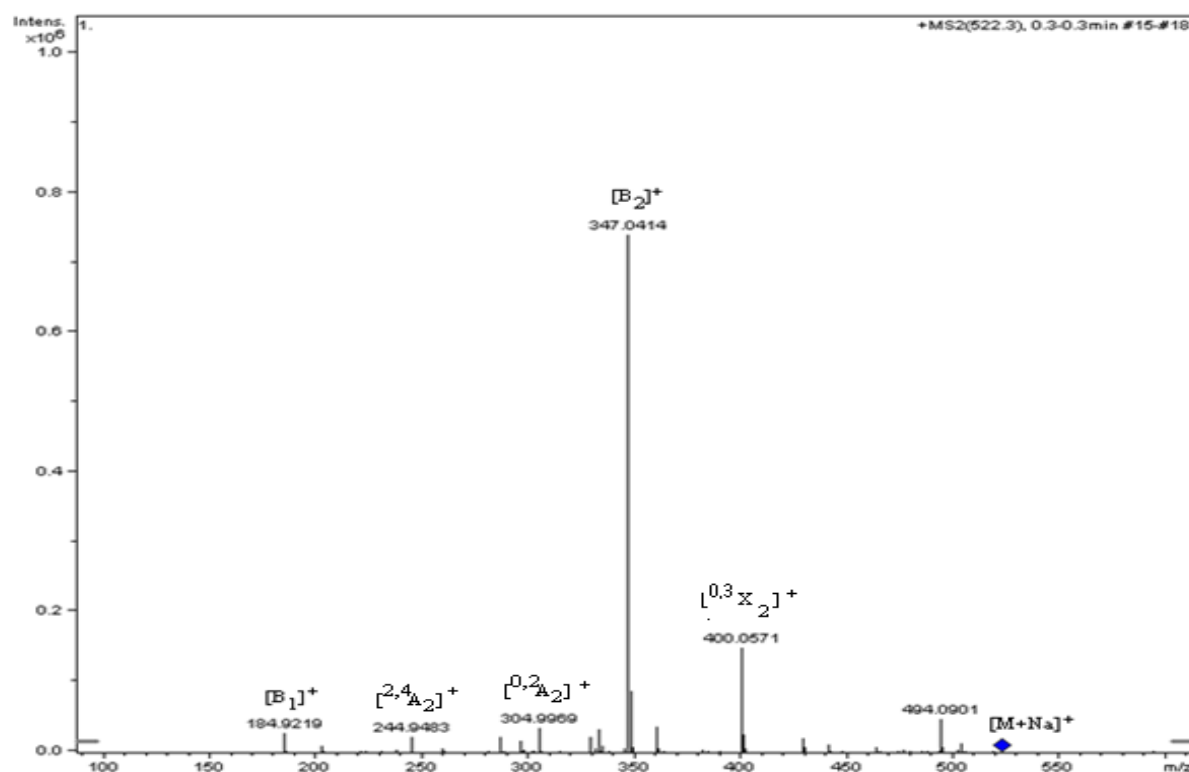
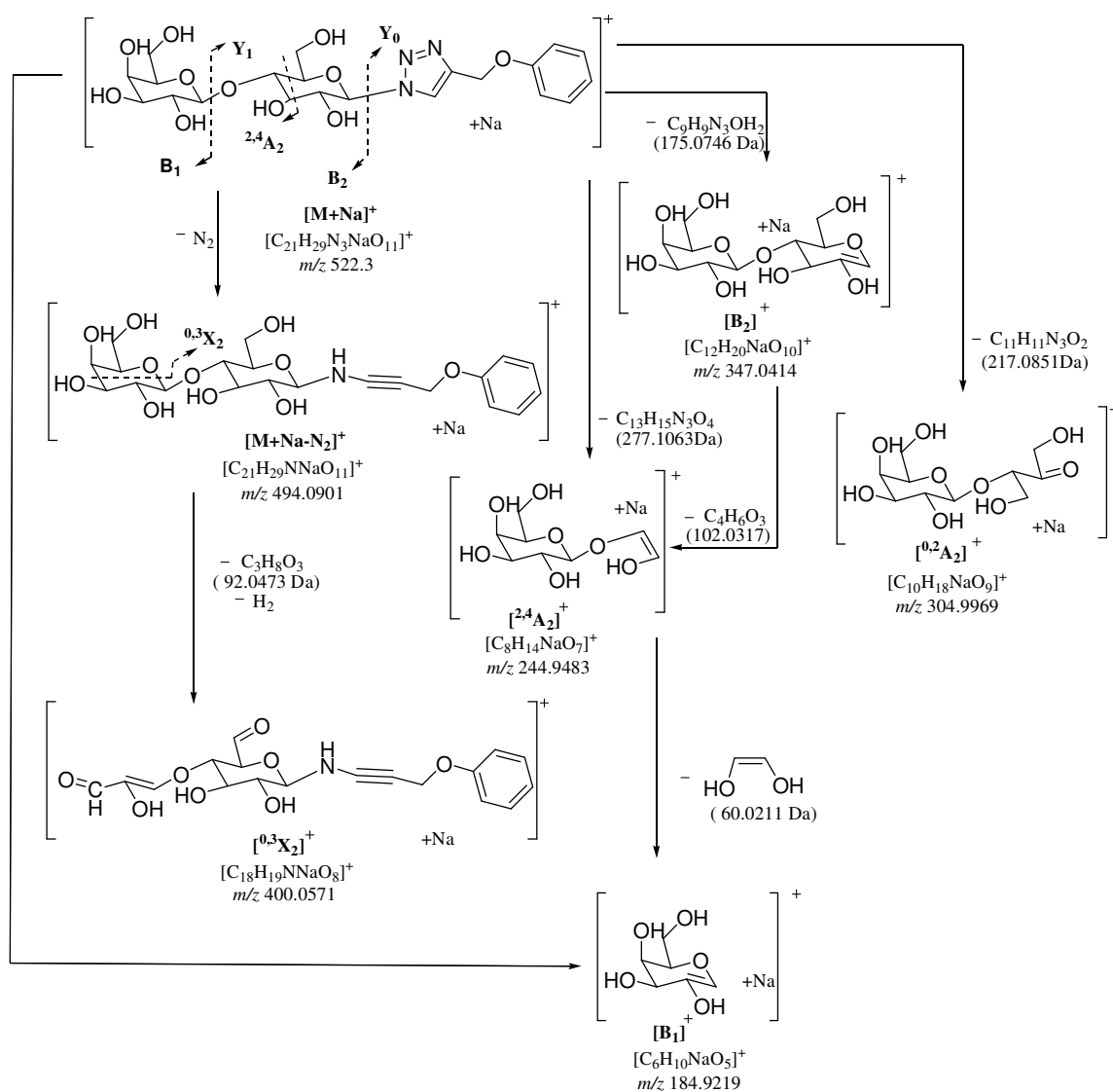


Figure 5.7(c): ESI-QIT-CID-MS/MS of the selected sodiated precursor ion $[M+Na]^+$ ion at m/z 522.0916 extracted from the anisoletriazole β -D-*N*-lactopyranosides derivatives (4).



Scheme 5.4(b): The tentative proposed fragmentation routes obtained during the low energy ESI-QIT-CID-MS/MS of the sodiated molecular ion $[M+Na]^+$ at m/z 522.0916 extracted from the anisoletriazole β -D-*N*-lactopyranosides derivatives (**4**)

5.3.9. Low energy ESI-QIT-CID-MS/MS of the protonated $[M+H]^+$ precursor ion at m/z 530.1297 selected from the dimethoxybenzenetriazole β -D-*N*-lactopyranosides derivatives (5)

The CID-MS/MS analysis of selected protonated molecular ion $[M+H]^+$ at m/z 530.1297 extracted from the dimethoxybenzene-substituted triazole β -D-*N*-lactopyranosides derivatives (5) shown in Figure 5.9(b) was recorded by ESI in the positive ion mode. It produced product ion at m/z 368.0100, 324.9960, and 205.9571. Their genesis are tentatively shown in Scheme 5.5(a).

The protonated precursor ion $[M+H]^+$ then fragmented to the product ion at m/z 368.0100 which is assigned as $[Y_1]^+$ by elimination of neutral sugar group $[(C_6H_{10}O), (162.0528 \text{ Da})]$. The protonated precursor ion $[M+H]^+$ also eliminates the neutral lactosyl moiety $[(C_{12}H_{20}O_{10}), (324.1056 \text{ Da})]$ to form triazole derivative ion $[Y_0]^+$ at m/z 205.9571. The precursor ion also eliminates a neutral triazole derivative $[(C_{10}H_{11}N_3O_2), (205.0851 \text{ Da})]$ to form the disaccharide oxonium ion which is assigned as $[B_2]^+$ at m/z 324.9960.

The proposed CID-MS/MS of protonated precursor ion $[M+H]^+$ fragmentation routes are tentatively shown in Scheme 5.5(a)

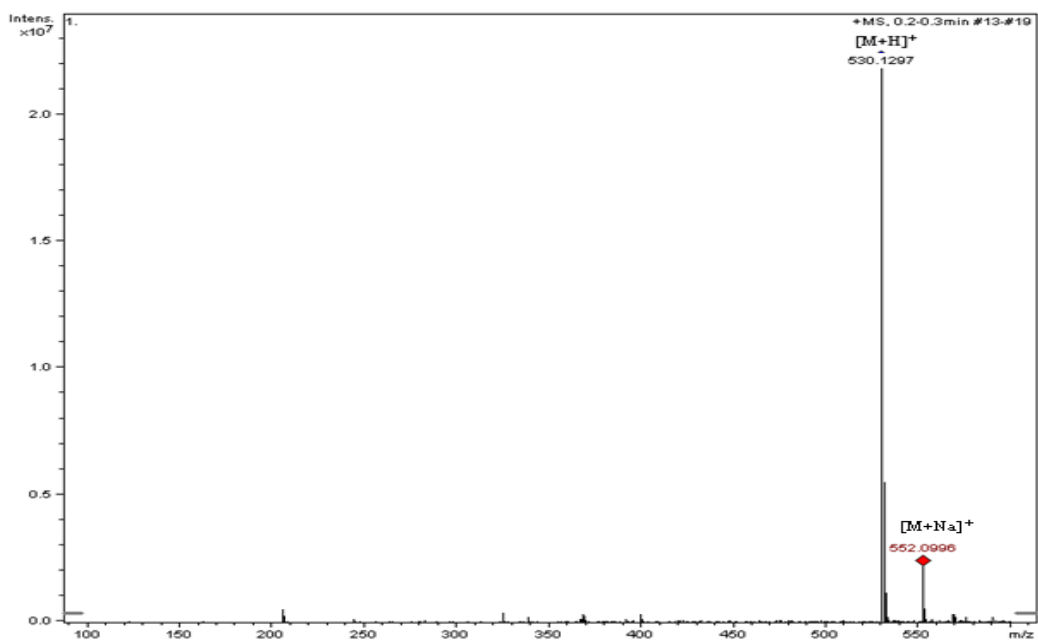


Figure 5.9(a): ESI-QIT-MS(+) of the dimethoxybenzenetriazole β -D-N-lactopyranosides derivatives (5)

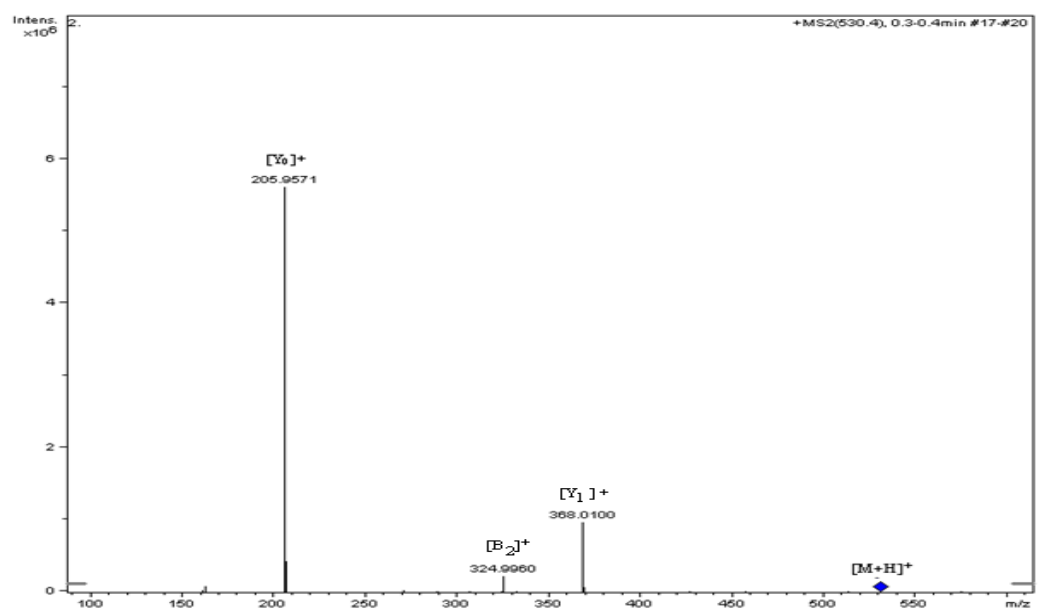
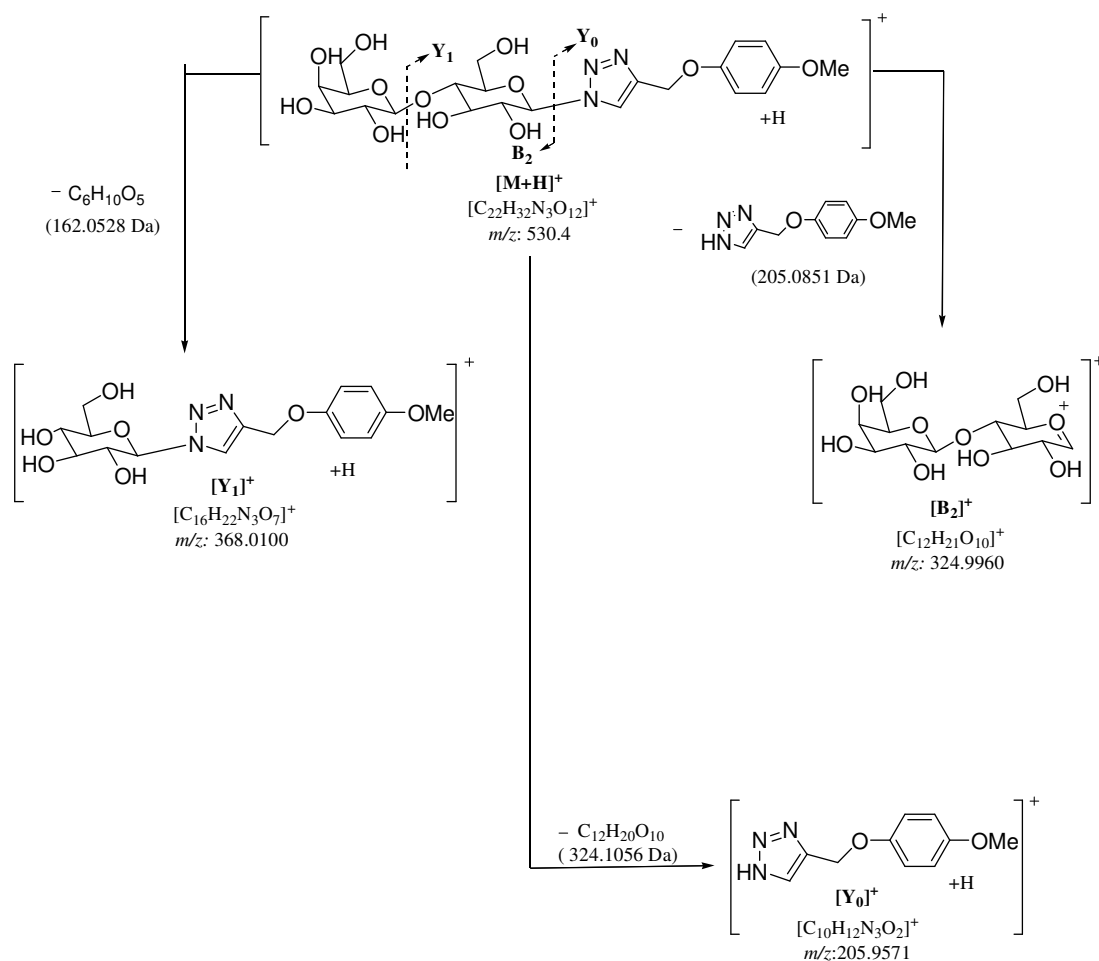


Figure 5.9(b): ESI-QIT-CID-MS/MS of the selected protonated precursor ion [M+H]⁺ at m/z 530.1297 extracted from the dimethoxybenzenetriazole β -D-N-lactopyranosides derivatives (5)



Scheme 5.5 (a): The tentatively proposed fragmentation routes obtained during the low energy ESI-QIT-CID-MS/MS of the protonated molecular ion $[\text{M}+\text{H}]^+$ at m/z 530.1297 extracted from the dimethoxybenzenetriazole β -D-*N*-lactopyranosides derivatives (**5**)

5.3.10. Low energy CID-MS/MS of the sodiated precursor $[\text{M}+\text{Na}]^+$ at m/z 552.0996 selected from the dimethoxybenzenetriazole β -D-*N*-lactopyranosides derivatives (**5**)

The CID-MS/MS of selected sodiated precursor ion $[\text{M}+\text{Na}]^+$ at m/z 552.0996 extracted from the dimethoxybenzene-substituted triazole β -D-*N*-lactopyranosides derivatives (**5**) shown in Figure 5.10(c) was recorded by ESI in the positive ion mode. It

produced product ion at m/z 524.1096, 429.0541, 400.0570, 347.0496, 296.0292, and 184.9560. Their geneses are tentatively shown in Scheme 5.5 (b).

The sodiated precursor ion $[M+Na]^+$ at m/z 552.3 eliminates nitrogen molecule to form the product ion at m/z 524.1096 which is assigned as the $[M+Na-N_2]^+$. The product ion at m/z 347.0496 can be found from the precursor ion at m/z 552.3 with the elimination of triazole derivative $[(C_{10}H_{11}N_3O_2), (205.0851 \text{ Da})]$ or it can also be found from the product ion the $[M+Na-N_2]^+$ with the elimination of neutral $[(C_{10}H_{11}NO_2), (177.0790 \text{ Da})]$ which is assigned as $[B_2]^+$ as shown in Scheme 5.5(b). The sodiated galactose ion $[B_1]^+$ at m/z 184.9560 is formed the precursor ion $[M+Na]^+$ by elimination of neutral fragment $[(C_{16}H_{21}N_3O_7), (367.1380 \text{ Da})]$. The precursor ion $[M+Na]^+$ also eliminates the neutral radical molecule $[(C_7H_7O_2^\cdot), (123.0446 \text{ Da})]$ to form the radical cation product ion at m/z 429.0541. Then the product ion at m/z 429.0541 eliminates [a nitrogen molecule and a proton, $(29.0145 \text{ Da})]$ to achieve the product ion at m/z 400.0570. After that the product ion at m/z 400.0570 loses neutral molecule $[(C_4H_8O_3), (104.0473 \text{ Da})]$ to form the product ion at m/z 296.0292 which is assigned as $[^{2,6}X_2]^+$.

The proposed CID-MS/MS of sodiated precursor ion $[M+Na]^+$ fragmentation routes are tentatively shown in Scheme 5.5(b)

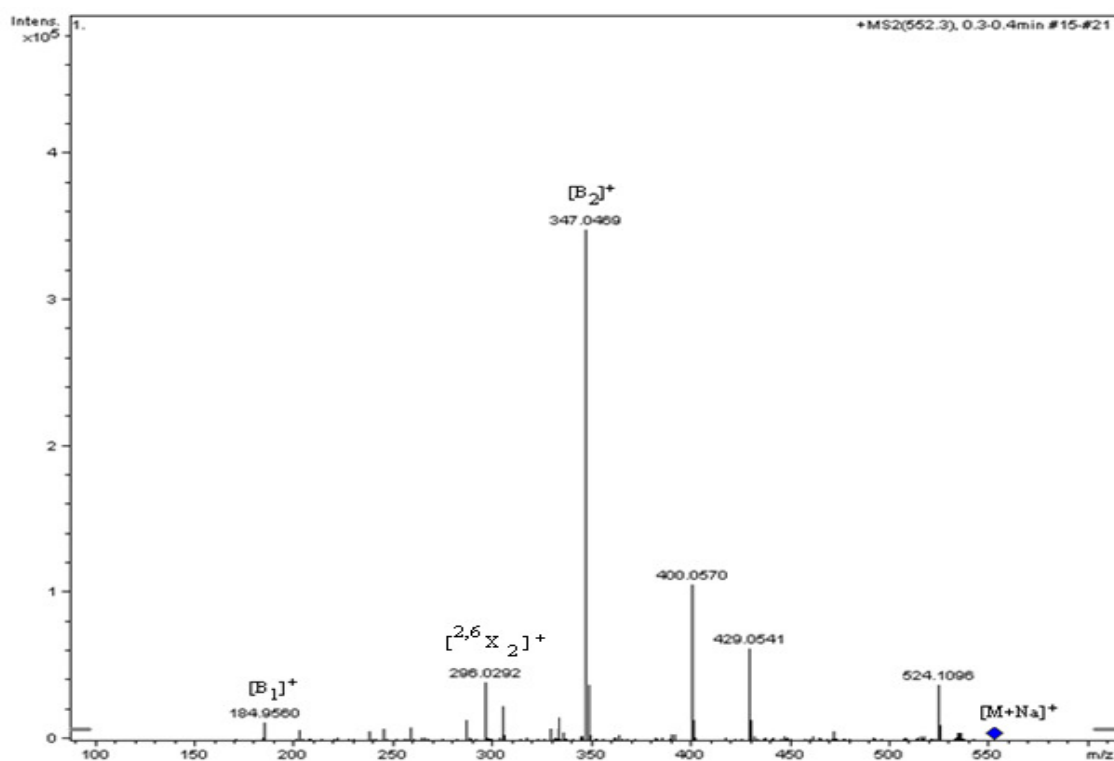
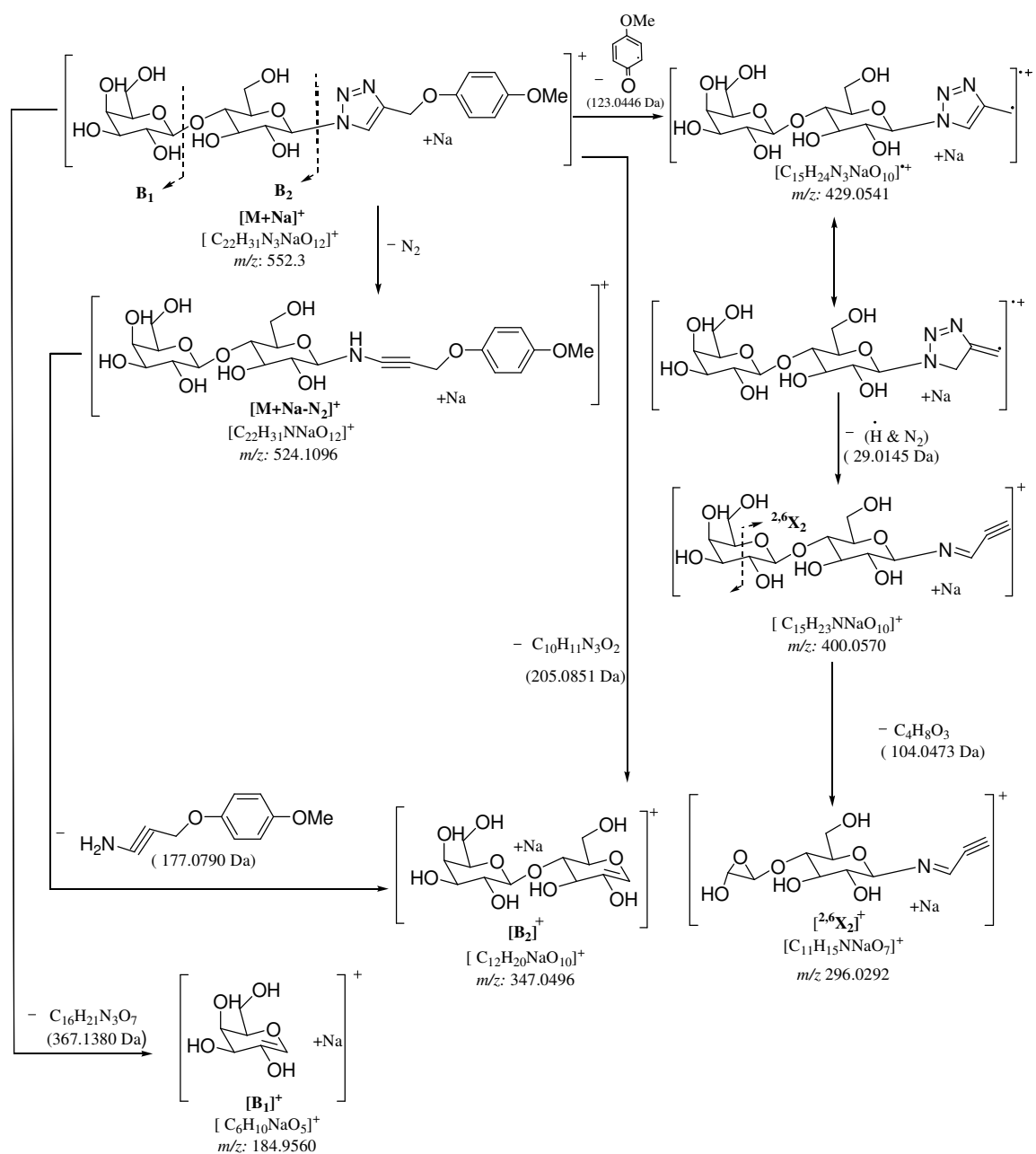


Figure 5.9(c): CID-QIT-MS/MS of the selected sodiated precursor ion $[M+Na]^+$ ion at m/z 552.0996 extracted from the dimethoxybenzenetriazole β -D-*N*-lactopyranosides derivatives (**5**)



Scheme 5.5(b): The tentative proposed fragmentation routes obtained during the low energy ESI-QIT-CID-MS/MS of the sodiated molecular ion $[M+Na]^+$ at m/z 552.0996 extracted from the dimethoxybenzenetriazole β -D-*N*-lactopyranosides derivatives (**5**)

5.3.11. Low energy ESI-QIT-CID-MS/MS of the protonated $[M+H]^+$ precursor ion at m/z 550.1177 selected from the methoxynaphthalene-triazole β -D-N-lactopyranosides derivatives (6)

The CID-MS/MS analysis of selected protonated precursor ion $[M+H]^+$ at m/z 550.1177 shown in Figure 5.11(b) was recorded with positive ion polarity by ESI. The afforded product ion at m/z 388.0519, 325.0000 and 225.9727 tentatively shown in Scheme 5.6(a)

The protonated precursor ion $[M+H]^+$ at m/z 550.3525 eliminates disaccharide moiety $[(C_{12}H_{20}O_{10}), (324.1056 \text{ Da})]$ to form the aglycone product ion at m/z 225.9727 which is assigned as $[Y_0]^+$. The precursor ion $[M+H]^+$ also eliminates anhydrous galactosyl moiety $[(C_6H_{10}O_5), (162.0528 \text{ Da})]$ to form the product ion at m/z 388.0519 which is assigned as $[Y_1]^+$. The precursor can also eliminate the aglycone moiety $[(C_{13}H_{11}N_3O), (225.0902 \text{ Da})]$ to form the disaccharide oxonium ion at m/z 325.0000.

The proposed CID-MS/MS of protonated precursor ion $[M+H]^+$ fragmentation routes are tentatively shown in Scheme 5.6(a)

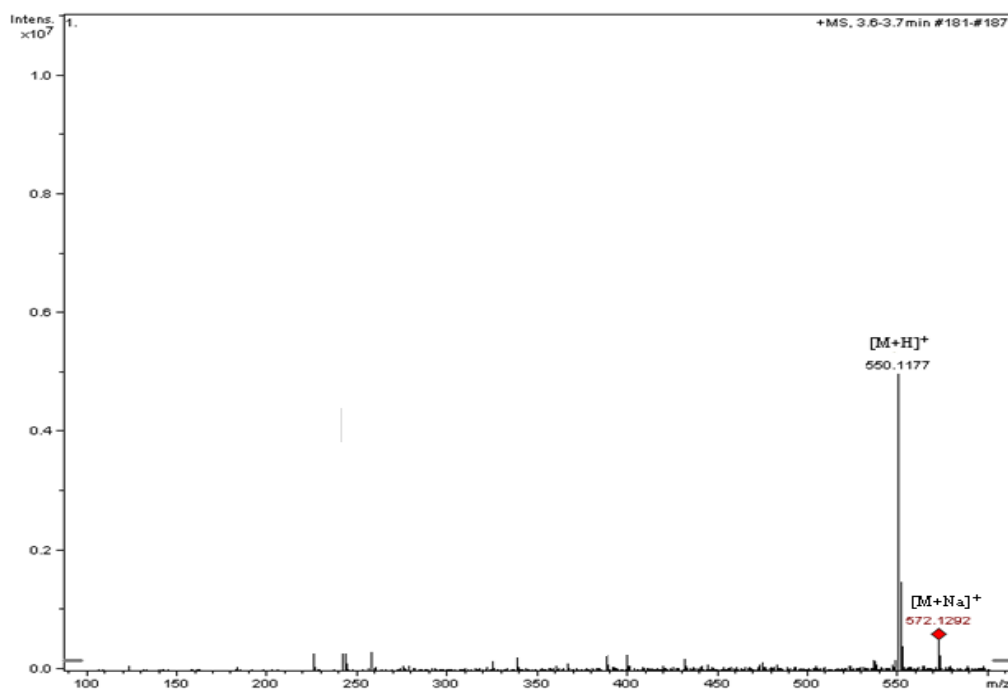


Figure 5.11(a): ESI-QIT-MS (+) of the methoxynaphthalene-triazole β -D-N-lactopyranosides derivatives (**6**)

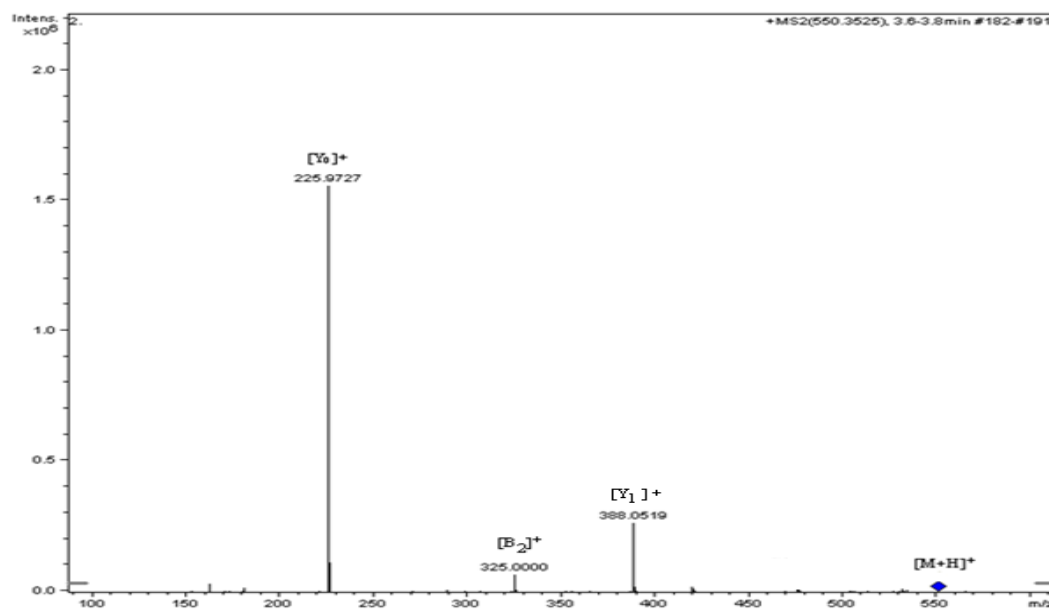
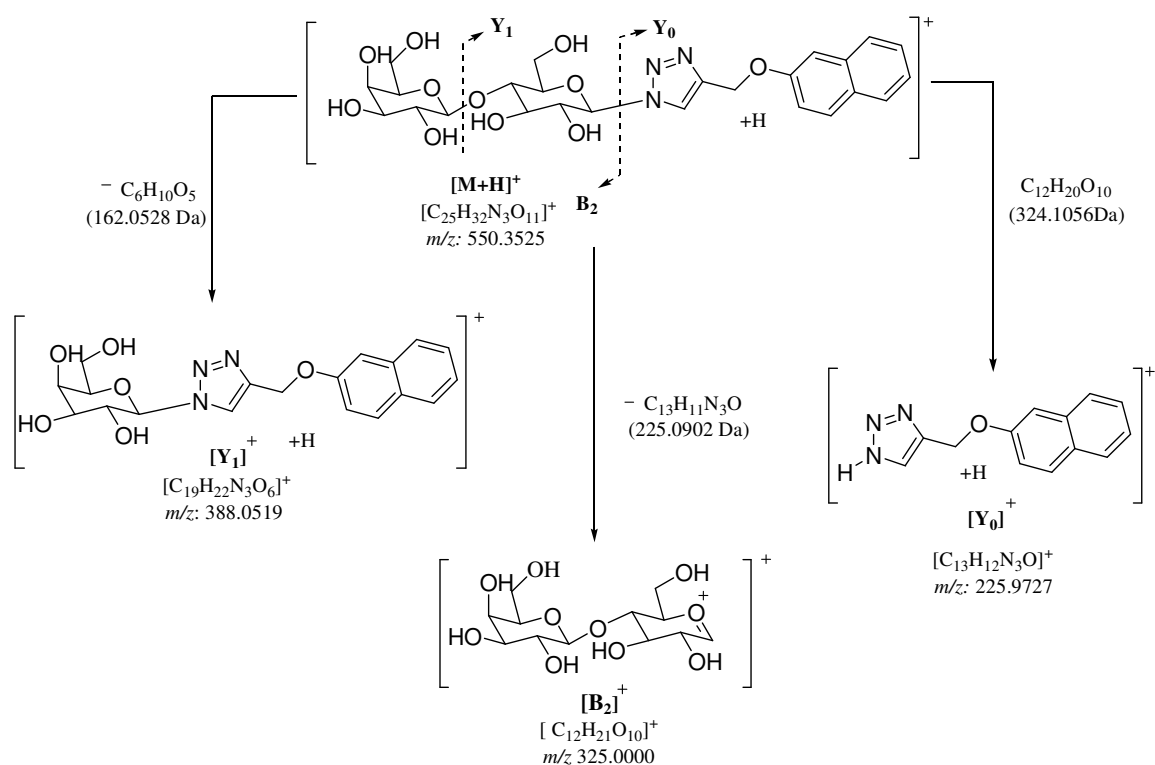


Figure 5.11(b): CID-QIT-MS/MS of the selected protonated precursor ion [M+H]⁺ at m/z 550.1177 extracted from the methoxynaphthalene-triazole β -D-N-lactopyranosides derivatives (**6**)



Scheme 5.6 (a): The tentative proposed fragmentation routes obtained during the low energy ESI-CID-QIT-MS/MS of the protonated molecule $[M+H]^+$ at m/z 550.1177 extracted from the methoxynaphthalene-triazole β -D-*N*-lactopyranosides derivatives (**6**)

5.3.12. Low energy ESI-QIT-CID-MS/MS of the sodiated precursor $[M+Na]^+$ at m/z 572.1292 selected from the methoxynaphthalene-triazole β -D-*N*-lactopyranosides derivatives (**6**)

The CID-MS/MS of the selected the sodiated molecular ion $[M+Na]^+$ at m/z 572.1292 extracted from the methoxynaphthalene-triazole β -D-*N*-lactopyranosides derivatives (**6**) shown in Figure 5.11(c) was recorded in the positive ion mode. The major product ions observed at m/z 544.0913, 400.0595, 347.0687, and 305.0136 tentatively shown in Scheme 5.12(b).

The precursor ion $[M+Na]^+$ at m/z 572.2784 eliminates nitrogen molecule to form the product ion at m/z 544.0913. The precursor ion $[M+Na]^+$ consecutively eliminates nitrogen molecule and naphthalen-2-ol to form the product ion at m/z 400.0595. The precursor goes glycosidic cleavage by elimination of aglycone moiety to form the product ion $[B_2]^+$ at m/z 347.0687. Then the precursor ion $[M+Na]^+$ undergoes ring fragmentation with the elimination of neutral fragment $[(C_{15}H_{13}N_3O_2), (267.1008 \text{ Da})]$ to form the product ion $[^{0,2}A_2]^+$ at m/z 305.0136.

The proposed CID-MS/MS of sodiated precursor ion $[M+Na]^+$ fragmentation routes are tentatively shown in Scheme 5.12(b)

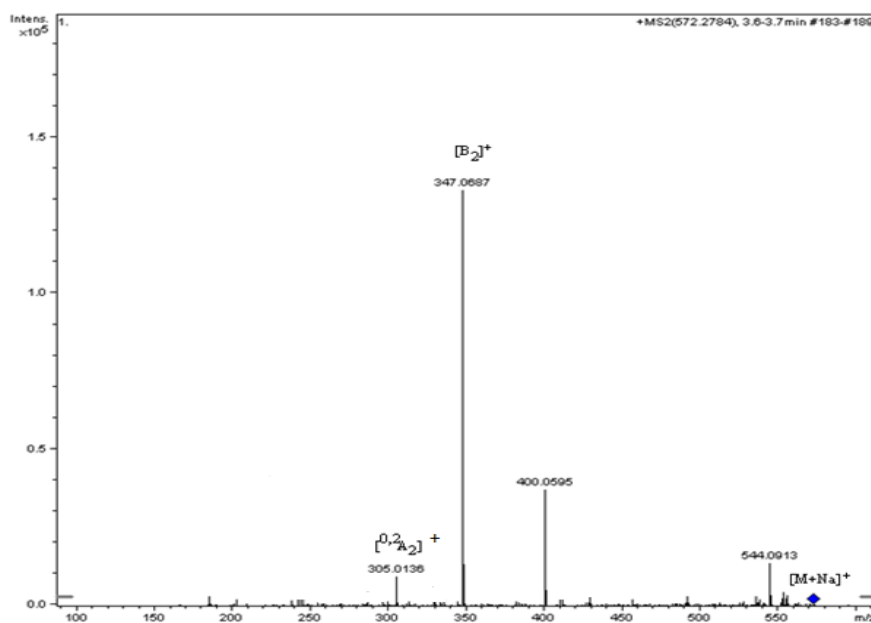
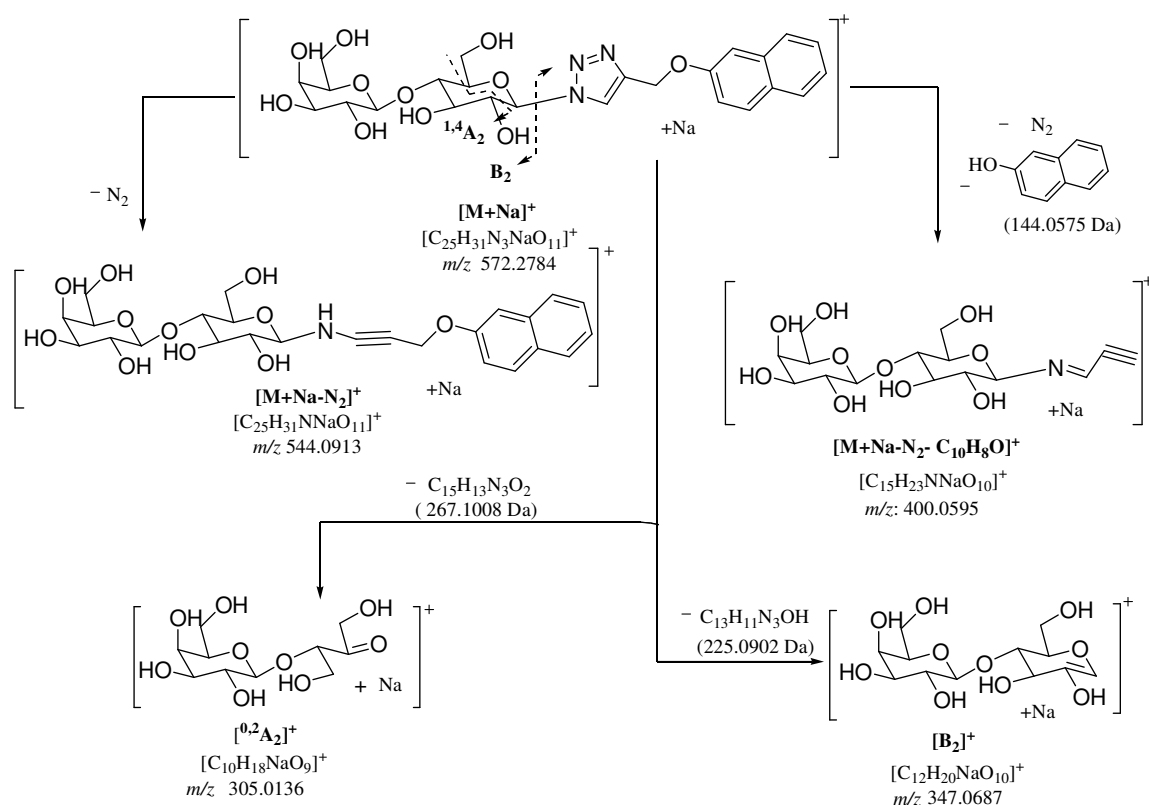


Figure 5.11(c): ESI-QIT-CID-MS/MS of the selected sodiated precursor ion $[M+Na]^+$ ion at m/z 572.1292 extracted from the methoxynaphthalene-triazole β -D-N-lactopyranosides derivatives (**6**)



Scheme 5.6(b): The tentatively proposed fragmentation routes obtained during the low energy ESI-QIT-CID-MS/MS of the sodiated molecule $[M+Na]^+$ at m/z 572.1292 extracted from the methoxynaphthalene-triazole β -D-*N*-lactopyranosides derivatives (**6**)

5.4. Conclusion

The capability of quadrupole ion-trap tandem mass spectrometric analyses of the protonated precursor molecules allowed for consecutive CID-fragmentations to be conducted and which were used for the structural elucidation of complex oligosaccharides.

In this study, the gas-phase fragmentations of the novel synthetic bivalent *N*-glycosides (**1-6**) using ESI-QIT-MS and QIT-CID-MS/MS analyses. The results presented in this chapter demonstrated that during ESI-QIT-MS and ESI-QIT-CID-MS/MS analyses, the bivalent *N*-glycosides follow universal CID-fragmentation routes for the carbohydrate moiety. These MS/MS investigations demonstrate without any doubts the full description of the proposed structures.

In addition, we have also studied the CID-MS/MS fragmentation behaviours of the sodiated molecular ion $[M+Na]^+$ were studied, which also gave us structural indices on the molecular structure of this series of compounds.

The following series of diagnostic product ions were observed in this work. Thus, the precursor protonated molecular ion isolated from methoxynaphthalene-substituted triazole β -D-*N*-galactopyranosides derivatives (**1**) afforded the only product ion found $[Y_0]^+$ at m/z 225.9706 and the sodiated precursor ion methoxynaphthalene-substituted triazole β -D-*N*-galactopyranosides derivatives (**1**) afforded the product ion at m/z 382.0698 and 237.9457. The protonated precursor ion isolated from ethyltriazole β -D-*N*-lactopyranosides derivative (**2**) afforded the product ions $[Y_1]^+$, radical cation product ion and $[M+H-H_2O]^+$ respectively at m/z 275.9904, 391.1729 (Elimination of N_2 and proton H^+) and 420.1551. The sodiated precursor molecular ion isolated from ethyltriazole β -D-*N*-lactopyranosides derivative (**2**) afforded the product ion $[Y_1]^+$, $[B_2]^+$, $[^{2,4}A_2]^+$, $[B_1]^+$, $[M+Na-N_2]^+$ respectively at m/z 298.0487, 347.0420, 245.0049, 184.9448 and 432.0714. The protonated precursor molecular ion isolated from butyltriazole β -D-*N*-lactopyranosides derivatives (**3**) afforded the product ion $[Y_1]^+$, $[Y_0]^+$ and a radical cation product ion at respectively m/z 304.0386, 419.2309, 419.2309 and 142.0236. The

sodiated precursor molecular ion isolated from butyltriazole β -D-*N*-lactopyranosides derivatives (**3**) afforded $[B_2]^+$, $[^{0,2}A_2]^+$, $[^{2,4}A_2]^+$, $[M+Na-N_2]^+$ respectively at m/z 347.0654, 305.0571, 245.0253, and 460.1280. The protonated precursor molecular ion isolated from anisoletriazole β -D-*N*-lactopyranosides derivatives (**4**) gave $[Y_1]^+$, $[Y_0]^+$ respectively at m/z 337.9837, 175.9751. The sodiated precursor molecular ion isolated from anisoletriazole β -D-*N*-lactopyranosides derivatives (**4**) gave $[B_1]^+$, $[B_2]^+$, $[^{0,2}A_2]^+$, $[^{2,4}A_2]^+$, $[^{0,3}X_2]^+$ and $[M+Na-N_2]^+$ respectively at m/z 184.9219, 347.0414, 304.9969, 244.9483, 400.0571, and 494.0901.

The protonated precursor molecular ion isolated from the dimethoxybenzenetriazole β -D-*N*-lactopyranosides derivatives (**5**) gave $[B_2]^+$, $[Y_0]^+$, $[Y_1]^+$ respectively at m/z 324.9960, 205.9571 and 368.0100. The sodiated precursor molecule isolated from the dimethoxybenzenetriazole β -D-*N*-lactopyranosides derivatives (**5**) gave $[B_1]^+$, radical cation product ions, $[B_2]^+$, $[^{2,6}X_2]^+$ and $[M+Na-N_2]^+$ respectively at m/z are 184.9560, 429.0541, 347.0496, 296.0292 and 524.1096. The protonated precursor molecular ion isolated from methoxynaphthalene-substituted triazole β -D-*N*-lactopyranosides derivatives (**6**) gave $[B_2]^+$, $[Y_0]^+$, $[Y_1]^+$ respectively at m/z 325.0000, 225.9727 and 388.0519. The sodiated precursor molecular ion isolated from methoxy-naphthalene substituted triazole β -D-*N*-lactopyranosides derivatives (**6**) $[M+Na-N_2-C_{10}H_8O]^+$, $[^{0,2}A_2]^+$, $[B_2]^+$, $[M+Na-N_2]^+$ respectively at m/z 400.0595, 305.0136, 347.0687 and 544.0913.

In general, it was observed that the CID-MS/MS fragmentation routes of the six precursor protonated molecules obtained from the bivalent *N*-glycosides (**1-6**) afforded a

series of product ions formed essentially by similar routes. As expected, it was noticed that as the collision energy of the CID-MS/MS was increased, an enhancement in the gas-phase fragmentation was produced.

The genesis of the MS/MS fragmentations and the structural identities of the product ions were also determined. This series of CID-MS/MS fragmentation routes can be used to easily predict the gas-phase fragmentation patterns of new compounds with the same general backbone structure.

CHAPTER 6: STRUCTURAL ELUCIDATION OF CIMV WHEAT LIGNIN USING MALDI-TOF/TOF-MS AND HIGH-ENERGY CID-MS/MS ANALYSIS.

6.1. Introduction

Anselme Payen who first recognized the composite nature of wood in 1838 observed that after treatment of wood with nitric acid to separate cellulose, he obtained left over a fibrous material. The isolated fibrous material had higher carbon content than the cellulose. He described this carbon-rich substance that embedded the cellulose in the wood, as an encrusting material.^[150] The term lignin, was introduced by Schulze in 1865 and it is now recognized to be one of the key components of the cell wall of all vascular plants.^[151] In 1907, Klason suggested that lignin is a high molecular weight substance consisting of coniferyl alcohol units joined together by ether linkages. Thus, the age of modern lignin chemistry began.^[152]

As a part of the cell wall, lignin does not just act as “encrusting materials”. To a certain extent, lignin performs many functions essential for the life of vascular plants. Lignin provides mechanical strength and structural support, particularly in the case of trees, to the growing plant. Lignin protects the permeation of water across the cell wall, thus facilitating vertical conduction of water, nutrients and metabolites in the xylem tissue. Lignified tissues effectively resist attack by microorganisms by impeding penetration of lignin and comprises from 15% to 36 % of the total dry weight of wood.

[151]

The types of subunits in lignin macromolecule are classified based on their monolignol origin, i.e., *p*-hydroxyphenyl (H) units arising from primarily *p*-coumaryl alcohol, guaiacyl (G) units from coniferyl alcohol, and syringyl (S) units from sinapyl

alcohol. The subunit composition of lignin varies with the content of three units.

Three kinds of lignins are well-differentiated: gymnosperm lignin contains mainly of G-units with a small amount of H-unit; both S-units and G-units are about the same components of angiosperm lignin; and significant amounts of all three units are contained in grass lignin.^[57] The difference of the structure in lignins as well comes from the frequency of the interlinkages in the lignin macromolecule whereas the general existing interlinkages in lignin are fairly similar in all plants. Hardwood lignin contains relative more β -O-4' and less 5-5' and β -5' interlinkages than softwood lignin, though generally the most abundant linkage in lignin is β -O-4'. The frequency of a β -O-4' interlinkage is approximately 45-50% of the phenylpropane units in softwood lignin, while approximately 60-85% phenylpropane units in hardwood lignin.^[153]

6.2. Isolation of Lignin

Separation of lignin from wood in a chemically unaltered form is one of the barriers to elucidation of the structure of lignin. Lignins in plant tissues are not extractable by organic solvents and isolation of lignin free from carbohydrates is not possible. Thus, the separation of lignin from carbohydrates is a tedious task, which can be achieved by chemical or physical treatment before lignin extraction. Traditionally, the acidic extracted lignin preparations were exclusively used for chemical characterization.^{[154], [155]} Brauns lignin, Milled Wood Lignin (MWL) and Cellulolytic Enzyme Lignin (CEL) were thought to be the preparations contained less chemical modification than from acid preparations.^[155]

6.3. Characterization of the structure of lignin by degradation methods

Wet chemistry techniques can be differentiated by functional group analysis (OMe, total OH, phenolic OH, carbonyl group, carboxyl groups) and degradation methods. The major advantage of degradation techniques is the possibility of analyzing lignin without its isolation. The relative accuracy of degradation techniques is pretty high. The general degradation methods include Nitrobenzene Oxidation (NBO)^[151], Thioacidolysis (TA)^[156], and derivative followed by reductive cleavage (DFRC)^[157], Permanganate Oxidation (PO)^[153] and Ozonolysis.^[158] We will not discuss these methods in my thesis

6.4. Pyrolysis-gas chromatography- mass spectrometry (Py-GC-MS)

Pyrolysis is designed to thermally degrade polymers into small fragments, which are then separated by gas chromatography and identified by MS.^[159] Pyrolysis-gas chromatography-mass spectrometry (Py-GC-MS) deserves mention as an important technique for characterizing polymeric samples. This technique involves fragmentation of the sample in an inert gas at high temperature, after which the fragments are separated in a gas chromatographic column and identified with a mass spectrometer. The analysis requires a minimal sample amount and it can be accomplished directly without an isolation procedure. The method is destructive, but only about 5-50 µg of sample is required. The technique allows the determination of *p*-hydroxyphenyl, guaiacyl, and syringyl structures as well as some other characteristic structures of lignin polymer.^[160],^[161],^[162] Information on the chemical structure of residual lignin is obtainable directly from pulp samples. The acquired pyrogram constitutes a “fingerprint” of the starting

macromolecules to give information about the relative amount of its monomeric components.^[163] It is well established that analytical pyrolysis can be used to quantitatively assess the content of carbohydrates^[164] and lignin^[165] in wood, and the lignin composition^{[160], [166]} of the wood.

Lignin can be thermally degraded by pyrolysis, which cleave the ether and certain C–C' interunit linkages, to produce a mixture of relatively simple phenols.^{[167], [168]} Given that the released methoxylated phenol monomers retain their original substitution patterns, it is possible to identify components from H, G and S lignin units in which the lignin propanoid side chains have been split off completely, shortened to one or two carbons, or fully conserved. New double bonds are also created in the side chains through pyrolytic dehydrogenation.

Although it is possible to obtain accurate quantification of monomeric lignin composition by Py-GC/MS, this technique is limited for the analysis of polar pyrolyzates generated from nitrogenous material, as these are associated with the secondary reactions during the pyrolysis process.^[169]

6.5. Mass Spectrometric analyses of lignin with different ionization sources

Mass spectrometry (MS), which offers advantages in terms of speed, specificity, and sensitivity, has revealed to be a very powerful technique in the structural elucidation of lignins. Electron ionization and chemical ionization-mass spectrometry have been used for the study and characterization of the derivatized lignol monomer constituents, released by either reductive cleavage or by pyrolysis. In this case, only the monomeric and, to a

small extent, dimeric products were identified by comparison of gas chromatographic retention times and mass spectra using authentic samples.^[170]

In the last few decades, hardly any reviews dealing with MS use in the structural elucidation of chemically degraded lignins have been published. These MS methods dealt with thermal degradation of lignins including the well-known pyrolysis method, which was (and still is) the method of choice for practicing lignin chemists.^[170]

Reale *et al.* have described in an elegant review article the uses of mass spectrometry, obtained with different ionization sources, for the study of lignin degradation products and the authors have also attempted to characterise the whole lignin macromolecule.^[170] The different ionization methods described in that review article covered respectively: chemical ionization (CI-MS), photoionization (PI-MS), single-photon ionization (SPI-MS), molecular-beam (MB-MS), fast-atom bombardment (FAB-MS) and resonance-enhanced multi-photon ionization (REMPI-MS) methods.^[170]

Likewise, the recent development in the last decades of new ionization techniques such as atmospheric pressure ionization, which includes electrospray ionization ESI-MS, atmospheric pressure chemical ionization (APCI) and atmospheric pressure photoionization (APPI) together with matrix-assisted laser desorption/ionization MALDI-MS have provided new possibilities to also analyze the lignin oligomers.^[170]

6.6 Atmospheric pressure photoionization mass spectrometry and low-energy CID-MS/MS of CIMV lignin measured with a QqTOF-MS/MS instrument

Previously Banoub *et al.* shown that ESI-, APCI-, APPI-MS could be used to characterization the molecular structure of wheat straw lignin oligomers. They also used low-energy collision-induced dissociation tandem mass spectrometry (CID-MS/MS) of various lignin precursor ions to establish the oligolignin of the diagnostic product ions which enabled the determination of the exact molecular structures and arrangement of the selected 57 different related ionic species.^{[171], [172]} Unfortunately, comparisons of dissociation behaviours of this series of unknown ions with those of commercial, synthesized standards and/or any reported structure of biologically-isolated lignin compounds, was impossible. Thus, the correlations of MS/MS spectra as these series of lignin compounds obtained from the technical wheat straw lignin, are indeed novel.

We have decided in this thesis to try to analyse the wheat straw lignin by MALDI-TOF/TOF-MS and with high-energy collision MALDI-TOF/TOF-CID-MS/MS in order to compare the results with those obtained by ESI-QqTOF-MS and CID-MS/MS and to observe the differences in the CID-fragmentation routes of this series of precursor ions obtained by MALDI.

6.7. MALDI-TOF/TOF-MS analysis of the Straw lignin

The MALDI-TOF/TOF-MS was recorded in the positive ion mode using α -cyano-4-hydroxycinnamic acid matrix and we observed a series of ions which resembled the series obtained by APPI-QqTOF-MS [Figure (6.4a-6.4b)]. The MALDI-TOF/TOF-MS afforded a complex series of ions appearing at every m/z unit of the recorded MS measured scale. We have attempted to identify a small number of these ions, which masses corresponded to same masses that were found for the APPI-QqTOF-MS recorded with the Qstar QqTOF-MS hybrid instrument. These series of ion was identified as follows: The protonated $[M+H]^+$ [4-hydroxy-(7 \rightarrow 4')-coniferyl ether (8 \rightarrow 5')-(3'-methoxybenzene)] ion (**1**) at m/z 331.1173; The precursor [4- hydroxyl-3-methoxy-(7 \rightarrow 4')-coniferyl ether (8 \rightarrow 5')-(1'-methylelene 3'-methoxybenzene)] ion $[M]^+$ at m/z 341.1011 (**2**); The phenylcoumaran derivatives ion $[M]^+$ (**3**) at m/z 369.1310; The protonated phenylcoumaran derivatives ion $[M+H]^+$ (**4**) at m/z 403.1349; The protonated trimeric precursor phenylcoumaran derivatives ion (**5**) at m/z 523.1926; The protonated $[M+H]^+$ trimeric phenylcoumaran derivative ion (**6**) at m/z 539.1888; The protonated $[M+H]^+$ tetrameric phenylcoumaran derivative ion (**7**) at m/z 655.2411; and The protonated ions $[M+H]^+$ phenylcoumaran derivatives ion (**8**) at m/z 671.2019; The phenylcoumaran derivative ion $[M]^+$ (**9**) at m/z 491.1652. The series of characteristic ions are listed in Table 6.A.

Table 6: Characteristic ions obtained from the MALDI-TOF/TOF-MS analysis of the wheat straw lignin

Characteristic ions	Cdp	Calculated (<i>m/z</i>)	Observed (<i>m/z</i>)	Difference (in ppm)
[C ₁₉ H ₁₇ O ₄] ⁺	1	309.1127	309.1130	13
[C ₁₈ H ₁₉ O ₆] ⁺	2	331.1182	331.1173	3
[C ₁₉ H ₁₇ O ₆] ⁺	3	341.1025	341.1011	4
[C ₁₉ H ₁₉ O ₆] ⁺	4	343.1182	343.1155	8
[C ₁₉ H ₁₅ O ₆] ⁺	5	351.0869	351.0851	5
[C ₂₀ H ₁₇ O ₆] ⁺	6	353.1025	353.099	10
[C ₂₀ H ₂₀ O ₈] ⁺	7	364.1158	364.1125	9
[C ₁₈ H ₂₁ O ₆] ⁺	8	369.1338	369.1310	8
[C ₂₁ H ₂₃ O ₈] ⁺	9	403.1393	403.1349	11
[C ₂₁ H ₂₁ O ₇] ⁺	10	433.1287	433.1322	8
[C ₂₈ H ₂₇ O ₈] ⁺	11	491.1706	491.1672	7
[C ₂₈ H ₂₇ O ₈] ⁺	12	493.1862	493.1921	12
[C ₂₈ H ₂₉ O ₉] ⁺	13	509.1890	509.1814	15
[C ₂₉ H ₃₁ O ₉] ⁺	14	521.1812	521.1869	11
[C ₂₉ H ₂₇ O ₉] ⁺	15	523.1968	523.1926	8
[C ₂₅ H ₃₁ O ₁₀] ⁺	16	539.1917	539.1888	5
[C ₃₀ H ₃₁ O ₁₀] ⁺	17	551.1917	551.1867	9
[C ₃₀ H ₃₃ O ₁₀] ⁺	18	553.2074	553.214	12
[C ₃₁ H ₃₁ O ₁₁] ⁺	19	579.1866	579.193	11
[C ₃₁ H ₃₃ O ₁₁] ⁺	20	581.2023	581.2093	12
[C ₃₇ H ₃₅ O ₈] ⁺	21	607.2332	607.2411	13
[C ₃₇ H ₃₃ O ₁₀] ⁺	22	637.2074	637.2119	7
[C ₃₈ H ₃₉ O ₁₀] ⁺	23	655.2543	655.2411	16

$[\text{C}_{37}\text{H}_{35}\text{O}_{12}]^+$	24	671.2129	671.2019	20
$[\text{C}_{38}\text{H}_{37}\text{O}_{12}]^+$	25	685.2285	685.2333	7
$[\text{C}_{39}\text{H}_{39}\text{O}_{13}]^+$	26	715.2547	715.2604	8
$[\text{C}_{40}\text{H}_{41}\text{O}_{13}]^+$	27	729.2848	729.2943	13
$[\text{C}_{41}\text{H}_{41}\text{O}_{14}]^+$	28	757.2496	757.2405	12
$[\text{C}_{46}\text{H}_{45}\text{O}_{12}]^+$	29	789.2911	789.2982	9
$[\text{C}_{47}\text{H}_{43}\text{O}_{14}]^+$	30	831.2653	831.2553	12

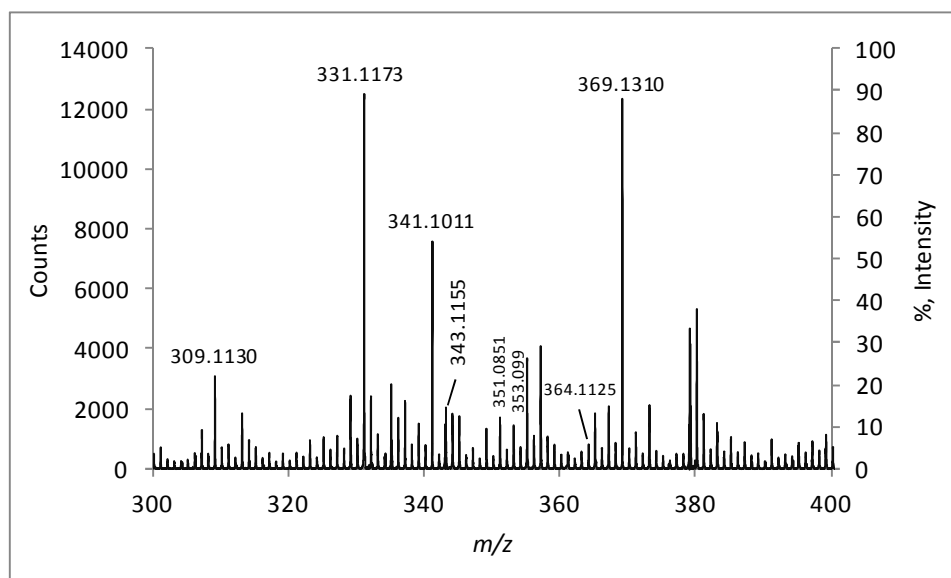


Figure 6.4 (a): Characteristic ions obtained from the MALDI-TOF/TOF-MS analysis of the wheat straw lignin recorded in the positive ion mode scanning m/z 300–400

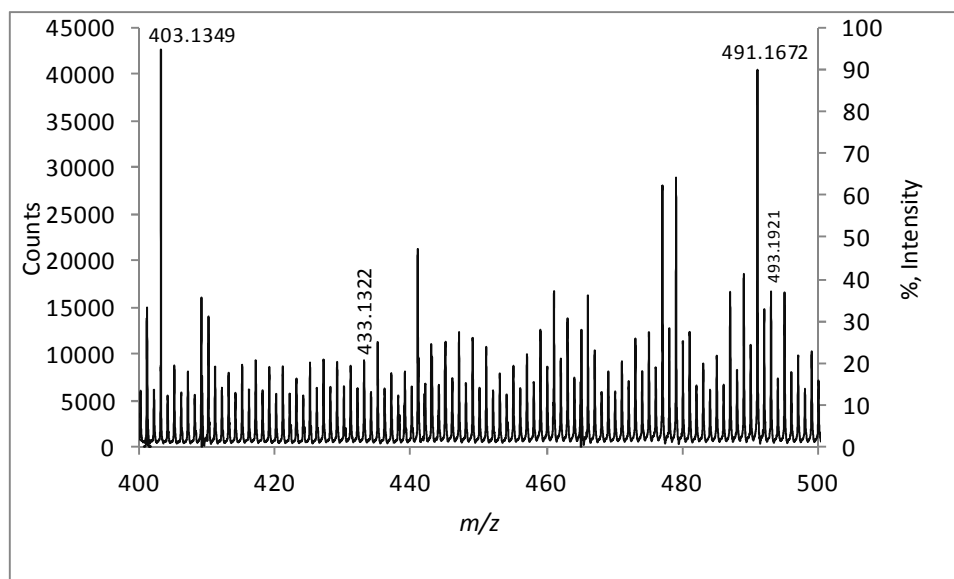


Figure 6.4(b): Characteristic ions obtained from the MALDI-TOF/TOF-MS analysis of the wheat straw lignin recorded in the positive ion mode scanning m/z 400–500

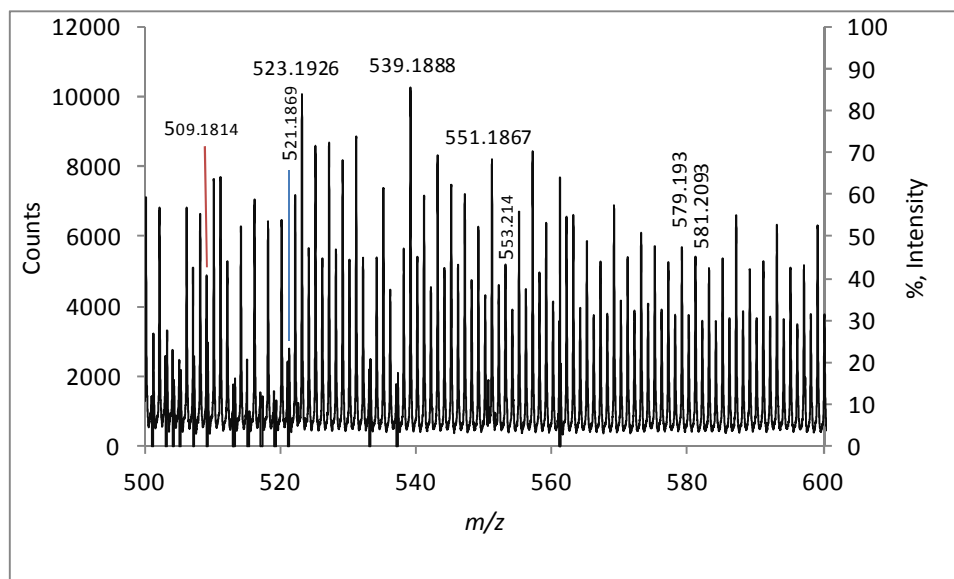


Figure 6.4(c): Characteristic ions obtained from the MALDI-TOF/TOF-MS analysis of the wheat straw lignin recorded in the positive ion mode scanning m/z 500 – 600

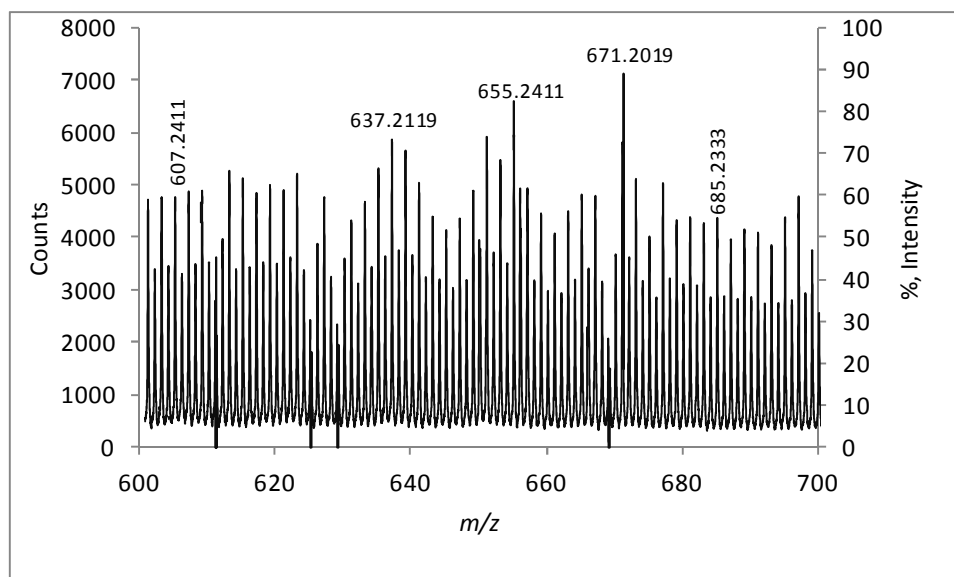


Figure 6.4(d): Characteristic ions obtained from the MALDI-TOF/TOF-MS analysis of the wheat straw lignin recorded in the positive ion mode scanning m/z 600–700.

As this stage, we here identified with a great confidence nine ions, whose tentative structure are shown in Figure 6.5(c)

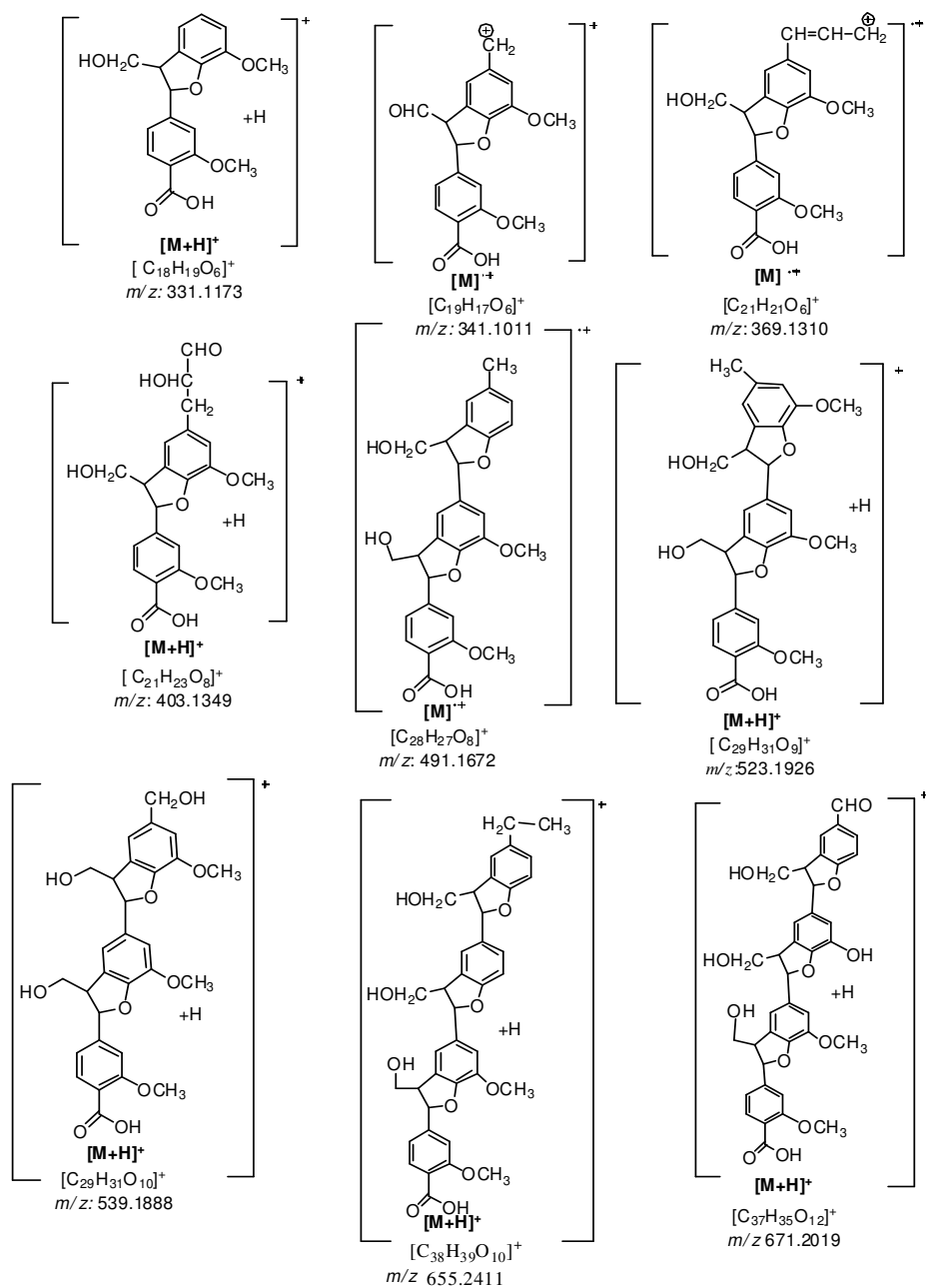


Figure 6.5: (c) Tentative structures of the nine different ions isolated obtained from the wheat straw lignin, recorded by positive mode by MALDI-TOF/TOF-MS.

To ascertain the correct structures of this series of ions, we have recorded the high-energy collision dissociation tandem mass spectrometry analyses of these various ions as described in the following section.

6.9. High energy MALDI-CID-TOF/TOF-MS/MS have been used to ascertain the molecular structure of these ions.

We have postulated that by using high-energy CID the precursor ions will promote and enhance the primary fragmentations of the lignin molecule, resulting in CID spectra containing more product ions in comparison to ESI-QqTOF-CID-MS/MS analysis which will help us identifying these species.

6.9.1. High energy MALDI-TOF/TOF-CID-MS/MS of the protonated $[M+H]^+$ [4-hydroxy-(7→4')-coniferyl ether (8→5')-(3' methoxybenzene)] ion (*I*) at m/z 331.1173

The product ion scan of the selected protonated molecular ion $[M+H]^+$ at m/z 331.1173 afforded product ions at m/z 329.0986, 327.0787, 316.0925, 287.1258, 270.0878, 241.0843, 223.0737, 203.0698, 179.0688, 153.041, and 121.028. [Figure 6.9.1]. The structural identities of these product ions are indicated in Table 6.A and their genesis are tentatively shown in Scheme 6.1. This series of product ion contained the coumaran five member ring furan ring of the coumaran unit which is linked by the (C₈→C_{5'}) covalent bond and the (C₇→C_{4'}) ether linkage formed between the first and second coniferyl unit .

Thus, the protonated precursor ion $[M+H]^+$ (*I*) at m/z 331.1222 loses hydrogen molecule assigned as $[M+H-H_2]^+$ to form the product ion *Ia* at m/z 329.0986. It appears

that this product ion **Ia** also loses once more hydrogen molecule again to form the product ion **Ib** at m/z 327.0787. The product ion also **Ib** can be formed from the precursor ion by elimination of two molecules of hydrogen assigned as $[M+H-2H_2]^+$. The product ion **Ic** at m/z 316.0925 is formed by elimination of the methyl radical from the precursor ion $[M+H]^+$ at m/z 331.1222. The product ion **Id** at m/z 287.1258 is formed with the elimination of CO_2 from the precursor ion $[M+H]^+$. In addition, the precursor ion $[M+H]^+$ can also lose consecutively both formaldehyde molecule and methoxyl radical to form the product ion **Ie** at m/z 270.0878. The precursor ion $[M+H]^+$ can also lose three molecules of formaldehyde to form the product ion **If** at m/z 241.0843. This latter product ion **If** loses water to form the product ion **Ig** at m/z 223.0737. The product ion **Ig** can be formed from the precursor ion by the consecutive elimination of two molecules of formaldehyde and water as shown in Scheme 6.1. The product ion **Ih** at m/z 203.0698 is formed from the precursor ion $[M+H]^+$ by elimination of the neutral fragment which occur by elimination of $[(C_6H_8O_3), (128.0473 \text{ Da})]$ by the cleavage of C_1-C_2 and C_5-C_6 of the first coniferyl unit. The product ion **Ii** at m/z 179.0688 is formed from the precursor by elimination of the first coniferyl unit $[(C_8H_8O_3), (152.0473 \text{ Da})]$. The product ion **Ij** at m/z 153.041 is formed from the precursor ion by elimination of the second coniferyl unit $[(C_{10}H_{10}O_3), (178.0630 \text{ Da})]$. Finally, The product ion **Ik** at m/z 121.028 is formed from the precursor ion by the consecutively elimination of second coniferyl unit $[(C_{10}H_{12}O_3), (180.0786 \text{ Da})]$ and a molecule of formaldehyde.

The high energy MALDI-TOF/TOF-CID-MS/MS fragmentation routes are tentatively proposed shown in Scheme 6.1

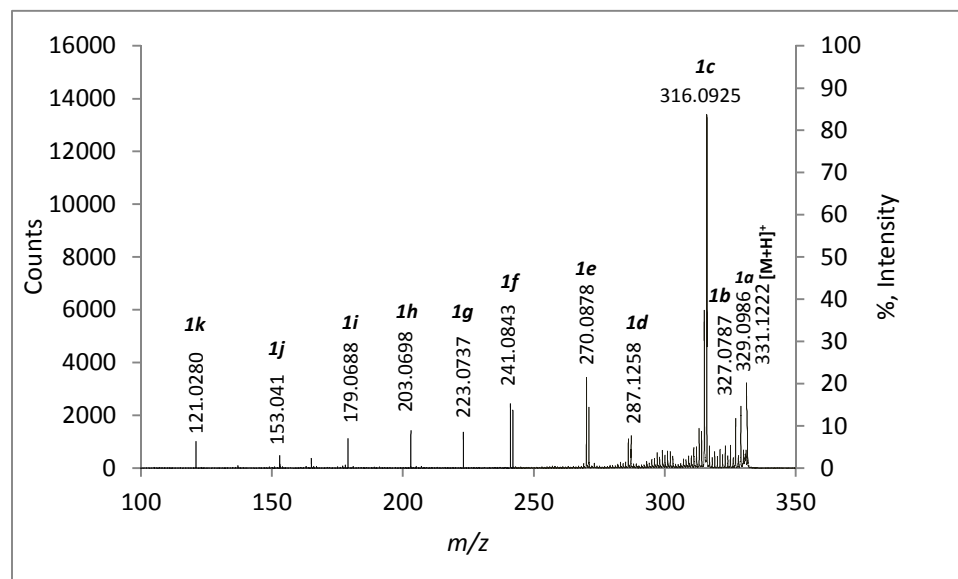
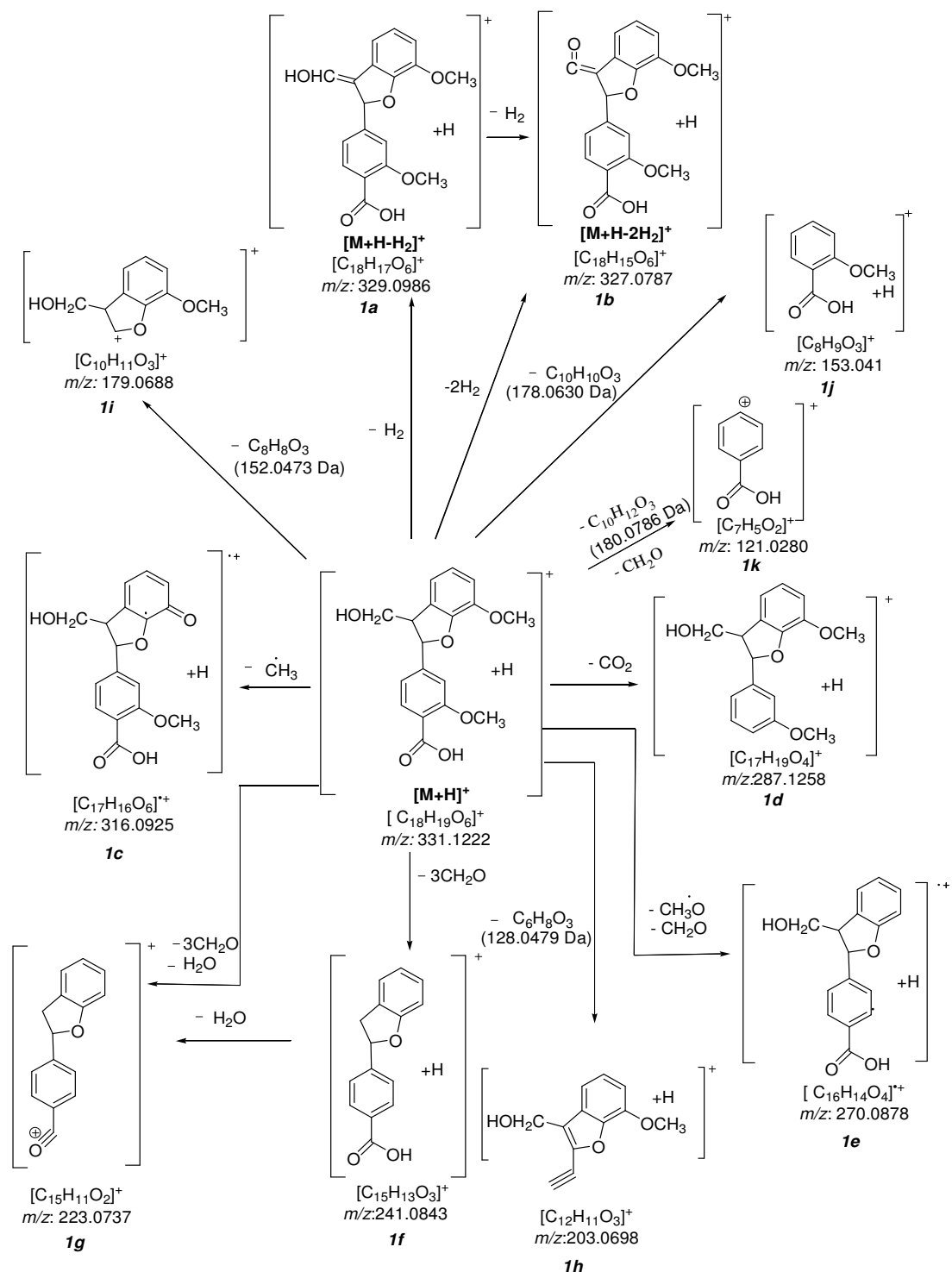


Figure 6.9.1: High Energy MALDI-TOF/TOF-CID-MS/MS of the selected protonated $[M+H]^+$ phenylcoumaran derivatives precursor ion (**I**) at m/z 331.1173



Scheme 6.1: The tentatively proposed fragmentation routes obtained during MALDI-TOF/TOF high energy CID-MS/MS of the protonated $[M+H]^+$ phenylcoumaran derivatives precursor ion (**I**) at m/z 331.1173

Table 6.A: Characteristic product ions observed in the high energy MALDI-TOF/TOF-CID-MS/MS of the protonated $[M+H]^+$ phenylcoumaran derivatives precursor ion (**1**) at m/z 331.1173

Characteristic ions	Calculated mass (m/z)	Observed mass (m/z)	Difference (in ppm)
$[C_{18}H_{19}O_6]^+$	331.1182	331.1222	12
$[C_{18}H_{17}O_6]^+$	329.1025	329.0986	12
$[C_{18}H_{15}O_6]^+$	327.0869	327.0787	10
$[C_{17}H_{16}O_6]^{++}$	316.0947	316.0925	7
$[C_{17}H_{19}O_4]^+$	287.1283	287.1258	9
$[C_{16}H_{14}O_4]^{++}$	270.0892	270.0878	5
$[C_{15}H_{13}O_3]^+$	241.0865	241.0843	9
$[C_{15}H_{11}O_2]^+$	223.0759	223.0737	10
$[C_{12}H_{11}O_3]^+$	203.0708	203.0698	5
$[C_{10}H_{11}O_3]^+$	179.0708	179.0688	11
$[C_8H_9O_3]^+$	153.0552	153.041	7
$[C_7H_5O_2]^+$	121.0290	121.0280	8

6.9.2. High energy MALDI-TOF/TOF-CID-MS/MS of the precursor [4-hydroxyl-3-methoxy-(7→4')-coniferyl ether (8→5')-(1'methylelene 3'methoxybenzene)] ion [M]⁺ or phenylcoumaran derivatives ion (2) at *m/z* 341.1011.

The product ion scan of the selected molecular ion [M]⁺ at *m/z* 341.1011 afforded a series of product ions at *m/z* 331.1142, 253.0883, 231.0467, 209.0951, 190.0619, 177.0570, 165.0544, 137.0247, and 123.0455 [Figure 6.9.2]. The structural identities of the major product ions are indicated in Table 6.B and their genesis are tentatively shown in Scheme 6. 2.

The precursor ion [M]⁺ phenylcoumaran derivative ion (2) at *m/z* 341.1049 loses methylene group followed by in-situ reduction to form the product ion **2a** at *m/z* 331.1142. This latter product ion **2a** eliminate a molecule of methane and a neutral fragment [(C₁₀H₁₀O₃, (178.0630 Da)] to give the product ion **2h** at *m/z* 137.0247. The product ion **2a** can also eliminate a neutral fragment [(C₉H₁₀O₃, (166.0635 Da)] to form the product ion **2g** at *m/z* 165.0544. This product ion **2g** can also be created from direct elimination of a neutral fragment [(C₁₀H₈O₃), (176.0473 Da)] from the precursor ion. The product ion **2a** eliminates two molecules of formaldehyde and one molecule of water to afford the product ion **2b** at *m/z* 253.0883. The product ion **2b** can also be directly formed from the precursor ion [M]⁺ by elimination of formaldehyde followed by reduction. The product ion **2b** can eliminate a benzyne molecule to form the product ion **2f** at *m/z* 177.0570. The product ion **2c** at *m/z* 231.0467 can be formed from the precursor ion [M]⁺ by elimination of two molecules of methanol , one molecule of formaldehyde and one molecule of water followed partially reduction. The radical cation product ion **2e** at *m/z*

190.0619 is formed from the precursor ion by the elimination of neutral radical fragment $[(C_8H_7O_3)^\cdot]$, (151.0395 Da). The product ion **2i** at m/z 123.0455 is formed from the precursor ion by elimination of formaldehyde and a neutral fragment $[(C_{11}H_{10}O_3)]$, (190.0630 Da) followed partial reduction from the precursor ion $[M]^{+\cdot}$. The product ion **2d** at m/z 209.0951 is formed simultaneously reduction and elimination of three molecules of formaldehyde and one molecule of carbon dioxide.

The proposed high energy MALDI-CID-MS/MS fragmentation routes are tentatively shown in Scheme 6.2

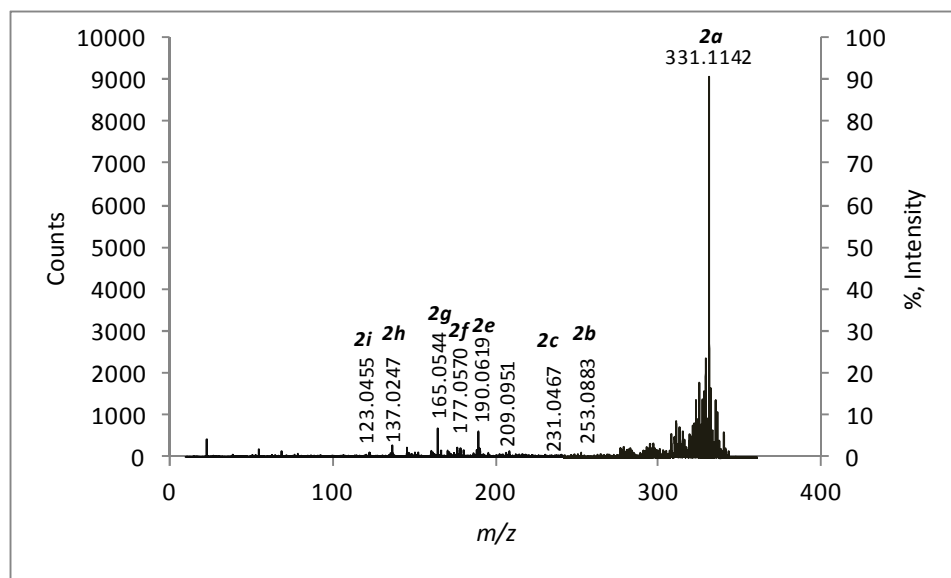
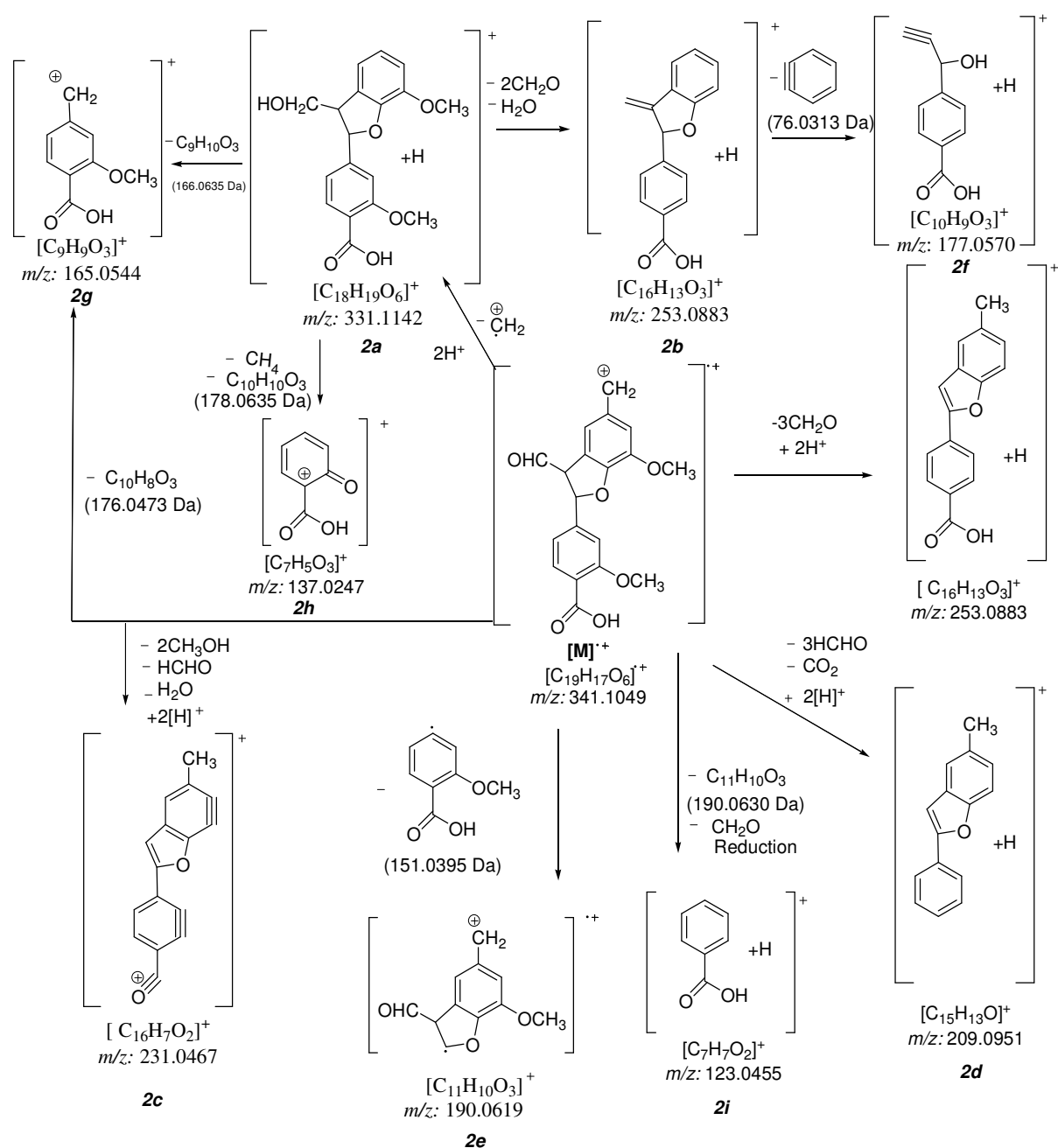


Figure 6.9.2: High energy MALDI-TOF/TOF-CID-MS/MS of the selected precursor ion $[M]^{+\cdot}$ phenylcoumaran derivatives ion (**2**) at m/z 341.1011.



Scheme 6.2: The tentatively proposed fragmentation routes obtained during MALDI-TOF/TOF high energy CID-MS/MS of the molecular ion $[M]^+$ phenylcoumaran derivatives ion (**2**) at m/z 341.1011

Table 6.B: Characteristic product ions observed in the high energy MALDI-TOF/TOF-CID-MS/MS of the molecular ion $[M]^+$ phenylcoumaran derivatives ion (2) at m/z 341.1011

Characteristic ions	Calculated mass (m/z)	Observed mass (m/z)	Difference (in ppm)
$[C_{19}H_{17}O_6]^+$	341.1025	341.1049	7
$[C_{18}H_{19}O_6]^+$	331.1182	331.1142	12
$[C_{16}H_{13}O_3]^+$	253.0865	253.0883	7
$[C_{16}H_7O_2]^+$	231.0446	231.0467	9
$[C_{15}H_{13}O]^+$	209.0966	209.0951	7
$[C_{11}H_{10}O_3]^+$	190.0630	190.0619	5
$[C_{10}H_9O_3]^+$	177.0552	177.0570	10
$[C_9H_9O_3]^+$	165.0552	165.0544	5
$[C_7H_5O_3]^+$	137.0239	137.0247	6
$[C_7H_7O_2]^+$	123.0446	123.0455	7

6.9.3. High energy MALDI-TOF/TOF-CID-MS/MS of the precursor phenylcoumaran derivatives ion $[M]^+$ (3) at m/z 369.1310.

The product ion scan of the selected precursor ion $[M]^+$ at m/z 369.1310 afforded a series of product ions at m/z 355.1189, 343.1192, 335.0936, 309.1112, 307.0991, 279.1043, 203.0684, 167.0140, 137.0976 [Figure 6.9.3]. The structural identities of the

major product ions are tentatively indicated in Table 6.C and their genesis are shown in Scheme 6.3.

The precursor ion $[M]^+$ appears to lose a methylene group to form the product ion **3a** at m/z 355.1189. The precursor ion $[M]^+$ (**3**) at m/z 369.1356 loses the neutral guaiacyl unit $[(C_8H_6O_8), (152.0473 \text{ Da})]$ to afford the product ion **3g** at m/z 203.0684. This latter product ion **3g** loses methanol and two hydrogen molecules to form the product ion **3h** at m/z 167.014. The precursor ion $[M]^+$ can also lose consecutively a hydrogen molecule and a molecule of methanol to form the product ion **3c** at m/z 335.0936. This latter product ion **3c** loses carbon monoxide to form the product ion **3e** at m/z 307.0991. The precursor ion $[M]^+$ also loses two molecules of formaldehyde to form the product ion **3d** at m/z 309.1112. This product ion **3i** at m/z 137.0976 can be afforded from the product ion **3d** by consecutive cleavage of C_8-C_5' and the ether linkage between C_7-O-C_4' located on the second coniferyl unit. The product ion **3i** is produced from the product ion **3d** by the elimination of the neutral fragments $[(C_9H_6O), (130.0419 \text{ Da})]$ and carbon-dioxide. The product ion **3b** at m/z 343.1192 is formed from precursor ion $[M]^+$ by elimination of ethene. Finally, the product ion **3f** at m/z 279.1043 is formed by elimination of three molecules of formaldehyde from the precursor ion $[M]^+$.

The proposed high energy MALDI-CID-MS/MS fragmentation routes are tentatively shown in Scheme 6.3

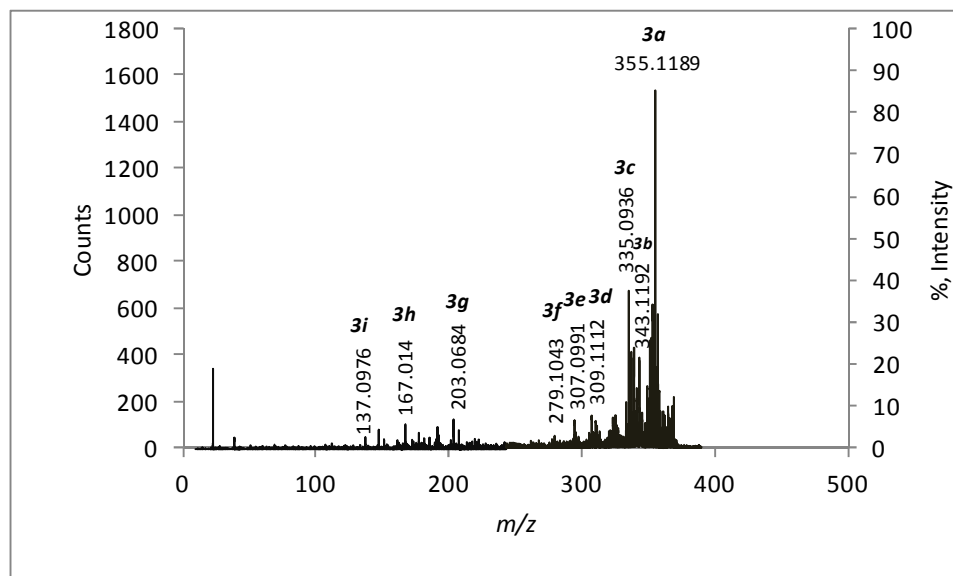
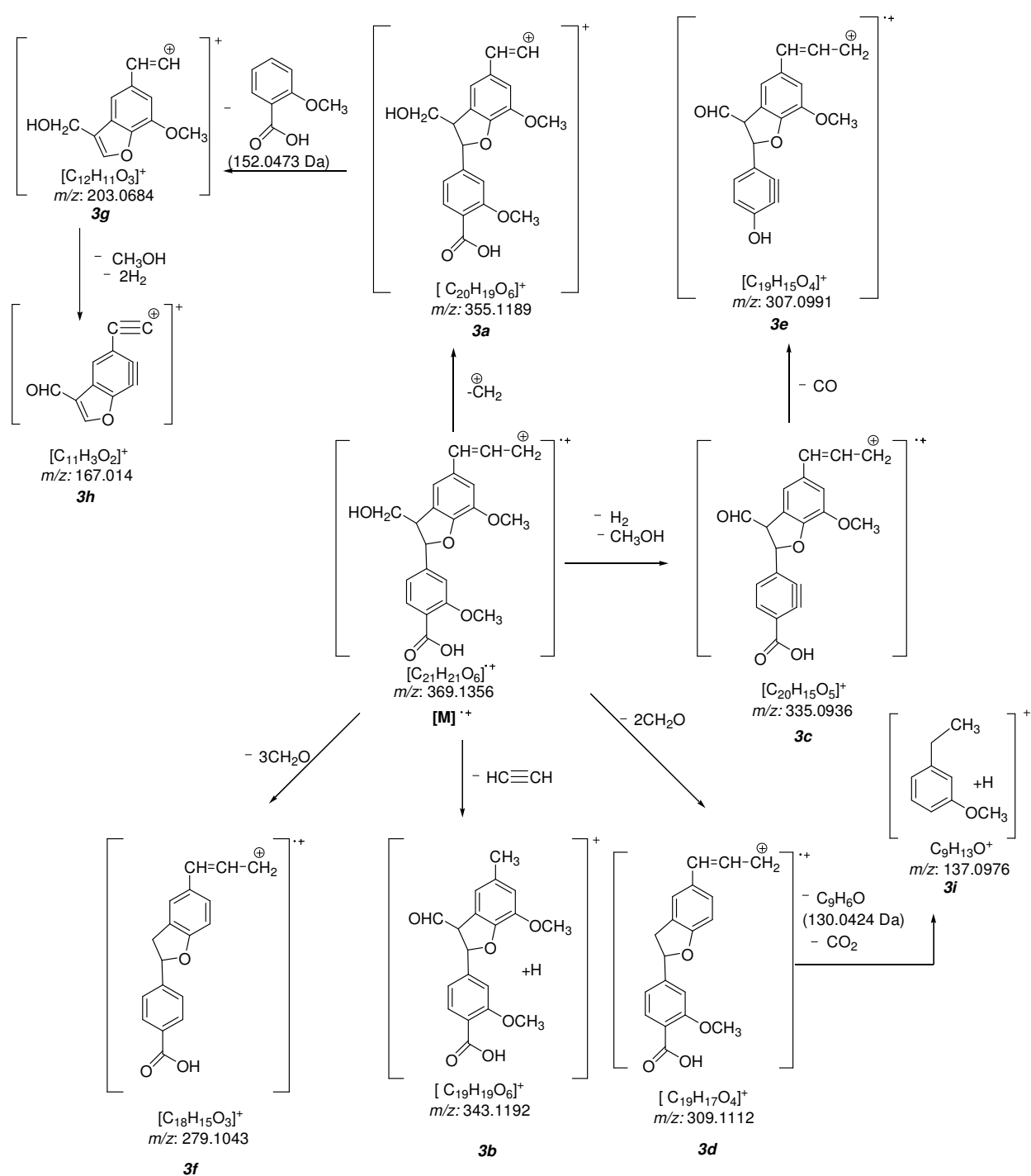


Figure 6.9.3: High energy MALDI-CID-MS/MS of the selected precursor ion $[M]^+$ phenylcoumaran derivatives ion (**3**) at m/z 369.1310



Scheme 6.3: The tentatively proposed fragmentation routes obtained during MALDI-TOF/TOF high energy CID-MS/MS of the protonated ion $[M]^+$ phenylcoumaran derivatives ion (**3**) at m/z 369.1310.

Table 6.C: Characteristic product ions observed in the high energy MALDI-TOF/TOF-CID-MS/MS of the precursor phenylcoumaran derivatives ion $[M]^+$ (**3**) at m/z 369.1310.

Characteristic ions	Calculated mass (m/z)	Observed mass (m/z)	Difference (in ppm)
$[C_{21}H_{21}O_6]^+$	369.1338	369.1356	5
$[C_{20}H_{19}O_6]^+$	355.1182	355.1189	2
$[C_{19}H_{19}O_6]^+$	343.1182	343.1192	3
$[C_{20}H_{15}O_5]^+$	335.0919	335.0936	5
$[C_{19}H_{17}O_4]^+$	309.1127	309.1112	5
$[C_{19}H_{15}O_4]^+$	307.0970	307.0991	7
$[C_{18}H_{15}O_3]^+$	279.1021	279.1043	8
$[C_{12}H_{11}O_3]^+$	203.0708	203.0684	12
$[C_{11}H_9O_2]^+$	167.0133	167.0140	4
$[C_9H_9O]^+$	137.0966	137.0976	7

6.9.4. High energy MALDI-TOF/TOF-CID-MS/MS of the protonated precursor phenylcoumaran derivatives ion $[M+H]^+$ (**4**) at m/z 403.1349 .

The product ion scan of the selected protonated molecular ion at m/z 403.1349 afforded a series of product ions at m/z 401.1258, 385.1183, 359.1466, 343.1165, 317.0450, 283.0928, 256.1073, 212.0805, 181.0488, and 167.0716 [Figure 6.9.4]. The structural identities of this series major product ions are indicated in Table 6.D and their genesis are tentatively shown in Scheme 6.4

The precursor derivative ion (**4**) $[M+H]^+$ at m/z 403.1321 loses a hydrogen molecule to form the product ion **4a** at m/z 401.1258. The precursor ion $[M+H]^+$ loses a water molecule to afford the product ion **4b** at m/z 385.1183. The product ion **4c** at m/z 359.1466 is formed from the precursor ion $[M+H]^+$ by elimination of carbon dioxide. The precursor ion $[M+H]^+$ can also lose a neutral fragment of $[(C_2H_4O_2), (60.0211 \text{ Da})]$ to form the product ion **4d** at m/z 343.1165. The product ion **4e** at m/z 317.0450 is formed from the product ion **4b** by the consecutive elimination of two molecules of hydrogen molecule, one molecule water and two molecules of methanol from the precursor ion $[M+H]^+$. The product ion **4f** at m/z 283.0928 is formed from the precursor ion $[M+H]^+$ by elimination of four molecules of formaldehyde. The product ion **4g** at m/z 256.1073 is formed from the precursor ion $[M+H]^+$ by consecutive eliminations of the neutral fragments $[(C_3H_4O_2), (72.0211 \text{ Da})]$, a molecule of formaldehyde and a carboxylic radical. The product ion **4h** at m/z 212.0805 is formed by the elimination of radical $[(CH_2CHO^\bullet), (43.0184 \text{ Da})]$ and carbon monoxide from the product ion **4f**. The product ion **4h** can also be formed from the precursor ion $[M+H]^+$ by the consecutive eliminations of a neutral radical fragment of $[(CH_2CHO^\bullet), (43.0184 \text{ Da})]$, four molecules of formaldehyde and one molecule of carbon monoxide as shown in Scheme 6.4. The precursor ion $[M+H]^+$ also eliminates a coniferyl unit $[(C_{12}H_{14}O_4), (222.0892 \text{ Da})]$ to form the product ion **4i** at m/z 181.0488 by the cleavage of C₈-C₉ of first coniferyl unit and C₇-O-C₄'. The product ion **4j** at m/z 167.0716 also is formed by elimination of $[(C_{12}H_{12}O_5), (236.0685 \text{ Da})]$ from the precursor ion.

The proposed high energy MALDI-TOF/TOF-CID-MS/MS fragmentation routes are tentatively shown in Scheme 6.4

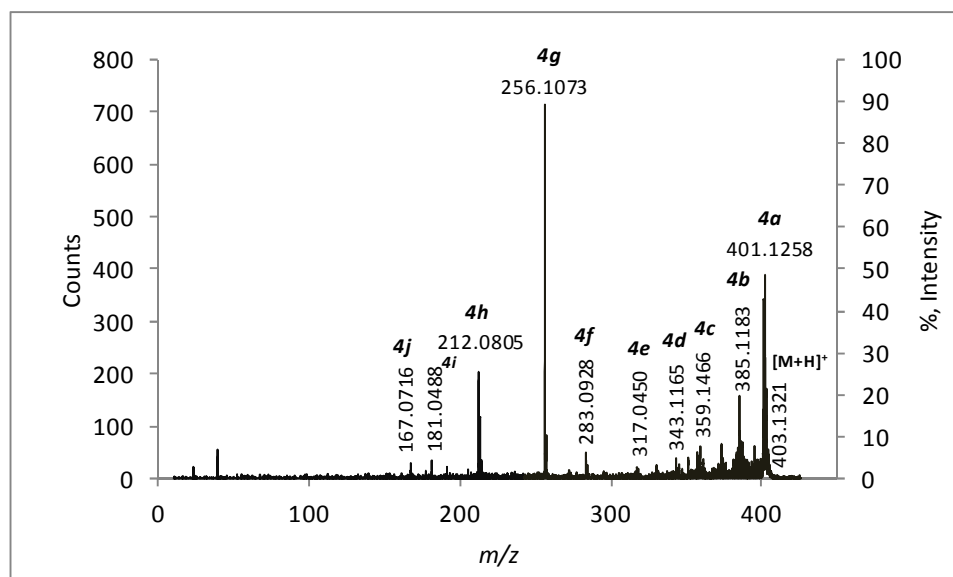
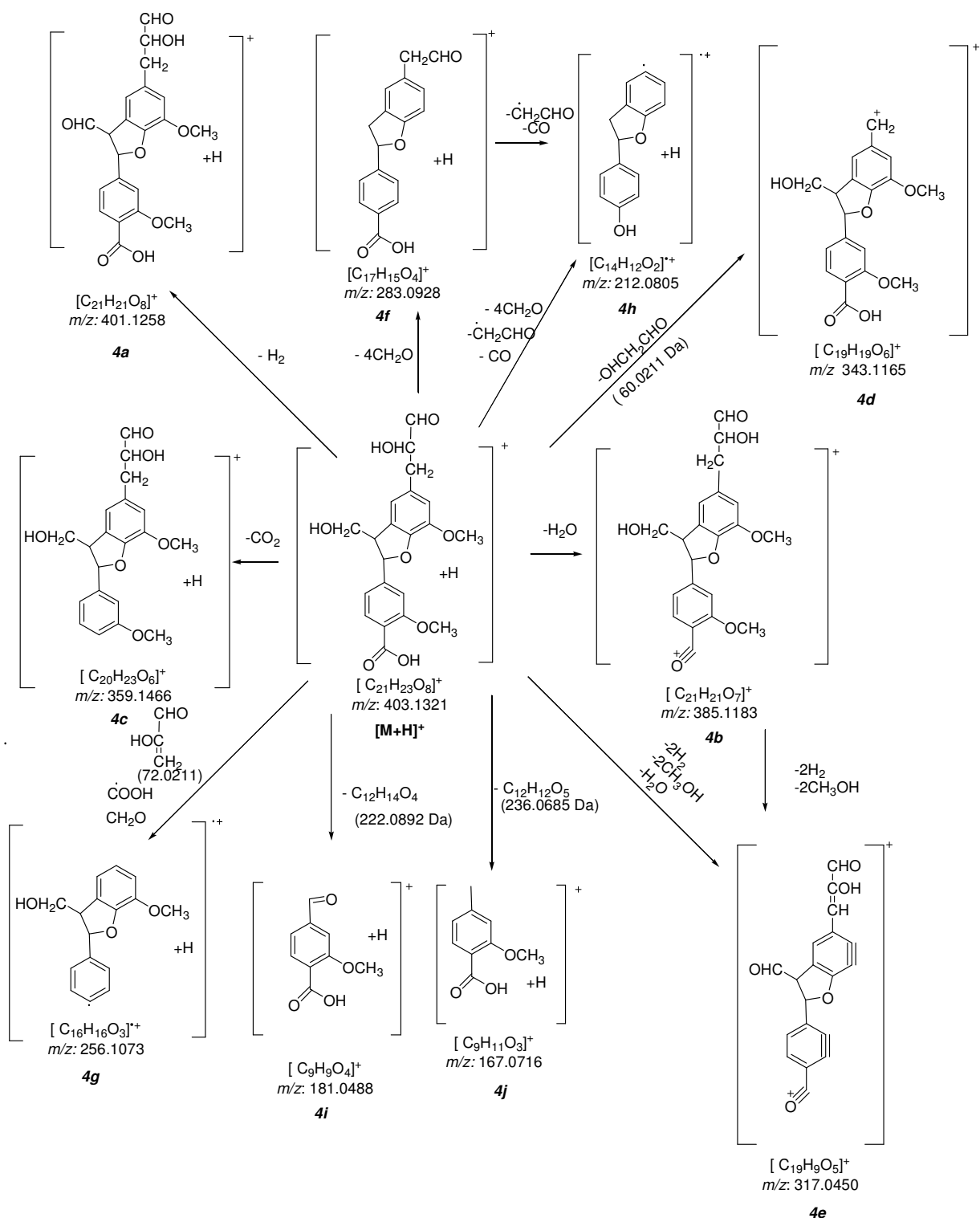


Figure 6.9.4: High energy MALDI-CID-MS/MS of the selected protonated precursor ion $[M+H]^+$ phenylcoumaran derivatives ion (**4**) at m/z 403.1349



Scheme 6.4: The tentatively proposed fragmentation routes obtained during MALDI-TOF/TOF high energy CID-MS/MS of the protonated ion $[M+H]^+$ phenylcoumaran derivatives ion (4) at m/z 403.1349

Table 6.D: Characteristic product ions observed in the high energy MALDI-TOF/TOF-CID-MS/MS of the protonated ion $[M+H]^+$ phenylcoumaran derivatives ion (**4**) at m/z 403.1234

Characteristic ions	Calculated mass (m/z)	Observed mass (m/z)	Difference (in ppm)
$[C_{21}H_{23}O_8]^+$	403.1393	403.1321	5
$[C_{21}H_{21}O_8]^+$	401.1236	401.1258	6
$[C_{21}H_{21}O_7]^+$	385.1287	385.1183	12
$[C_{20}H_{23}O_6]^+$	359.1495	359.1466	8
$[C_{19}H_{19}O_6]^+$	343.1182	343.1165	5
$[C_{19}H_9O_5]^+$	317.0450	317.0450	7
$[C_{17}H_{15}O_4]^+$	283.0970	283.0928	9
$[C_{16}H_{16}O_3]^{++}$	256.1099	256.1073	10
$[C_{14}H_{12}O_2]^{++}$	212.0837	212.0805	12
$[C_9H_9O_4]^+$	181.0501	181.0488	7
$[C_9H_{11}O_3]^+$	167.0708	167.0716	5

6.9.5. High energy MALDI-TOF/TOF-CID-MS/MS of the protonated $[M+H]^+$ trimeric phenylcoumaran precursor ion (5**) at m/z 523.1926.**

The product ion scan of the selected protonated molecular ion at m/z 523.1926 afforded a series of product ions at m/z 521.1783, 391.0990, 355.137, 343.1161, 331.1162, 181.0847, and 137.0229 [Figure 6.9.5]. The structural identities of this major product ions are indicated in Table 6.E and their genesis are tentatively shown in Scheme 6.5.

The precursor ion $[M+H]^+$ ion (**5**) at m/z 523.1910 loses a hydrogen molecule to form the product ion **5a** at m/z 521.1783. The precursor ion $[M+H]^+$ can lose consecutively, three molecules of methanol and two molecules of water to form the product ion **5b** at m/z 391.0990. The product ion **5c** at m/z 355.1370 is formed from the precursor ion by the consecutive elimination of two molecules of formaldehyde, two molecules of methanol and a molecule of carbon-dioxide. The precursor ion can also eliminate the fragment $[(C_{10}H_{12}O_3), (180.0786 \text{ Da})]$ by the cleavage of $C_7'-C_8'$ covalent bond and $C_7'-O-C_4''$ ether linkage to form the product ion **5d** at m/z 343.1161. The precursor ion $[M+H]^+$ also eliminates a coniferyl unit $[(C_{11}H_{12}O_3), (192.0786 \text{ Da})]$ to form the product ion **5e** at m/z 331.1162. The precursor ion $[M+H]^+$ eliminates $[(C_{19}H_{18}O_6), (342.1013 \text{ Da})]$ to afford the product ion **5f** at m/z 181.0847. The product ion **5g** at m/z 137.0229 is formed by the elimination of dimeric coniferyl unit $[(C_{21}H_{22}O_6), (370.1416 \text{ Da})]$ and a molecule of methanol from the precursor ion $[M+H]^+$.

The proposed high energy MALDI-TOF/TOF-CID-MS/MS fragmentation routes are tentatively shown in Scheme 6.5

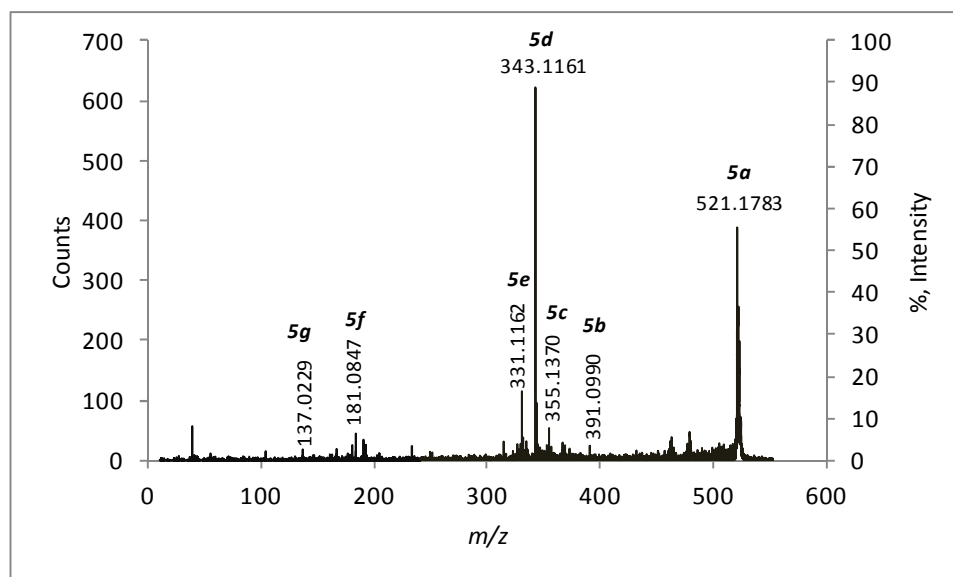
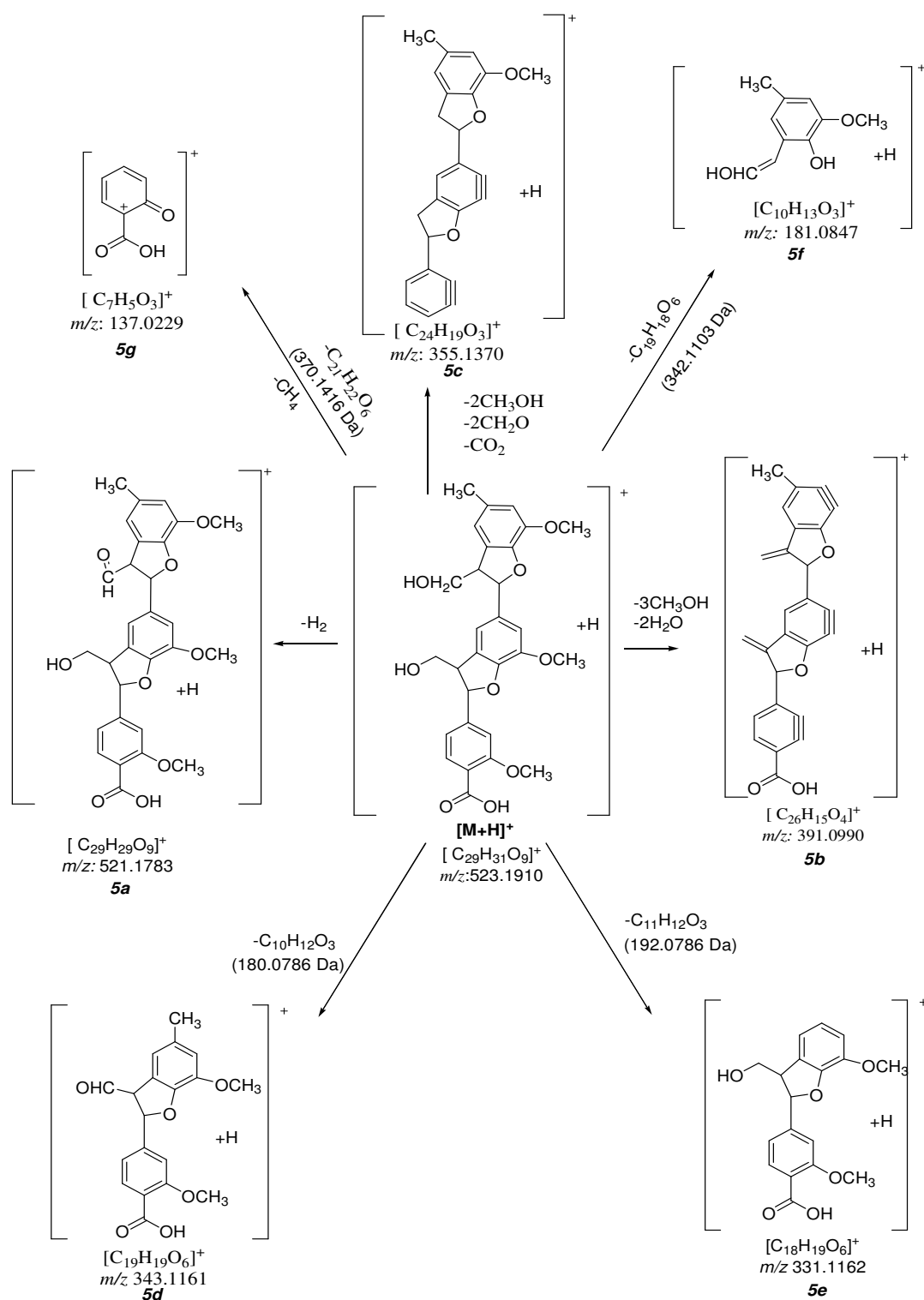


Figure 6.9.5: High energy MALDI-TOF/TOF-CID-MS/MS of the selected protonated precursor ion $[M+H]^+$ phenylcoumaran derivatives ion (**5**) at m/z 523.1926



Scheme 6.5: The tentatively proposed fragmentation routes obtained during MALDI-TOF/TOF high energy CID-MS/MS of the protonated phenylcoumaran derivatives ion (**5**) $[M+H]^+$ at m/z 523.1926

Table 6.E: Characteristic product ions observed in the high energy MALDI-TOF/TOF-CID-MS/MS of the selected protonated precursor ion $[M+H]^+$ (**5**) at m/z 523.1926

Characteristic ions	Calculated mass (m/z)	Observed mass (m/z)	Difference (in ppm)
$[C_{29}H_{31}O_9]^+$	523.1968	523.1910	11
$[C_{29}H_{29}O_9]^+$	521.1812	521.1783	6
$[C_{26}H_{15}O_4]^+$	391.0970	391.0990	5
$[C_{24}H_{19}O_3]^+$	355.1334	355.1370	10
$[C_{19}H_{19}O_6]^+$	343.1182	343.1161	6
$[C_{18}H_{19}O_6]^+$	331.1182	331.1162	17
$[C_{10}H_{13}O_3]^+$	181.0865	181.0847	24
$[C_7H_5O_3]^+$	137.0239	137.0229	15

6.9.6. High energy MALDI-TOF/TOF-CID-MS/MS of the protonated $[M+H]^+$ trimer phenylcoumaran derivatives precursor ion (**6**) at m/z 539.1888 .

The product ion scan of the selected protonated molecular ion at m/z 539.1888 afforded series of product ions at m/z 537.1825, 521.1837, 491.1686, 407.0899, 365.0836, 355.0981, 343.1158, 331.1199, 184.0178, 167.0693, and 149.025 [Figure 6.9.6]. The structural identities of the major product ions are indicated in Table 6.F and their genesis are tentatively shown in Scheme 6.6. The precursor ion $[M+H]^+$ at m/z 539.1944 lose hydrogen molecule to afford the product ion **6a** at m/z 537.1825. The precursor ion $[M+H]^+$ again loses a water molecule to form the product ion **6b** at m/z 521.1837. The product ion **6d** at m/z 407.0899 can be formed from the precursor ion $[M+H]^+$ by the consecutive elimination of three molecules of methanol and two molecules of water. The

precursor ion $[M+H]^+$ loses also formaldehyde and water molecules to form the product ion **6c** at m/z 491.1686. The precursor ion $[M+H]^+$ may also lose consecutively three molecules of methanol, two molecules of formaldehyde and a water molecules to form the product ion **6e** at m/z 365.0836. The precursor ion $[M+H]^+$ also loses three molecules of methanol, two molecules of formaldehyde and one molecule carbon-monoxide to form the product ion **6f** at m/z 355.0981. The precursor ion loses the fragment $[(C_{10}H_{12}O_4), (196.0736 \text{ Da})]$ to form the product ion **6g** at m/z 343.1158 by the cleavage of $C_7'-C_8'$ and the $C_7'-O-C_4''$ located on the third coniferyl unit. The product ion **6h** at m/z 331.1199 is formed by elimination of third coniferyl unit $[(C_{11}H_{12}O_4), (208.0736 \text{ Da})]$ from the precursor $[M+H]^+$ unit. The product ion **6i** at m/z 184.0178 is found by the consecutive eliminations of a neutral fragment $[(C_{16}H_{18}O_5), (290.1154 \text{ Da})]$, methanol, hydroxyl radical and a methane molecule. The product ion **6k** at m/z 167.0693 is formed by fragmentation of coniferyl dimeric $[(C_{20}H_{20}O_7), (372.1209 \text{ Da})]$ unit as shown in Scheme 6.6 by the cleavage of C_7-C_8 and the ether linkage of C_7 and oxygen located at C_4' of the second coniferyl unit. The product ion **6l** at m/z 149.025 is formed by the elimination of a neutral fragment $[(C_{18}H_{10}O_2), (258.0681 \text{ Da})]$ from the precursor ion. $[M+H]^+$.

The proposed high energy MALDI-TOF/TOF-CID-MS/MS fragmentation routes are tentatively shown in Scheme 6.6

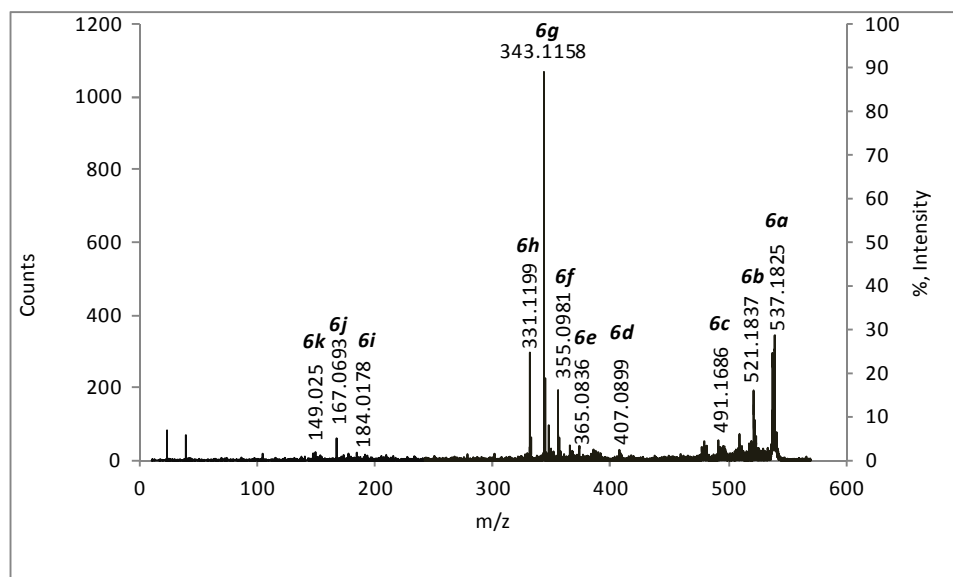
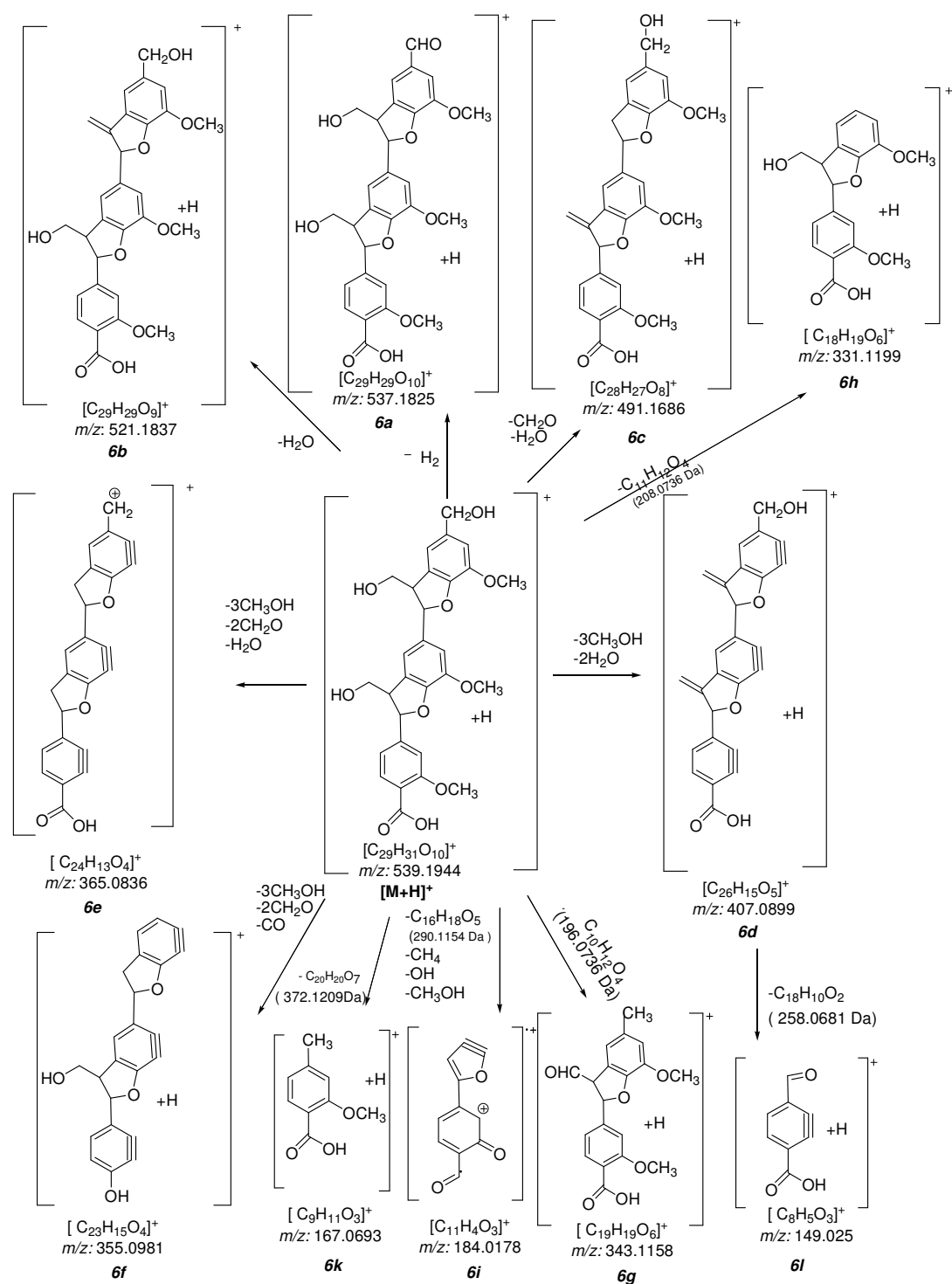


Figure 6.9.6: High energy MALDI-TOF/TOF-CID-MS/MS of the selected protonated $[M+H]^+$ precursor ion phenylcoumaran derivatives ion (**6**) at m/z 539.1888



Scheme 6.6: The tentative proposed fragmentation routes obtained during MALDI-TOF/TOF high energy CID-MS/MS of the protonated ion $[M+H]^+$ phenylcoumaran derivatives ion (**6**) at m/z 539.1888.

Table 6.F: Characteristic product ions observed in the high energy MALDI-TOF/TOF-CID-MS/MS of the selected protonated $[M+H]^+$ precursor ion phenylcoumaran derivatives ion (**6**) at m/z 539.1888

Characteristic ions	Calculated mass (m/z)	Observed mass (m/z)	Difference (in ppm)
$[C_{29}H_{31}O_{10}]^+$	539.1917	539.1944	5
$[C_{29}H_{29}O_{10}]^+$	537.1761	537.1825	12
$[C_{29}H_{29}O_9]^+$	521.1812	521.1837	5
$[C_{28}H_{27}O_8]^+$	491.1706	491.1686	4
$[C_{26}H_{15}O_5]^+$	407.0919	407.0899	5
$[C_{24}H_{13}O_4]^+$	365.0814	365.0836	6
$[C_{23}H_{15}O_4]^+$	355.0970	355.0981	3
$[C_{19}H_{19}O_6]^+$	343.1182	343.1158	7
$[C_{18}H_{19}O_6]^+$	331.1182	331.1199	5
$[C_{11}H_4O_3]^+$	184.0160	184.0178	10
$[C_9H_{11}O_3]^+$	167.0708	167.0693	9
$[C_8H_5O_3]^+$	149.0239	149.025	7

6.9.7. High energy MALDI-TOF/TOF-CID-MS/MS of the protonated $[M+H]^+$ tetrameric phenylcoumaran precursor derivative ion (7**) at m/z 655.2411.**

The product ion scan of the selected protonated molecular ion at m/z 655.2411 shown as afforded product ions at m/z 606.2212, 503.1813, 467.1624, 445.1256, 343.1172, 256.1089, 234.0655, 190.0617, 177.0925, and 137.0255 [Figure 6.9.7]. The

structural identities of this major product ions are tentatively indicated in Table 6.G and their genesis are shown in Scheme 6.7.

The precursor ion (**7**) $[M+H]^+$ at m/z 655.2459 can lose methanol and a hydroxy radical to form the radical cation product ion **7a** at m/z 606.2212. The precursor ion $[M+H]^+$ also eliminate consecutively two molecules of methanol, two molecules of formaldehyde and carbon monoxide to afford the product ion **7b** at m/z 503.1813. The product ion **7c** at m/z 467.1624 is formed from precursor ion $[M+H]^+$ with the consecutive eliminations of two molecules of methanol, two molecules of formaldehyde, two molecules of water and a carbon monoxide molecules from the precursor ion. The precursor ion also eliminates the fourth coniferyl unit $[(C_{11}H_{12}O_2), (176.0837 \text{ Da})]$, methanol, and hydrogen molecules to afford the product ion **7d** at m/z 445.1256. The precursor ion also eliminates the dimeric coniferyl unit (3rd and 4rd) $[(C_{19}H_{20}O_4), (312.1362 \text{ Da})]$ to form the product ion **7e** at m/z 343.1172. The precursor ion eliminates the consecutively dimeric radical $[(C_{20}H_{21}O_4^{\cdot}), (325.1440 \text{ Da})]$, a formaldehyde molecule and carbon dioxide to afford the radical cation product ion **7f** at m/z 256.1089. The radical cation product ion **7g** at m/z 234.0655 is formed from the product ion **7b** by elimination of $[(C_{17}H_{15}O_2^{\cdot}), (251.1072 \text{ Da})]$ and water molecule. The product ion **7e** at m/z 343.1172 eliminates the radical fragment $[(C_8H_7O_3^{\cdot}), (151.0395 \text{ Da})]$ and a hydrogen molecule to afford the radical cation ion **7h** at m/z 190.0588. The precursor ion also eliminates the trimeric coniferyl unit (1st +2nd +3rd) $[(C_{27}H_{26}O_8), (478.1628 \text{ Da})]$ to afford the product ion **7i** at m/z 177.0925. The precursor ion also eliminates consecutively trimeric coniferyl unit (2nd+ 3rd+4rd) $[(C_{30}H_{39}O_7), (502.1992 \text{ Da})]$ and methanol molecules to get the product ion **7j** at m/z 137.0255.

The proposed high energy MALDI-TOF/TOF-CID-MS/MS fragmentation routes are tentatively shown in Scheme 6.7

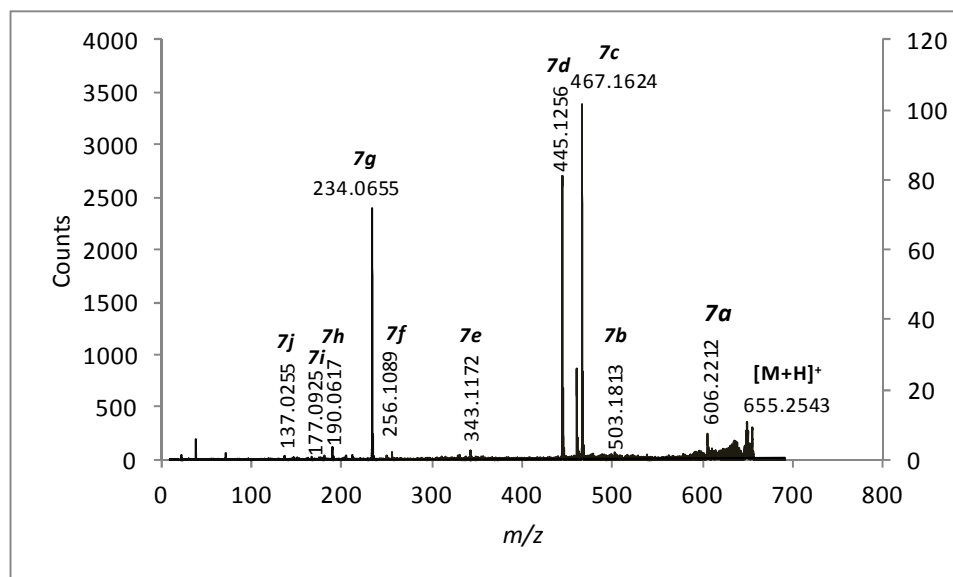
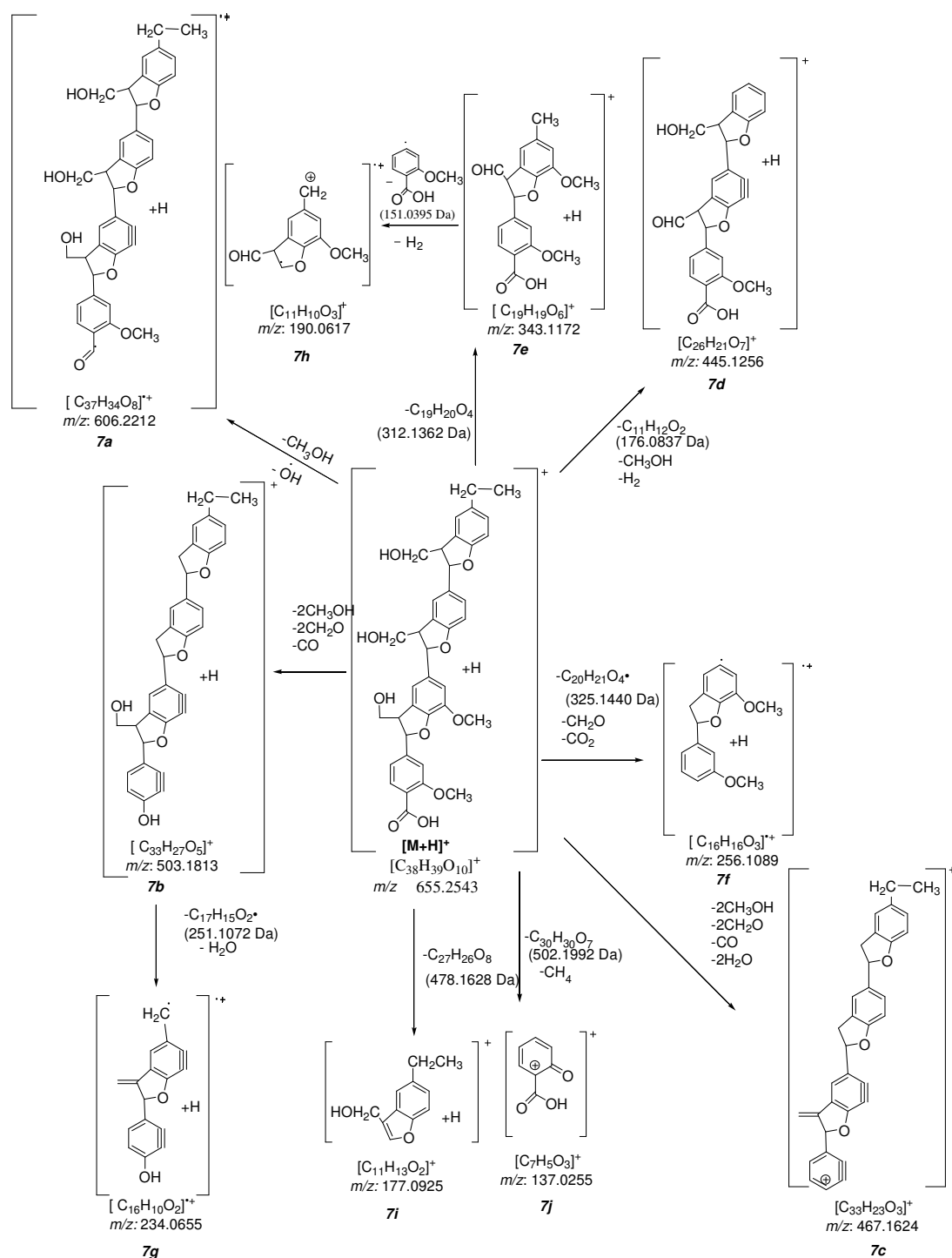


Figure 6.9.7: High energy MALDI-CID-MS/MS of the selected protonated $[M+H]^+$ phenylcoumaran derivatives precursor ion (**7**) at m/z 655.2411.



Scheme 6.7: The tentative proposed fragmentation routes obtained during MALDI-TOF/TOF high energy CID-MS/MS of the protonated ion $[M+H]^+$ (**7**) at m/z 655.2411

Table 6.G: Characteristic product ions observed in the high energy MALDI-TOF/TOF-CID-MS/MS of the protonated $[M+H]^+$ ion (**7**) at m/z 655.2411

Characteristic ions	Calculated mass (m/z)	Observed mass (m/z)	Difference (in ppm)
$[C_{38}H_{39}O_{10}]^+$	655.2543	655.2543	6
$[C_{37}H_{34}O_8]^{++}$	606.2254	606.2212	7
$[C_{33}H_{27}O_5]^+$	503.1858	503.1813	9
$[C_{33}H_{23}O_3]^+$	467.1647	467.1624	5
$[C_{26}H_{21}O_7]^+$	445.1287	445.1256	7
$[C_{19}H_{19}O_6]^+$	343.1182	343.1172	3
$[C_{16}H_{16}O_3]^{++}$	256.1099	256.1089	4
$[C_{16}H_{10}O_2]^{++}$	234.0681	234.0655	11
$[C_{11}H_{10}O_3]^+$	190.0630	190.0617	7
$[C_{11}H_{13}O_2]^+$	177.0916	177.0925	5
$[C_7H_5O_3]^+$	137.0239	137.0255	12

6.9.8. High energy MALDI-TOF/TOF-CID-MS/MS of the protonated $[M+H]^+$ tetrameric phenylcoumaran derivative (**8**) at m/z 671.2019

The product ion scan of the selected protonated molecular ion at m/z 671.2019 afforded product ions at m/z 669.1932, 653.2075, 611.1874, 539.1077, 483.1396, 461.1190, 445.0883, 343.1223, 331.1152, 250.1007, 234.0665, 137.0255 [Figure 6.9.8]. The structural identities of the major product ions are tentatively indicated in Table 6.H and their genesis are shown in Scheme 6.8.

The precursor ion $[M+H]^+$ (**8**) at m/z 671.2069 loses a hydrogen molecule to form the product ion **8a** at m/z 669.1932. The precursor ion may lose again a water molecule to form the product ion **8b** at m/z 653.2075. The product ion **8c** at m/z 611.1874 is formed from the precursor ion by elimination of a methanol molecule and carbon dioxide. The precursor ion may also lose consecutively three molecules of methanol, two molecules of water, one molecule of formaldehyde and a hydrogen molecule to form the product ion **8d** at m/z 539.1077. The precursor ion eliminates consecutively the 1st coniferyl unit $[(C_8H_8O_3), (152.0473 \text{ Da})]$ and two molecules of water to form the product ion **8e** at m/z 483.1396. The precursor ion may also lose the fourth coniferyl unit $[(C_{10}H_8O_3), (176.043 \text{ Da})]$, methanol and hydrogen molecules to form the product ion **8f** at m/z 461.1190. The latter product ion **8f** loses a molecule of methane to form the product ion **8g** at m/z 445.0883. The product ion **8h** at m/z 343.1223 can be created from the precursor by the elimination of the dimeric coniferyl unit (3rd+ 4rd) $[(C_{18}H_{16}O_6), (328.0947 \text{ Da})]$. The precursor ion $[M+H]^+$ also eliminates $[(C_{18}H_{10}O_6), (340.0947 \text{ Da})]$ to form the product ion **8i** at m/z 331.1152. The precursor ion $[M+H]^+$ also eliminates $[(C_{16}H_{10}O_6), (284.0685 \text{ Da})]$, methoxy radical, carbondioxide, formaldehyde and methanol molecules to form the product ion **8j** at m/z 250.1007. The precursor ion also remove $[(C_{10}H_8O_3), (176.0473 \text{ Da})]$, $[(C_8H_8O_3), (152.0473 \text{ Da})]$, one molecule of water, two molecules of formaldehyde and methoxy radical to form the product ion **8k** at m/z 234.0665. The precursor ion again eliminates trimeric coniferyl unit (1st, 2nd and 3rd) $[(C_{29}H_{26}O_9), (518.1577 \text{ Da})]$ and methane molecule to give the product ion **8l** at m/z 137.0255.

The proposed high energy MALDI-TOF/TOF-CID-MS/MS fragmentation routes are tentatively shown in Scheme 6.8

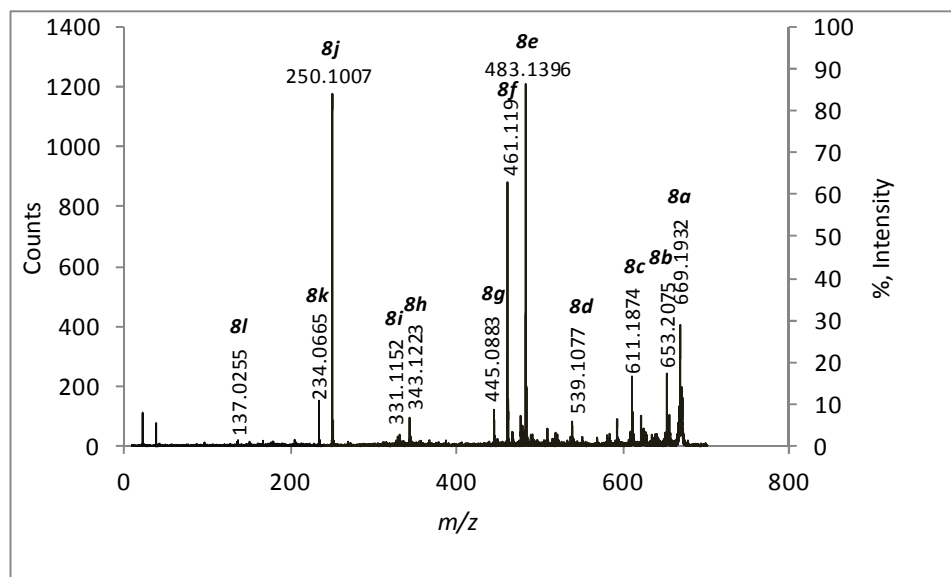
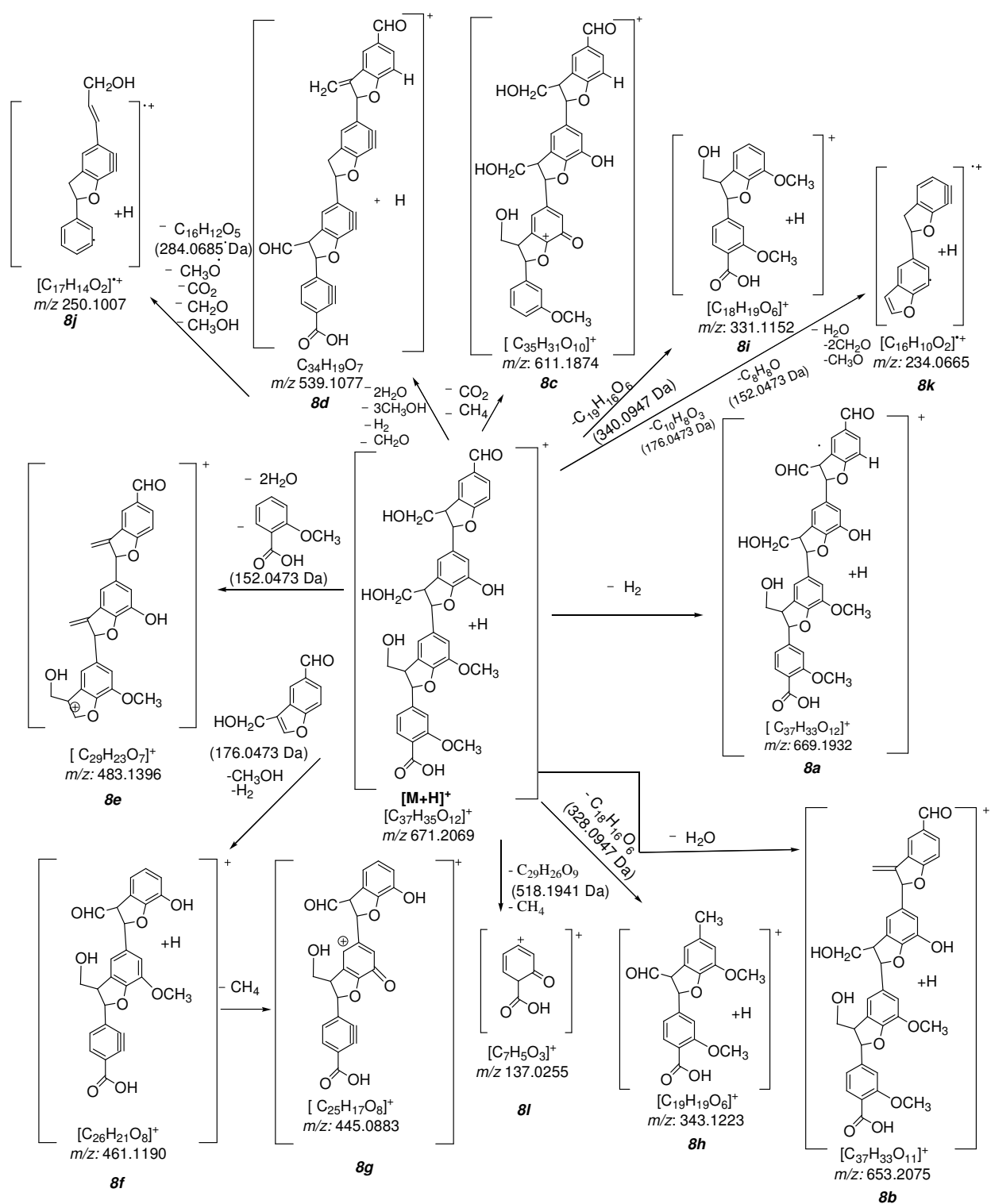


Figure 6.9.8: High energy MALDI-TOF/TOF-CID-MS/MS of the selected protonated $[M+H]^+$ ion (**8**) at m/z 671.2019



Scheme 6.8: The tentative proposed fragmentation routes obtained during MALDI-TOF/TOF high energy CID-MS/MS of the protonated ion $[M+H]^+$ (**8**) at m/z 671.2019

Table 6.H: Characteristic product ions observed in the high energy MALDI-TOF/TOF-CID-MS/MS of the protonated $[M+H]^+$ precursor ion (**8**) at m/z 671.2019.

Characteristic ions	Calculated mass (m/z)	Observed mass (m/z)	Difference (in ppm)
$[C_{37}H_{35}O_{12}]^+$	671.2129	671.2069	9
$[C_{37}H_{33}O_{12}]^+$	669.1972	669.1932	6
$[C_{37}H_{33}O_{11}]^+$	653.2023	653.2075	8
$[C_{35}H_{31}O_{10}]^+$	611.1917	611.1874	7
$[C_{34}H_{19}O_7]^+$	539.1131	539.1077	10
$[C_{29}H_{23}O_7]^+$	483.1444	483.1396	10
$[C_{26}H_{21}O_8]^+$	461.1236	461.1190	10
$[C_{26}H_{21}O_8]^+$	445.0923	445.0883	9
$[C_{19}H_{19}O_6]^+$	343.1182	343.1223	12
$[C_{18}H_{19}O_6]^+$	331.1182	331.1152	9
$[C_{17}H_{14}O_2]^{++}$	250.0994	250.1007	5
$[C_{16}H_{10}O_2]^{++}$	234.0681	234.0665	7
$[C_7H_5O_3]^+$	137.0239	137.0255	12

6.9.9. High energy MALDI-TOF/TOF-CID-MS/MS of the radical precursor ion $[M]^{\cdot+}$ at m/z 491.1672

The product ion scan of the selected radical precursor ion $[M]^{\cdot+}$ at m/z 491.1672 afforded a series of product ions at m/z 489.1500, 473.1557, 463.1729, 459.1476, 431.1517, 401.1389, 355.1355, 343.1222, 331.1156, 313.1060, 295.0938, 181.0849,

167.0721, and 137.0227 [Figure 6.9.9]. The structural identities of the major product ions are tentatively proposed in Table 6.I and their genesis are shown in Scheme 6.9.

The precursor radical ion (**9**) $[M]^{\cdot+}$ at m/z 491.1677 loses hydrogen molecule to afford the product ion **9a** at m/z 489.1500. The precursor ion may lose a molecule water to form the product ion **9b** at m/z 473.1557. The precursor ion may also eliminate carbon monoxide to form the product ion **9c** at m/z 463.1729. The product ion **9d** at m/z 459.1476 is formed by elimination of a methanol molecule from the precursor ion. The precursor ion consecutively eliminates two molecules formaldehyde to afford the product ion **9e** at m/z 431.1517. The product ion **9f** at m/z 401.1389 is formed from the product ion **9e** by elimination of formaldehyde. The precursor ion may also eliminate consecutively molecules of methanol, two molecules of formaldehyde and carbon dioxide to afford the product ion **9g** at m/z 355.1355. For the formation of product ion **9h** at m/z 343.1222, the precursor ion $[M]^{\cdot+}$ first reduced eliminates $[(C_9H_8O_2), (148.0524 \text{ Da})]$ and a hydrogen molecule. The precursor ion is reduced and eliminates a neutral fragment $[(C_{10}H_8O_2), (160.0524 \text{ Da})]$ to form the product ion **9i** at m/z 331.1156. The product ion **9j** at m/z 313.1060 is formed from the product ion **9i** by elimination of water molecule. The product ion **9i** loses water to afford the product ion **9k** at m/z 295.0938. The precursor ion can be subsequently reduced and loses a neutral fragment $[(C_{17}H_{14}O_4), (282.0892 \text{ Da})]$ and formaldehyde molecule to form the product ion **9l** at m/z 181.0849. The precursor ion once more may be reduced the following the subsequent loss of the fragment $[(C_{19}H_{18}O_5), (326.1154 \text{ Da})]$ to form the product ion **9m** at m/z 167.0721. The product ion **9n** at m/z 137.0227 was formed by the elimination of $[(C_{20}H_{21}O_5), (341.1389 \text{ Da})]$ and followed reduction.

The proposed high energy MALDI-CID-MS/MS fragmentation routes are tentatively shown in Scheme 6.9

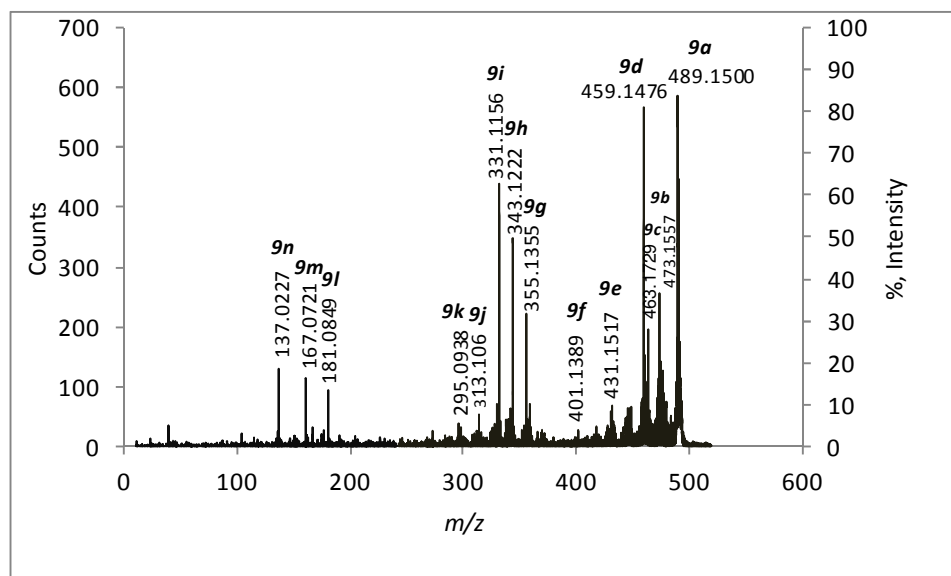
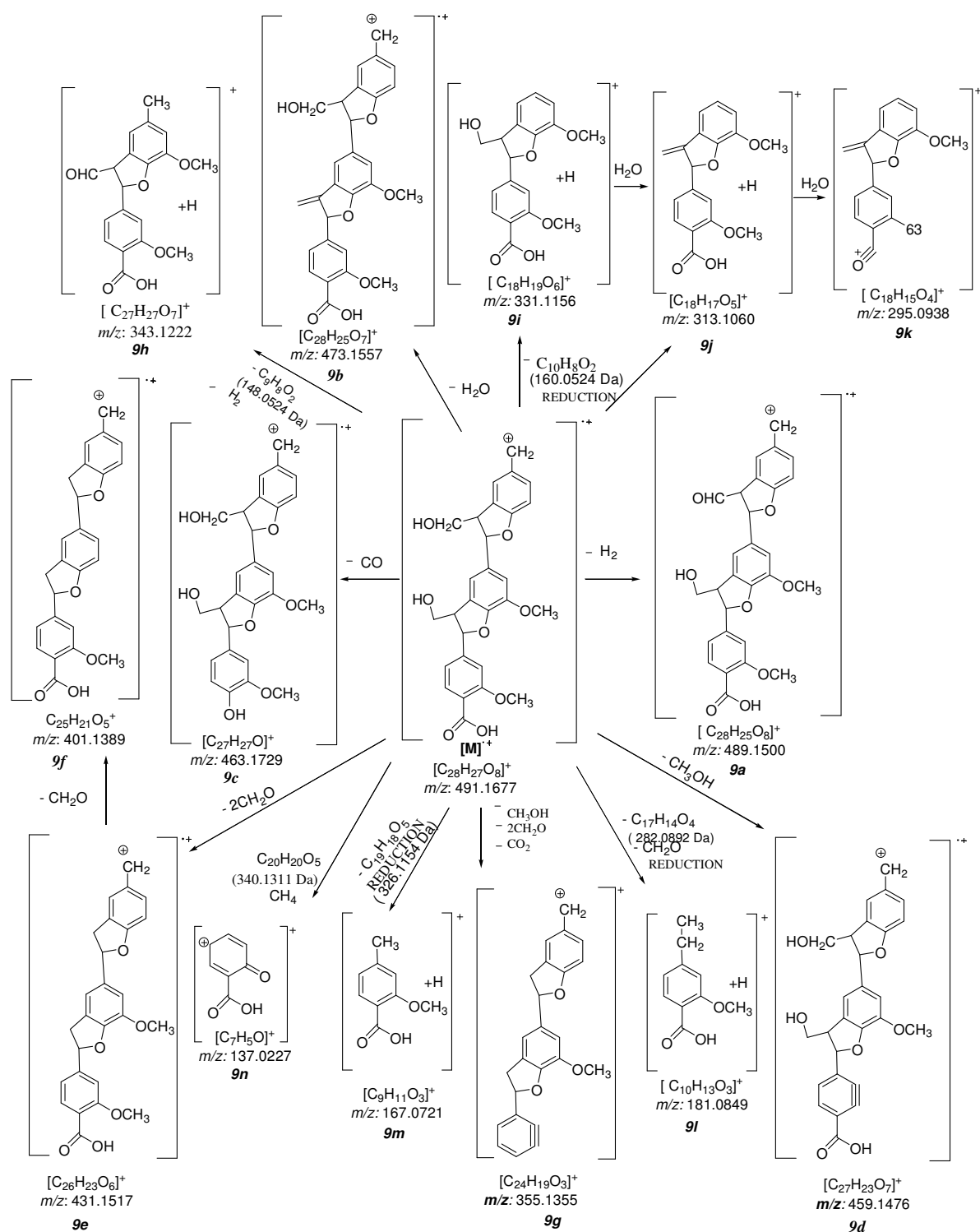


Figure 6.9.9: High energy MALDI-CID-MS/MS of the selected radical precursor ion $[M]^{\cdot+}$ (**9**) at m/z 491.1672.



Scheme 6.9: The tentative proposed fragmentation routes obtained during MALDI-TOF/TOF high energy CID-MS/MS of the $[M]^+$ (9) at m/z 491.1652

Table 6.I: Characteristic product ions observed in the high energy MALDI-TOF/TOF-CID-MS/MS of the precursor ion $[M]^{++}$ (**9**) at m/z 491.1652.

Characteristic ions	Calculated mass (m/z)	Observed mass (m/z)	Difference (in ppm)
$[C_{28}H_{27}O_8]^+$	491.1706	491.1677	6
$[C_{28}H_{25}O_8]^{++}$	489.1549	489.1500	10
$[C_{28}H_{25}O_7]^{++}$	473.1600	473.1557	9
$[C_{27}H_{27}O]^{++}$	463.1757	463.1729	6
$[C_{27}H_{23}O_7]^{++}$	459.1444	459.1476	7
$[C_{26}H_{23}O_6]^{++}$	431.1495	431.1517	5
$[C_{25}H_{21}O_5]^{++}$	401.1389	401.1389	9
$[C_{24}H_{19}O_3]^{++}$	355.1334	355.1355	6
$[C_{27}H_{27}O_7]^+$	343.1182	343.1222	12
$[C_{18}H_{19}O_6]^+$	331.1182	331.1156	8
$[C_{18}H_{17}O_5]^+$	313.1071	313.1060	3
$[C_{18}H_{15}O_4]^+$	295.0970	295.0938	11
$[C_{10}H_{13}O_3]^+$	181.0865	181.0849	9
$[C_9H_{11}O_3]^+$	167.0708	167.0721	8
$[C_7H_5O]^+$	137.0239	137.0227	9

6.6. Conclusion

Moreover, previously shown by Banoub *et al.* in the APPI-QqTOF-CID-MS/MS analyses, conducted on the same series of related oligomeric ions, MALDI-TOF/TOF-CID-MS/MS elucidated and confirmed the proposed structures of the oligomers that I presented in Table 6.A. These findings confirmed the universal comparable fragmentation patterns of this series of phenylcoumaran oligomers of the wheat straw lignin. Although, the MALDI-CID-fragmentation were carried by high-energy collision (CE=1KV) the product ion scans bared a resemblance to the low-energy APPI-CID-MS/MS performed with the QqTOF-MS/MS hybrid instrument. Thus, we have noticed that in all the product ion scans of this series of selected linear oligomeric ions, the main dissociation reactions occurred by eliminations of small molecules such as carbon dioxide and formic acid, which were indicative of the presence of the carboxyl group on the C-4 of the first coniferyl residue. In addition, we have noted eliminations of formaldehyde molecules from the respective methoxylated group present on the coniferyl residues. We also noticed the losses of methane molecules and methyl radicals from the selected precursor ions, consequently affording the cyclic ketone group on the respective coniferyl unit. The loss of the carbonyl group generally occurred by a ring contraction, to afford the five-membered rings in the respective coniferyl units. It is imperative to mention that the majority of the product ion scans of this series of protonated molecules indicated the presence of the intermediate five membered furan-like rings in the oligomers, formed by the C-8–C-5' covalent bond and the C-7–O-4' ether linkage between every other contiguous di-coniferyl unit.

GENERAL CONCLUSION OF CARBOHYDRARE AND LIGNIN.

In this research work, we have evaluated the gas-phase fragmentations of the novel synthetic bivalent *N*-glycosides (**1-6**) using ESI-MS and low energy-collision CID-MS/MS analyses with performed with two different instruments, namely: the QqTOF-MS/MS hybrid instrument performing MS/MS analysis in space and the QIT-MSⁿ instrument allowing recording of MS/MS in time. The results presented in this rationale have demonstrated that during low-energy CID-MS/MS analyses using both instruments, the selected protonated molecules extracted from the bivalent *N*-glycosides followed essentially a universal fragmentation pattern and afforded similar series of product ions formed essentially by the same gas-phase mechanisms. Accordingly, this series of precursor ions afforded upon CID-MS/MS analyses gave the diagnostic product ion [B₁]⁺, [B₂]⁺, [Y₁]⁺ and [Y₀]⁺. Additionally, these CID-fragmentation routes could be used in future to predict the structures of similar new compounds having the same general backbone structure. In addition, we have also studied the gas-phase CID-MS/MS fragmentation using the QIT-MSⁿ instrument of the selected sodiated molecules [M+Na]⁺ which also gave us additional structural information indices on the molecular structure of this series of compounds. The following series of diagnostic product ions were observed in this work. [Y₀]⁺, [Y₁]⁺, [B₂]⁺, [^{0,2}A₂]⁺, [^{2,4}A₂]⁺, [B₁]⁺, [M+Na-N₂]⁺ for the majority of analytes. These QIT-MSⁿ investigations demonstrated without any doubts the full description of the proposed structures. Nevertheless, it is interesting to mention that the precursor sodiated molecules [M+Na]⁺ did not CID-fragment when they were analyzed with the QqTOF-MS/MS hybrid instrument because of low energy CID. In a second part of this study, we have recorded the MALDI-TOF/TOF-MS of the same series of

compounds using a MALDI-TOF/TOF-MS instrument. The MALDI-TOF/TOF-MS of this series of compounds afforded the sodiated molecules $[M+Na]^+$ (base peak) with very low abundances of the protonated molecules. High-energy CID-TOF/TOF-MS/MS of the sodiated precursor molecule allowed the differentiation between the isomeric structures, and the linkage position. In the MALDI-CID-MS/MS spectra a considerably greater number of fragments were found in comparison to other mass spectrometry fragmentation techniques. These, although complicating their interpretation, allowed us to gather more information on the linkage position and points of branching. A macro (Microsoft Excel) was used to automate the interpretation of the peaks present in MALDI-CID-TOF/TOF spectra. The series of the identified product ions were identified as follows: $[B_2]^+$, $[Y_0]^+$, $[^{0,2}A_2]^+$, $[B_1]^+$, $[C_1]^+$, $[Y_1]^+$, $[^{0,3}X_2]^+$, $[^{2,6}X_2]^+$ and $[M+Na-N_2]^+$. In the third part of this thesis, I presented the MALDI-TOF/TOF-MS spectra recorded on CIMV wheat straw lignin. This MALDI-TOF/TOF-MS afforded similar series of ions which were comparable to the one acquired with APPI-QqTOF-CID-MS. High-energy MALDI-TOF/TOF-CID-MS/MS elucidated and confirmed the proposed structures of the oligomeric ions. These findings confirmed the universal comparable fragmentation patterns of this series of phenylcoumaran oligomers of the wheat straw lignin. Although, the MALDI-CID-fragmentation were carried by high-energy collision (CE=1KV) the product ion scans bore a resemblance to the low-energy APPI-CID-MS/MS performed with the QqTOF-MS/MS hybrid instrument.

REFERENCES

- [1]. R. A. Dwek. Glycobiology: Toward understanding the function of sugars. *Chem. Rev.* **1996**, 96, 683-72
- [2]. C. R. Bertozzi, L. L. Kiessling. Chemical glycobiology. *Science*. **2001**, 291, 2357-2364.
- [3]. A. Varki. *Glycobiology*. **1993**, 3, 97–130.
- [4]. R. A. Dwek. Biological importance of glycosylation. *Dev. Biol. Stand.* **1998**, 96, 43-47.
- [5]. Y. C. Lee, R. T. Lee. Carbohydrate-Protein interactions: Basis of glycobiology. *Acc. Chem. Res.* **1995**, 28, 321–327.
- [6]. D. A. Mann, M. Kanai, D. J. Maly, L. L. Kiessling. Probing low affinity and multivalent interactions with surface plasmon resonance: Ligands for concanavalin A. *J. Am. Chem. Soc.* **1998**, 120, 10575–10582.
- [7]. T. K. Dam, R. Roy, D. Page, C. F. Brewer. Thermodynamic binding parameters of individual epitopes of multivalent carbohydrates to concanavalin A as determined by “Reverse” isothermal titration microcalorimetry. *Biochemistry*. **2002**, 41, 1359–1363.
- [8]. (a) J. L. Lundquist, E. J. Toone. The Cluster glycoside effect. *Chem. Rev.* **2002**, 102, 555–578.
- b) Y. M. Chabre, R. Roy. Recent trends in glycodendrimer syntheses and applications. *Curr. Top. Med. Chem.* **2008**, 8, 1237–1285;
- c) Y. M. Chabre, R. Roy. In the sugar Code: Fundamentals of glycosciences (Ed.: H.-J. Gabius), Wiley-VCH, Weinheim. **2009**, 53–70;

- d) L. L. Kiessling, J. E. Gestwicki, L. E. Strong. Synthetische multivalente liganden als sonden fur die signaltransduktion. *Angew. Chem.* **2006**, *118*, 2408–2429.
- [9]. a) S. K. Choi. Synthetic multivalent molecules: Concepts and biomedical applications. *Wiley, New York*, **2004**.
- b) M. Mammen, S. K. Choi, G. M. Whitesides. Polyvalente wechselwirkungen in biologischen systemen: auswirkungen auf das design und die verwendung multivalenter liganden und inhibitoren. *Angew. Chem.* **1998**, *110*, 2908–2953.
- [10] a) L. L. Kiessling, J. E. Gestwicki, L. E. Strong. Synthetic multivalent ligands in the exploration of cell-surface interactions. *Curr. Opin. Chem. Biol.* **2000**, *4*, 696 –703;
- b). L. L. Kiessling, L. E. Strong, J. E. Gestwicki. Principles for multivalent ligand design *Annu. Rep. Med. Chem.* **2000**, *35*, 321–330.
- [11]. a) Y. M. Chabre, R. Roy. Adv. carbohydrate. *Chem. Biochem.* **2010**, *63*, 165 – 393;
- b) R. Roy. Trends glycosci. *Glycotechnol.* **2003**, *15*, 291–310;
- c) F. Perez-Balderas, J. Morales-Sanfrutos, F. Hernandez-Mateo, J. Isac-Garca, F. Santoyo-Gonzlez. Click multivalent homogeneous neoglycoconjugates–synthesis and evaluation of their binding affinities. *J. Org. Chem.* **2009**, 2441 – 2453;
- d) M. Ortega-Mucoz, F. Perez-Balderas, J. Morales-Sanfrutos, F. Hernandez-Mateo, J. Isac-Garca, F. Santoyo-Gonzlez. Click multivalent heterogeneous neoglycoconjugates – modular synthesis and evaluation of their binding affinities. *Eur. J. Org. Chem.* **2009**, 2454–2473.
- [12]. A. Imberty, Y. M. Chabre, R. Roy. Glycomimmetics and glycodendrimer as high affinity microbial anti-adhesions. *Chem. Eur. J.* **2008**, *14*, 7490–7499.

- [13]. P. Roussel, G. Lamblin. The glycosylation of airway mucins in cystic fibrosis and its relationship with lung infection by *Pseudomonas aeruginosa*. *Med. Biol.* **2003**, 535, 17–32.
- [14]. N. Gilboa-Garber. Lectins-Biology, Biochemistry, Clinical Biochemistry (4th edition), Vol. 3 Walter de Gruyter & Co, Berlin. *Clin. Biochem.* **1983**, 3, 495–502.
- [15]. M. Schuster, C. P. Lostroh, T. Ogi, E. P. Greenberg. Identification, Timing, and Signal Specificity of *Pseudomonas aeruginosa* Quorum-controlled genes: A Transcriptome Analysis. *J. Bacteriol.* **2003**, 185, 2066–2079.
- [16]. K. Winzer, C. Falconer, N. C. Garber, S. P. Diggle, M. Camara, P. Williams. The *Pseudomonas Aeruginosa* lectins PA-IL and PA-IIL are controlled by quorum sensing and by RpoS. *J. Bacteriol.* **2000**, 182, 6401–6411.
- [17]. S. P. Diggle, R. E. Stacey, C. Dodd, M. Camara, P. Williams, K. Winzer. The galactophilic: Lectin, lecA, contributes to biofilm development in *Pseudomonas aeruginosa* *Environ. Microbiol.* **2006**, 8, 1095–1104.
- [18]. A. Imberty, M. Wimmerova, E. P. Mitchell, N. Gilboa-Garber. Structure of the lectins from *Pseudomonas aeruginosa*: insight into the molecular basis for the host glycan recognition. *Microbes Infect.* **2004**, 6, 221–228.

- [19]. O. Bajolet-Laudinat, S. Girod-de Bentzmann, J. M. Tournier, C. Madoulet, M. C. Plotkowski, C. Chippaux, E. Puchelle. Cytotoxicity of *Pseudomonas Aeruginosa* internal lectin PA-I to respiratory epithelial cells in primary culture. *Infect. Immun.* **1994**, 62, 4481–4487.
- [20]. R. S. Laughlin, M. W. Musch, C. J. Hollbrook, F. M. Rocha, E. B. Chang, J. C. Alverdy. The key role of *Pseudomonas Aeruginosa* PA-I lectin on experimental gut-derived sepsis *Ann. Surg.* **2000**, 232, 133–142.
- [21]. C. Chemani, A. Imberty, S. de Bentzmann, M. Pierre, M. Wimmerova, B. P. Guery, K. Faure. Role of LecA and LecB Lectins in *Pseudomonas aeruginosa* induced lung injury and effect of carbohydrate ligands. *Infect. Immun.* **2009**, 77, 2065–2075.
- [22]. D. Avichezer, D. J. Katcoff, N. C. Garber, N. Gilboa-Garber. Analysis of The Amino Acid Sequence of the *Pseudomonas Aeruginosa* galactophilic PA-I lectin. *J. Biol. Chem.* **1992**, 267, 23023–23027.
- [23]. N. Garber, U. Guempel, A. Belz, N. Gilboa-Garber, R. J. Doyle. On the Specificity of the D-galactose-binding Lectin (PA-I) of *Pseudomonas aeruginosa* and its strong binding to hydrophobic derivatives of D-galactose and thiogalactose. *Biochim. Biophys. Acta Gen. Subj.* **1992**, 1116, 33–333.
- [24]. H. Lis, N. Sharon. Carbohydrate-specific proteins that mediate cellular recognition. *Chem. Rev.* **1998**, 98, 637-674.
- [25]. N. Sharon, H. Lis. Specificity and affinity in lectins, 2nd ed.; N. Sharon, H. Lis. Eds.; *Kluwer Academic Publishers: Dordrecht. The Netherlands.* **2003**, pp 63–104.

- [26]. H. J. Gabius. Cell Surface Glycans: The why and how of their functionality as biochemical signals in lectin-mediated information transfer. *Crit Rev Immunol.* **2006**, *26*, 43-80.
- [27]. W. I. Weis and K. Drickamer. Structural basis of lectin-carbohydrate recognition *Annu. Rev. Biochem.* **1996**, *65*, 441– 473.
- [28]. Y. M. Chabre, R. Roy. Creativity in design and synthesis of multivalent neoglycoconjugates. *Adv. Carbohydr. Chem. Biochem.* **2010**, *63*, 165-393.
- [29]. M. Bergeron-Brlek, T. C. Shiao, M. C. Trono, R. Roy. Synthesis of a small library of bivalent for lectin mannopyranosides a D-cross-linking. *Carbohydr Res.* **2011**, *346* (12), 1479-89.
- [30]. E. Lameignere, T. C. Shiao, R. Roy, M. Wimmerova, F. Dubreuil, A. Varrot, A. Imberty. Structural basis of the affinity for oligomannosides and analogs by BC2L displayed as *Burkholderia cenocepacia* soluble lectin. *Glycobiology.* **2010**, *20* (1), 87-98.
- [31]. S. Andre, B. Liu, H. J. Gabius, R. Roy. First demonstration of differential inhibition of lectin binding by synthetic tri-and tetravalent glycoclusters from cross-coupling of rigidified 2-propynyl lactosides. *Org. Biomol. Chem.* **2003**, *1*, 3909-3916.
- [32]. D. Page et al. Optimizing lectin-carbohydrate interactions: Improved binding of divalent ligands ctmannosylated towards Concanavalin A. *Glycoconjugate J.* **1997**, *14*, 345-356.
- [33]. R. J. Pieters et al. Wedgelike glycodendrimers as inhibitors of binding of mammalian galectins to glycoproteins, lactose maxiclusters, and cell surface glycoconjugates. *ChemBioChem.* **2001**, *2* (11), 822-830.

- [34]. M. W. Steward. Outline Studies in Biology: *Immunochemistry*. London: Chapman and Hall, **1974**.
- [35]. M. W. Steward. Antibodies: Their structure and function. London and New York: Chapman and Hall, **1984**.
- [37]. Eli Benhamini, Richard Coico, and Geoffrey Sunshine. Immunology-A Short Course, USA: Wiley-Liss, Inc. **2000**.
- [37]. R. Hatfield, W. Vermerris. Lignin formation in plants. The dilemma of linkage specificity. *Plant Physiol.* **2001**, 126, 1351.
- [38]. J. Bidlack, M. Malone, R. Benson. Molecular structure and component integration of secondary cell walls in plants. *Proc. Okla. Acad. Sc.* **1992**, 72, 51.
- [39]. K. Esau. Cell wall. In Plant anatomy, *John Wiley and Sons, New York, NY.* **1977**, pp 43.
- [40]. K. Keegstra, K. W. Talmadge, W. D. Bauer, P. Albersheim. The structure of plant cell walls. III. A model of the walls of suspension-cultured sycamore cells based on the interconnections of the macromolecular components. *Plant Physiol.* **1973**, 51, 188.
- [41]. D. W. Jones. In *Cellulose and Cellulose Derivatives*, vol. 5, part 4, *High Polymers*, Bikales M.N., Segal L. (eds). Wiley Interscience: New York, **1971**; 117; Ellefsen O., Tonnesen B.A. In *ibid.* **1971**; 151; Tonnesen B.A., Ellefsen O. In *ibid.* **1971**; 265; Atalla R.H. *Adv. Chem. Ser.* **1979**; 181: 55.
- [42]. T. W. Goodwin, E. I. Mercer. The Plant Cell Wall In: Introduction to plant biochemistry. *Pergamon Press, New York. NY* **1983**, pp 55.
- [43]. F. B. Salisbury, C. W. Ross. Plant physiology and plant cells In: Plant Physiology. *Wadsworth, Inc. Belmont. CA.* **1992**, pp 3.

- [44]. W. D. Bauer, K. W. Talmadge, K. Keegstra, P. Albersheim. The structure of plant cell walls. II. The hemicellulose of the walls of suspension-cultured Sycamore cells. *Plant Physiol.* **1973**, *51*, 174.
- [45]. J. H. Banoub, M. Delmas. Structural elucidation of the wheat straw lignin polymer by atmospheric pressure chemical ionization tandem mass spectrometry and matrix-assisted laser desorption/ionization time-of-flight mass spectrometry. *J. Mass Spectrom.* **2003**, *38*, 900.
- [46]. K. W. Talmadge, K. Keegstra, W. D. Bauer, P. Albersheim. The structure of plant cell walls: I. The macromolecular components of the walls of suspension-cultured Sycamore cells with a detailed analysis of the pectic polysaccharides. *Plant Physiol.* **1973**, *51*, 158.
- [47]. R. D. Preston. Polysaccharides conformation and cell wall function. *Ann. Rev. Plant. Physiol.* **1979**, *30*, 55.
- [48]. C. T. Brett, K. W. Waldron. Physiology and biochemistry of plant cell walls. **1996**.
- [49]. D. S. Argyropoulos, L. Jurasek, L. Kristofova, Z. Xia, Y. Sun and E. Palus. Abundance and reactivity of dibenzodioxocins in softwood lignin. *Journal of Agricultural and Food Chemistry*. **2002**, *50* (4), 658-666.
- [50]. Peter M. Froass, Arthur J. Ragauskas, Jian E. Jiang. Chemical structure of residual lignin from kraft pulp. *Journal of Wood Chemistry and Technology*, **1996**, *16* (4), 347-365.
- [51]. E. M. Kukkola, S. Koutaniemi, E. Poellaenen, M. Gustafsson, P. Karhunen, T. K. Lundell, P. Saranpaae, I. Kilpelaeinen, T. H. Teeri and, K. V. Fagerstedt. The

dibenzodioxocin lignin substructure is abundant in the inner part of the secondary wall in Norway spruce and silver birch xylem. *Planta*. **2004**, 218 (3), 497-500.

[52]. Anvar U. Buranov, G. Mazza. Lignin in straw of herbaceous crops. *Industrial crops and products*. **2008**, 28, 237–259.

[53]. S. Reale, A. D. Tullio, N. Spreti, and F. D. Angelis. Mass Spectrometry in the biosynthetic and structural investigation of lignin. *Mass Spectrometry Reviews by Wiley Periodicals, Inc.*, **2004**, 23, 87–126.

[54]. M. Delmas. Vegetal refining and agrochemistry. *Chem. Eng. Technol.* **2008**, 31(5), 792.

[55]. F. G. Kitson, B. S. Larsen, C. N. McEwen. Gas chromatography and mass spectrometry. *A practical Guide; Academic Press:San Diego*. **1996**.

[56]. J. B. Fenn, M. Mann, C. K. Meng, S. F. Wong, C. M .Whitehouse. Electrospray ionisation of mass spectrometry of large molecules. *Science*. **1989**, 246, 64-71.

[57]. K. Tanaka. The origin of macromolecules ionisation by Laser Irradiation (Nobel lecture). *Angrew.chem.Int.Ed.* **2003**, 42, 3860-3870.

[58]. M. Barber, R. S. Bordoli, R. D. Sedgwick, A. Tayler. Fast atom bombardment of solids as an ion sources in mass spectrometry. *Nature*. **1981**, 293, 270-275.

[59]. H. R. Morris, M. Panica, M. Barber, R. S. Bordoli, R. D. Sedgwick, A. Tyler. Fast atom bombard: A new mass spectrometric method for peptide sequence analysis. *Biochem. Biohys. Res.commun.* **1981**, 101, 623-631.

[60]. C. H. Shackleton, K. M. Straub. Direct analysis of steroid conjugates: The use of secondary in mass spectrometry. *Steroids*. **1982**, 40, 35-51.

- [61]. K. Tanaka, Y. Waki, Y. Ido, S. Akita, Y. Yoshida, T. Yoshida. Protein and polymer analysis up to m/z 10000 by laser ionisation time of flight mass spectrometry. *Rapid Commun. Mass spectrum.* **1988**, 2, 151-153.
- [62]. M. B. Karas, A. Inehold, E. Nordhoff, B. Stahl, K. Strupat, F. Hillenkamp. Principles and applications of matrix assisted UV-laser desorption/Ionisation mass spectrometry. *Anal. Chim. Acta.* **1990**, 241, 175- 185.
- [63]. M. Yamashita, J. B. Fenn. Electrospray ion sources. Another variation on the Free-jet theme. *J. Phys. Chem.* **1984**, 88, 4451-4459.
- [64]. M. Karas, D. Bachmann, F. Hillenkamp. Influence of the wavelength in high-irradiance ultraviolet laser desorption mass spectrometry of organic molecule. *Anal. Chem.* **1985**, 57 (14), 2935–9
- [65]. M. Karas, F. Hillenkamp. Laser desorption ionisation of protein with molecular masses exceeding 10000 dalton. *Anal. Chem.* **1988**, 60, 2299-2301.
- [66]. F. Hillenkamp, M. Karas, A. Ingendoh, B. Stahl. Matrix-assisted UV laser desorption/ionization: A new approach to mass spectrometry of large biomolecules. In: A.L. Burlingame, J.A. McCloskey, editors. Biological Mass Spectrometry. *Elsevier Science Publishers, Amsterdam.* **1990**, pp. 49–60.
- [67]. M. J. Stump, R. C. Fleming, W. H. Gong, A. J. Jaber, J. J. Jones, C. W. Surber, C. L. Wilkins. Matrix assisted laser desorption mass spectrometry. *Appl. Spectrosc. Rev.* **2002**, 37, 275-303.
- [68]. X. J. Chen, J. A. Carroll, and R. C. Beavis. Near-ultraviolet-induced matrix-assisted laser desorption/ionization as a function of wavelength. *Journal of the American Society for Mass Spectrometry.* **1998**, 9 (9), 885-891.

- [69]. C.G. Herbert, R. A. W. Johnstone. Mass spectrometry basics. *CRC press; Boca London, New York Washington. D.C.* **2003**, pp 11.
- [70]. D. J. Harvey. Matrix-assisted laser desorption/ionization mass spectrometry of carbohydrates and glycoconjugates. *Int. J. Mass Spectrom.* **2003**, 226, 1–35.
- [71]. M. Balazy. Eicosanomics: Targeted lipidomics of eicosanoids in biological systems. *Prostag. Other Lipid Mediat.* **2004**, 73, 173–180.
- [72]. J. H. Banoub, P. Thibault, A. Mansour, A. Cohen, D. H. Heeley and D. Jackman. Characterisation of the intact rainbow trout vitellogenin protein and analysis of its derived tryptic and cyanogen bromide peptides by matrix-assisted laser desorption/ionisation time-of-flight-mass spectrometry and electrospray ionisation quadrupole/time-of-flight mass spectrometry. *Eur. J. Mass Spectrom. (Chichester, Eng).* **2003**, 9, 509–524.
- [73]. H. Therisod, V. Labas, M. Caroff. Direct micro extraction and analysis of rough-type lipopolysaccharides by combined thin-layer chromatography and MALDI mass spectrometry. *Anal Chem.* **2001**, 73, 3804-3807.
- [74]. G. B. Hurst, T. K. Lankford, S. J. Kennel. Mass Spectrometric Detection of Affinity Purified Crosslinked Peptides. *J. Am. Soc. Mass Spectrom.* **2004**, 15, 832-839.
- [75]. I. G. Gut. DNA analysis by MALDI-TOF mass spectrometry. *Hum. Mutat.* **2004**, 23, 437–441.
- [76]. R. C. Beavis, B. T. Chait. Factors Affecting the UltravioletLaser Desorption of Proteins. *Rapid Commun. Mass Spectrom.* **1989**, 3(7), 233–237.
- [77]. R. C. Beavis, T. Chaudhary, and B. T. Chait. A-Cyano-4-hydroxycinnamic Acid as a Matrix for Matrix-assisted Laser Desorption Mass Spectrometry. *Organic Mass Spectrom.* **1992**, 27, 156-158.

- [78]. R. Knochenmuss. A quantitative model of UV matrix-assisted laser desorption/ionization. *J. Mass Spectrom.* **2002**, 37, 867.
- [79]. M. Karas, and R. Kruger. Ion formation in MALDI: The cluster ionisation mechanism. *Chem. Rev.* **2003**, 103, 427.
- [80]. K. Dreisewerd. The desorption process in MALDI. *Chem. Rev.* **2003**, 103, 395.
- [81]. V. V. Laiko, M. A. Baldwin and A. L. Burlingame. Atmospheric pressure matrix-assisted laser desorption/ionization mass spectrometry. *Anal. Chem.* **2000**, 72, 652–7.
- [82]. V. V. Laiko, S. C. Moyer, R. J. Cotter. Atmospheric Pressure MALDI/Ion Trap Mass Spectrometry. *Anal. Chem.* **2000**, 72, 5239–43.
- [83]. Y. C. Chen, J. Shiea, and J. Sunner. Thin-layer chromatography-mass spectrometry using activated carbon, surface-assisted laser desorption/ionization. *J. Chromatogr. A.* 1998, 826, 77.
- [84]. Z. X. Shen, J. J. Thomas, C. Averbuj *et al.* Porous Silicon as a Versatile Platform for Laser Desorption/Ionization Mass Spectrometry. *Anal. Chem.* **2001**, 73, 612.
- [85]. J. F. de la Mora, G. J. Van Berkel, C. G. Enke *et al.* Electrochemical processes in electrospray ionization mass spectrometry. *J. Mass. Spectrom.* **2000**, 35, 939–52.
- [86]. E. D. Hoffmann, V. Stroobant. Principles and application mass spectrometry. Third edition. *John wily and sons. Ltd.* **2007**, pp 43.
- [87]. N. B. Cech, and C. G. Enke. Practical implications of some recent studies in electrospray ionization fundamentals. *Mass Spectrom. Rev.* **2001**, 20, 362–87.
- [88]. T. C. Rohner, N. Lion, and H. H. Girault. Electrochemical and theoretical aspects of electrospray ionisation. *Chem. Phys.* **2004**, 6, 3056–68.

- [89]. M. Yamashita, and J. B. Fenn. Electrospray ion source. Another variation on the free-jet theme. *Phys. Chem.* **1984**, 88, 4451.
- [90]. J. A. Loo, H. R. Udseth, and R. D. Smith. Peptide and protein analysis by electrospray ionization-mass spectrometry and capillary electrophoresis-mass spectrometry. *Anal. Biochem.* **1989**, 179, 404.
- [91]. M. G. Ikonomou, A. T. Blades, P. Kebarle. Investigations of the Electrospray Interface for Liquid Chromatography/Mass Spectrometry. *Anal. Chem.* **1990**, 62, 957-967.
- [92]. R. D. Smith, J. A. Loo, C. G. Edmons, H. R. Udseth. New developments in biochemical mass spectrometry: Electrospray ionization. *Anal. Chem.* **1990**, 62, 882.
- [93]. M. Mann. Electrospray: It's potential and limitations as an ionization method for biomolecules. *Org. Mass Spectrom.* **1990**, 25, 575.
- [94]. E. D. Hoffmann, V. Stroobant. Principles and application mass spectrometry. *Third edition. John wily and sons. Ltd.* **2007**, pp 44.
- [95]. J. V. Iribarne, B. A. Thomson. On the evaporation of small ions from charged droplets. *J. Chem. Phys.* **1976**, 64, 2287–2294.
- [96]. P. Kebarle. A brief overview of the present status of the mechanisms involved in electrospray mass spectrometry. *J. Mass Spectrom.* **2000**, 35, 804–817.
- [97]. R. E. Ferguson, K. E. McKulloh, H. M. Rosenstock. Observation of product of ionic collision process and ion decomposition. *J. Chem. Phys.* **1965**, 42, 100.

- [98]. H. Kienitz. Massenspektrometrie, editor; Verlag Chemie: Weinheim. **1968**, pp 125-154.
- [99]. D. C. Imrie, J. M. Pentney, and J. S. Cottrell. A Faraday cup detector for high-mass ions in matrix-assisted laser desorption/ionization time-of-flight mass spectrometry. *Rapid Commun. Mass Spectrom.* **1995**, 9, 1293.
- [100]. M. Moniatte, F. G. Vander Goot, J. T. Buckley, F. Pattus, A. van Dorsselaer. Characterisation of the heptameric pore-forming complex of the *Aeromonas* toxin aerolysin using MALDI-TOF mass spectrometry. *FEBS Lett.* **1996**, 384 (3), 269–72.
- [101]. L. Yang, T. D. Mann, D. Little, N. Wu, R. P. Clement, P. J. Rudewicz. Evaluation of a four-channel MUX ESI-MS/MS for the simultaneous validation of LC-MS/MS methods in four different pre-clinical matrix. *Anal. Chem.* **2001**, 73, 1740.
- [102]. O. Fiehn, J. Kopka, R. N. Trethewey, L. Willmitzer. Identification of uncommon plant metabolites based on calculation of elemental compositions using gas chromatography and quadrupole mass spectrometry. *Anal. Chem.* **2000**, 72, 3573–3580.
- [103]. P. Schmitt-Kopplin, M. Frommberger. Capillary electrophoresis-mass spectrometry: 15 years of development and application. *Electrophoresis.* **2003**, 24, 3837–3867.
- [104]. R. E. March. Ion trap mass spectrometry. *Int. J. Mass Spectrometrom. Ion Process.* **1992**, 118, 71.
- [105]. R. G. Cooks, G. L. Glish, S. A. McLuckey, R. E. Kaiser. Ion trap mass spectrometry. *Chem. Eng. News.* **1991**, 69, 26.
- [106]. M. B. Comisarow, and A.G. Marshall. Fourier transform ion cyclotron resonance

spectroscopy. *Chem. Phys. Lett.* **1974**, 25, 282–3.

[107]. M. B. Comisarow, A. G. Marshall. Frequency sweep fourier transform ion cyclotron resonance spectroscopy. *Chem. Phys. Lett.* **1974**, 26, 489–90.

[108]. I. J. Amster. Fourier transforms mass spectrometry. *J. Mass Spectrom.* **1996**, 31, 1325–37.

[109]. A. G. Marshall, C. L. Hendrickson, and G. S. Jackson. Fourier transform ion cyclotron resonance mass spectrometry: a primer. *Mass Spectrom. Rev.* **1998**, 17, 1–35.

[110]. R. N. Schwartz, Z. I. Slawsky, K. F. Herzfeld. Calculation of vibrational relaxation times in gases. *J. Chem. Phys.* **1952**, 20, 1591.

[111]. J. N. Louris, J. S. Brodbelt-Lusting, R. G. Cooks, G. L. Glish, G. J. Van Berkel and S. A. McLuckey. Ion isolation and sequential stages of mass spectrometry in a quadrupole ion trap mass spectrometer. *Int. J. Mass Spectrom. Ion Process.* **1990**, 96, 117–137.

[112]. R. A. Yost, C. G. Enke. Selected ion fragmentation with a tandem quadrupole mass spectrometer. *J. Am. Chem. Soc.* **1978**, 100, 2274-2275.

[113]. M. A. Cohn, F. Jahouh, S. Soiad, M. R. Rideout, M. J. Morgan, J. H. Banoub.

Quantitification of Greenland Halibut serum Vitellogenin: atrip from the deep sea to the mass spectrometer. *R.commun. Mass. Spectrom.* **2009**, 23, 1049-1060.

[114]. (a) J. H. Banoub, A. El-Aneed, A. Cohen, P. Martin. Characterisation of the O-4 Phosphorylated and O-5 Substituted Kdo Reducing end Group and Sequencing of the core Oligosaccharide of *Aeromonas salmonicida* ssp *Salmonicida* Lypopolysaccaride using Tandem mass spectrometry. *Eur.j.mass.spectroum.* **2004a**, 10, 715-730.

- (b) J. H. Banoub, A. Cohen, A. El-aneed, P. Martin, V. LeQuart. Structural Reinvestigation of the core Oligosaccharide of a Mutant from *Aeromonas Salmonicida* Lipopolysaccharides containing an *O*-4 Phosphorylated and *O*-6 substituted Kdo reducing end group using electrospray quadrupole Time-of-Flight Tandem Mass spectrometry. *Eur. J. Mass Spectrom.* **2004b**, *10*, 541-554.
- [115]. A. Sinz, S. Kalkhof, C. Ihling. Mapping protein interference by a trifluorofunctional cross-linker combined with Maldi-tof and ESI-FTICR Mass. Spectrom. *J. Am. Soc. Mass spectrom.* **2005**, *16*, 1921-1931.
- [116]. A. G. Harrison, R. S. Mercer, E. J. Reiner, A. B. Young, R. K. Boyd, R. E. March, C. J. Porter. A Hybrid Beq Mass-Spectrometer for Studies in Gaseous Ion Chemistry. *Int. J. Mass Spectrom. Ion Processes.* **1986**, *74*, 13-31.
- [117]. D. Suckau, A. Resemann, M. Schuerenberg, P. Hufnagel, J. Franzen, A. Holle. A novel MALDI-LIFT-TOF/TOF mass spectrometer for proteomics. *Analytical and Bioanalytical Chemistry.* **2003**, *376* (7), 952–965.
- [118]. K. R. Jennings. Collision-induced decompositions of aromatic molecular ions. *Int J. Mass Spectrom. Ion Phys.* **1968**, *1*, 227–235.
- [119]. F. W. McLafferty, P. F. Bente, R. Kornfeld, S. Tsai and I. Howe. Metastable ion characteristics. XXII. Collisional activation spectra of organic ions. *J. Am. Chem. Soc.* **1972**, *95*, 2120–2129.
- [120]. (a) B. Domon, C. E. Costello. Structure elucidation of glycosphingolipids and gangliosides using high-performance tandem mass spectrometry. *Biochemistry.* **1988**, *27*, 1534-1543.

(b) B. Domon, C. E. Costello. A systematic nomenclature for carbohydrate fragmentations in FAB-MS/MS spectra of glycoconjugates. *Glycoconjugate J.* **1988b**, 5, 397–409.

[121]. (a) J. H. Banoub, A. El-Aneed, A. cohen, P. Martin. Characterisation of the *O*-4 Phosphorylated and *O*-5 Substituted Kdo Reducing end Group and Sequencing of the core Oligosaccharide of *Aeromonas salmonicida* ssp *Salmonicida* Lipopolysaccharide using Tandem mass spectrometry. *Eur.j.mass.spectroum.* **2004a**, 10, 715-730.

(b) J. H. Banoub, A. Cohen, A. El-aneed, P. Martin, V. LeQuart. Structural reinvestigation of the core oligosaccaside of a mutant from of *Aeromonas Salmonicida* lipopolysaccharides containing an *O*-4 Phosphorylated and O-% substituted Kdo reducing end group using electrospray quadreoupole time-of-flight Tandem Mass spectrometry. *Eur.J.Mass Spectrum.* **2004b**, 10, 541-554.

[122]. http://www.chemistry.wustl.edu/msf/damon/sample_prep_toc.html" (21 March 2007).

[123]. <http://www.nist.gov/maldi> (21 March 2007).

[124]. L. R. Lynd. Overview and evaluation of fuel ethanol from cellulosic biomass: technology, economics, the environment, and policy. *Annu. Rev. Energy Env.* **1996**, 21, 403.

[125]. J. R. Obst, T. K. Kirk. Isolation of lignin. In methods in enzymology: biomass, wood WA, Kellog ST (eds). *Academic Press: San Diego.* **1998**, pp 3.

[126]. B. Benjelloun-Mlayah, M. Delmas, G. Avignon. Installation for implementing a method for producing paper pulp, lignins and sugars and production method using such an installation, Patent no. WO2006117295, **2006**.

- [127]. H. R. Morris, T. Paxton, M. Panico, R. McDowell, A. Dell. A novel geometry mass spectrometer, the Q-TOF, for low femtomole/attomole-range biopolymer sequencing. *J. Protein Chem.* **1997**, *16*, 469–479.
- [128]. A. Shevchenko, I. Chernushevich, W. Ens, K.G. Standing, B. Thomson, M. Wilm, M. Mann. Rapid ‘de novo’ peptide sequencing by a combination of nanoelectrospray, isotopic labeling and a quadrupole/time-of-flight mass spectrometer. *Rapid Commun Mass Spectrom.* **1997**, *11*, 1015–1024.
- [129]. E. D. Hoffmann, V. Stroobant. Principles and application mass spectrometry. Third edition. *John wily and sons. Ltd.* **2007**. pp 198.
- [130]. J. H. Banoub , R. P. Newton , E. Esmans , D. F. Ewing , and G. Mackenzie. Recent developments in mass spectrometry for the characterization of nucleosides, nucleotides, oligonucleotides, and nucleic Acids. *Chem. Rev.* **2005**, *105* (5), 1869–1916.
- [131]. M. Karas, D. Bachmann, U. Bahr, F. Hillenkamp. Matrix-assisted ultraviolet laser desorption of non-volatile compounds. *Int. J. Mass Spectrom. Ion Processes.* **1987**, *78*, 53.
- [132]. D. Garozzo, E .Spina, L. Sturiale, G. Montaudo, R. Rizzo. Quantitative determination of b (1-2) cyclic glucans by matrix-assisted laser desorption mass spectrometry. *Rapid Commun Mass Spectrom.* **1994**, *8*, 358-360.
- [133]. B. Spengler, D. Kirsch, R. Kaufmann, J. Lemoine. Structure analysis of branched Oligosaccharides Using Post source Decay in Matrix Assisted Laser Desorption Ionization Mass Spectrometry. *J. Mass Spectrom.* **1995**, *30*, 782-787.

- [134]. R. Kaufmann, P. Chaurand, D. Kirsch and B. Spengler. Post-source decay and delayed extraction in matrix-assisted laser desorption/ionization-reflectron time-of-flight mass spectrometry. *Rapid Commun. Mass Spectrom.* **1996**, *10*, 1199.
- [135]. Y. Mechref, C. Krishnan, and M. V. Novotny. Structural characterization of oligosaccharides using MALDI-TOF/TOF tandem mass spectrometry. *Anal Chem.* **2003**, *75*, 4895–4903.
- [136]. E. Spina, L. Sturiale, D. Romeo, G. Impallomeni, D. Garozzo, D. Waidelich, and M. Glueckmann. New fragmentation mechanisms in matrix-assisted laser desorption/ionization time-of-flight/time-of-flight tandem mass spectrometry of carbohydrates. *Rapid Commun. Mass Spectrom.* **2004**, *18*, 392–398.
- [137]. B. Spengler, J. W. Dolce, R. J. Cotter. Infrared-Laser Desorption Mass-Spectrometry of Oligosaccharides-Fragmentation Mechanisms and Isomer Analysis. *Anal. Chem.* **1990**, *62*, 1731-1737.
- [138]. G. E. Hofmeister, Z. Zhou, J. A. Leary. Linkage position determination in lithium cationized disaccharides: tandem mass spectrometry and semiempirical calculations. *J. Am. Chem. Soc.* **1991**, *113*, 5964–5970.
- [139]. R. Orlando, C. A. Bush, C. Fenselau. Structural analysis of oligosaccharides by tandem mass spectrometry: Collisional activation of sodium adduct ions. *Biomed. Environ. Mass Spectrom.* **1990**, *19*, 747–754.
- [140]. E. D. Hoffmann, V. Stroobant. Principles and application mass spectrometry. Third edition. *John wily and sons. Ltd.* **2007**, pp 159.

- [141]. J. V. Johnson, R. A. Yost, P. E. Kelley, D. C. Bradford. Tandem-in-space and tandem-in-time mass spectrometry: Triple quadrupoles and quadrupole ion traps. *Anal Chem.* **1990**, *62*, 2162–2172.
- [142]. J. F. J. Todd. Ion-trap mass spectrometer-past, present, and future. *Mass Spectrom Rev.* **1991**, *10*, 3–52.
- [143]. R. E. March. Quadrupole ion-trap mass spectrometry: Theory, simulation, recent developments and applications. *Rapid Commun Mass Spectrom.* **1998**, *12*, 1543–1554.
- [144]. R. E. March. Quadrupole ion trap mass spectrometry: A view at the turn of the century. *Int J. Mass Spectrom.* **2000**, *200*, 285–312.
- [145]. V. N. Reinhold, D. M. Sheeley. Detailed characterization of carbohydrate linkage and sequence in an ion-trap mass spectrometer: Glycosphingolipids. *Anal Biochem.* **1998**, *259*, 28–33.
- [146]. D. M. Sheeley, V. N. Reinhold. Structural characterization of carbohydrate sequence, linkage, and branching in a quadrupole ion-trap mass spectrometer: Neutral oligosaccharides and *N*-linked glycans. *Anal Chem.* **1998**, *70*, 3053–3059.
- [147]. A. S. Weiskopf, P. Vouros, D. J. Harvey. Electrospray ionization-ion trap mass spectrometry for structural analysis of complex *N*-linked glycoprotein oligosaccharides. *AnalChem.* **1998**, *70*, 444–4447.
- [148]. N. Viseux, E. D. Hoffmann, B. Domon. Structural assignment of permethylated oligosaccharide subunits using sequential tandem mass spectrometry. *Anal Chem.* **1998**, *70*, 4951–4959.
- [149]. K. Tseng, J. L. Hedrick, C. B. Lebrilla. Catalog-library approach for the rapid and sensitive structural elucidation of oligosaccharides. *Anal Chem.* **1999**, *71*, 3747–3754.

- [150]. A. Payen. Comptes Rendus De L Academie Des Sciences Serie Iii-Sciences De La Vie. *Life Sciences*. **1838**, 7, 1052-1054.
- [151]. K. V. Sarkanen, H. L. Hergert. Classification and distribution. In Lignins: Occurrence, Formation, Structure and Reactions. Sarkanen, K.V., Ludwig, C.H. New York, NY, *Wiley-interscience*. **1971a**, pp 43-94. K. V. Sarkanen., C.H . Ludwig, Definition and nomenclature. In Lignins: Occurrence, Formation, Structure and Reaction. *New York, NY, Wiley interscience*. **1971b**. pp. 1-41.
- [152]. E. Sjöström. Wood chemistry: fundamentals and applications. *New York, NY, Academic Press*. **1981**. pp 68-82.
- [153]. C. L. Chen. Lignins: Occurrence in woody tissues, isolation, reactions, and structure. In wood structure and composition. Lewin, M, Goldstein, I.S. *New York, Marcel Dekker, Inc.***1991**. pp 183-261.
- [154]. A. Björkm-an. Isolation of lignin from finely divided wood with neutral solvents. *Nature*. **1954**, 174, 1057-1058.
- [155]. Y. Z. Lai, K. V. Sarkanen. Isolation and structural studies. In lignins: occurrence, formation, structure and reactions. K. V. Sarkanen, C. H. Cludwig, New York, *Wiley interscience*. **1971**. pp 165-230.
- [156]. E. Adler. Lignin chemistry-past, present and future. *Wood Science and Technology* **1977**, 11, 169-218.
- [157]. A. Sakakibara. Chemistry of lignin. In Wood and Cellulose Chemistry. Hon, D.-S., Shiraishi, N. *New York, NY, Marcel Dekker Inc*. **1991**, pp 113-175.
- [158]. S. Y. Lin, C. W. Dence. Methods in lignin chemistry. *Springer-Verlag, Berlin*. **(1992)**

- [159]. P. Bocchini, G.C. Galletti, S. Camarero, A.T. Martinez. Absolute quantitation of lignin pyrolysis products using an internal standard. *J. Chromatogr. A*, **1999**, 773, 227
- [160]. J. Rodrigues, D. Meier, O. Faix, H. Pereira, Determination of tree to tree variation in syringyl/guaiacyl ratio of *Eucalyptus globulus* wood lignin by analytical pyrolysis. *J. Anal. Appl. Pyrolysis* **1999**, 48, 121
- [161]. T. Sonoda, T. Ona, H. Yokoi, Y. Ishida, H. Ohtani, S. Tsuge. Quantitative analysis of detailed lignin monomer composition by pyrolysis-gas chromatography combined with preliminary acetylation of the samples. *Anal. Chem.* **2001**, 73, 5429
- [162]. J.C. del Río, A. Gutiérrez, J. Romero, M.J. Martínez, A.T. Martínez. Identification of residual lignin markers in eucalypt kraft pulps by Py-GC/MS. *J. Anal. Appl. Pyrolysis* **2001**, 58, 425.
- [163]. W.J. Irwin. *Analytical Pyrolysis - A Comprehensive Guide*. New York, John Wiley & Sons, **1982**.
- [164]. K. Syverud, I. Leirset, D. Vaaler. Characterization of carbohydrates in chemical pulps by pyrolysis gas chromatography/mass spectrometry. *J. Anal. Appl. Pyrolysis* **2003**, 67, 381
- [165]. A. Alves, M. Schwanninger, H. Pereira, J. Rodrigues. Analytical pyrolysis as a direct method to determine the lignin content in wood: Part 1: Comparison of pyrolysis lignin with Klason lignin. *J. Anal. Appl. Pyrolysis* **2006**, 76, 209
- [166]. O. Faix, J. Bremer, D. Meier, I. Fortmann, M.A. Scheijen, J.J. Boon. Characterization of tobacco lignin by analytical pyrolysis and Fourier transform-infrared spectroscopy. *J. Anal. Appl. Pyrolysis* **1992**, 22, 239

- [167]. O. Faix, D. Meier, I. Fortman. Thermal degradation products of wood Gas chromatographic separation and mass spectrometric characterization of monomeric lignin derived products. *Holz Roh-Werkst.* **1990**, 48, 281
- [168]. J. Ralph, R.D. Hatfield. Pyrolysis-GC-MS characterization of forage materials. *J. Agric. Food Chem.* **1991**, 39, 1426
- [169]. H. Yokoi, T. Nakase, Y. Ishida, H. Ohtani, S. Tsuge, T. Sonoda, T. Ona. Discriminative analysis of *Eucalyptus camaldulensis* grown from seeds of various origins based on lignin components measured by pyrolysis-gas chromatography. *J. Anal. Appl. Pyrolysis* **2001**, 57, 145
- [170]. S. Reale, A. Di Tullio, N. Spreti, F. De Angelis. Mass spectrometry in the biosynthetic and structural investigation of lignins. *Mass Spectrom. Rev.* **2004**, 23, 87.
- [171]. J. H. Banoub, B. B. Mlayah, F. Ziarelli, N. Joly and M. Delmas. Elucidation of the complex molecular structure of wheat straw lignin polymer by atmospheric pressure photoionization quadrupole time-of-flight tandem mass spectrometry. *Rapid Commun. Mass Spectrom.* **2007**, 21, 2867–2888
- [172]. J. H. Banoub. Structural elucidation of the wheat straw lignin polymer by atmospheric pressure chemical ionization tandem mass spectrometry and matrix-assisted laser desorption/ionization time-of-flight mass spectrometry. *J. Mass Spectrom.* **2003**, 38, 900–903